Modelling the collective migration of neural crest cells



Rasa Giniūnaitė

Jesus College

University of Oxford

A thesis submitted for the degree of

Doctor of Philosophy

Hilary 2021

Acknowledgments

Firstly, I would like to express my sincere gratitude to my supervisors Prof. Ruth E. Baker and Prof. Philip K. Maini for their continuous support in difficult situations, patience and immense knowledge. Their inspirational ideas, motivation and wise advice made my DPhil interesting and enjoyable. My genuine thanks also goes to Dr. Martin Robinson for his valuable help with the technical part of the project.

Besides my supervisors, I would like to thank our experimental colleagues, Dr. Paul Kulesa, Dr. Rebecca McLennan, Jason Morrison and Dr. Cathy McKinney, at the Stowers Institute for Medical Research, for their insightful ideas and willingness to share their biological findings. I am also very grateful for their warm welcome and constructive discussions during our visit to the Stowers Institute.

I am grateful to my Doctoral Training Centre and Wolfson Centre for Mathematical Biology colleagues for friendly scientific atmosphere, useful conversations about our work and issues that we all face.

I would like to acknowledge the UK Engineering and Physical Sciences Research Council for funding my work through a studentship at the Systems Biology Doctoral Training Centre.

Finally, I would like to thank my family and friends for their constant encouragement, joyful moments and support.

Abstract

Collective neural crest cell migration contributes to the formation of several spatially and biologically diverse tissues during vertebrate development. If neural crest cells fail to reach a target or populate an incorrect location, then those cells may undergo improper cell differentiation or uncontrolled cell proliferation, leading to developmental defects. A wide range of mechanisms that drive collective cell migration are displayed by distinct types of neural crest cells that emerge at different axial levels of the neural tube and are affected by different local signals. For example, chick cranial neural crest cells are understood to be guided by a cell-induced chemotactic gradient and their migration occurs within a growing tissue, whilst in Xenopus, cranial neural crest cells are understood to be guided by co-attractive and co-repulsive intercellular interactions in the absence of growth. However, there are still many open questions as to how neural crest cells interact with each other and their microenvironment to undergo successful migration. Answers to these questions would not only help us understand embryonic development, but also provide insights into other less experimentally tractable collective migration phenomena, such as wound healing and tumour formation.

In this thesis we investigate the migration of chick cranial neural crest cells using a hybrid computational model, which consists of a discrete, off-lattice model for the motile behaviour of neural crest cells coupled with a continuum, reaction-diffusion model for the chemoattractant concentration. We work in parallel with our experimental colleagues who perform imaging of chick embryos under certain perturbations. In particular, we use our model to explore the role of the water-specific aquaporin 1 channel and spatial confinement on the migration of neural crest cells. We also investigate how domain growth affects collective cell migration. In the final part of the thesis, we develop a unified individual-based stochastic model to include the different cell-cell interaction mechanisms observed in Xenopus and chick. The model is used to compare and contrast the behaviour of neural crest cells in different organisms and to further investigate the cell-cell interaction mechanisms in chick.

Abbreviations

AQP-1 aquaporin 1

BrdU Bromodeoxyuridine

CiL contact inhibition of locomotion

ECM extracellular matrix

HH Hamburger Hamilton

IBM individual-based model

MMP matrix metalloproteinase

NCC neural crest cells

PCP planar cell polarity

PDE partial differential equation

SDF1 stromal cell-derived factor 1

VEGF vascular endothelial growth factor

Contents

1 Introduction **1**

1.1 Biological background 4

1.1.1 Contact inhibition of locomotion 5

1.1.2 Co-attraction 6

1.1.3 External guidance 6

1.1.4 Chick cranial neural crest cells 8

1.2 Modelling neural crest cell migration 10

1.2.1 Individual-based models for neural crest cell migration on a fixed domain 10

1.2.2 Individual-based models for neural crest cell migration on a growing domain 12

1.2.3 Partial differential equation models for neural crest cell migration . . . 13

1.2.4 Integro-partial differential equation models for neural crest cell migration 14

1.2.5 Modelling chick cranial neural crest cell migration 16

1.3 Aims of this thesis 23

2 How can directional guidance cues facilitate collective cell migration? 26

2.1 Biological background 27

2.1.1 The role of AQP-1 in cranial neural crest cell migration 27

2.1.2 Neural crest cell confinement 28

2.2 Incorporating AQP-1 into the computational model 31

2.3 Effect of changes in cell speed, stabilisation, polarisation and number of filopodia induced by manipulation of AQP-1 expression 45

2.4 Effect of extracellular matrix degradation induced by AQP-1 overexpression . . 52

2.5 Investigation of neural crest cell spatial confinement 53

2.5.1 Results 57

2.6 Conclusions and discussion 63

3 Spatially non-uniform domain growth 66

3.1 Biological background 67

3.2 Extension of the model to allow for spatially non-uniform domain growth . . . 74

3.3 Effect of different domain growth profiles on the furthest distance travelled . . 77

3.4 Cell speed on a growing domain 85

3.4.1 Observed cell speed for different growth profiles 88

3.4.2 Leader-follower cell speed 91

3.5 What does the model predict if we use experimentally observed domain growth profiles? . . . 92

3.6 Physical ablation of neural crest cells . . . 96

3.7 Chemical inhibition of mesodermal cell proliferation . . . 99

3.8 How do neural crest cells affect domain growth? . . . 101

3.8.1 NCC-induced growth profile: physical neural crest cell ablation . . . 105

3.8.2 NCC-induced growth profile: chemical growth inhibition . . . 105

3.9 Conclusions and discussion . . . 110

4 Comparison of different interaction mechanisms in chick and Xenopus 113

4.1 Biological background . . . 115

4.2 Detailed review of the key computational models used for cranial neural crest cell invasion in Xenopus and chick . . . 117

4.3 A flexible computational model to incorporate simple cell-cell interactions . . . 121

4.3.1 Lennard-Jones potential . . . 124

4.4 Definitions and techniques . . . 127

4.5 Methods . . . 134

4.6 Modelling Xenopus cranial neural crest cell invasion . . . 136

4.6.1 Xenopus: results . . . 137

4.6.2 Xenopus: conclusions . . . 142

4.7 Modelling chick cranial neural crest cell invasion . . . 143

4.7.1 Chick: results . . . 144

4.7.2 Chick: conclusions . . . 152

4.8 Comparison of the modelling results for Xenopus and chick . . . 154

4.9 Conclusions and discussion . . . 158

5 Discussion and future work **160**

5.1 Summary . . . 161

5.2 Future work . . . 163

Appendices **169**

A Numerical methods and convergence for Chapter 2 . . . 170

B Numerical methods and convergence for Chapter 3 . . . 173

C Numerical methods and convergence for Chapter 4 . . . 175

D Xenopus data . . . 180

D.1 Successful invasion . . . 180

D.2 Time to invasion . . . 181

E Chick data . . . 184

E.1 Invasion . . . 184

E.2 Stream breakage . . . 187

E.3 Time to invasion 190

Chapter 1

Introduction

Cell migration is crucial in many areas of biology and medicine, including embryonic development, cancer, wound healing and tissue regeneration (Friedl and Gilmour, 2009). In most of these biological systems, cells migrate in groups as a result of cell-cell communication and cell-tissue interactions; a phenomenon known as collective cell migration. Understanding the mechanisms that underpin and control collective cell migration can help us to prevent mis-targeted or uncontrolled migration, which can result in abnormalities such as developmental defects, or diseases such as cancer metastasis.

One of the key challenges we face when trying to understand collective cell migration arises due to the multiscale nature of the phenomenon where, by multiscale, we mean the interaction of processes acting across a range of spatial scales, from the intracellular to the tissue level. Collective cell migration is usually characterised not only by cell-cell communication, but also by cell-tissue interactions, which require careful understanding of the surrounding tissue through which, or on which, the cells are moving. Interactions can range from those that occur locally via, for example, cell body contact, to those that are highly non-local via, for example, extended cell protrusions (Tucker and Erickson, 1986; Teddy and Kulesa, 2004). Complex feedback mechanisms may be involved in both cell-cell and cell-

tissue interactions. The combination of all these phenomena makes collective cell migration a highly complex process, and individual fields, including biology and mathematics, have to be integrated to fully interpret data and understand the process.

In this thesis we focus on the collective migration of embryonic neural crest cells (NCCs). NCCs are multipotent, highly migratory cells that delaminate from the neural tube all along the vertebrate axis and traverse along well-defined migratory routes to precise targets, where they differentiate (Figure 1.1). NCCs exemplify the diverse mechanisms that drive collective cell migration because, even within a single species, a wide range of mechanisms are displayed by distinct types of NCCs that emerge at different locations (for example, cranial, cardiac, vagal, and trunk), and are affected by different signalling pathways (see, for example, the reviews by Theveneau et al. (2010); Schumacher et al. (2016); Szabó and Mayor (2016); Szabó and Mayor (2018)). Moreover, there are differences across different species, such as different guidance mechanisms in chick and Xenopus, and different gene expressions in non-mammalian species in comparison with mouse (Theveneau and Mayor, 2012; Barriga et al., 2015).

In addition, the collective migration of NCCs has been studied not only to understand embryonic development and the reasons for developmental defects, but also to gain insights into metastatic cancer. This is possible due to the remarkable similarities between the gene expression profiles of migrating NCCs and highly invasive tumour cells (Theveneau and Mayor, 2011; Kulesa et al., 2013). Experiments on, and observations of, *in vivo* cancer cells are highly challenging, so the study of the more experimentally tractable system of NCCs can provide clues for potential therapeutic intervention in cancer.

The great variety of different mechanisms of migration, together with the experimental tractability of the NCC system, ensure the generation of extensive biological data which can, in turn, be used to generate experimental hypotheses. Due to the fact that the system exhibits complex, nonlinear, local and non-local feedback, which is difficult to interpret, it is typically the case that the hypotheses are verified using computational modelling

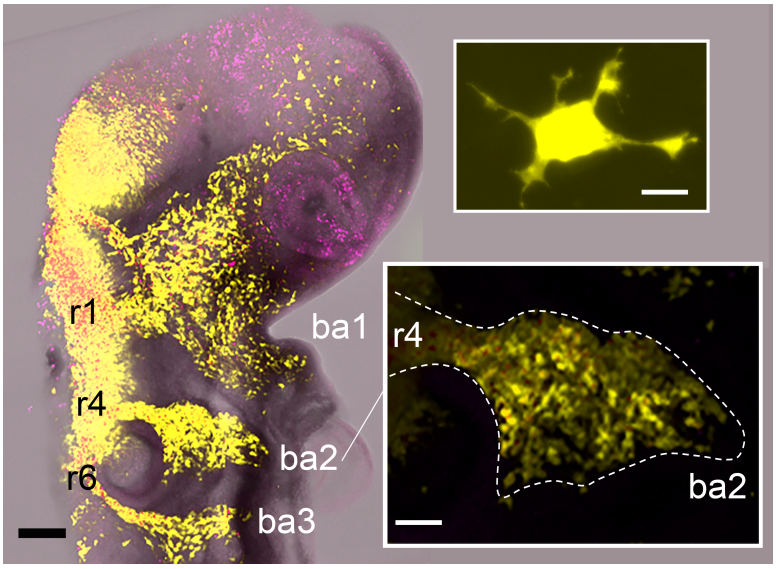


Figure 1.1: NCC migratory streams in the chick head co-labelled with pMES (EGFP) in yellow and DiI in purple. Rhombomeric segments of the hindbrain, from which some of the cranial NCCs emerge, are labelled rhombomere 1 (r1), r4 and r6, with branchial arch (ba) target sites, ba1, ba2, ba3, and the scale bar is 200μm (black). The top inset shows a typical individual migrating NCC, and the scale bar is 10μm (white). The bottom inset is the NCC migratory stream adjacent to r4 and the scale bar is 100μm (white). Figure reproduced from Giniūnaitė et al. (2020a) with permission from Springer.

and then model predictions can be tested through custom-designed experiments. Computational models are particularly useful because they can be used to extract unifying principles underlying the complex mechanisms of collective migration and explore cell behaviours under various perturbations.

Despite the tractability of the NCC system, there are still many unanswered questions about the mechanisms underlying the successful invasion of NCCs. For example, we still do not know the precise mechanisms of cell-cell and cell-tissue interactions in NCCs nor the reasons for the differences across animal species or at different axial levels. In this thesis we address a number of aspects of these key questions.

In the remainder of this chapter, we give a brief introduction to the biology of NCCs

and review the current state of the field in terms of experimental understanding and previous mathematical models. We end the chapter by stating the aims and outline of this thesis.

1.1 Biological background

NCCs originate from the ectoderm, which is one of the layers of tissue formed after gastrulation in the early vertebrate embryo. More specifically, in the early stage of development the ectoderm sinks into the mesoderm and forms a structure called the neural tube, which gives rise to the brain and spinal cord. At the crest of the neural tube, NCCs undergo an epithelial to mesenchymal transition. This transition means that NCCs acquire new properties, such as motility, invasiveness and apoptotic resistance (Kalluri and Weinberg, 2009). Subsequently, they are released to migrate away from the neural tube and settle at different sites. Depending on environmental cues, they generate a prodigious number of differentiated cell types. These cell types include: (1) pigment cells; (2) structures of the sensory, sympathetic, and parasympathetic nervous systems, including the neurons and glial cells; and (3) skeletal and connective tissue components, in addition to most of the cranial and visceral skeleton (Gilbert, 2000). The collective migration of NCCs is affected by multiple factors such as cell-cell interactions, cell-environmental interactions and cell heterogeneity. These factors include contact inhibition, interactions with the extracellular matrix (ECM), as well as repulsive cell-cell guidance via the EphB/EphrinB and semaphorin/neuropilin signalling pathways (Sanes, 2012), and attractive cell-environment guidance via vascular endothelial growth factor (VEGF) and stromal cell-derived factor 1 (SDF1) (McLennan et al., 2010; Theveneau et al., 2010). In addition, NCCs migrate through the growing embryonic tissue, therefore their migration is influenced by tissue growth. While it is known that the aforementioned guidance cues and environmental factors affect NCC migration, precisely how NCCs respond to different microenvironments to maintain persistent direction and cohesion in multicellular streams is still an open question, which we will try to answer in this thesis

by exploring the role of different guidance mechanisms and microenvironments.

It is important to note that different organisms have different NCC systems which vary in cell density, cell structure and migration mechanisms. In this thesis we mostly restrict our focus to chick cranial NCC migration, but later expand our investigations with a comparison of chick and Xenopus cranial NCC migration. Finding similarities and differences between these systems may help identify some unifying mechanisms for collective migration.

In the next sections we review the currently accepted mechanisms for how NCCs interact with each other and their environment. We finish this biological background review with a more detailed description of the biology of chick cranial NCC migration, the modelling of which is the main focus of this thesis.

1.1.1 Contact inhibition of locomotion

Contact inhibition of locomotion (CiL) is an important complex cell-cell interaction mechanism that causes migratory cells to momentarily stop upon physical contact with one another and subsequently repolarise in the opposite direction from the contact (Mayor and Carmona-Fontaine, 2010). The phenomenon was first described in the 1950s (Abercrombie and Heaysman, 1953), and suggested as an explanation for the collective migration of NCCs in the avian embryo in the 1980s (Erickson, 1985). The molecular mechanisms of CiL in NCCs, and its influence on the migration of NCCs, have been explored using Xenopus and zebrafish cranial NCCs (Carmona-Fontaine et al., 2008; Theveneau et al., 2010). Carmona-Fontaine et al. (2008) found that transient contacts between two colliding NCCs involve N-cadherin and lead to a local activation of the Wnt/PCP pathway which, in turn, activates the GTPase RhoA and inhibits Rac1, thus repolarising the cell. A role for Wnt/PCP in trunk NCC migration has also been found in chick, zebrafish and mouse, but its connection with CiL has not been analysed (Banerjee et al., 2011; Rios et al., 2011).

1.1.2 Co-attraction

CiL induces dispersion of cells, therefore if we assume that the cell population is not confined, for example, in tunnels, then it cannot lead to collective migration on its own. This suggests that there should be an "opposite" phenomenon, namely co-attraction, to ensure that cells remain in a group. Based on this intuition, Carmona-Fontaine et al. (2011) demonstrated, using experiments on cranial NCCs in Xenopus, that there is co-attraction between cells via the cell secretion of the complement factor C3a and expression of receptor C3aR on the cell surface. C3aR signalling activates Rac1, which polarises the cells and directs them towards the others. Co-attraction happens at longer ranges than CiL because the contact is not direct, but via a secreted chemical. Co-attraction can therefore help to avoid dispersion of cells and facilitate collective cell migration. However, the experimentally observed migration of NCCs is not only collective, but also highly directed, which suggests that CiL and co-attraction are not the only mechanisms that control cell migration.

1.1.3 External guidance

The combination of CiL and co-attraction is sufficient for cells to stay in a loosely connected group and move randomly, but can they exhibit directed migration over long distances if these two factors are the only driving forces? In some organisms there is clear evidence that additional, external factors are necessary for successful cell invasion. In the migration of chick cranial NCCs, for example, there is strong evidence that the cells are guided via VEGF, which acts as a chemoattractant (McLennan et al., 2010). McLennan et al. (2010) demonstrated that invasion of cranial NCCs, specifically the rhombomere 4 migratory stream into branchial arch 2 (Figure 1.1), is due to chemoattraction through neuropilin-1-VEGF interactions. They injected soluble VEGF receptor 1 (sVEGFR1) into the tissue ahead of the migratory front, to bind endogenous VEGF, and then observed that NCCs failed to completely invade branchial arch 2. This experiment demonstrated that VEGF acts as a

guidance cue because, in the absence of VEGF, NCCs failed to invade the domain. Similarly, Belmadani et al. (2009) showed that the chemokine SDF1 provides attractive guidance for melanocyte progenitors in mouse hair follicles.

When cells are guided by a chemoattractant, they move up the gradient of chemoattractant by sensing the concentration at their position or where their sensory protrusions are located. If the gradient is formed because the cells consume or degrade the chemoattractant, then it is known as a cell-induced gradient, whereas if the concentration of chemoattractant is independent of cell positions, then the gradient is said to be fixed or variable but independent of cell positions. Internalisation of chemoattractant, and thus a cell-induced gradient, has been observed and studied in collective migration of cells in the zebrafish lateral line primordium (Streichan et al., 2011) and in chick cranial NCC migration (Kulesa et al., 2010; McLennan et al., 2012, 2015b, 2017).

Another interesting hypothesis for the external guidance of NCCs involves their interaction with placodal cells, which emerge in the ectoderm and form an epithelial tissue that contributes to the sensory organs (Theveneau et al., 2013). Theveneau et al. (2013) investigated the interaction of cranial NCCs in Xenopus with placodal cells, and concluded that NCCs "chase" placodal cells by chemotaxis, and placodal cells "run" when contacted by NCCs. The molecular mechanisms involved in this process were also revealed, namely chemotaxis to SDF1 secreted by placodal cells underlies the chase (attraction), while repulsion, i.e. the run, involves PCP and N-cadherin signalling. This is yet another intriguing finding on the directed movement of NCCs in a particular system.

Shellard et al. (2018) suggested a hypothesis that collective cell movement is driven by polarised contractility. They successfully used *in vivo* and *in vitro* systems of Xenopus and zebrafish NCCs to demonstrate that the cells are driven by chemotaxis to SDF1 which is induced through the intercalation of rear cells via asymmetric actomyosin contraction.

1.1.4 Chick cranial neural crest cells

In our work, we will investigate the collective migration of chick cranial NCCs, so here we will explicitly review the current knowledge in this area. A combination of experimental and computational studies on the collective migration of chick cranial NCCs has provided valuable insights for collective cell migration, specifically in elucidating how different guidance mechanisms may enable coherent movement. More specifically, McLennan and co-workers have shown that in order for cranial NCCs to reach their distal target, which is branchial arch 2 (Figure 1.2), the cells have to be heterogeneous, meaning that they possess different phenotypes (McLennan et al., 2012). In their computational model, they observed that if there was a single cell phenotype guided by a cell-induced chemoattractant VEGF gradient, then the cells could not invade as a coherent stream, because there would be a group of cells that would be left behind at the origin of the migratory domain due to the lack of chemoattractant gradient. However, if they introduced two NCC phenotypes, so-called "leaders" that generate and move up the gradient of chemoattractant and "followers", that follow (unspecified) signals from the leaders, then the simulations exhibited successful streaming migration (Figure 1.2, right). These findings were verified experimentally in multiplexed imaging of mRNA expression using fluorescent hybridisation chain reaction, where McLennan et al. (2012) observed that the gene expression profiles of the leader cells differed from the profiles of the followers. McLennan et al. (2012) carried out tissue transplantation studies in which leader cells were placed in the trailing stream or vice versa. These studies showed that NCC behaviours and gene expression profiles are not predetermined, but depend on stream position.

Further refinement of the computational model coupled with experimental manipulations showed that a small fraction of leader cells is optimal for successful collective invasion (McLennan et al., 2015a). In addition, McLennan et al. (2017) demonstrated that NCC speed is regulated by an extracellular protein antagonist, DAN, using knockdown and overexpression experiments together with computational modelling.

These are just some of the important characteristics of the collective migration of cranial NCCs. However, there are many other factors affecting cell-cell and cell-tissue interactions, and we will investigate a number of these in this thesis.

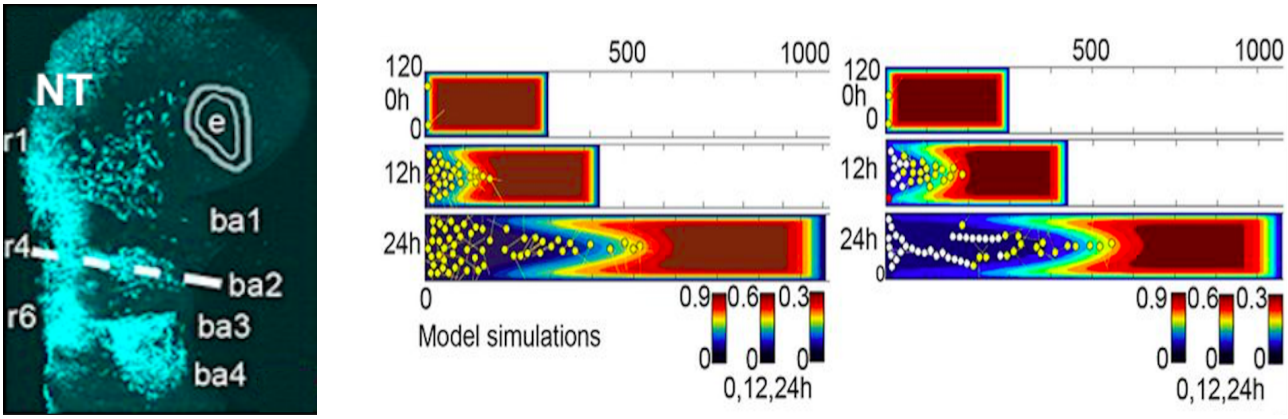


Figure 1.2: Left – migration of NCCs in the chick embryo, r4 corresponds to rhombomere 4, the position from which cranial NCCs emerge, NT – neural tube. Right – model simulations: left – model with one cell phenotype; right – model with two cell phenotypes. Yellow – leader cells, white – follower cells, chemoattractant concentration is represented by the colour bar. Left figure reproduced from McLennan et al. (2015a) with permission from the Company of Biologists Limited. Right figure reproduced from McLennan et al. (2012) with permission from the Company of Biologists Limited.

There are a great variety of NCC stream behaviours and guidance mechanisms, depending on the axial level of origin (e.g. cranial, cardiac, vagal, or trunk), and on the model organism. A natural question to ask is: are there certain universal principles that must be obeyed for successful collective cell invasion, and do the variations we observe simply correspond to different biological ways to implement and satisfy these principles? To address this question, computational modelling is particularly useful because it allows us to include and distinguish potential mechanisms and seek unifying principles. To this end, we dedicate Chapter 4 to comparing and contrasting cranial NCC migration in chick and Xenopus. In the following section we review a number of computational models that have already been used to model the migration of distinct populations of NCCs.

1.2 Modelling neural crest cell migration

Recent advances in biotechnology have contributed to an increase in the availability of quantitative biological data on NCCs, such as individual cell trajectories and cell gene expression. To process such large amounts of data on highly complex interacting systems and reach valid conclusions in many cases requires us to move beyond verbal reasoning, and use computational tools to process and interpret data. In particular, mathematical models are useful for this purpose because they allow researchers to capture the features of complex biological systems and to understand how biological systems respond to external or internal signals and perturbations. In the context of NCC migration, the increasing number of experimental observations over many different space and time scales requires the use of different modelling frameworks, from cell-level individual-based models (IBMs) to high-level partial differential equation (PDE) models (Schumacher et al., 2016; Giniūnaitė et al., 2020a). We summarise here a few of the key studies that illustrate the diversity of such models.

1.2.1 Individual-based models for neural crest cell migration on a fixed domain

An IBM on a two-dimensional fixed lattice was used by Carmona-Fontaine et al. (2011) to model collective cell motility of cranial NCCs in Xenopus driven by CiL and co-attraction, described in Sections 1.1.1, 1.1.2, respectively. Their IBM incorporated short-range repulsive interactions aimed to emulate CiL, and longer-range attractive interactions for co-attraction as a signal released by cells. CiL was modelled by enforcing alignment of cells (alignment corresponds to a low angle between the cell migratory path and the average path of all cells at all times) after a collision between two cells and then inducing a "bounce" from each other with some noise. Co-attraction was modelled in two ways: either enforcing cells within a certain radius to move towards each other, or in response to a diffusible co-attractant released by cells. Both implementations produced similar results. Their modelling results

supported conclusions drawn from experimental findings on these guidance mechanisms, i.e. that the combination of CiL and co-attraction is essential for cells to self-organise and respond efficiently to external signals. Woods et al. (2014) further extended Carmona-Fontaine et al.'s (2011) model and incorporated elastic collisions to account for the deformation of cell shape. Their simulation results lent further support to the findings that CiL and co-attraction are, together, sufficient mechanisms for successful invasion in cranial NCCs in Xenopus.

Another model which includes the biological assumptions of CiL and co-attraction was developed by Szabó et al. (2016). They used a Cellular Potts model to investigate the effect of confinement on the collective migration of NCCs. The optimal number of cells in a corridor of a given confinement width predicted by their computational results coincided with the width of NCC migratory streams across different species. They suggest that this result may explain the evolutionarily conserved nature of NCC streams.

Merchant et al. (2018) used a mechanochemical model of NCC migration based on the signalling proteins Rac1 and RhoA, which regulate cell polarity. They represented each cell as a polygon with nodes connected by elastic membranes. Their model reproduced the random walk of a single cell in a weak gradient and two modes of cell-cell interaction: CiL and co-attraction. Their simulations revealed that the simultaneous action of CiL and co-attraction suppresses random Rac1 bursts on the membrane and serves to preserve existing protrusions. Polar protrusions enhance the ability of a cluster of NCCs to chemotax in a weak gradient, thereby making collective cell migration advantageous (better invasive abilities) to single cell movement.

Colombi et al. (2020) used an IBM for NCCs to investigate the interactions between NCCs and placode cells. They built their model based on experimental observations in Xenopus cranial NCCs (Theveneau et al., 2013). The model incorporated experimental findings such as the chemotactic movement of NCCs in response to a placode-secreted chemoattractant (SDF1, modelled by a reaction-diffusion equation) and repulsion induced from CiL between NCCs. These modelling assumptions were sufficient to semi-quantitatively replicate

the multispecies phenomenon of "chase-and-run", in which NCCs chase evasive placode cells. Their model not only replicated experimental *in vitro* manipulations, but also generated new hypotheses explaining cell-cell interactions based on the perturbations of guidance signals.

1.2.2 Individual-based models for neural crest cell migration on a growing domain

The above models were all implemented on fixed (non-growing) domains. However, since NCC migration occurs in a growing embryo, there are many cases where domain growth occurs on the same timescale as NCC migration and so must be taken into account (reviewed in Giniūnaitė et al. (2020a)). We now proceed to review some models for different NCC systems that incorporate domain growth and external cell guidance cues.

Computational and experimental studies by McLennan et al. have provided a number of insights into the collective migration of chick cranial NCCs (McLennan et al., 2012, 2015a,b, 2017). To model cell dynamics they used a two-dimensional off-lattice IBM with volume exclusion, which was coupled to a continuum reaction-diffusion model for the dynamics of the chemoattractant VEGF on a growing domain. We provide a more detailed description and critique of this model in Section 1.2.5 because we use this model as the basis of our work in a significant part of this thesis.

Another IBM, which also incorporates domain growth, was used to model the development of the embryonic gut of avian embryos (Binder et al., 2012; Cheeseman et al., 2014; Newgreen et al., 2009; Zhang et al., 2010). In these studies, domain growth was incorporated using random insertion of lattice sites. This framework allowed for the implementation of different types of domain growth, including spatially non-uniform domain growth.

An application of an IBM on a growing domain to investigate the formation of diffuse clones, chimeric stripes and belly spots induced by the migration of melanoblasts

(NCC–derived specific precursors of melanocytes) in mouse chimeras has been carried out by Mort et al. (2016). They demonstrated that melanoblast colonisation is likely to proceed through a process of undirected migration, proliferation and tissue expansion, and that reduced proliferation is the main cause of the belly spots in mouse.

Spatially non-uniform domain growth has been recently observed in chick cranial NCCs (McKinney et al., 2020). However, the effect of such growth on collective cell migration and successful colonisation of the domain in hybrid or continuum models, for example, the aforementioned works of McLennan et al. (2012, 2015a,b, 2017), is an open question which we will address in this thesis.

1.2.3 Partial differential equation models for neural crest cell migration

Simpson et al. (2007) used a continuum model to investigate the roles of proliferation and migration for successful invasion and colonisation of the gut by vagal NCCs that establish the enteric nervous system. More specifically, they were looking for the main causes that inhibit NCCs from reaching the end of the gut, which can result in abnormal development (Newgreen et al., 1996). They developed their model based on experimental studies of chick and quail embryos. Simpson et al. (2007) proposed a coupled system of PDEs for the two cell types (chick and quail NCCs), which were observed to differ experimentally, and modelled migration by diffusion, and proliferation by logistic growth:

$$\frac{\partial D}{\partial t} = \alpha_D \frac{\partial^2 D}{\partial x^2} + \lambda_D D \left[1 - \left(\frac{D+H}{C}\right)\right]; \tag{1.1}$$

$$\frac{\partial H}{\partial t} = \alpha_H \frac{\partial^2 H}{\partial x^2} + \lambda_H H \left[1 - \left(\frac{D+H}{C}\right)\right]. \tag{1.2}$$

They modelled the gut as a one-dimensional domain, $x \in [0, L]$, for $L \geq 0$ constant and $t \geq 0$, $D(x,t)$ denotes donor cell density (usually quail), $H(x,t)$ host cell density (usually chick), $C(> 0)$ is the carrying capacity, $\alpha_D, \alpha_H \geq 0$ are the respective diffusion coefficients

and $\lambda_D, \lambda_H \geq 0$ are the respective proliferation rates. They considered the cases in which donor and host cells were identical and where donor cells were non-proliferative, i.e. $\lambda_D = 0$.

Simpson et al. (2007) analysed their model mathematically and provided predictions that were validated experimentally. In particular, they identified that cell invasion waves are organised in such a way that the NCCs at the front of the stream are responsible for proliferation and motility, while the NCCs behind the front are not proliferative and do not contribute to invasion of unoccupied tissues. These differences were not induced by intrinsic cell properties (verified using their mathematical model and grafting experiments involving identical and non-identical cells) but whether or not the cells were adjacent to NCC-free tissue. The model was further used to investigate possible reasons for developmental defects, including Hirschsprung's disease (Landman et al., 2007). Hirschsprung's disease is a motor disorder of the gut, which is caused by the failure of NCCs to fully invade and populate the gut. Landman et al.'s (2007) results revealed that directional invasion of the gut is driven by a combination of NCC proliferation and migration. This suggests that, to understand Hirschsprung's disease, the experimental focus should be on examining the mechanisms that regulate the balance between cell proliferation and migration, rather than focusing simply on migration.

1.2.4 Integro-partial differential equation models for neural crest cell migration

Another continuum approach to model the collective migration of NCCs was considered by Painter et al. (2015). They investigated different cell-cell interactions through a non-local PDE modelling framework. This is a very promising approach because, as mentioned above, there is ample biological evidence that cell behaviour is influenced by non-local interactions, for example, cranial and trunk NCCs often use long membrane protrusions, such as lamellipodia and filopodia, to sense their non-local environment (Clay and Hallo-

ran, 2010). Painter et al. (2015) used an abstracted phenomenological argument, based on a classical continuum approach (Murray, 2002), to include mechanisms such as CiL and co-attraction between NCCs (described in Section 1.2.1). Here, we provide a short description of their model to convey the main idea of their approach. Painter et al. (2015) developed a modelling framework for an n-dimensional system in space, but restricted attention to the one-dimensional case for their application to model NCCs. For an n-dimensional system, they considered a mass conservation equation for cell density, $p(\boldsymbol{x}, t)$:

$$\frac{\partial p}{\partial t} = -\nabla \cdot \boldsymbol{J}, \tag{1.3}$$

where $\boldsymbol{J}$ represents cell flux and $\boldsymbol{x} \in \mathbb{R}^n$. The flux consists of two parts, namely random, and interaction, $\boldsymbol{J} = \boldsymbol{J}_{\text{random}} + \boldsymbol{J}_{\text{interaction}}$. The random flux was defined as $\boldsymbol{J}_{\text{random}} = -D_p \nabla p$, where D_p is the constant cell diffusion coefficient. The interaction flux was of the form

$$\boldsymbol{J}_{\text{interaction}}(\boldsymbol{x}, t) = p f(p) \omega \int_{\mathbb{R}^n} \frac{\boldsymbol{s}}{|\boldsymbol{s}|} \Omega(|\boldsymbol{s}|; \xi, \mu) g(p(\boldsymbol{x} + \boldsymbol{s}, t)) \mathrm{d}\boldsymbol{s}, \tag{1.4}$$

where ω is a proportionality constant that depends on factors such as the viscosity of the medium, $f(p)$ is a packing or volume-filling function, $\Omega(|\boldsymbol{s}|, \xi, \mu) : [0, \infty) \to \mathbb{R}$ is the interaction function, ξ is the interaction range, μ is the interaction strength, and $g(p(\boldsymbol{x} + \boldsymbol{s}, t))$ is the functional dependence on cells at $\boldsymbol{x} + \boldsymbol{s}$, which corresponds to the strength of the signal exerted on cells at $\boldsymbol{x}$ due to the cells at $\boldsymbol{x} + \boldsymbol{s}$. They used different forms of the interaction function, such as a step function or exponential function, to incorporate CiL and co-attraction.

Painter et al. (2015) also extended this model to include two populations with varying interactions, but used a one-population model to investigate NCC migration and provided simulation results that demonstrate how interaction strength and range affect invasion depth and dispersal. They observed that solutions of their model appear to evolve to travelling waves. However, it is still an open question to determine the dependence of the wave speed on the parameters μ and ξ analytically. Painter et al. (2015) hypothesised that if NCCs communicated at longer distances than previously assumed by Carmona-Fontaine et al. (2008),

then invasion could be significantly improved. These results suggest that it could be fruitful experimentally to look for mechanical or chemical interactions between cells at different distances via, for example, extension of filopodia of varying lengths.

1.2.5 Modelling chick cranial neural crest cell migration

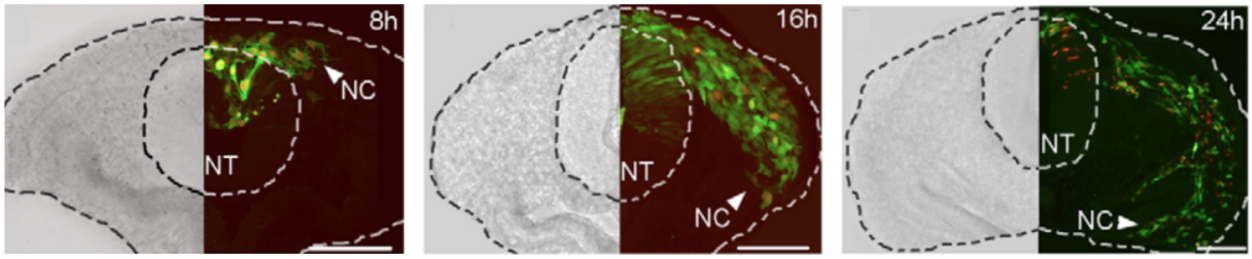
In this subsection, we provide a detailed description of the hybrid model for chick cranial NCC migration which, in parallel with experimental findings, has provided multiple biological insights (McLennan et al., 2012, 2015a,b, 2017). McLennan et al.'s key results included evidence of guidance via a cell-induced gradient of VEGF, which acts as a chemoattractant, heterogeneity of cell phenotypes, namely leaders and followers, and the possibility of phenotypic transitions (reviewed in Giniūnaitė et al. (2020b)). To model cell dynamics McLennan et al. (2012) used an off-lattice IBM with volume exclusion, which was coupled to a continuum reaction-diffusion model for the dynamics of the chemoattractant VEGF. In the next part of this section, we provide a description of various features of the model and discuss areas for extension. We refer the reader to the supplementary information of McLennan (2015a,b, 2017) for full details of the model. We provide a detailed description of our implementation of this modelling framework in Chapter 2.

Model dimensionality and geometry

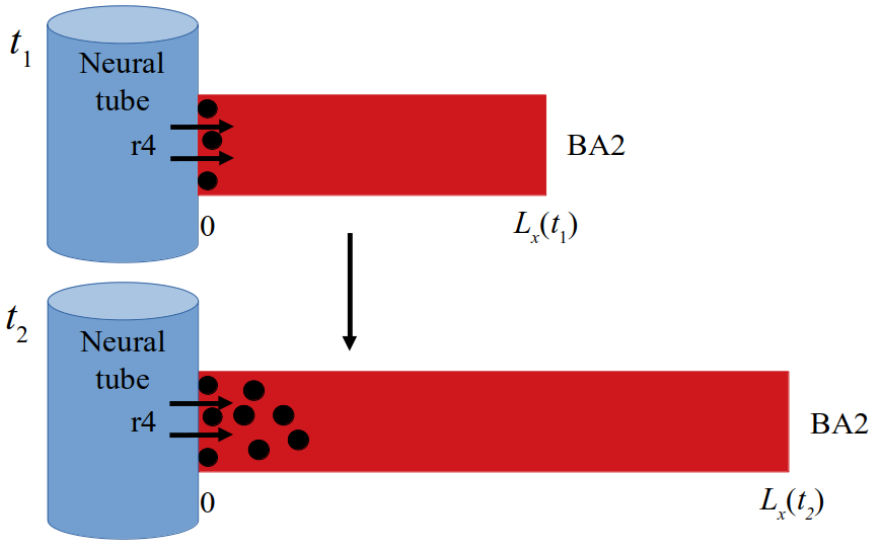
NCC migration *in vivo* occurs in the three-dimensional curved mesenchyme of the embryo. Chick cranial NCC migration from rhombomere 4 occurs in streams that are long and thin (Figure 1.2(a)). *In vivo*, the stream of cells migrating from rhombomere 4 is about six cells wide and four cells high and the initial and final lengths of the domain are around 300μm and 1100μm, respectively (Paul Kulesa, personal communication). To model NCC migration, McLennan et al. (2012, 2015a,b, 2017) used a two-dimensional rectangular domain as an approximation of the system (Figure 1.3). They justified their choice using the following

argument. A one-dimensional approximation is not realistic because the cells cannot move around each other and would block each other unrealistically frequently, so a two-dimensional domain is the simplest, biologically reasonable approximation of the domain. In addition, the chemoattractant VEGF is expressed by the ectoderm (McLennan et al., 2010) which can be well-represented by a two-dimensional layer along the NCC stream. VEGF distribution along the transverse direction of the embryo has not yet been quantified. Therefore, the two-dimensional model could, in fact, be used to represent the layer of cells closest to the ectoderm to avoid additional assumptions about VEGF concentration along the third dimension (Figure 1.3(a)). These arguments explain why McLennan et al. (2012, 2015a,b, 2017) chose a two-dimensional model and not a more realistic three-dimensional model which would also be more computationally expensive.

McLennan et al. (2012, 2015a,b, 2017) used a rectangular domain as an approximation of the transverse section instead of the curved one (Figure 1.3) because it is computationally more simplistic and the biological significance of the curvature is yet unknown. Computational modelling could be used to investigate the effect of the curvature on the migration of NCCs. However, since there are no experimental hypotheses or observations on the role of the curvature, its effect has not been the focus of previous works and we do not investigate it in this thesis.



(a)



(b)

Figure 1.3: (a) Typical projected images from three-dimensional confocal z-stacks of transverse sections through the rhombomere 4 NC migratory stream at 8, 16 and 24 hours after electroporation. This curved domain was approximated by a rectangular domain in the model of McLennan et al. (2012, 2015a,b, 2017). Scale bars: 100μm. NT, neural tube. Figure reproduced from McLennan et al. (2012) with permission from the Company of Biologists. (b) Schematic (not to scale) of the model: red rectangle represents the migratory domain taken to be the plane perpendicular to the vertical axis of the neural tube, that is, in the trasverse plane, blue circle – a transverse section of the neural tube, black circles – NCCs, and black arrows – emergence of the NCCs, r4 – rhombomere 4, BA2 – branchial arch 2. In this system the domain grows along the x-axis ($x = 0$ being the neural tube). $L_x(t_1)$, $L_x(t_2)$ are the lengths of the domain at different times, t_1 and t_2.

Domain growth

The NCC dynamics were modelled on a rectangular domain growing in the x-direction only (from the neural tube to the target tissue, Figure 1.3(b)). Based on measurements of the length of the domain, McLennan et al. (2012, 2015a,b, 2017) used a non-uniform in time domain growth profile but assumed that the growth was spatially uniform. They used Equation (1.5) as a (non-mechanistic) description of the growing length $L_x(t)$ of the domain in the x-direction with a sufficient number of parameters to fit experimental data:

$$L_x(t) = L_0 \left(\frac{L_\infty e^{b(t-t_s)L_\infty}}{L_\infty - 1 + e^{b(t-t_s)L_\infty}} + 1 - \frac{L_\infty e^{b(-t_s)L_\infty}}{L_\infty - 1 + e^{b(-t_s)L_\infty}} \right), \tag{1.5}$$

with $b, t_s, L_\infty, L_0 > 0$ being parameters inferred from experimental measurements (McLennan et al., 2012). McLennan et al. (2012) modelled the impact of domain growth upon cell motility by introducing an additional advective flux for the cells. Since the growth was uniform in space, the advective flux was implemented by multiplying the x-coordinate of each cell by $L_x(t)/L_x(t - \Delta t)$ at each time step of length Δt.

However, recent experimental studies have revealed that growth might be spatially non-uniform (McKinney et al., 2020). Hence, domain growth might have a more complex effect on the migration of NCCs, for example, the rate of advection of the cells may vary at different parts of the domain. Therefore, it is important to investigate to what extent such spatial heterogeneities in domain growth might facilitate or impede NCC migration. In this thesis we relax the assumption of spatially uniform domain growth and investigate the effect of spatially heterogeneous domain growth on NCC invasion.

Cell-induced chemoattractant

McLennan et al. (2012) showed that NCCs are guided by a cell-induced chemoattractant (VEGF) gradient. In their computational model, VEGF dynamics were modelled using a reaction-diffusion equation on a spatially uniformly growing domain. We provide the

details of this equation, posed on a spatially uniformly growing domain, in Chapter 2. In Chapter 3 we relax the assumption of spatially uniform domain growth and derive the form of this equation in the general setting of spatially non-uniform growth. This extension of the model allows us to investigate the effect of different domain growth profiles on the migration of NCCs.

Cell heterogeneity

As discussed in Section 1.1.4, McLennan et al.'s (2012) model predicted that two distinct cell phenotypes are required to ensure that NCCs invade the domain successfully. Therefore two cell phenotypes, namely leaders and followers, were included in the subsequent computational model of McLennan et al. (2015a,b, 2017). McLennan et al. (2015a) identified that there is a small number of leader cells, called trailblazers, that can efficiently guide the rest of the population and have a unique molecular signature.

Phenotype switching

In McLennan et al. (2015b), plasticity of cell phenotypes was identified. Supported by experimental evidence, McLennan et al. (2015b) included in their model a phenotype switching mechanism between the cell phenotypes, so that, in the absence of VEGF, leader cells acquired follower cell behaviour. They demonstrated that this feature makes NCC invasion more robust.

Cell movement

Cell movement was made up of two components: passive advection due to domain growth and active cell movement. Advection of the cells by domain growth was realised by updating cell positions uniformly based on domain growth. Active cell movement was

modelled as follows: leaders undertake a biased random walk up a cell-induced gradient of chemoattractant, whereas followers are guided by the leaders, if sufficiently close to them, or move randomly. We discuss the guidance mechanism used in the model in the following paragraph.

Cell-cell interactions

McLennan et al. (2012, 2015a,b, 2017) made the assumption that leaders guide followers by physical contact via filopodia, giving rise to chain-like structures, which are observed experimentally (Wynn et al., 2013). However, the exact guidance mechanism is still unknown. For example, follower cells could obtain directional cues from the leader cells through secreted signals, physical pulling or via paths through the ECM left by the leaders. Due to the uncertainty of this important feature, we dedicate part of this thesis to exploring this phenomenon in greater detail and shed new light on potential guidance mechanisms, including the creation of tunnels in the ECM.

Cell proliferation

McLennan et al. (2012, 2015a,b, 2017) did not include cell proliferation in their model based on the evidence which suggests that NCC mitotic activity is relatively quiescent during migration until they reach the branchial arches (Ridenour et al., 2014). Cell proliferation may still have an effect on NCC invasion but we do not anticipate this effect to be significant. Therefore, in this thesis, we also assume that NCCs do not proliferate during migration.

Initial conditions

The initial conditions were as follows: based on experimental data, the domain was initially empty of NCCs (Figure 1.3(b)). The initial conditions for VEGF were as follows: $c(x, y, 0) \equiv 1$, for $(x, y) \in [0, L_x(0)] \times [0, L_y]$, where $L_x(0)$ is the length of the domain at time $t = 0$ and L_y is the width of the domain, based on the experimental observation that VEGF is uniformly distributed prior to NCC migration.

Boundary conditions

The boundary conditions were modelled as follows: new cells entered the domain at a constant rate at the left-hand boundary (next to the neural tube, Figure 1.3(b)). A new cell attempted to enter the domain every 10 minutes provided there was sufficient space available. The influx of NCCs was only set at the left-hand boundary of the rectangular domain, while zero-flux boundary conditions for cells were set at the other three boundaries of the rectangular domain. Zero-flux boundary conditions for the cells are defined as follows: a cell may extend its filopodia outside the domain, but if all of its filopodia are extended outside the domain, then the cell does not move. McLennan et al. (2012) assumed that the VEGF concentration is zero at each of the four boundaries of the domain. However, the following models, namely McLennan et al. (2015a,b, 2017), changed this assumption due to an unrealistically large loss of chemoattractant at the boundaries, predicted by the homogeneous Dirichlet boundary conditions, and considered zero-flux boundary conditions instead (Schumacher, 2015). They found that model predictions were robust to this change in boundary conditions and that they also allowed for a wider, more representative stream profile. Even though the zero-flux boundary condition may give rise to more biologically realistic simulations, there is no clear evidence as to what confines the cells to move along a corridor joining rhombomere 4 and branchial arch 2. McLennan et al. (2017) investigated expression of the gene DAN, which acts as a cell movement inhibitor, and found that it

was expressed in a strip next to the neural tube at the onset of migration. As the NCCs emerged into the domain, DAN expression in the corridor of invasion slowly disappeared but remained fully expressed in the tissue on either side of the entrance to the corridor. While it is reasonable to assume that DAN expression may effectively impose a zero-flux boundary condition for NCCs, McLennan et al. (2017) did not investigate how the extent of this spatially imposed confining boundary condition along the corridor affected subsequent movement beyond the DAN strip, assuming, for simplicity, that the confinement extends along the total length of the boundary.

To investigate how NCCs stay confined in narrow corridors, we relax the assumption of the narrow rectangular migratory domain with imposed zero-flux boundary conditions set along the full extent of the bounding edges parallel to the corridor of migration. Instead, we consider a wider domain and investigate how invasion changes if the cells are not confined into narrow streams by internally imposed boundary conditions.

1.3 Aims of this thesis

In this chapter, we have provided multiple examples of how modelling frameworks can be used to answer biological questions in the context of collective cell migration. Interdisciplinary studies of NCC migration have revealed a huge variety of cell-cell and cell-tissue interactions across various NCC types and different species. However, there are still many gaps in our knowledge concerning what the crucial cell-cell and cell-tissue interactions are, or how variations in the tissue, such as tissue growth or chemical composition, affect collective NCC migration. Furthermore, the variety of key driving mechanisms within, and across, different animal species makes us question the reasons for these differences and seek generalisations. The aim of this thesis is to use a combination of different modelling techniques, in close collaboration with our experimental colleagues, to investigate the mechanisms of NCC migration.

In Chapter 2, we focus on the investigation of various guidance mechanisms that are crucial to ensure successful invasion. Based on experimental findings, we choose two factors that affect both cell-cell and cell-tissue interactions, namely the role of the water channel protein aquaporin-1 (AQP-1) and the effect of spatial confinement. We extend the hybrid model, consisting of the IBM for NCCs and the reaction-diffusion model of the chemoattractant (McLennan et al., 2012), to investigate the role of AQP-1 on the migration of NCCs. Most importantly, we include an additional cell-cell interaction mechanism – guidance by tunnels in the ECM. We explore the effect of different cell properties which are shown experimentally to be affected by the regulation of AQP-1 expression. To probe the question relating to how NCCs stay confined to a corridor, and whether spatial confinement contributes to successful invasion, we investigate the effect of varying the extent of imposed spatial confinement.

In Chapter 3, motivated by the experimental findings suggesting that tissue growth along the domain might not be spatially uniform in space, as previously assumed, we generalise our model to allow for non-uniform domain growth profiles in both time and space. We explore the effects of different domain growth profiles and identify a possible mechanism to explain the interactions between NCC migration and tissue growth.

In Chapter 4, we investigate the reasons for the differences between the key underlying invasion mechanisms of NCC migration across different species. To compare and contrast the differences between chick and Xenopus cranial NCC migration, we develop a unified modelling framework that includes the key cell-cell interaction forces, namely attraction and repulsion at various ranges, and directional bias. We perform parameter sensitivity analysis and classify the behaviour of chick and Xenopus NCCs under different forces. We suggest possible reasons for the underlying nature of the differences across animal species. In so doing, we uncover an alternative chick cell-cell interaction mechanism to that suggested by McLennan et al. (2012, 2015a,b, 2017).

Finally, in Chapter 5 we summarise and discuss our findings. Motivated by our

results from Chapter 4, we also present a preliminary study on the alternative chick cell-cell interaction mechanism and suggest other future directions and extensions of our work.

Chapter 2

How can directional guidance cues facilitate collective cell migration?

Leader cells at the front of the NCC stream exhibit polarised movement up a cell-induced chemoattractant gradient (McLennan et al., 2012). However, it is an open question as to what induces polarised collective cell migration. A contact signalling mechanism (Clay and Halloran, 2010), which corresponds to guidance through physical cell-cell contact via filopodia has, to-date, been assumed to drive the collective cell migration observed in chick cranial NC (McLennan et al., 2012, 2015a,b, 2017). However, the precise mechanism of how the cell-cell guidance signal is transmitted along the stream is still unknown. NCCs travel in narrow streams but we do not yet understand what mechanism confines the cells into these narrow streams and whether this confinement acts as an additional guidance cue for the cells. In this chapter, motivated by recent experimental findings, we consider two factors involved in determining cell signalling and directionality: the water channel protein AQP-1 and cell confinement via expression of the cell movement inhibitor DAN.

The outline of this chapter is as follows: in Section 2.1, we first introduce the reader to the biology behind the regulation of AQP-1 and to the possible role of DAN in

confining cell movement. In Section 2.2, we describe the framework that we use to model the changes in AQP-1 expression, including a simplified version of ECM degradation. In Section 2.3, we discuss our computational results on the effects of changes in cell speed, and the stabilisation, polarisation and number of filopodia induced by experimental manipulation of AQP-1 expression. We continue our exploration of the importance of ECM degradation, induced by the overexpression of AQP-1, in Section 2.4. We then investigate the effect of spatial confinement in Section 2.5. We finish with conclusions and discussion in Section 2.6.

2.1 Biological background

In this section we describe the biology behind the role of AQP-1 and NCC spatial confinement – the two factors whose effect on the migration of NCCs we will investigate in this chapter.

2.1.1 The role of AQP-1 in cranial neural crest cell migration

This work is based on the McLennan et al. (2020) paper in which my contribution was the computational modelling. In this paper, it was shown that mRNA and protein expression of AQP-1 (AQP-1 is a water channel protein that regulates cellular water flow across the cell membrane (Conner et al., 2012)) preferentially occurs in lead cranial NCCs. High resolution structured illumination microscopy showed that AQP-1 protein is expressed in the tips of NCC filopodial protrusions, preferentially higher within the leader cell subpopulation. It was further demonstrated that AQP-1 inhibition by morpholino (a type of molecule used to modify gene expression) reduced the number of migrating NCCs, as well as NCC speed and directionality, both *in vivo*, and in explanted neural tube *in vitro* assays. In contrast, overexpression of AQP-1 enhanced NCC speed and distance migrated in comparison to control embryos. Using fast confocal microscopy it was observed that perturbations in AQP-1

water channels significantly altered the length and stability of NCC filopodial protrusions *in vivo*. In addition, it was observed that APQ-1 induced matrix metalloproteinase (MMP – matrix degrading protein) activity and phosphorylated focal adhesion kinase, while AQP-1 inhibition induced a significant reduction in MMP activity when analysed by in gel zymography. These data suggest that AQP-1 is involved in the promotion of ECM degradation, which could be interpreted as the creation of tunnels in dense ECM (Perris and Perissinotto, 2000) that facilitate cell migration.

The aforementioned brief review highlights the features of NCCs that were shown experimentally to be affected by regulation of AQP-1. However, it was unknown how each of these features contributes to the success of NCC invasion, and it is highly challenging to individually regulate these features experimentally. Therefore, in McLennan et al. (2020), my contribution was to computationally explore the effect of each of these factors separately. Our study helped to identify which of the affected factors are the most important to ensure successful invasion.

2.1.2 Neural crest cell confinement

Cranial NCCs migrate in confined streams but it is unknown whether this observed spatial confinement results from inhibitory signals outside the migratory domain, directed external guidance cues or cell-cell interactions. In Xenopus, Szabó et al. (2016) demonstrated that the proteoglycan versican (Landolt et al., 1995) forms an inhibitory boundary that constrains NCCs to remain in confined corridors, in turn facilitating their migration (Figure 2.1). However, in chick, the importance of spatial confinement on NCC guidance and migration has not been fully investigated.

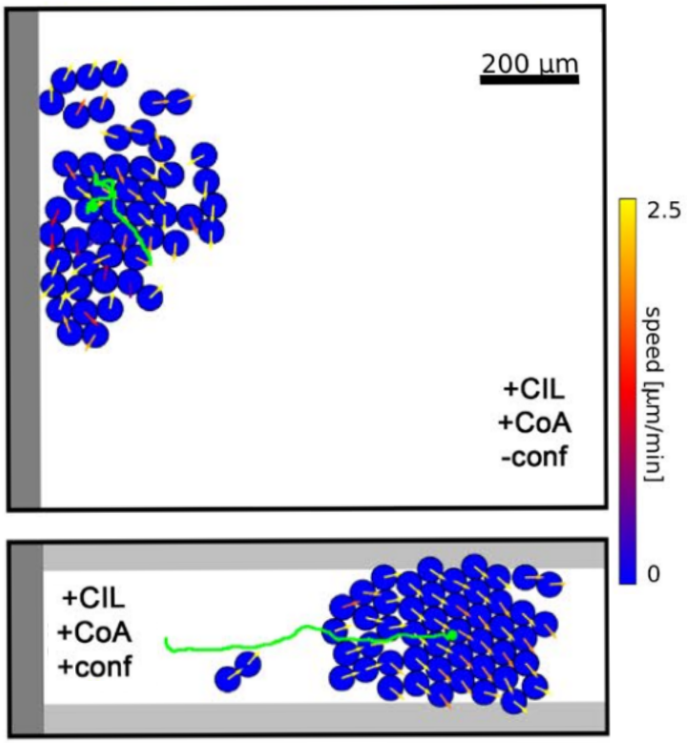


Figure 2.1: *In silico* configuration of cells with and without confinement. Confinement due to expression of versican and imposed via a restrictive boundary facilitates directed NCC migration in Xenopus. The cells need to travel from the left (neural tube) to the right (branchial arches). CIL – contact inhibition of locomotion, CoA – co-attraction, conf – confinement. Green line corresponds to the track of the centre of mass. Figure reproduced from Szabó et al. (2016) with permission from the Company of Biologists Limited.

McLennan et al. (2017) investigated the role of the inhibitory gene DAN, which acts as a bone morphogenetic protein antagonist. *In vitro* experiments revealed that NCCs avoid the regions with high expression of DAN. *In vivo*, DAN was identified to be uniformly distributed adjacent to the neural tube (in a region around 200μm along the migration corridor, see Figure 2.2(c)) prior to NCC migration and only in NCC-free regions after the emergence of the NCCs into their migratory domain (Figure 2.2(a),(b)). DAN expression in the NCC-free regions (Figure 2.2(a),(b)) suggests that DAN may act as an inhibitor confining NCCs. However, if that was the case, then why is it not expressed along the total boundary of the corridor? Moreover, it is an open question as to whether such externally imposed

confinement is crucial for directed cell migration. To address these questions, we use our computational framework to investigate and suggest further hypotheses as to how confinement contributes to cell guidance in chick.

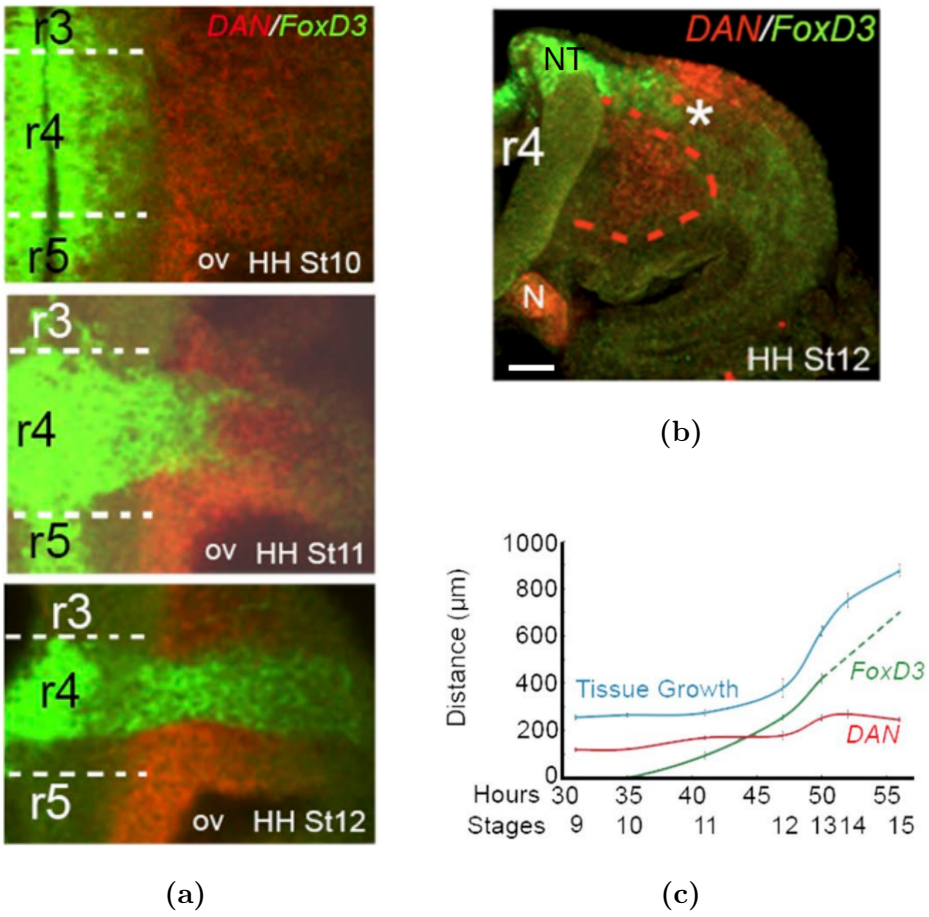


Figure 2.2: DAN is expressed adjacent to the neural tube (white dashed lines in (a)) in chick. (a) DAN and FoxD3 (NCCs) expression at the axial level of rhombomere 4 (r4) at Hamburger Hamilton (HH) stages (St) 10, 11, 12. (b) Transverse section of DAN and FoxD3 (NCCs) expression at r4 axial level at HH St 12. (c) Length of FoxD3 (NCCs) and DAN expression measured as the distance from the edge of the neural tube to the end of expression region over time (hours and HH stages shown). Initially, DAN is expressed uniformly adjacent to the neural tube, but only in NCC-free regions after the emergence of the NCCs into their migratory domain. DAN is only expressed in a stripe of width up to around 200μm away from the neural tube. Scale bar in (a) and (b) is 50μm, ov – otic vesicle, N – notochord, NT – neural tube. Figures reproduced from McLennan et al. (2017) with permission from the Rockefeller University Press.

In the next section we turn our focus back on AQP-1 and discuss how we incorporate factors affected by its expression into the computational modelling framework.

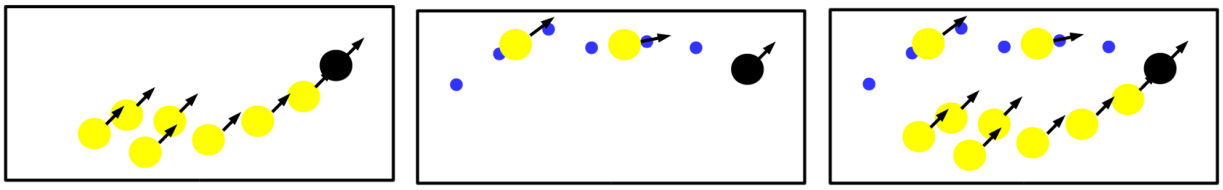
2.2 Incorporating AQP-1 into the computational model

To computationally investigate the effect of AQP-1 on the migration of NCCs we use the model developed by McLennan et al. (2012, 2015a,b) as the basis for our modelling framework. We extend the model to allow us to manipulate the features of the NCCs affected by the expression of AQP-1. As mentioned briefly in Chapter 1, the model consists of a two-dimensional, off-lattice IBM for NCCs that is coupled to a continuum, reaction-diffusion model for the dynamics of the chemoattractant VEGF on a rectangular, spatially uniformly growing domain in the x-direction (Figure 1.3). We implement the model using Aboria (Robinson and Bruna, 2017, https://martinjrobins.github.io/Aboria/), a C++ library for particle-based numerical methods. We use this library because it allows us to define a wide range of interactions between cells, and we can exploit the fact that it has a number of key algorithmic aspects implemented efficiently, including neighbourhood searches, which we use widely in our work. Aboria is particularly useful for simulating IBMs and, due to its flexibility, is also very convenient for simulating hybrid models that couple IBMs with PDE models, as in our case. We now proceed with a detailed explanation of the different components of our model.

Dynamics of cells

We describe briefly how we incorporate the dynamics of cells. The cells are defined by points in the domain that indicate their centre. They are modelled as hard discs which all have the same fixed radius and they are not allowed to overlap (volume exclusion). If a cell cannot make a movement due to volume exclusion, the cell stays in its original position. We

assume that there are two types of cells, namely "leaders" and "followers". Leaders undertake a biased random walk up a cell-induced gradient of chemoattractant. They do so by sending out a certain number of filopodia in random directions, which are generated from a uniform random distribution. These filopodia can sense the concentration of chemoattractant at their tip, and the cell then moves in the direction of the highest concentration sensed, provided it is higher than that at the central position of the cell. If this is not the case, then the cell picks a direction in which to move from a uniform random distribution. On the other hand, followers are either in a chain or move randomly. A chain consists of a group of followers that are close (defined by a threshold distance) to each other and at least one of them is close to a leader. All the followers in a chain move in the same direction as the cell that is at the front of the chain. A follower may leave a chain if it is a distance $l_{\text{filo}}^{\max}$ further away from the cell to which it was attached in the chain. This phenomenon may happen due to volume exclusion or a change in the distance between the cells due to domain growth. If a follower, which is not in a chain, is relatively close to more than one cell, so it could join more than one chain, then it randomly chooses one to follow and remains in that chain. We define this type of guidance by chains as "contact guidance". As well as having this model of contact guidance, we implement a new simplistic model of tunnelling in the ECM (motivated by experimental results on the regulation of MMP activity by the expression of AQP-1) by recording the history of leader positions, which we define as a "tunnel" (Figure 2.3). If a follower is sufficiently close to a tunnel, then it starts moving along that tunnel towards the front of the stream. If a cell is close to more than one tunnel, then it enters the closest tunnel. We assume that guidance via contact dominates over the tunnelling mechanism, i.e. if a follower cell is in a chain then it does not enter a tunnel even if it is sufficiently close to it. This assumption can be explained by hypothesising a possibly stronger effect of cell-cell forces than tunnelling in the ECM but the opposite assumption does not lead to significant change in collective cell invasive abilities (results not shown).



(a) (b) (c)

Figure 2.3: Schematics of contact migration versus tunnelling. (a) Contact migration. Followers (yellow) within a threshold distance of each other all adopt the direction of movement of the leader (black). (b) Tunnel movement: the tunnel (blue) forged by a leader guides followers that enter the tunnel to move along the tunnel. (c) A leader can guide followers both via the tunnel it has created and by the creation of chains (contact). We use (c) when we add a tunnelling mechanism to the model.

To simplify the model, we assume that phenotype switching between the leader and follower cell types occurs based on the position of a cell within the invading stream rather than on the chemoattractant concentration (McLennan et al., 2015b). This simplification is consistent with the experimental observation that gene expression profiles depend on the position of a cell within a migratory stream with a small number of leaders at the very front of the stream where the concentration of VEGF is the highest in our simulations (McLennan et al., 2015b). A constant number of leaders is a reasonable assumption in our model because we are not modelling the system with experimental perturbations in VEGF distribution which have been shown to alter the number of leaders (McLennan et al., 2015a). We check whether there is a phenotype switching event after the movement of each follower cell.

We also include other biological features that are affected by the regulation of AQP-1 expression. **Filopodium stabilisation** is realised by a leader sampling its environment every n_{filo} time steps and moving persistently in between those steps, as opposed to sampling and potentially moving in a different direction at each time step. **Filopodium polarisation** entails a leader only stabilising its filopodium when it makes an informed movement towards a higher concentration of VEGF as opposed to a random movement. **Filopodia number**

extended by a cell is the number of random directions a leader samples per time step.

Model assumptions

We now list the key assumptions used in our model. Firstly, we use a fixed time-step ($\Delta t = 1$min) during which we assume that each cell senses its environment and attempts to make a move. Secondly, we assume that the entire cell has to be inside the rectangular domain, that is, the centre of mass is at least a distance R from the boundary, where R is the cell radius. We allow a cell to extend its filopodium outside the domain, but if all of its filopodia are extended outside the domain, the cell does not move. These are the boundary constraints for cells everywhere apart from the left-hand boundary (neural tube) where there is an influx of cells (Figure 1.3(b)). There is an attempt to insert a new cell at every time step with a centre at a random position along the y-axis with the coordinate "$x =$ cell radius", but volume exclusion impedes constant influx, i.e. a new cell may not be inserted if by entering the domain it would overlap with another cell which is already in the domain. For the cells already inside the domain, the left-hand boundary constraint is the same as that described above for all the other boundaries. In other words, cells cannot exit the domain through the left-hand boundary. Thirdly, we assume that when cells enter tunnels they move along them, in the direction of the front of the stream. This entails the further assumption that there is a guidance cue distinguishing this direction within a tunnel.

Domain growth

We use a logistic equation to describe the growth of the domain in the x-direction:

$$L_x(t) = \frac{L_\infty e^{b(t-t_s)}}{L_\infty/L_0 + e^{b(t-t_s)} - 1} + k_0, \tag{2.1}$$

where $L_x(t)$ is the length of the domain, $b = 0.23\text{h}^{-1}$, $t_s = 15.9$h, $L_\infty = 867.6\mu$m, $L_0 = 300.0\mu$m and $k_0 = 291.2\mu$m, where the parameters are inferred from experimental data using

the MATLAB least-square fitting function "lsqcurvefit" (Figure 2.4). Note that Equation (2.1) is an equivalent, simplified version of Equation (1.5) used in McLennan et al. (2012, 2015a,b, 2017).

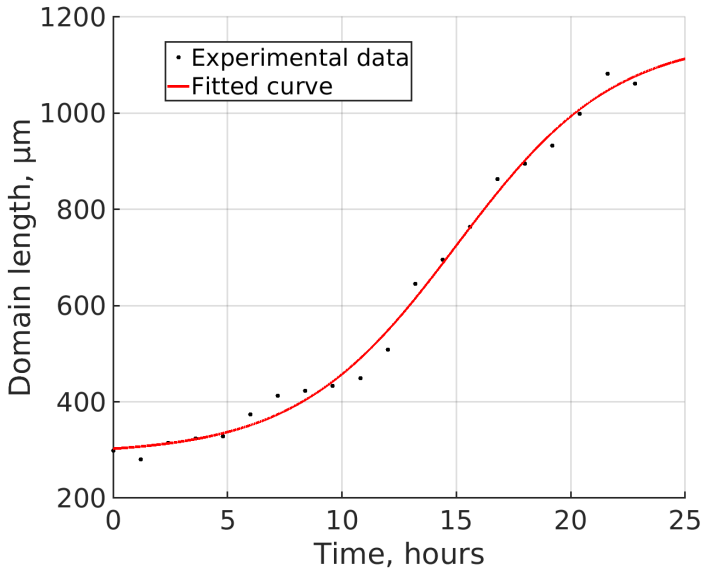


Figure 2.4: Growth profile for the domain of migration (Figure 1.3), showing experimental data (McLennan et al., 2012) and fitted Equation (2.1).

Chemoattractant dynamics

We use a reaction-diffusion equation to model the dynamics of the chemoattractant VEGF based on the work of McLennan et al. (2012, 2015a,b, 2017). We scale the concentration of VEGF, $c(x, y, t)$, to $c \in [0, 1]$ and define the equation on the growing domain with $(x, y) \in [0, L_x(t)] \times [0, L_y]$ (parameter values in Table 2.2):

$$\underbrace{\frac{\partial c}{\partial t} + \frac{\partial (ac)}{\partial x}}_{(i)} = \underbrace{D\left(\frac{\partial^2 c}{\partial x^2} + \frac{\partial^2 c}{\partial y^2}\right)}_{(ii)} \underbrace{- c \sum_{i=1}^{N(t)} \frac{\lambda}{2\pi R^2} \exp\left[-\frac{(x - x_i)^2 + (y - y_i)^2}{2R^2}\right]}_{(iii)} + \underbrace{\kappa c(1 - c)}_{(iv)}, \quad (2.2)$$

where D is the diffusion coefficient of the chemoattractant, R is the cell radius, λ is the internalisation rate of VEGF by cells, κ is the production rate of the chemoattractant, a is the flow due to domain growth, $N(t)$ is the number of cells at time t, and (x_i, y_i), $i = 1, \ldots, N(t)$

is the position of the centre of cell i. We assume zero-flux boundary conditions and initial conditions $c(x, y, 0) \equiv 1$. We assume a uniform initial condition for VEGF based on the observations that prior to NCC migration, VEGF is spatially uniform in the tissue up to the entrance to branchial arch 2 (McLennan et al., 2010).

We briefly explain the reasoning behind each of the terms in Equation (2.2). Term (i) corresponds to the effect of domain growth. It consists of an advection term, $a \times \partial c/\partial x$, corresponding to elemental areas moving with the flow due to local growth, and a dilution term, $c \times \partial a/\partial x$, due to local area change. Term (ii) corresponds to the diffusion of chemoattractant with diffusion coefficient D. Term (iii) represents the internalisation of chemoattractant by cells. Term (iv) models the production of chemoattractant. We assume standard logistic production of chemoattractant throughout the region with linear production rate, κ. This choice guarantees that the rescaled concentration of chemoattractant remains restricted between zero and one, i.e. in the absence of NCCs, the VEGF concentration is at saturated level of one. We tested a number of different VEGF production terms in our model and found that the VEGF profiles over time were qualitatively similar in all cases, provided that the rate of internalisation of VEGF by cells was sufficient to stop VEGF levels becoming excessively high (results not shown).

Assuming that the flow is specified using a growth function Γ, the Lagrangian description is

$$x = \Gamma(X, t), \quad x \in [0, L_x(t)], \tag{2.3}$$

where $X \in [0, X_0]$ is an initial position marker with $X_0 = L_x(0)$, and $\Gamma(X, 0) = X$. The local flow is determined by

$$a(x, t) = \frac{\partial x}{\partial t}. \tag{2.4}$$

In the spatially uniform domain growth case, the growth function can be expressed as follows:

$$\Gamma(X, t) = Xl(t) = x, \quad l(0) = 1, \tag{2.5}$$

where $l(t)$ is the rescaled domain length, $l(t) = L_x(t)/L_0$ with $L_0 = L_x(0)$. Then the flow is

determined by

$$a(x,t) = X\dot{l}(t) = x\frac{\dot{l}(t)}{l(t)}, \tag{2.6}$$

where $\cdot$ denotes $\mathrm{d}/\mathrm{d}t$. Substituting expression (2.6) into Equation (2.2), we obtain the equation

$$\frac{\partial c}{\partial t} = D\left(\frac{\partial^2 c}{\partial x^2} + \frac{\partial^2 c}{\partial y^2}\right) - c\sum_{i=1}^{N(t)} \frac{\lambda}{2\pi R^2}\exp\left[-\frac{(x-x_i)^2 + (y-y_i)^2}{2R^2}\right] + \kappa c(1-c) - \frac{\dot{l}}{l}\left[x\frac{\partial c}{\partial x} + c\right]. \tag{2.7}$$

We use the following transformation to map the x-coordinate to the unit interval:

$$(x,t) \to (\bar{x},\bar{t}) = \left(\frac{x}{l(t)}, t\right). \tag{2.8}$$

Under this mapping

$$\frac{\partial c}{\partial \bar{t}} = \frac{\partial c}{\partial t} + x\frac{\dot{l}}{l}\frac{\partial c}{\partial x}, \tag{2.9}$$

which leads to the elimination of the advective term in Equation (2.7). Therefore, if we use the transformation (2.8), but for the sake of simplicity now drop the bars, then Equation (2.7) becomes

$$\frac{\partial c}{\partial t} = D\left(\frac{1}{l(t)^2}\frac{\partial^2 c}{\partial x^2} + \frac{\partial^2 c}{\partial y^2}\right) - c\sum_{i=1}^{N(t)} \frac{\lambda}{2\pi R^2}\exp\left[-\frac{l(t)^2(x-x_i)^2 + (y-y_i)^2}{2R^2}\right] + \kappa c(1-c) - \frac{\dot{l}(t)}{l(t)}c. \tag{2.10}$$

We describe the numerical implementation and verification of convergence of Equation (2.10) in Appendix A.

Pseudocode

We provide a pseudocode that explains how we incorporate the migration of cells. The text in blue corresponds to the steps that are only applicable to the model with a tunnelling mechanism. The full code is available at https://github.com/rginiunaite/NC-cells.git. We provide two versions of the code: NC-model, where the interactions between the cells in the model are only by contact; NC-model-tunnelling, where interactions are by

both contact and tunnelling mechanisms. Note that a user first needs to install the Aboria library to run the code (https://martinjrobins.github.io/Aboria/).

Main steps

1. initialise model parameters and N_{leader} leader cells, set $t = 0$
2. **if** $t =$ insertion time (k_{in}), **then**: attempt to insert a new cell at the left-hand boundary of the domain **end if**
3. solve chemoattractant profile
4. grow domain, update cell positions
5. move cells
6. phenotype switching

Internal steps

move cells

1. **for** $i = 1$ to number of cells **do**
2. pick a cell at random without replacement
3. **if** the cell is a leader, **then**
4. **if** filopodium is stabilised and the cell has not finished moving three steps in the same direction, **then** move in the same direction as before **end if**
5. **if** there is no filopodium stability mechanism or the cell has finished moving three steps in the same direction, **then**
6. pick n_{filo} random directions and measure chemoattractant concentration in those random direction(s) at distance l_{filo} away from its centre, pick the highest concentration and set it to c_{new}
7. measure chemoattractant concentration at cell position and call it c_{old}
8. **if** $\frac{c_{\text{new}} - c_{\text{old}}}{\sqrt{c_{\text{old}}}} \geq$ sensing accuracy, **then**
9. move in chosen direction, stabilise filopodia (provided that stabilisation

mechanism is on)

10. **else**

11. move in random direction, stabilise filopodia (provided that stabilisation mechanism is on and the stabilisation is non-polar)

12. **end if**

13. **end if**

14. record the position of the leader if the cell is a distance s away from the previous position tracked, call it a "tunnel"

15. **end if**

16. **else** (the cell is a follower)

17. **if** the cell is in a chain, **then**

18. move in the same direction as the leader at the front of the chain

19. **if** the cell is further away than $l_{\text{filo}}^{\max}$ from the cell to which it was attached in the chain, **then**

20. detach it and all the cells that were following it from the chain

21. **end**

22. **if** the cell is not in a chain, **then**

23. **if** there is a leader or a follower in a chain l_{filo} distance apart, **then**

24. join that chain (if there are multiple possibilities, pick one randomly) and move in the same direction as the cell ahead in the chain

25. **end if**

26. **else if** the cell is less than the threshold distance d from one of the tunnels (if there are multiple tunnels, pick the closest), **then**

27. move along the tunnel

28. **end if**

29. **else** move in a random direction

30. **end if**

phenotype switching

1. **if** a cell is a follower **then**
2. **if** it is a distance ϵ ahead in the x-direction than the closest leader, **then**
3. swap their phenotypes
4. **end if**
5. **end if**

Model parameters

We choose most of our parameters based on those from McLennan et al. (2015a,b, 2017). We adapt some of the parameters to recapitulate the experimental results. We run the simulations for 18 hours, from HH stage 10, when NCCs emerge, to stage 15, when the experiment is ended. Table 2.1 contains the values we used for the computational results of this chapter.

Comments

- N_{leader} – number of leaders. We choose a fixed number of five leaders based on the work of McLennan et al. (2015b) which identifies a small number of leader cells as optimal for successful invasion, and because this number of leader cells can guide the rest of the population successfully in our computational model (either by contact or tunnels). A larger number of leaders makes collective invasion less efficient (McLennan et al., 2015b).

- *ratio* – ratio of follower to leader cell speed. Kulesa et al. (2008) demonstrated that the speed of the followers is higher than that of the leaders. According to their studies the ratio should be 1.2. However, due to volume exclusion in the crowded follower-cell environment, which restricts follower movement and thus reduces effective follower

	Description	**Value**	Reference
N_{leader}	number of leaders	5	comments
n_{filo}	directions sampled per time step (filopodia number)	1-3	results section
Δt	simulation time step, min	1	n/a
R	cell radius (nuclear), μm	7.5	McLennan (2010)
ν	leader cell speed, μm/h, control case, AQP-1 overexpression and AQP-1 downregulation, respectively	62, 82, 57	results section
$ratio$	ratio of follower to leader speed	1.3	comments
L_y	width of migratory domain, μm	120	McLennan et al. (2012)
L_x	length of migratory domain (grows logistically, Eq. (2.1)), μm	300 to 1100	McLennan et al. (2012)
	Parameters for domain growth Equation (2.1)		
b	n/a, h^{-1}	0.23	experimental data
t_s	n/a, h	15.9	experimental data
L_∞	increase in domain length in the x-direction, μm	867.6	experimental data
L_0	initial length of the domain, μm	300	experimental data
k_0	n/a, μm	291.2	experimental data
l_{filo}	sensing radius, μm	27.5	comments
$l_{\text{filo}}^{\max}$	maximum cell separation before contact is lost, μm	45	comments
b_{ext}	number of additional time steps cells moved in the same direction	0-2	results section
ξ	sensing accuracy	0.1	comments
D	diffusion coefficient of chemoattractant, $\mu\text{m}^2\text{h}^{-1}$	$0.1\text{-}10^5$	comments
χ	production rate of chemoattractant, h^{-1}	0.006	comments
λ	chemoattractant internalisation rate, h^{-1}	0.02	comments
k_{in}	rate at which new cells attempt to enter the domain	one every minute	comments
ϵ	distance a follower has to be ahead of a leader to swap phenotypes, μm	10	comments
	Extra parameters for model with tunnelling		
d	threshold distance to tunnel to enter it, μm	10	comments
s	track spacing, μm	20	comments
n_t	number of leader positions tracked	60	comments

Table 2.1: Model parameters used in the simulations in this chapter.

speed, we set this ratio to a higher value, i.e. 1.3.

- l_{filo} – sensing radius. We use the value calculated by McLennan et al. (2015b) as the sum of the cell radius and the mean filopodial length.

- $l_{\text{filo}}^{\max}$ – maximum cell separation before contact is lost. We use the value calculated by McLennan et al. (2015b), obtained as half of the maximum cell size including filopodium.

- ξ – sensing accuracy. We use the same argument for the accuracy with which the cells can sense a chemical gradient as in McLennan et al. (2015b,b, 2017). They base their work on the biophysical limit for sensing accuracy derived by Berg and Purcell (1977). Briefly, they assume that fluctuations in molecule number are proportional to $\sqrt{N}$, where N is molecule number. Since we use a continuum variable for the chemoattractant, fluctuations can be expressed as $\sqrt{Ac}$ where A is some area of interest, and c is the average concentration in that area. The accuracy of concentration measurements is inversely proportional to fluctuations, which gives

$$\frac{\Delta c}{c} \approx \frac{1}{\sqrt{N}} = \frac{1}{\sqrt{Ac}} = \frac{\xi}{\sqrt{c}}. \tag{2.11}$$

  where $\Delta c = c_{\text{new}} - c_{\text{old}}$ and we define ξ as the sensing accuracy. We choose ξ sufficiently high to ensure that the movement is not always informed, that is, sometimes movement is not up the gradient of chemoattractant. Simulations are generally robust to changes in ξ, however, there is a trade-off between ξ and the internalisation rate, λ.

- D – diffusion coefficient of chemoattractant. The exact value of the diffusion coefficient is unknown for the system. We use a relatively small value because it has been shown that only around 1% of VEGF freely diffuses, whilst the rest binds to the ECM (MacGabhann et al., 2006). We found that our results were robust to a range of values of D, as listed in Table 2.1.

- χ – production rate of chemoattractant. The VEGF production rate in the tissue is unknown, but since experimental results show that there is almost no VEGF produced

where the cells have already internalised it (McLennan et al., 2010), we assume that the production rate is small.

- λ – chemoattractant internalisation rate. The internalisation rate of VEGF is also unknown but this parameter regulates the creation of the VEGF gradient, and thus how quickly the cells advance, so we adjust this parameter to ensure that a realistic distance is travelled by cells. The results are robust if we make simultaneous changes in the sensing accuracy, ξ, and λ, therefore we adapted the internalisation rate to our chosen sensing accuracy, ξ. There is a trade-off between λ and κ, so, for simplicity, we fixed κ and focused on changing λ.

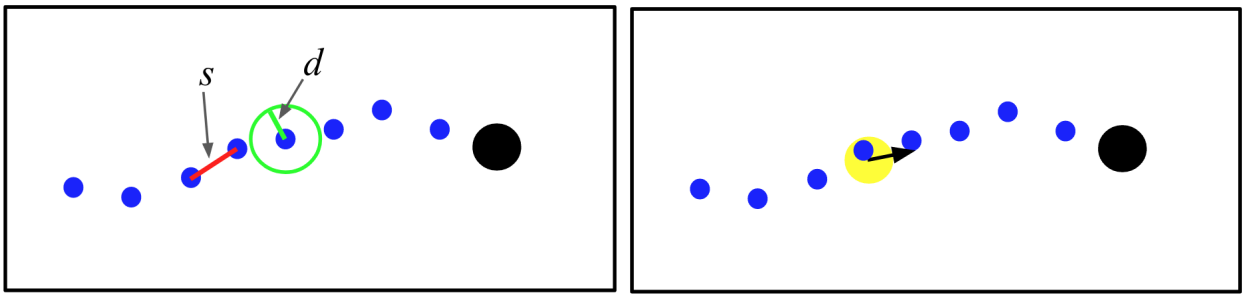
- k_{in} – the rate at which cells enter the domain. This is the rate of attempted cell insertions, and not the effective rate seen *in vivo* because of volume exclusion. We attempt to insert one new cell every minute to ensure that there is a sufficient number of cells in the domain, recalling again that our simulations are a two-dimensional abstraction of the three-dimensional migratory stream, which may contain four to five times as many cells *in vivo* in the transverse direction (Paul Kulesa, personal communication). Since it appears, experimentally, that entering cells do not push the cells ahead of them, we only allow cells to enter the domain when there is adequate space.

- ϵ – distance a follower has to be ahead of a leader to swap phenotypes. As discussed in Section 1.4, we use a simplified version of the switching mechanism based on cell position in the stream. We assume that a follower has to be $\epsilon = 10\mu$m ahead of a leader for their phenotypes to swap to ensure that switching does not occur too frequently. The results are robust to changes in this parameter because we have a fixed number of leaders.

- d – threshold distance to a tunnel to enter it (Figure 2.5). It is advisable to set d to be at most half the track spacing s, so that the cells are not close to two tunnel positions at the same time. However, it is unrealistic to choose $d \ll 10\mu$m because this would mean that follower cells have a very small chance of finding the track.

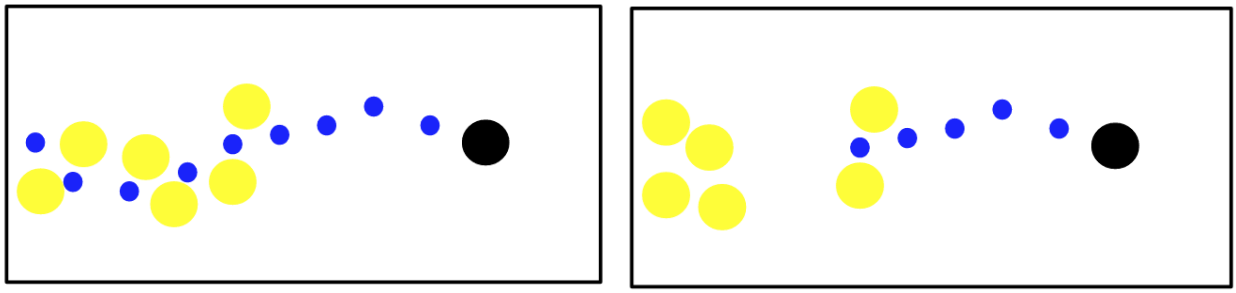
- s – track spacing (Figure 2.5). This is a parameter that determines the distance between leader positions that we record, corresponding to a "tunnel". We choose a small value to represent a continuous tunnel on a scale of cell sensing, but not too small to avoid high computational costs. The model is robust to smaller values of s ($s < 20\mu$m), but not for significantly larger values because, in those cases, follower cells rarely find tracks and guidance by tunnelling does not add additional value.

- n_t – number of leader positions tracked (Figure 2.5). We choose this parameter such that $s \times n_t > L_x$. This means that the tunnel has to be all along the domain to guide all the cells (Figure 2.6). We found that if a tunnel was shorter than the length of the domain, then the likelihood of a stream breakage increases, so the tunnelling mechanism would not provide a significant advantage to ensure coherent cell migration. We assume that the track is permanently in place and so does not degrade over time. We do not explicitly include reinforcement of the track by followers but our assumption that the track does not degrade over time could be viewed as reinforcement of the track by followers.



(a) **(b)**

Figure 2.5: (a) Schematic to illustrate the parameters of the tunnelling model: d – threshold distance to tunnel to enter it; s – track spacing; number of leader positions tracked, n_t, is the number of blue circles (eight in this example). (b) Schematic to represent a follower in a tunnel. Black circle represents a leader cell, yellow circle – follower cell, blue circles – track left by the leader and black arrow – direction of follower cell movement.



(a) (b)

Figure 2.6: Schematic to illustrate how an insufficient number of leader positions tracked (n_t) may not ensure reliable guidance. (a) Full track – follower cells are guided by the track left by the leader. (b) Insufficient track – the track is not sufficiently long and some followers are left behind. Black circle – leader cell, yellow circles – follower cells, blue circles – track left by the leader.

2.3 Effect of changes in cell speed, stabilisation, polarisation and number of filopodia induced by manipulation of AQP-1 expression

Experimental findings have revealed multiple features that are affected by the regulation of AQP-1 expression. However, it is not experimentally possible to identify the effect of each of these features separately. Instead, to address this question, we employ our computational model. We modify five parameters, or features, of the model to simulate the mechanisms by which AQP-1 influences cell migration: cell speed; filopodia stability; filopodia polarity; filopodia number and ECM degradation (Table 2.2).

In our computational model, we initially quantified changes in the dynamics of cells when we introduced the effects of overexpression and downregulation of AQP-1. Different combinations of parameter perturbations are labelled as "Model x" (x from 1 to 11) and the

values of the parameters for different models can be found in Table 2.2. We choose this set of models based on experimental considerations. We measured the density of cells along the domain and the likelihood of stream breakage, defined as the proportion of cells not in chains or tunnels at the end of a simulation. Specifically, in the control case, the cell speed was set to 62 μm/h, filopodia were not stabilised, and there was a representative number of three filopodia per cell (Model 1). To simulate AQP-1 overexpression, we approximated biological observations and increased the cell speed to 82 μm/h, stabilised filopodia and set the number of filopodia to two per cell (Model 2). To simulate inhibition of AQP-1, the cell speed was decreased to 57 μm/h, and cells only had one filopodium, which was not stabilised (Model 3). Initially, we did not incorporate ECM degradation into our models, that is, there is no tunnelling mechanism in Models 1-9. Simulations were run one hundred times with each parameter set and the results at $t = 18$ hours (the length of an experiment was 24 hours but NCC only emerge after six hours) were averaged to account for random variations (Figure 2.7, 2.8, 2.9). As expected, cells at the front travelled further when their speed was increased (Model 2) and less far when it was decreased (Model 3) (Figure 2.7(a)). However, when the cell speed was increased, the simulated streams broke apart more frequently, and so the model could not sustain collective migration (Figure 2.8). Stream breakage is not observed *in vivo* and therefore this observation led us to further investigate speed versus filopodia dynamics with regards to their effects upon collective cell migration *in silico*.

	speed, μm/h	stabilisation of filopodia	number of filopodia	tunnelling or contact signalling
Model 1 (control)	62	no	3	contact
Model 2 (AQP-1 up)	82	yes	2	contact
Model 3 (AQP-1 down)	57	no	1	contact
Model 4	82	no	3	contact
Model 5	82	yes	3	contact
Model 6	62	yes	3	contact
Model 7	62	yes	2	contact
Model 8	62	yes (polar)	2	contact
Model 9	82	yes (polar)	2	contact
Model 10	62	yes	2	contact + tunnelling
Model 11	82	yes	2	contact + tunnelling

Table 2.2: Model parameters for various experimental and hypothetical scenarios.

In our simulations, when cell speed was increased, with or without filopodium stabilisation, cells at the front travelled farther compared to the control case (Models 4 and 5 compared to Model 1) but stream breakage was much more likely to occur (Figure 2.7(a), (b), Figure 2.8). This happens because leader cells move so fast up the gradient of chemoattractant that followers lose contact. The number of filopodia (two or three) affects the likelihood of stream breakage at control speeds, with more filopodia resulting in a higher likelihood of breakage but with little impact upon the distance migrated (compare Model 6 with Model 7) (Figure 2.7(b), Figure 2.8). At control speeds, an increase in the likelihood of stream breakage is likely to be due to higher cell directionality induced by a higher number of filopodia (with a higher number of filopodia, the cells explore their environment better, and thus undergo more directed motion). At higher speeds, whether cells have two or three filopodia does not significantly affect the probability of stream breakage (it is high regardless of the number of

filopodia) or the distance the cells migrate (compare Model 2 to Model 5) (Figure 2.7(a), (b), Figure 2.8). Stabilisation of filopodia increases the furthest distance travelled by cells regardless of the cell speed because it allows the cells to "bulldoze" through the embryonic environment. It also has a noticeable effect on the likelihood of stream breakage at control speeds, but a small effect at high speeds (compare Model 1 with Model 6 and Model 4 with Model 5) (Figure 2.7(a), Figure 2.8). This effect at control speeds is due to improved invasion by leader cells and the inability of follower cells to catch up. Whereas at high speeds, the likelihood of stream breakage is already large due to high cell speed, and so filopodium stabilisation does not change it significantly. Finally, polarity does not have a significant effect on the migration (compare Model 7 with Model 8 and Model 2 with Model 9) (Figure 2.7(c), Figure 2.8). We demonstrate that since the cell movement is already polar, up the cell-induced gradient of VEGF, an enhancement of the polarity does not alter collective cell invasive ability.

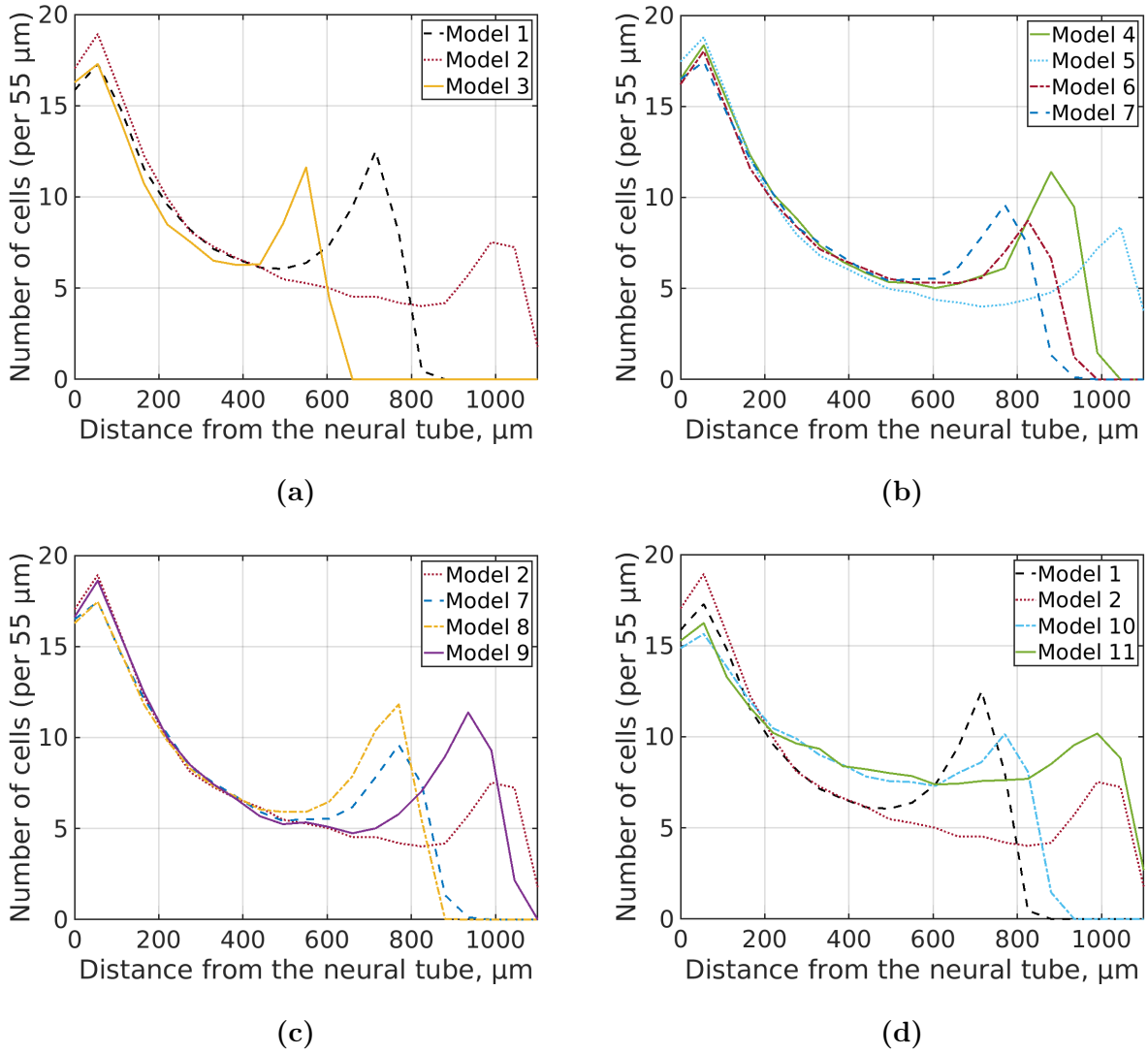


Figure 2.7: Distribution of cells along the domain for different models (Table 2.2), average of one hundred simulations after 18 hours. (a) When AQP-1 is overexpressed (Model 2), NCCs travel further than in the control case (Model 1) with a lower density at the front. When AQP-1 is downregulated (Model 3), NCCs travel less than in the control case also with a slightly lower density. (b) When NCC speed is increased and the number of filopodia is as in the control case, NCCs migrate further if filopodia are stabilised (compare Model 4 and Model 5). When NCC filopodia are stabilised and the number of filopodia is as in the control case, an increase in cell speed leads to better invasion (compare Model 6 and Model 5). A decrease in the number of filopodia has a minor effect on the density of cells with control speed and stabilised filopodia (compare Model 6 and Model 7). (c) Polarity does not lead to an increased furthest distance travelled by cells at control speeds (compare Model 7 and Model 8) and at high speeds (compare Model 2 and Model 9). (d) When the tunnelling mechanism is included, the furthest distance travelled by cells is not altered significantly but the density of cells is higher (compare Model 1 and Model 10; Model 2 and Model 11).

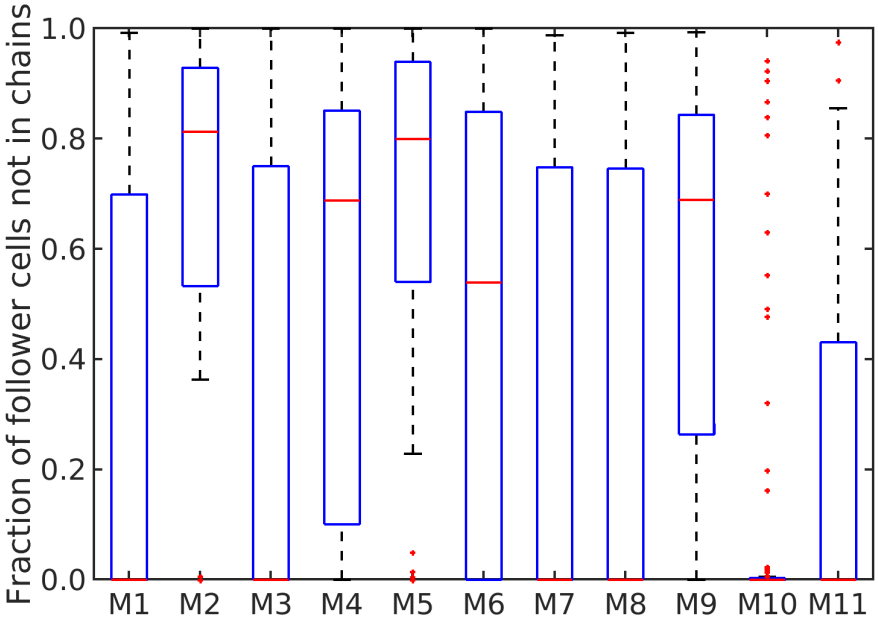
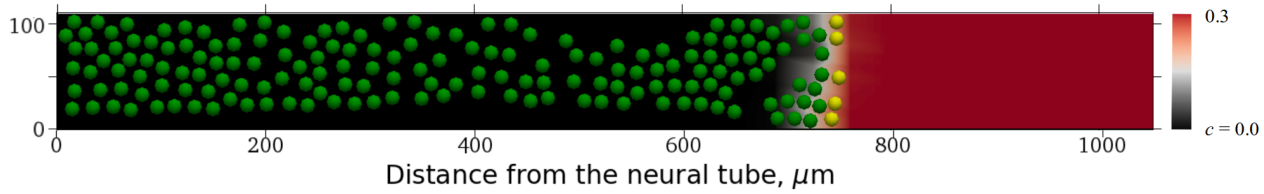
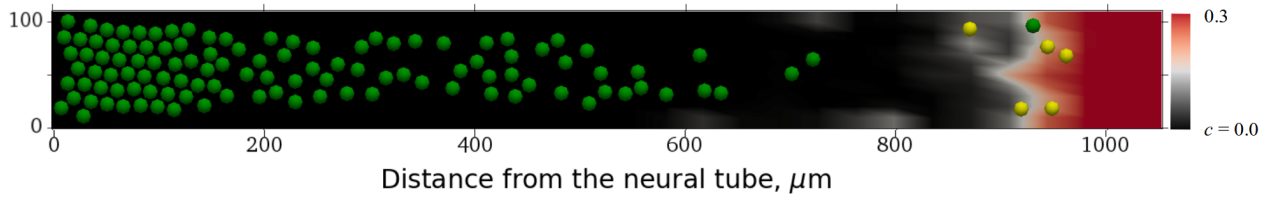


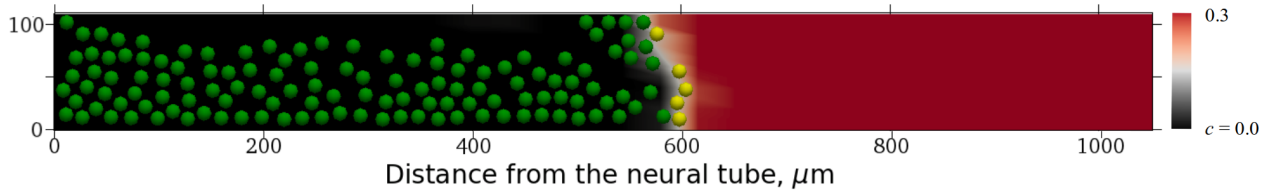
Figure 2.8: Boxplots of fractions of follower cells not in chains (also not in tunnels in Model 10 and Model 11) at $t = 18$ hours. Results are averaged over one hundred simulations. For each model, the red line indicates the median, and the bottom and top edges of the box indicate the 25th and 75th percentiles, respectively. The dotted lines extend to the most extreme data points not considered outliers, and the outliers are plotted individually as red dots. M – Model. Stream breakage is most likely for the variation of AQP-1 overexpression models with contact only signalling mechanism (Models 2, 5 and 9 from Table 2.2).



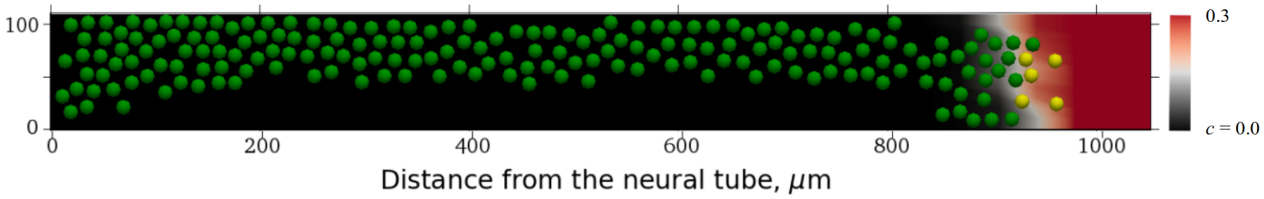
(a) Model 1, control.



(b) Model 2, AQP-1 overexpression.



(c) Model 3, AQP-1 knockdown.



(d) Model 11, AQP-1 overexpression with tunnelling.

Figure 2.9: Snapshots from four selected models at $t = 18$ hours. (a) Control case. (b) Overexpression of AQP-1 results in cells travelling further than in the control case. (c) AQP-1 knockdown leads to shorter distances travelled by the cells than in the control case. (d) Overexpression of AQP-1 with tunnelling mechanism results in cells travelling further than in the control case and the stream remains coherent. Yellow circles – leader cells, green circles – follower cells, c – concentration of chemoattractant (VEGF).

2.4 Effect of extracellular matrix degradation induced by AQP-1 overexpression

Even though our model simulations indicate that speed and filopodium stabilisation are both key parameters for controlling cell invasion, the stream breakage displayed *in silico* is inconsistent with our *in vivo* data. This suggests that there is another signalling mechanism from leaders to followers that ensures continuity of the invading stream. Our experimental findings suggest that increasing AQP-1 activity leads to an increase in MMP activity and thus to an increase in degradation of the ECM. It is therefore possible that ECM degradation could contribute to collective migration of the stream through the generation of "tunnels" within the ECM. Therefore, we included the formation of tunnels by leader cells *in silico*. The addition of tunnelling into the control model has no significant effect on cell migration (compare Model 1 with Model 10) (Figure 2.7(d), Figure 2.8). To simulate overexpression of AQP-1 in the model and include the effects of increased MMP activity, cell speed was increased, filopodia were stabilised and decreased in number from three to two, and the leaders generated tunnels for the followers. In this scenario, our model predicts that the stream is unlikely to break up and invasion is very robust (compare Model 2 with Model 11) (Figure 2.7(d), Figure 2.8). Overall, these simulations demonstrate that ECM degradation is a crucial factor, which is induced by AQP-1, to ensure successful collective cell invasion.

Having explored the features that account for leader cell polarisation and a candidate for cell-cell guidance mechanism, we next study the effect of spatial confinement on the migration of NCCs.

2.5 Investigation of neural crest cell spatial confinement

We now investigate the effect of externally imposed confinement on collective NCC migration. As discussed in Section 2.1, the proteoglycan versican has been shown to act as an inhibitor for cranial NCC migration in Xenopus (Szabó et al., 2016). In chick, the mechanisms that regulate chick cranial NCC confinement into streams are unknown. A potential candidate is the inhibitory gene DAN which is expressed in NCC-free regions close to the neural tube during NCC migration (McLennan et al., 2017). Since it is uniformly distributed prior to migration, it is likely that NCCs can degrade DAN expression, creating a confined region for the rest of the cells. However, it is an open question as to whether DAN is indeed the key contributor to confinement because McLennan et al. (2017) demonstrated that DAN only slows the cells down and makes them less directional rather than fully inhibits their movement. It is also possible that in chick, directional guidance by the chemoattractant VEGF, which is expressed in a narrow corridor, is sufficient to ensure that the cells do not spread out but, instead, travel in that narrow corridor. Here, we investigate the effect of confinement on the guidance and successful invasion of NCCs.

For the sake of simplicity, zero Dirichlet boundary conditions were initially used for the chemoattractant (VEGF) concentration (McLennan et al., 2012) to ensure that cells did not leave the domain, as this boundary condition created an inward chemotactic gradient. However, they were then replaced, due to the biologically unrealistic flow of chemoattractant out of the domain (Schumacher, 2015), by zero-flux boundary conditions for VEGF (McLennan et al., 2015a,b, 2017). However, at that time, it was not clear if there were inhibitory signals outside the migratory domain.

Computational modelling is particularly useful in investigating the effect of confinement because it is difficult to experimentally investigate its effect without knowing the inhibitors. In our modelling framework, we relax the assumption of the narrow rectangular migratory domain with zero-flux boundary conditions set along the top and bottom bounding

edges for VEGF and NCCs[1]. To this end, we consider a wider domain (width 360μm instead of 120μm) and, in this wider domain, the boundary along the corridor of width 120μm is now an internal boundary (Figure 2.10). We will refer to this internal boundary as the internal confinement boundary. To assess how confinement affects the efficacy of invasion, we will vary the length of the internal confinement boundary and observe how the cells behave.

We define three different cases: a full internal confinement boundary, no internal confinement boundary and a partial internal confinement boundary (Figure 2.10). In the full internal confinement boundary case, the migratory domain is defined as a rectangular domain of width $L_y = 120\mu$m with the zero-flux boundary conditions for VEGF and NCCs imposed along the top and bottom bounding edges, ceteris paribus (Figure 2.10(a)). To model the case with no internal confinement boundary, we simply use the domain of width 360μm with the zero-flux boundary conditions for VEGF and NCCs imposed along the top and bottom bounding edges (Figure 2.10(b)). In the partial internal confinement boundary case, part of the domain is modelled as in the full internal confinement boundary case, and part of the domain as in the no internal confinement boundary case (Figure 2.10(c)). In the no internal confinement case, we still assume that the cells only enter the domain in a confined region, rather than along the full width of the domain, because we focus on the cells emerging at rhombomere 4. The relaxation of this assumption, could be an interesting area for future investigations.

In our computational modelling framework, we make the following assumptions. We assume that the length of the internal confinement boundary does not elongate as the domain grows. This assumption is used to clearly distinguish the effect of a fixed internal confinement boundary length but in reality, the boundary could be elongating. We also assume that the internal confinement boundary is imposed for both NCCs and VEGF even though, to our knowledge, there is no known interaction between DAN and VEGF. We make this assumption

[1]Zero-flux boundary conditions for the NCCs are defined as follows: a cell may extend its filopodia outside the domain, but if all of its filopodia are extended outside the domain, then the cell does not move.

for simplicity but even if there was flux of VEGF leading to outward chemotactic gradient, NCCs could not move in that direction. In addition, if DAN is the inhibitor that we model, then imposing zero-flux boundary conditions along the top and bottom bounding edges as the internal confinement boundary is a model simplification, since DAN does not fully inhibit cell movement. However, we do not restrict ourselves to DAN as the only inhibitor but are open to the possibility that other inhibitors may be present.

We compare two different NCC stream characteristics. The first is the likelihood of stream breakage, as defined in Section 2.3. The second summarises how widely spread out the cells are in the direction perpendicular to the net movement direction. To this end, we define three regions: Region 1 is the $120\mu m$ width rectangle (Figure 2.11(a)), Region 2 consists of two rectangles of width 60μm outside Region 1 (Figure 2.11(b)), Region 3 consists of two rectangles of width 60μm outside Regions 1 and 2 (Figure 2.11(c)). We check the y-coordinate of each cell (cell_y) at the end of simulations to verify in which region the cells are distributed:

– if $120 \leq \text{cell}_y \leq 240\mu$m, then that cell is defined as being in Region 1;

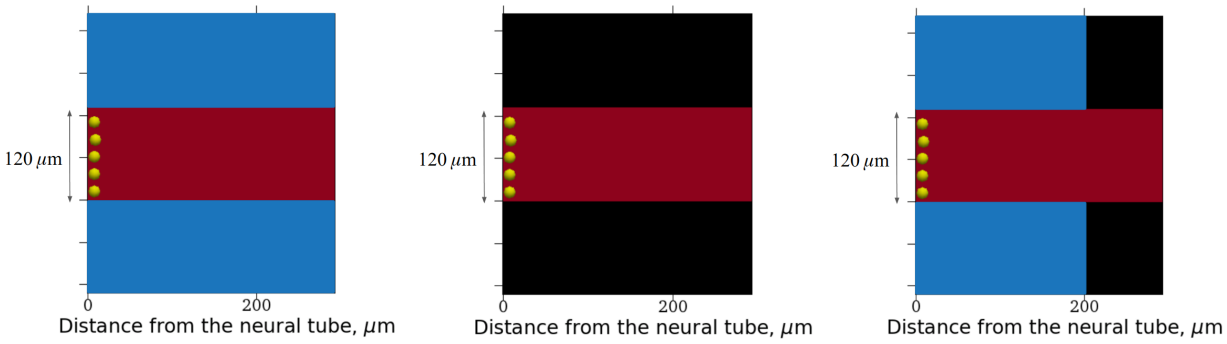
– if $60 \leq \text{cell}_y < 120\mu$m or $240 < \text{cell}_y \leq 300\mu$m, then that cell is defined as being in Region 2;

– if $0 \leq \text{cell}_y < 60\mu$m or $300 < \text{cell}_y \leq 360\mu$m, then that cell is defined as being in Region 3.

We then calculate the fractions of cells in different regions. Region 1 corresponds to the biologically realistic migratory domain. The presence of cells in Region 2 corresponds to a weak deviation from the biologically realistic migratory domain. The presence of cells in Region 3 corresponds to a large deviation from the biologically realistic migratory domain. We investigate how these statistics change when we assume different levels of confinement.

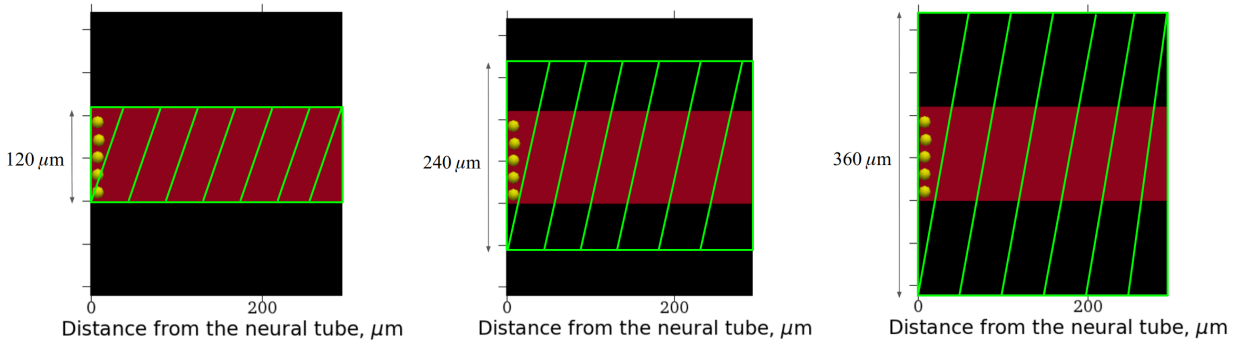
We perform the investigation described above for two different models (Model 1 and Model 11 in Table 2.2). We choose these two models to demonstrate that the results are robust to changes in model parameters, such as cell speed and filopodia number, and model

features, such as cell-cell interactions (either by contact only in Model 1 or by contact and tunnelling in Model 11). We choose Model 11, in addition to the control Model 1, because in this model the cells travel further than in the control case but the likelihood of stream breakage is low. Simulations were run one hundred times for each level of spatial confinement and the results at $t = 18$ hours were averaged to account for random variations.



(a) **(b)** **(c)**

Figure 2.10: Different confinement possibilities for the initial set up: (a) full internal confinement boundary; (b) no internal confinement boundary; (c) partial internal confinement boundary. The red rectangle corresponds to the region with uniform initial chemoattractant concentration, $c = 1$. The chemoattractant concentration in the black region is zero, $c = 0$. The blue rectangles correspond to confinement. Yellow circles represent NCCs.



(a) **(b)** **(c)**

Figure 2.11: Different regions (indicated by the green diagonal lines) that determine how widely the cells are spread out: (a) Region 1 – a narrow stream; (b) Region 2 – the cells weakly deviate from the narrow stream; (c) Region 3 – the cells largely deviate from the narrow stream. The red rectangle corresponds to the region with uniform initial chemoattractant concentration, $c = 1$. The chemoattractant concentration in the black region is initially zero, $c = 0$. Yellow circles represent NCCs.

2.5.1 Results

We start with a visualisation of cell distributions when full, no and partial internal confinement boundaries are considered. We showcase the snapshots of simulations from Model 11 because in this model the cells are more motile than in the control case and the effect of confinement can be seen more clearly. Figure 2.12 is an example of the case with a full internal confinement boundary in which, evidently, all the cells are in the narrow Region 1. Figure 2.13 is an example of the case in which there is no internal confinement boundary and the cells spread into all three regions, there is a large deviation from the biologically realistic migratory domain. Figure 2.14 is an example of the case in which there is a partial internal confinement boundary, showing a weak deviation from the biologically realistic migratory domain.

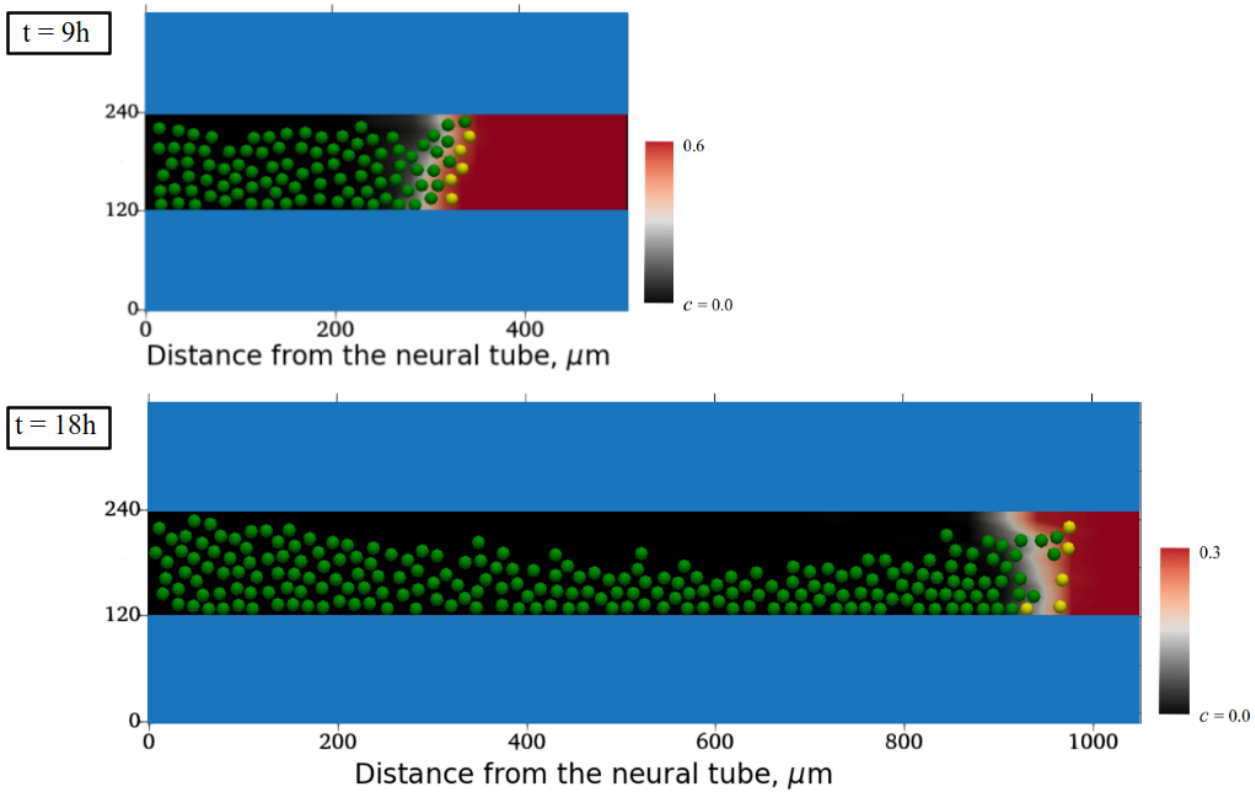


Figure 2.12: Snapshots from Model 11 (parameters in Table 2.2) at $t = 9, 18$ hours with an internal confinement boundary all along the domain. Yellow circles correspond to leader cells, green circles correspond to follower cells, and c is the concentration of chemoattractant. The blue rectangle represents confinement.

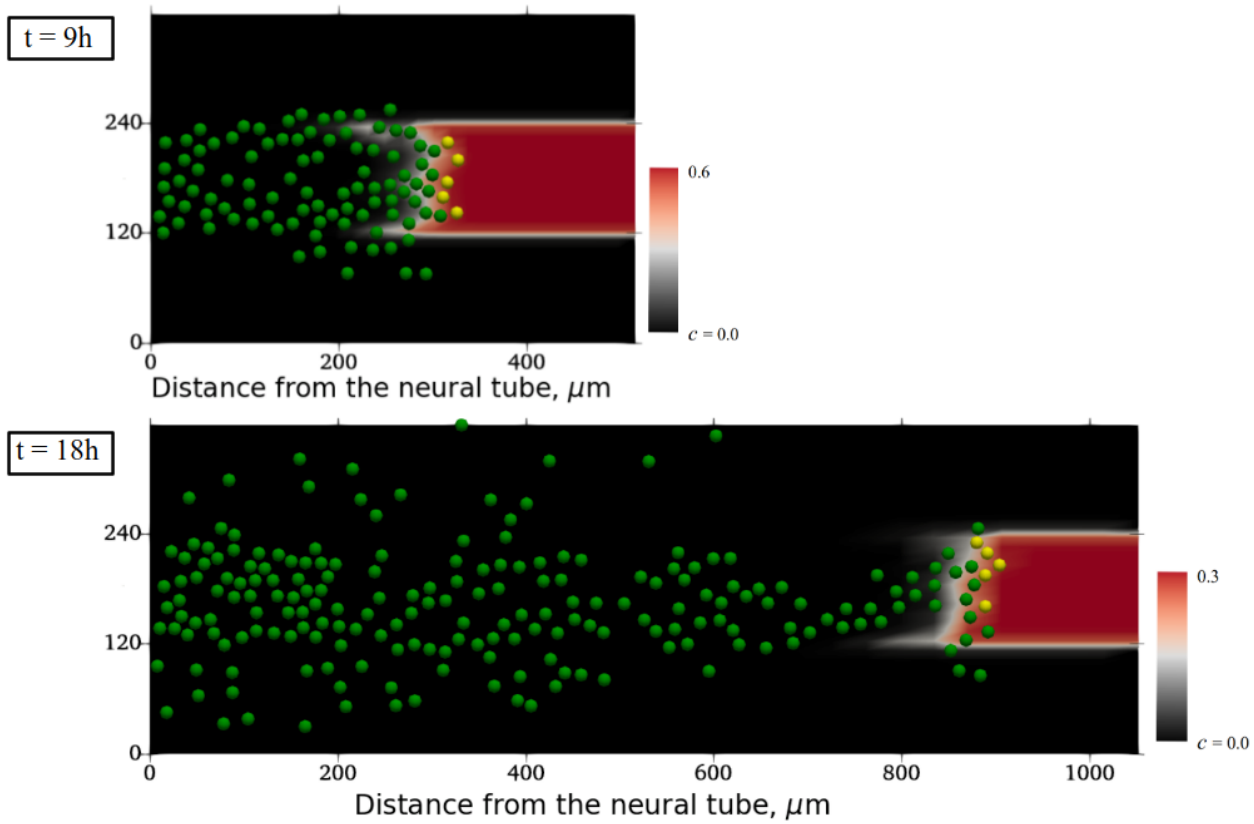


Figure 2.13: Snapshots from Model 11 (parameters in Table 2.2) at $t = 9, 18$ hours with no internal confinement boundary. Yellow circles correspond to leader cells, green circles correspond to follower cells, and c is the concentration of chemoattractant.

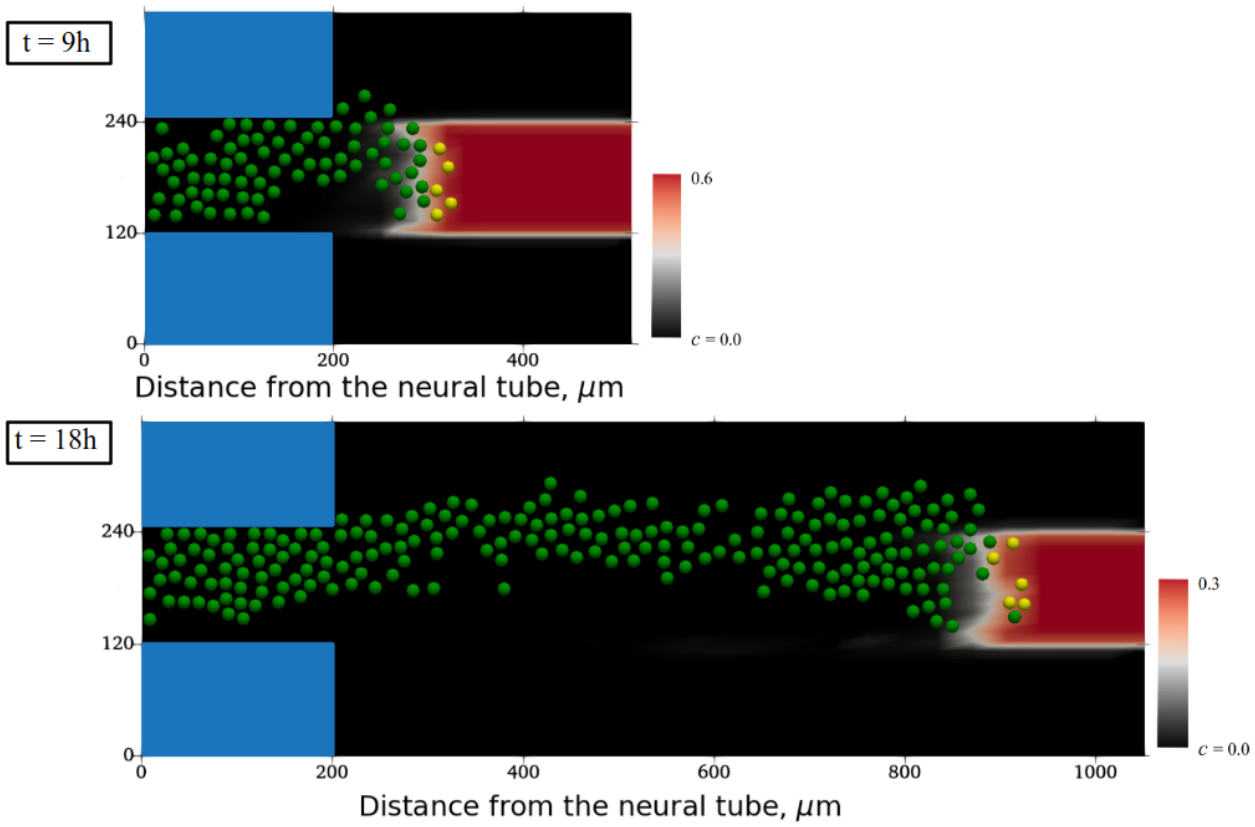
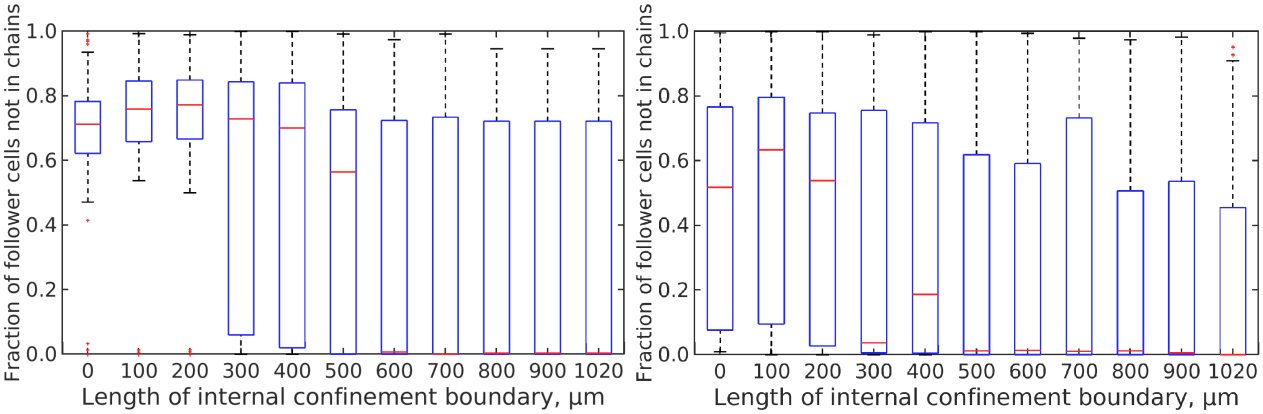


Figure 2.14: Snapshots from Model 11 (parameters in Table 2.2) at $t = 9, 18$ hours with an internal confinement boundary running from 0μm to 200μm from the neural tube. Yellow circles correspond to leader cells, green circles correspond to follower cells, and c is the concentration of chemoattractant. The blue rectangle represents confinement.

We now examine the likelihood of stream breakage for different levels of spatial confinement. Figure 2.15 demonstrates that stream breakage is most likely when the internal confinement boundary is short $(0 - 200\mu\text{m})$ for both models. This is to be expected because when the cells are free to travel in a wider region, it is more difficult for them to find chains or tunnels, which leads to stream breakage. The likelihood of stream breakage decreases as the length of the internal confinement boundary is increased, again, as expected. However, there is a sharp decrease in the likelihood of stream breakage, especially for Model 11 (Figure 2.15(b)), when the length of the internal confinement boundary is greater than 200μm, implying the importance of an internal confinement boundary close to the neural tube. The

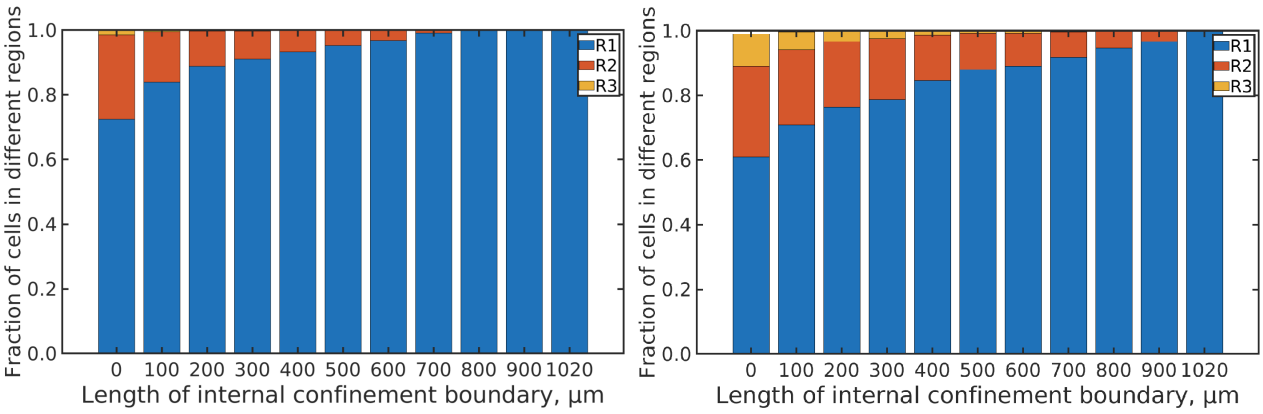
average likelihood of stream breakage is almost zero for an internal confinement boundary of length 600μm (for Model 1) and 500μm (for Model 11), and it remains small after that point. Therefore, we suggest that a full internal confinement boundary is not necessary to ensure low likelihood of stream breakage – an internal boundary of about half the length of the full domain is sufficient. We also suggest that if the tunnelling interaction mechanism is included in addition to the contact interaction mechanism, then a shorter internal confinement boundary is sufficient to ensure a low likelihood of stream breakage (compare Figure 2.15(a) and (b)).

We now investigate to what extent the cells spread out when different lengths of internal confinement boundary are considered. Figure 2.16 demonstrates that there is a monotone decrease in the fractions of cells in Regions 2 and 3 when the length of the internal confinement boundary is increased. There are more cells in Regions 2 and 3 when the internal confinement boundary is short for Model 11 than for Model 1 (compare Figure 2.16(a) and (b)) because in Model 11 the cells move at higher speeds and explore their environment to a lesser extent (two filopodia in Model 11 instead of three filopodia in Model 1), so they are less directional. We do not observe any significant variations in fractions of cells in different regions when the length of the internal confinement boundary is increased.



(a) Model 1. **(b)** Model 11.

Figure 2.15: Boxplots of fractions of follower cells not in chains (or tunnels for Model 11) at $t = 18$ hours. This statistic correspond to the likelihood of stream breakage. Results are averaged over one hundred simulations. For each model, the red line indicates the median, and the bottom and top edges of the box indicate the 25th and 75th percentiles, respectively. The dotted lines extend to the most extreme data points not considered outliers, and the outliers are plotted individually as red dots. Stream breakage is most likely when there is a short internal confinement boundary length. For the same internal confinement boundary length, the stream is less likely to break for Model 11 than for Model 1. 1020μm corresponds to a full internal confinement boundary.



(a) Model 1. **(b)** Model 11.

Figure 2.16: Fraction of cells in different regions for different levels of cell confinement. Results are averaged over one hundred simulations. R1 – Region 1, R2 – Region 2, R3 – Region 3. There is a monotone decrease in cell numbers in Regions 2 and 3 as cell confinement is increased. When the internal confinement boundary is short, the cells are more dispersed, i.e. there are more cells in Regions 2 and 3, for Model 11 than for Model 1. 1020μm corresponds to a full internal confinement boundary.

We recall that the cell inhibitory gene DAN is only expressed in the region from zero to $100 - 200\mu$m from the neural tube (Figure 2.2). In our simulations, we observed that such a short internal confinement boundary would not ensure that all the cells are restricted to the biologically realistic migratory domain but we observe that there is a sharp decrease in the likelihood of stream breakage for internal confinement boundaries of length greater than 200μm. We therefore conclude that other inhibitors may be present to ensure cell confinement, or there may be other factors that help the cells to stay in narrow streams, for example, fibre alignment.

2.6 Conclusions and discussion

Previous computational models for the migration of chick cranial NCCs did not explore in detail aspects such as the nature of cell polarity, cell-cell signalling and the role of spatial confinement. We dedicated this chapter to investigate these aspects. In the first part, we investigated the nature of cell polarity and cell-cell signalling by exploring the role of AQP-1. In the second part, we explored the effect of spatial confinement on the migration of NCCs.

We have extended the computational model developed by McLennan et al. (2012, 2015a,b, 2017) to test the experimentally generated hypotheses that AQP-1 influences cell migration through the regulation of experimentally identified features such as cell speed, filopodium polarity, filopodium stabilisation, filopodium number and ECM degradation. Our computational model investigated the consequences on collective NCC migration of perturbing these features. We identified cell speed, filopodium stabilisation and ECM degradation as key parameters for controlling NCC invasion. When we increase or decrease cell speed, together with other affected features, to simulate AQP-1 gain or loss of function, respectively, we observe changes in the maximum distance travelled by cells. However, a breakdown of the cell migratory stream occurs *in silico* when the cell speed is increased, a pattern that is not

observed *in vivo*. Examination of cell speed versus filopodial dynamics revealed that stabilisation of filopodia, rather than filopodia number or polarity, increases the furthest distance travelled by cells (regardless of speed) and reduces the likelihood of stream breakage. Thus, our computational model simulations support a role for AQP-1 in promoting NCC invasion through ECM degradation, stabilisation of filopodia and regulation of cell speed.

The creation of tunnels may be one of the ways in which the degradation of ECM can affect NCC migration. However, to perform a thorough study of NCC-ECM interactions, the dynamics of the ECM should be incorporated into the model in a more detailed and explicit manner. Explicit modelling of cell-ECM adhesion in cancer, for example, using non-local PDEs, has been successfully used to verify experimental hypotheses and generate new insights (Chaplain et al., 2011; Gerisch and Chaplain, 2008; Sherratt et al., 2009; Kim et al., 2009). Therefore, the role of ECM in NCC migration could, in the future, be investigated using similar modelling frameworks. Our experimental colleagues have been recently investigating the role of fibronectin, which is a glycoprotein found in the ECM, on the migration of NCCs. Data on the expression of fibronectin could be incorporated into the computational model of NCC migration to explore the effect of ECM remodelling on migration of NCCs. This may bear similarities to the role of fibronectin in tumour angiogenesis (Chaplain, 2000).

In this chapter, we also investigated the effect of confinement on the dynamics of NCCs. We demonstrated that the spread of the cells increases monotonically with the length of the internal confinement boundary. We observed the same trend for the likelihood of stream breakage, i.e. the stream is less likely to break for longer internal confinement length. There was a sharp decrease in the likelihood of stream breakage when the length of the internal confinement boundary is 200μm in comparison with 300μm, suggesting that this might be the region where a strong inhibitory signal is required. We also demonstrated that if the tunnelling interaction mechanism is employed in addition to the contact mechanism, then a shorter internal confinement boundary is sufficient to ensure a low likelihood of stream breakage. Another noticeable change occurred at 500μm. At this point, approximately half

of the total number of cells are already in the domain and they have travelled approximately half of the full domain length, so cell-cell connections are likely to be formed and maintained throughout the rest of migration. These results are robust to biologically realistic changes in parameters (simulations not shown). In general, we suggest that confinement effectively acts as a directional cue to facilitate collective cell migration by restricting cell movement, especially at the start of migration.

Further experimental investigations are necessary to verify whether the partial internal confinement boundary is indeed sufficient to ensure robust invasion. Perturbations of DAN in NCC-free regions would help us to verify its role as a confining agent. A more detailed study of the ECM would also provide insights into the role of the boundary, for example, a specific alignment of fibres might contribute to the confinement of the stream.

Chapter 3

Spatially non-uniform domain growth

In Chapter 2, and the previous models of chick cranial NCCs (McLennan et al., 2012, 2015a,b, 2017), domain growth was assumed to be spatially uniform but changing in time. This was motivated by measurements of the total length of the domain at different time points (Figure 2.4). However, recent experimental findings suggest that domain growth is not spatially uniform (McKinney et al., 2020). It is then a natural question to ask as to whether this makes migration more or less robust. Also, could there be a feedback loop between the migrating NCCs and the microenvironment (ECM and other cells), in which the former control domain growth? Alternatively, is spatially non-uniform domain growth necessary for other processes occurring in development, and so must NCC migration be robust to such non-uniformities? It is challenging to manipulate domain growth experimentally, therefore, computational modelling provides a natural means to investigate the effect of changes in domain growth profiles on collective cell migration. We dedicate this chapter to addressing these questions.

We explore the effect of spatially non-uniform domain growth on the migration of NCCs. We identify the regions in which enhanced domain growth facilitates invasion and in which it impedes invasion. Furthermore, we investigate whether NCCs can feedback on tissue

growth. We link some of the findings presented in this chapter with the paper published in collaboration with Paul Kulesa's lab (McKinney et al., 2020) in which my contribution was the computational modelling.

The structure of this chapter is as follows. In Section 3.1, we provide details of the relevant biology that suggests that tissue growth is spatially heterogeneous. We present the extension of our modelling framework to capture non-uniform domain growth in space in Section 3.2. Computational results on the impact of different domain growth profiles are presented in Section 3.3. In Section 3.4, we investigate the changes in the observed cell speed caused by different domain growth profiles. In Section 3.5, we consider domain growth profiles that replicate experimental findings and present model predictions. We perform *in silico* physical ablation of NCCs and chemical inhibition of tissue growth experiments in Sections 3.6 and 3.7, respectively. Motivated by the mismatch of *in vivo* perturbation experiments and *in silico* predictions, we further suggest a potential feedback mechanism between NCCs and domain growth in Section 3.8. We finish with a discussion in Section 3.9.

3.1 Biological background

NCCs travel through dense ECM and mesoderm, subjacent to the ectoderm (Figure 3.1), while the tissue is growing (Tosney, 1982; Noden, 1988). Similarly to NCCs, mesodermal cells are migratory but, in contrast with NCCs, they are also highly proliferative during the period of NCC migration (Kontges and Lumsden, 1996; Hacker and Guthrie, 1998; Evans and Noden, 2006) and two to three times more dense than neural crest (Paul Kulesa, personal communication). It is an open question as to how mesodermal cells, NCCs and tissue growth influence each other[1].

[1]McKinney et al. (2020) ruled out any significant contribution of ectoderm to lateral tissue growth because, despite significant ectodermal cell proliferation, the increased density of ectodermal cells suggests that proliferation does not lead to tissue expansion.

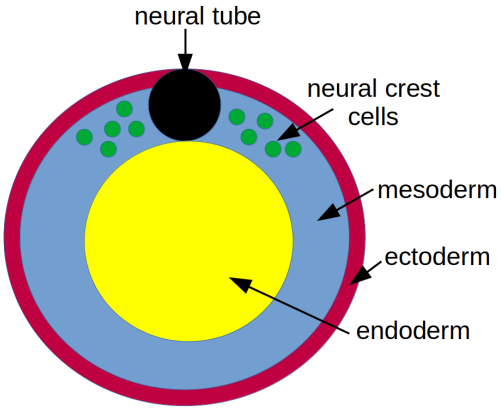
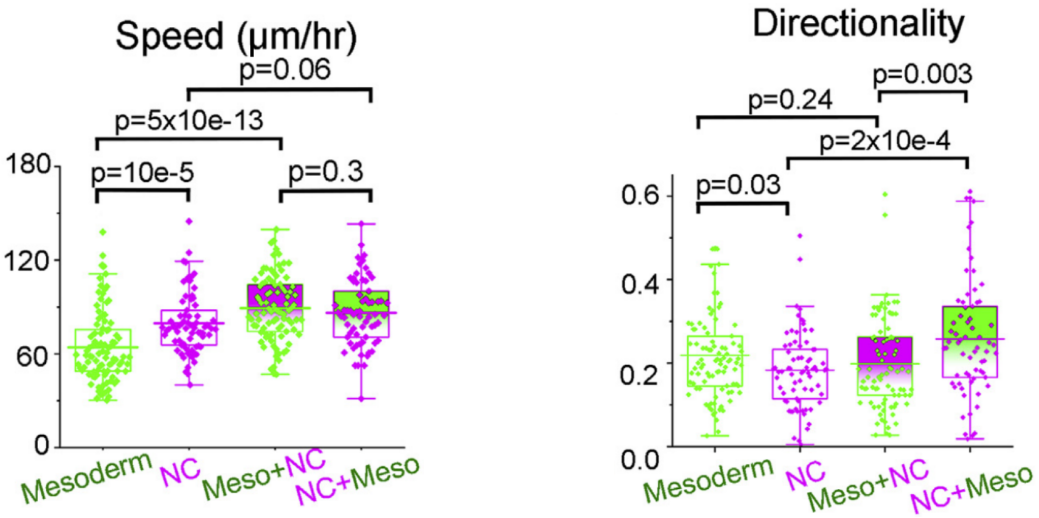


Figure 3.1: Schematic of a transverse section of an embryo representing the different germ layers (endoderm, ectoderm and mesoderm), NCCs and neural tube.

Recently, our experimental collaborators have investigated the spatial and temporal dynamics of individual mesodermal cells, and their interactions with chick cranial NCCs (McKinney et al., 2020). They examined and quantified the inherent migratory properties of mesodermal cells, either isolated from, or together with, NCCs *in vitro*, and compared these with *in vivo* behaviour. In culture, mesodermal cells moved more slowly than NCCs (with a speed of 64μm/h in comparison to 79μm/h, Figure 3.2(a)) but were slightly more directional[2] than NCCs (with a directionality of 0.22 in comparison to 0.19, Figure 3.2(b)). When NCCs were mixed with mesodermal cells, both cell populations moved faster (with speeds of 89 and 86 μm/h, respectively), with a more significant increase in mesodermal cell speed (Figure 3.2(a)). This result suggests that NCCs and mesodermal cells may advect each other or stimulate active movement. The directionality of mesodermal cells did not change significantly in the presence of NCCs but NCC directionality increased in the presence of mesodermal cells (Figure 3.2(b)).

[2]Directionality is defined as distance from start to finish divided by the total distance travelled.



(a) **(b)**

Figure 3.2: *In vitro* (a) speed and (b) directionality of mesoderm only (green, number of *in vitro* experiments, $n = 5$, 94 cells total), NCCs only (magenta, $n = 4$, 73 cells total), mesodermal cells in the presence of NCCs (green markers with magenta box, $n = 3$, 91 cells total) and NCCs in the presence of mesodermal cells (magenta markers with green box, $n = 3$, 66 cells total). Mesodermal cell speed increases significantly in the presence of NCCs. NCC speed increases to a lesser extent in the presence of mesodermal cells. Mesodermal cell directionality does not increase in the presence of NCCs. NCC directionality increases in the presence of mesodermal cells. In this figure, NC denotes neural crest cells. Figure reproduced from McKinney et al. (2020) with permission from Elsevier.

Furthermore, *in vivo* time-lapse images demonstrated that mesodermal cells moved in a counter-clockwise whirling pattern but after the emergence of NCCs from the neural tube, they transitioned to slightly slower but directed, lateral movement towards the branchial arches. NCCs migrated significantly faster than the mesodermal cells (53 vs 38μm/h for mesoderm) and with higher directionality (0.40 vs 0.26 for mesoderm).

The studies above reveal that NCCs influence mesodermal cell behaviour and vice versa. However, the interplay between tissue growth, NCCs and mesodermal cells is still

unclear. To tackle this question, McKinney et al. (2020) performed BrdU[3] labelling of mesodermal cells to measure the number of proliferating cells. They categorised the cells as proliferating if BrdU intensity was above a certain threshold level. They observed that there is substantial heterogeneity in cell proliferation in space and time (Figure 3.3). To ensure that mesodermal cell proliferation is a good statistic to describe non-uniformities in tissue growth, McKinney et al. (2020) investigated whether mesodermal cell density along the domain changes in time and, using the averaged nearest neighbour distance as a proxy for cell density, discovered that the cell density is relatively constant (Figure 3.4). They concluded that if cells proliferate intensely in certain regions and the density does not increase, then it is likely that the tissue is expanding in those regions. This result supports the hypothesis that mesodermal cell proliferation leads to tissue growth and that it varies in both space and time.

[3]BrdU is a synthetic thymidine analogue that can be used to label cells in S-phase (DNA replication) of the cell cycle. It is routinely used to measure whether or not cells are proliferating (Plickert and Kroiher, 1988)

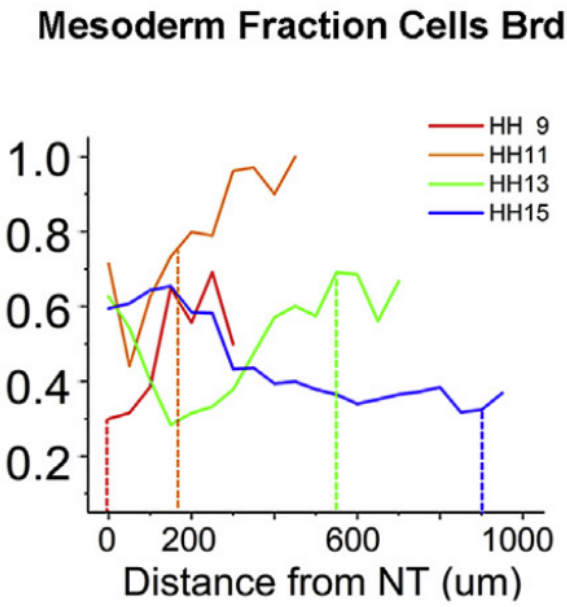


Figure 3.3: Fraction of mesodermal cells which are BrdU positive. We observe that initially, there are more BrdU positive cells in the distal part of the domain, and after 18 hours (approximately stage HH13) more BrdU positive cells in the proximal part of the domain. Dashed lines correspond to the front of the NCCs. We assume that higher fractions of BrdU positive mesodermal cells correspond to enhanced domain growth in that region. Figure reproduced from McKinney et al. (2020) with permission from Elsevier.

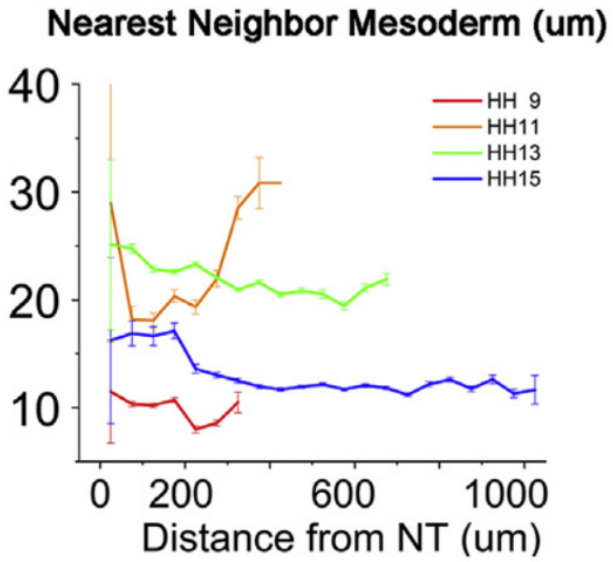


Figure 3.4: Nearest neighbour distance between mesoderm neighbours in 50μm bins along the domain from rhombomere 4 to the end of branchial arch 2. Density of cells remains relatively constant throughout the NCC pathway. Figure reproduced from McKinney et al. (2020) with permission from Elsevier.

McKinney et al. (2020) further investigated the interactions between tissue growth and NCC migration by ablating premigratory NCCs and inhibiting mesodermal cell proliferation. Ablation of premigratory NCCs led to a significant reduction in the length of the migratory domain, suggesting that NCCs influence domain growth (Figure 3.5). Furthermore, the NCCs that escaped ablation travelled a shorter distance than in control cases (Figure 3.5). Inhibition of mesodermal cell proliferation reduced the domain length and the furthest distance travelled by NCCs (Figure 3.6). Moreover, the ratio of the length of the NCC migratory stream to the domain length was significantly reduced (Figure 3.6). These studies further support McLennan et al.'s (2020) hypothesis that mesodermal cell proliferation directly affects tissue growth and NCCs are advected along the migratory route as the tissue grows.

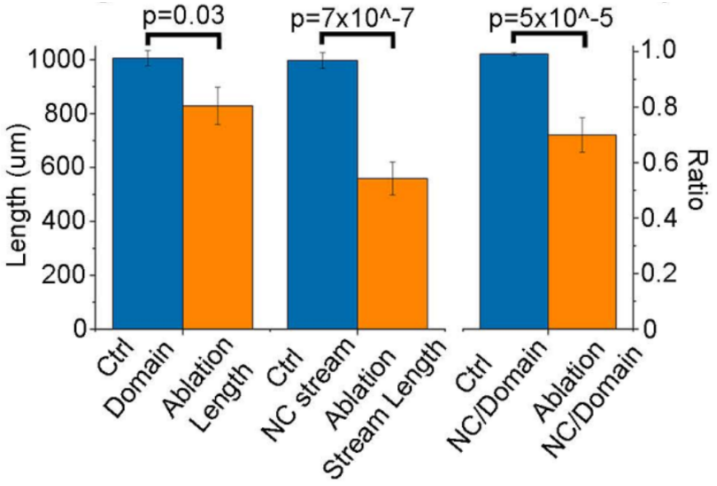


Figure 3.5: Length of the domain and NCC stream and the ratio for control and ablated embryos, $n = 10$ for ablated and $n = 12$ for control at 24 hours, where n is the number of embryos. The domain grows less after the ablation of NCCs, and NCCs also invade the domain to a lesser extent. Figure reproduced from McKinney et al. (2020) with permission from Elsevier.

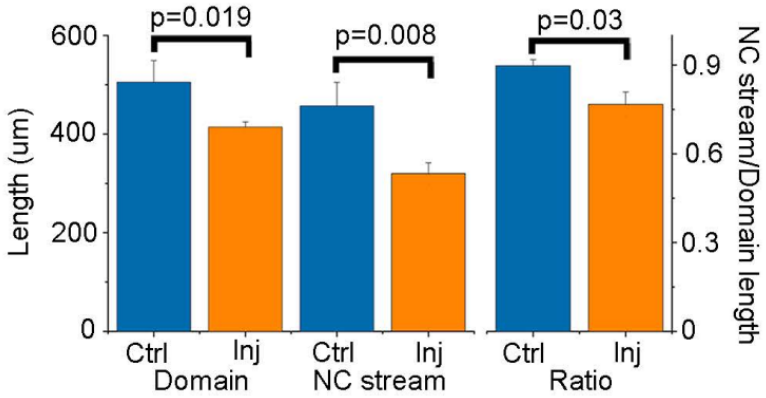


Figure 3.6: Length of the domain and NCC stream and ratio for eight embryos treated with growth inhibitor and eight control embryos at 12 hours. In the treated embryos (denoted by Inj), the length of the domain is reduced and the NCCs invade the domain to a lesser extent in comparison with the control embryos. Figure reproduced from McKinney et al. (2020) with permission from Elsevier.

The above results shed light on some of the questions that we raised about the role

of tissue growth on the migration of NCCs. For example, mesodermal cell proliferation was shown to be heterogeneous in space and it was hypothesised to act as the key component of tissue growth. Experimental results support the assumption that NCCs are advected by growth but the ablation experiment suggests that a more complex feedback mechanism between NCCs and tissue growth may be present. To systematically analyse the effect of spatially heterogeneous tissue growth on the migration of NCCs, as well as invasion robustness in the presence of non-uniform domain growth and potential feedback mechanisms, we employ our computational modelling framework. In the next section we describe the extension of our model to allow for inclusion of general spatially heterogeneous domain growth profiles.

3.2 Extension of the model to allow for spatially non-uniform domain growth

We extend the modelling framework developed in Section 2.2 in which domain growth was non-uniform in time but uniform in space. Experimental data suggest that there is no significant change in the depth of the mesoderm on the timescale of NCC migration and the domain growth mainly occurs in the x-direction. Therefore, motivated by the same arguments as in Section 1.2.5, we continue using a two-dimensional approximation of the three-dimensional system. In this chapter, we relax this assumption and allow for a general form of spatially non-uniform growth in the x-direction. The dynamics of cells, model assumptions, and pseudocode are the same as in the model described in Section 2.2. We use cell-cell interactions by contact, without the tunnelling mechanism described in Chapter 2, because they are computationally cheaper to simulate and the focus of this chapter is not on cell-cell interactions. Initial and boundary conditions are the same as in Section 2.2. We use zero-flux boundary conditions for NCCs and VEGF at the top and bottom boundaries of a domain of width 120μm due to the lack of detailed experimental data to support our hypothesis of a smaller confinement boundary discussed in Section 2.5. In the following subsections

we describe changes in the way we incorporate a general spatial profile for domain growth in the chemoattractant equation.

Chemoattractant dynamics

In Section 2.2 the reaction-diffusion equation used to model the dynamics of the chemoattractant VEGF was restricted to spatially uniform domain growth. We extend this model to incorporate a general domain growth profile (Crampin et al., 1999, 2002). We start with the same general form of the reaction-diffusion equation on a growing domain (Equation (2.2)):

$$\frac{\partial c}{\partial t}+\frac{\partial (ac)}{\partial x}=D\left(\frac{\partial^2 c}{\partial x^2}+\frac{\partial^2 c}{\partial y^2}\right)-c\sum_{i=1}^{N(t)}\frac{\lambda}{2\pi R^2}\exp\left[-\frac{(x-x_i)^2+(y-y_i)^2}{2R^2}\right]+\kappa c(1-c), \quad (3.1)$$

where $(x, y) \in [0, L_x(t)] \times [0, L_y]$ (parameter values in Table 2.2). All the terms, boundary and initial conditions are the same as for Equation (2.2). Again, assuming that the flow can be specified using a growth function Γ, the Lagrangian description is

$$x = \Gamma(X, t), \quad x \in [0, L_x(t)], \quad (3.2)$$

where $X \in [0, X_0]$ is an initial position marker with $X_0 = L_x(0)$, and $\Gamma(X, 0) = X$. The local flow is determined by

$$a(x, t) = \frac{\partial x}{\partial t}. \quad (3.3)$$

The term that specifies growth is $\partial a/\partial x$. In this case, growth is no longer uniform in space, so let us assume that the growth can be expressed as

$$\frac{\partial a}{\partial x} = S(X, t), \quad (3.4)$$

where $S(X, t)$ is the strain rate. Our Lagrangian form gives the description of the flow as

$$a(x, t) = a(\Gamma(X, t), t) = \frac{\partial \Gamma}{\partial t}. \quad (3.5)$$

Combining Equations (3.4) and (3.5) yields

$$\frac{\partial^2 \Gamma}{\partial t \partial X} = \frac{\partial a}{\partial X} = S(X,t)\frac{\partial \Gamma}{\partial X}, \tag{3.6}$$

with initial condition $\Gamma(X,0) = X$ and boundary conditions $\Gamma(0,t) = 0$ and $\Gamma(1,t) = L_x(t)$. The solution to Equation (3.6) is

$$\Gamma(X,t) = \int_0^X \exp\left(\int_0^t S(z,\tau)\mathrm{d}\tau\right)\mathrm{d}z. \tag{3.7}$$

It can sometimes be difficult to evaluate $\Gamma(X,t)$ for a given strain rate $S(X,t)$. Therefore, it is useful to switch to Lagrangian coordinates to solve the PDE. Writing the variables as functions of initial position (X,y) and time t (setting $C(X,y,t) = c(x,y,t)$) in Equation (3.1) and using Equations (3.2)-(3.6) gives

$$\frac{\partial C}{\partial t} + CS(X,t) = D\left(\frac{1}{\Gamma_X}\frac{\partial}{\partial X}\left(\frac{1}{\Gamma_X}\frac{\partial C}{\partial X}\right) + \frac{\partial^2 C}{\partial y^2}\right) + f(C), \tag{3.8}$$

where $(X,y) \in [0, X_0] \times [0, L_y]$ and

$$f(C) = \kappa C(1-C) - C\sum_{i=1}^{N(t)} \frac{\lambda}{2\pi R^2}\exp\left[-\frac{(\Gamma(X) - x_i)^2 + (y - y_i)^2}{2R^2}\right]. \tag{3.9}$$

Equation (3.8) only requires us to determine Γ_X, which can be done using Equation (3.6). We use this form because we want our framework to be flexible enough to incorporate any strain rate, $S(X,t)$, which we estimate from experimental data. We set zero-flux boundary conditions and initial conditions $C(X,y,0) \equiv 1$ for $(X,y) \in [0, X_0] \times [0, L_y(0)]$.

We describe the method of numerical approximation and the verification of numerical convergence of Equation (3.8) in Appendix B.

Domain growth: cell dynamics

We also have to change the way in which we update cell positions when domain growth is non-uniform in space. To update the position of each cell at each time step, we

first find the maximum $x_{\max} \in [0, L_x(t)]$ such that $\Gamma(x_{\max}, t) = \text{cell}_x(t)$ where $\text{cell}_x(t)$ is the x-coordinate of the cell position at time t. We then update the position of that cell as follows:

$$\text{cell}_x(t + \Delta t) = \text{cell}_x(t) + \Gamma(x_{\max}, t + \Delta t) - \Gamma(x_{\max}, t). \tag{3.10}$$

3.3 Effect of different domain growth profiles on the furthest distance travelled

Our goal is to answer the open question as to what extent NCC migration is altered by different domain growth profiles. We address this question by first investigating whether the dynamics of the NCCs changes when the growth is concentrated either distally or proximally. We split the domain into two parts and assume different domain growth rates in those parts: we call them Part 1 and Part 2, respectively (Figure 3.7). We investigate and compare cell dynamics when the seven different domain growth profiles depicted in Figure 3.8 are implemented. Initially, we consider uniform in space domain growth, then we split the domain as described above. We carry out two different studies: one in which we assume that Part 1(2) elongates twice as fast as Part 2(1) (Figure 3.8). To approximate total domain length, we use experimental data on the initial and final lengths of the domain. Instead of Equation (2.1) used in Section 2.2 to approximate the experimentally measured domain length, we used an exponential domain growth profile for its simplicity:

$$L_x(t) = L_0 \exp(\sigma t), \tag{3.11}$$

where L_0 is the initial domain length and, for the spatially uniform domain growth case, σ is the exponential domain growth rate inferred from experimental data. The approximation of the experimental data from McKinney et al. (2020) by an exponential is shown in Figure 3.9. The invasive abilities are slightly improved if the exponential domain growth profile (Equation (3.11)) is used instead of the logistic type domain growth profile (Equation (2.1))

in the control case (average length of the stream is 859μm for the model with domain length as in Equation (3.11) and 827μm for the model with Equation (2.1), ceteris paribus). This increase in the stream length still corresponds to a biologically realistic scenario and so we can use Equation (3.11) to model the spatially uniform domain growth.

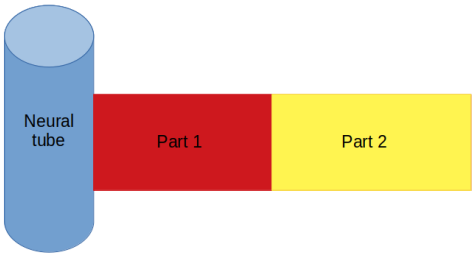


Figure 3.7: We divide the domain into two parts, Part 1 and Part 2. Part 1 is the portion of the domain proximal to the neural tube, while Part 2 is the portion of the domain distal to the neural tube. We vary the sizes of Part 1 and Part 2, as shown in Figure 3.8.

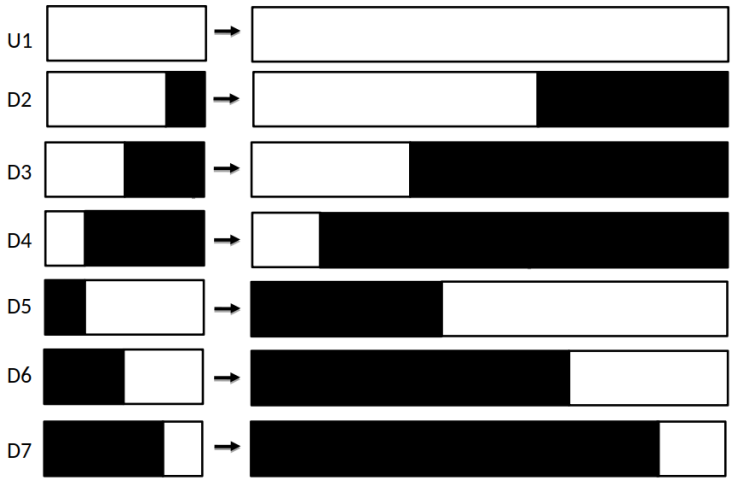


Figure 3.8: Growth profiles: different parts of the domain grow at different rates. The black part grows twice as fast as the white part. U1 represents spatially uniform growth. D2-7 represent the different growth profiles examined. In all cases, the total length of the domain increases to the same fixed final length.

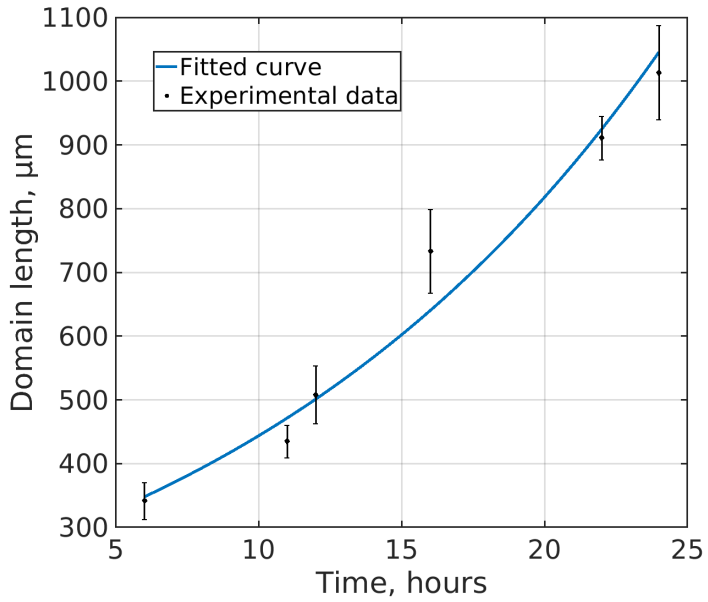


Figure 3.9: Growth profile for the domain of migration, showing experimental data (McKinney et al., 2020) and exponential curve fitted using the Least Squares Method (Equation (3.11)). We obtain that $\sigma = 0.06\text{min}^{-1}$. The measurements start at six hours because this is when the NCCs enter the domain. Error bars represent standard error.

For the spatially non-uniform case, we pick the growth rates in such a way that each of the growth profiles leads to the same total domain length after 24 hours. We use experimental data on the initial and final lengths of the domain to estimate the growth parameters. To find the two different growth rates we solve Equation (3.12):

$$P_1\exp(A_1\alpha t_{\text{final}}) + P_2\exp(A_2\alpha t_{\text{final}}) = L_{\text{final}}, \tag{3.12}$$

for α, where P_1 is the initial length of Part 1, P_2 is the initial length of Part 2, L_{final} is the final total length of the domain and the factors A_1 and A_2 determine the ratio of domain growth rates, for example, if Part 1 grows twice as fast as Part 2, then $A_1 = 2$ and $A_2 = 1$.

We run twenty simulations for each model and we store statistics after 18 hours (since the cells enter the domain six hours after a typical experiment begins and the experiment ends after 24 hours) on the density of cells along the domain, and the furthest distance

travelled, which we quantify as the average distance travelled by the leader cells. We choose these statistics because they provide information on how far the cells have travelled and whether there are significant variations in cell density along the stream. These statistics allow us to observe whether the cells have invaded the domain in a coherent manner. Other statistics, for example, the coherence parameter estimated as the sum of the normalised cell velocities averaged over the number of cells, could also be used to quantify collective NCC invasion (Szabo et al., 2006).

Uniform growth

We start our investigation by simulating the migration of NCCs on a uniformly growing domain (Figure 3.8, U1) for 18 hours. On average, the furthest distance travelled by the leader cells is 859μm with standard deviation 23μm, and the final domain length is 1010μm. The density of cells along the domain is plotted in Figure 3.10. There is an increase in cell density at the front of the stream due to the influence of leaders on followers being maximum here, and then another increase in cell density close to the neural tube due to the constant influx of cells and minimum guidance from the leaders. We will use the results of these simulations as our control case, and compare them with the dynamics of NCCs when different domain growth profiles are considered.

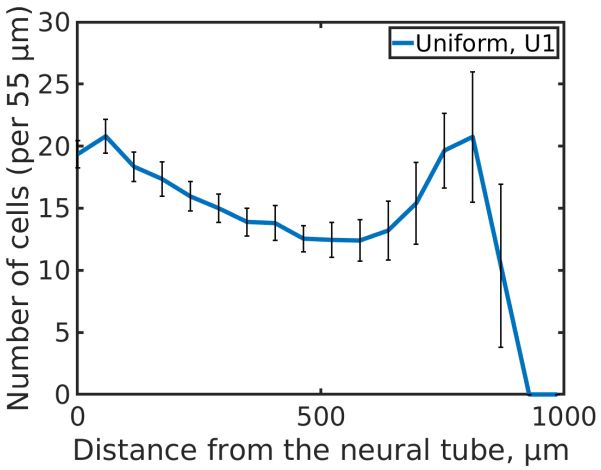


Figure 3.10: Distribution of cells along the domain for the uniform domain growth model (average of 20 simulations after 18 hours). The length of the domain is modelled using Equation (3.11) with $L_0 = 342\mu$m and $\sigma = 0.06\text{min}^{-1}$.

Piece-wise non-uniform growth

We proceed with some simple alterations in the growth profile and divide the domain into two parts, Part 1 and Part 2, of different lengths (Figure 3.8). We first assume that Part 2 grows twice as fast as Part 1 (Figure 3.8, D2-D4). In all of these models, the furthest distance travelled by cells was reduced in comparison with the uniform growth model (Figure 3.11(a)). The cell distribution along the domain is plotted in Figure 3.12(a) and a typical snapshot of the model D3 at the end of the simulations is depicted in Figure 3.13(b). These results show that if the growth is twice as large in Part 2 as in Part 1 then the cells tend to invade less. This is due to less intensive cell advection by domain growth in Part 1. The cell density is of a similar form as in the uniform domain growth case with a decrease in cell density in the middle of the stream. There is a smaller decrease in cell density due to the weaker advection of the cells upon their entrance to the domain.

We next investigate the opposite case, i.e. when Part 1 of the domain grows twice as fast as Part 2 (Figure 3.8, D5-D7). As we would expect, due to intensive advection on

entry, the cells travel further than in the uniform domain growth case (Figure 3.11). The cell distribution along the domain is plotted in Figure 3.12(b) and typical snapshots of the D6 model at the end of the simulations are depicted in Figure 3.13(c). The cell density profile is similar to the uniform domain growth case but there is a greater decrease in cell density in the middle of the stream when proximal growth is enhanced. This phenomenon is due to the strong advection of the cells as soon as they enter the domain.

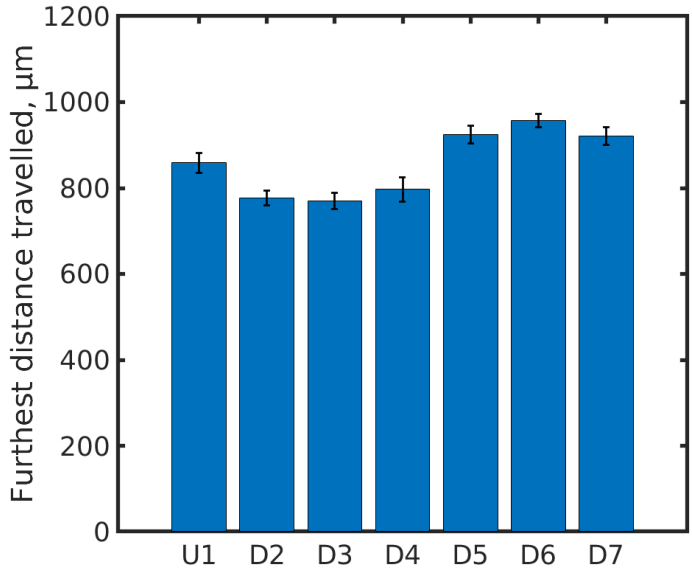
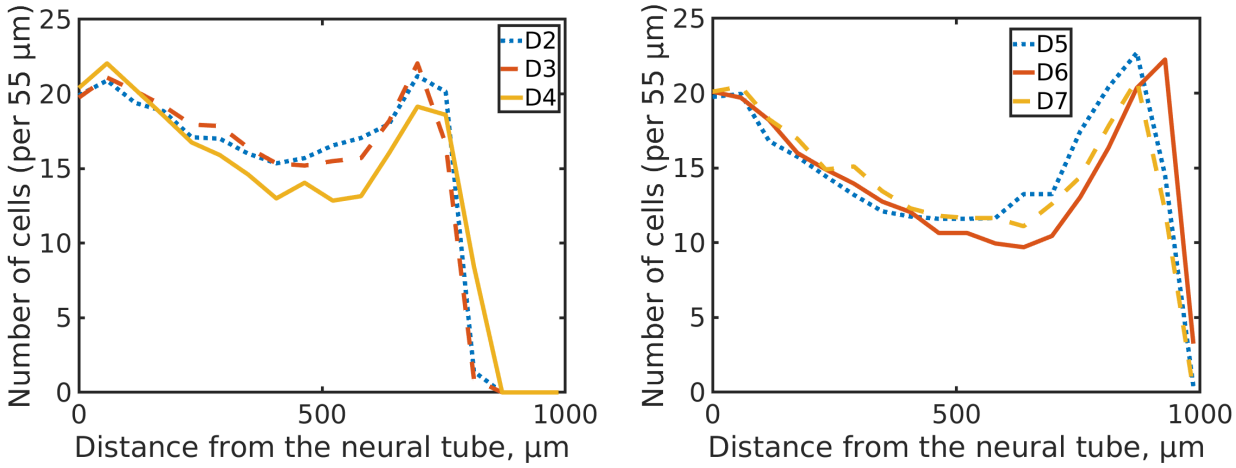


Figure 3.11: Average furthest distance travelled by leader cells, with error bars, over twenty simulations after 18 hours. Domain growth profiles U1, D2-D7 from Figure 3.8, i.e. one part of the domain grows twice as fast as the other part.



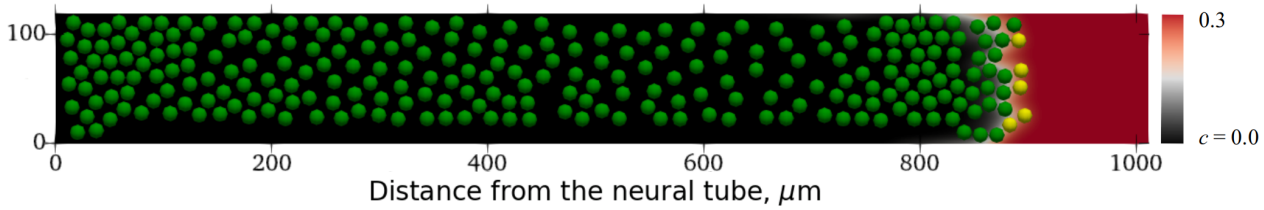
(a) Enhanced distal growth.

(b) Enhanced proximal growth.

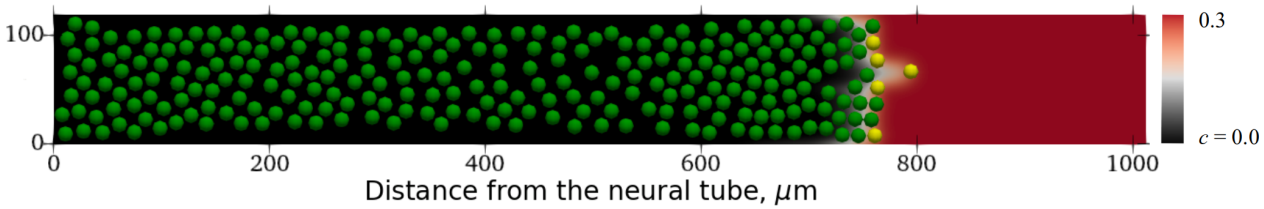
Figure 3.12: Distribution of cells along the domain for the different models, average of 20 simulations after 18 hours. Comparison of cases when one part of the domain grows twice as fast as the other part. (a) Part 2 grows twice as fast as Part 1. (b) Part 1 grows twice as fast as Part 2. We see that the cells invade the domain to a greater extent if there is more proximal growth (b) than distal growth (a) because the cells are advected more quickly as soon as they enter the domain. There is a larger decrease in cell density in the middle of the stream when proximal growth is enhanced. Error bars are removed for the sake of clarity but the standard deviation for the models varies from 1 to 7 cells at different parts of the stream. The length of the domain is modelled using Equation (3.12) with the parameters given in Table 3.1.

	D2	D3	D4	D5	D6	D7
P_1	256.5	171.0	85.5	85.5	171.0	256.5
P_2	85.5	171.0	256.5	256.5	171.0	85.5
A_1	1	1	1	2	2	2
A_2	2	2	2	1	1	1
α	0.016	0.013	0.010	0.010	0.013	0.016

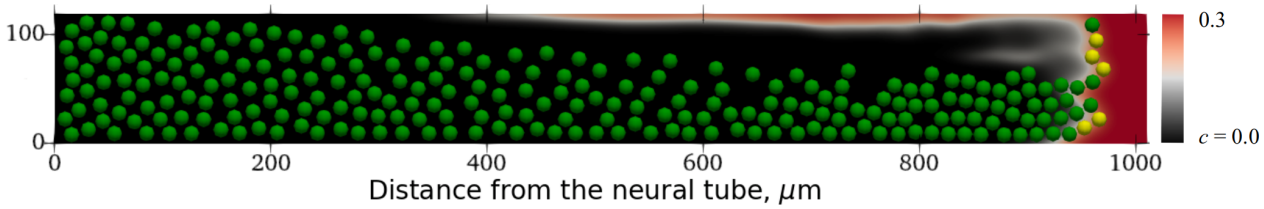
Table 3.1: Parameters for Equation (3.12) for different models. $L_{\text{final}} = 1010\mu$m and $t_{\text{final}} = 18$ hours for all the models. We fix all the parameters in Equation (3.12) and solve for α.



(a) U1



(b) D3



(c) D6

Figure 3.13: Typical snapshots from the selected models from Figure 3.8 at $t = 18$ hours. (a) Uniform domain growth. (b) Distal domain growth. (c) Proximal domain growth. In (a), the length of the domain is modelled using Equation (3.11) with $L_0 = 342\mu$m and $\sigma = 0.06\text{min}^{-1}$. In (b) and (c), the length of the domain is modelled using Equation (3.12) with parameter values as in Table 3.1. Yellow circles correspond to leader cells, green circles correspond to follower cells, and c is the concentration of chemoattractant. Distal growth slows migration whereas proximal growth enhances invasion in comparison with the uniform growth case.

The main difference exhibited by the solutions of the models with two distinct parts of the domain growing at different rates in comparison with the uniform growth model is the total distance travelled by cells, differing by around 70μm in each case, more when the growth is enhanced proximally, less when the growth is enhanced distally. There is a stronger variation in the furthest distance travelled for different piecewise non-uniform domain growth

profiles if a triple, instead of a double, difference in domain growth rate in different parts is chosen (results not shown).

The results in this section demonstrate that NCC invasion is affected by the specific choice of domain growth profile. In particular, if Part 2 grows twice as fast as Part 1, then the cells invade less than in the uniform domain growth case. If Part 1 grows twice as fast as Part 2, then the cells invade more than in the uniform domain growth case. These changes occur due to the cells being strongly advected as soon as they enter the domain when the growth is enhanced proximally. Therefore, at the end of the simulations, they tend to be advected more significantly if the advection occurs earlier during their migration. We conclude that NCC invasive abilities can be altered significantly by different heterogeneous domain growth profiles.

The observed changes in the distance travelled by the cells when different domain growth profiles are considered make us question what happens to the NCC speed. We input the same speed (model parameter) in all the simulations but the cells end up travelling different distances. Therefore their speed (observed cell speed) is likely to be affected by advection due to domain growth and we dedicate the next section to investigating the changes in NCC speed throughout migration.

3.4 Cell speed on a growing domain

Motivated by the changes in the distance travelled by the cells when different domain growth profiles are considered, in this section we investigate how the observed cell speed changes throughout migration. We define the observed cell speed as the distance travelled by a cell in a time period relative to a fixed framework; this is how speed is measured from the experimental data. In our code we set the parameter that controls the leader cell speed to 42μm/h to replicate the control case. However, cell speed in the model is just an

input parameter and it is not the observed cell speed. The observed cell speed is altered by advection of the cells due to domain growth and volume exclusion. Figure 3.14 shows how volume exclusion and advection by growth contribute to the observed cell speed.

To measure observed cell speed, we track cell positions every 7 min (this time frame is chosen based on the method our experimental colleagues use to measure cell speed). Then we calculate distances between pairs of consecutive cell positions and average them to estimate the cell speed per hour. We consider leader and follower cell speeds separately because it has been demonstrated experimentally that they are different (Kulesa et al., 2008). For the leader cells, we keep track of the speed of all five leader cells throughout their entire migration and run the simulations twenty times. For the follower cells, we pick five followers that enter the domain at different times, thus at different distances from the leaders, and keep track of their positions throughout their entire migration. For each parameter set and domain growth profile, we run twenty simulations.

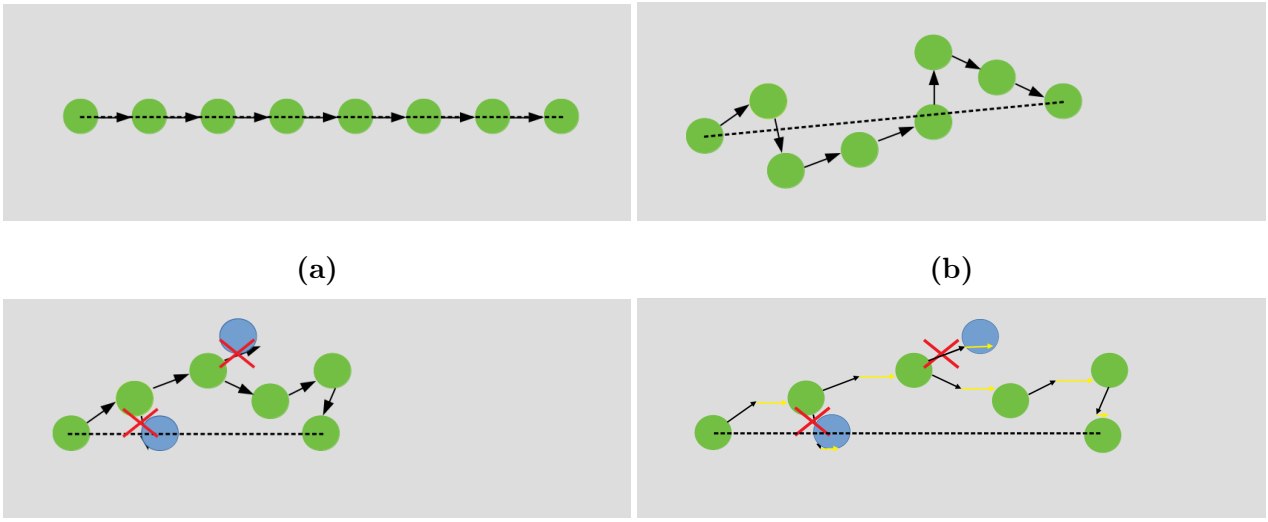


Figure 3.14: Schematics to represent how the observed cell speed is affected by external factors. Black arrows correspond to the distance moved in one time step, which is determined by the input speed. Dashed line is the distance travelled over seven minutes. We calculate the observed speed by dividing this distance by seven minutes. We keep track of the positions of a cell, represented by green circles. Blue circles denote other cells, red crosses correspond to rejected steps due to volume exclusion, and yellow arrows represent the movement of the cell induced by domain growth in the x-direction. (a) Fixed domain, straight movement. The observed cell speed is equivalent to the one we input. (b) Fixed domain, random movement. The observed cell speed can be smaller than the one we input because the cell does not move in a straight line. (c) Fixed domain, random movement with volume exclusion. The observed cell speed can be smaller than the one we input because the cell does not move in a straight line and there is volume exclusion, which prohibits movement. (d) Growing domain, random movement with volume exclusion. The observed cell speed can be smaller than the one we input because the cell does not move in a straight line and there is volume exclusion, but the observed cell speed can be increased due to advection by growth of the tissue depending on the domain growth profile.

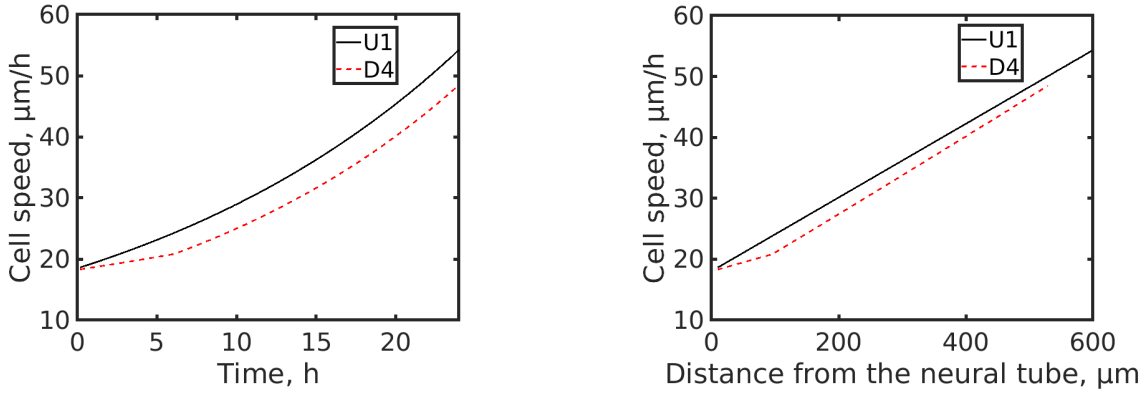
3.4.1 Observed cell speed for different growth profiles

To highlight the effect of growth-driven advection on the observed cell speed, we calculate the observed cell speed profile for a single cell that moves ballistically with a fixed actual speed (18μm/h). Figure 3.15 demonstrates that if domain growth is uniform in space (recall that the domain length is exponentially increasing in time), then the observed cell speed increases exponentially with respect to time and linearly with respect to the distance from the neural tube, respectively. It is linear with respect to the distance from the neural tube because the speed and domain length both increase exponentially in time. If we assume that the domain growth rate is non-uniform in space, for example, the rate is twice as large in the distal 75% of the domain compared to the proximal 25% (D4), then there is a change in the observed cell speed profile (the speed increases twice as fast) when the cell enters the region with higher domain growth rate (Figure 3.15). In the rest of this chapter we will use the plots of cell speed versus distance from the neural tube because this comparison is more compatible with experimental observations.

We now turn back to the full model and compare leader cell speed on a non-growing domain versus a growing domain. This comparison allows us to identify how far a cell moves actively and how far it is passively advected by the growth of the domain. Figure 3.16(a) shows that if there is no domain growth, then the cell moves on average at a constant speed of around 27μm/h, whereas if the domain grows uniformly (Equation (3.11)) its speed increases due to advection by the growth to be almost three times higher (Figure 3.16(a)).

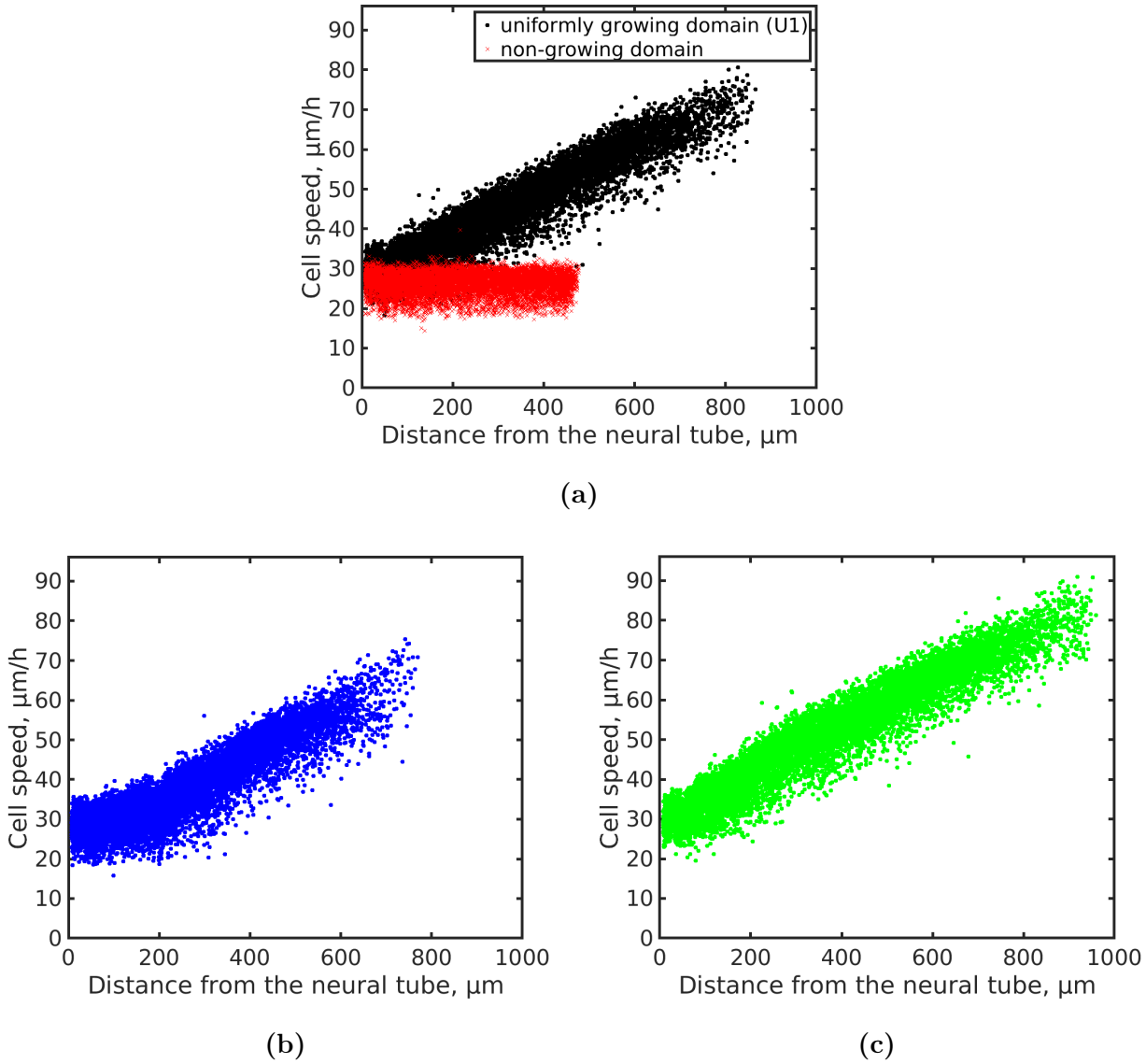
Figures 3.16(b),(c) demonstrate how the leader NCC speed is affected by changes in the domain growth profile. If the distal part of the domain grows faster than the proximal part, then the rate of increase of speed increases further away from the tube (Figure 3.16(b)) and vice versa when the proximal part of the domain grows faster than the distal part (Figure 3.16(c)). This result shows that it may be possible to predict a domain growth profile by looking at the NCC speed if the migration of NCCs is indeed affected by domain growth.

However, to do so would require us to be able to track cells at a sufficiently high resolution and this technology is not yet available.



(a) **(b)**

Figure 3.15: Observed cell speed of a single cell that moves with a fixed input speed (18μm/h). (a) Cell speed versus time: when the domain growth is uniform in space (U1), cell speed increases exponentially (because domain length is exponentially increasing in time); when the domain growth is non-uniform (D4), cell speed increases exponentially in time but there is a change in the growth rate when the cell enters the region with higher domain growth rate. (b) Cell speed versus distance from the neural tube: when the domain growth is uniform in space (U1), cell speed increases linearly with respect to the exponentially (in time) growing domain; when the domain growth is non-uniform in space (D4), cell speed increases linearly in space but there is a change in the linear growth rate when the cell enters the region with higher domain growth rate.



(a)

(b)

(c)

Figure 3.16: Leader cell speed (all five leaders) along the domain measured every seven minutes, over twenty simulations. (a) Comparison of leader cell speed along the domain when there is no domain growth, and when the domain grows uniformly in space (U1). Volume exclusion and random direction choices account for the spread of cell speed values at any given distance from the neural tube. (b) Leader cell speed for model D2, where the distal part of the domain grows twice as fast as the proximal part. (c) Leader cell speed for model D6, where the proximal part of the domain grows twice as fast as the distal part.

3.4.2 Leader-follower cell speed

Leaders travel at the front of the stream and guide the cells behind them. Based on experimental findings (Kulesa et al., 2008), to ensure robust invasion for the uniform growth case, we set the ratio of follower to leader cell speed to be fixed at 1.3 – that is, the followers travel at a speed 1.3 times that of the leaders (model parameter). However, we do not know the actual ratio of follower to leader cell speed that emerges from the simulations. To this end, we compare leader and follower cell speeds at different positions along the domain when the growth is uniform in space. We choose follower cells based on the order of their entrance to the domain (every twentieth cell starting from the tenth).

Figure 3.17 demonstrates that the observed average speed of follower cells is higher than the speed of leader cells, but on average this ratio is 1.1. The ratio is decreased compared to the one we input due to volume exclusion because follower cells are surrounded by other cells. We notice a greater variation in follower cell speed than in leader cell speed. Followers close to the leaders travel at the speed most similar to leader cell speed. Followers at the origin of the migratory domain travel slowly due to volume exclusion and weak guidance by the leaders. Followers in the middle of the stream travel at the highest speeds due to the decrease in cell density in the middle of the stream, and thus more space for the cells to move (Figure 3.10). Since followers often travel at a higher speed than leaders, they can overtake leaders but our model includes phenotype switching, so those followers become leaders. If the cells we track switch phenotypes, we keep track of the speed of the cells with which they switched their phenotypes. We conclude that the observed cell speeds of leaders and followers differ but to a smaller extent than we would expect from the values we input.

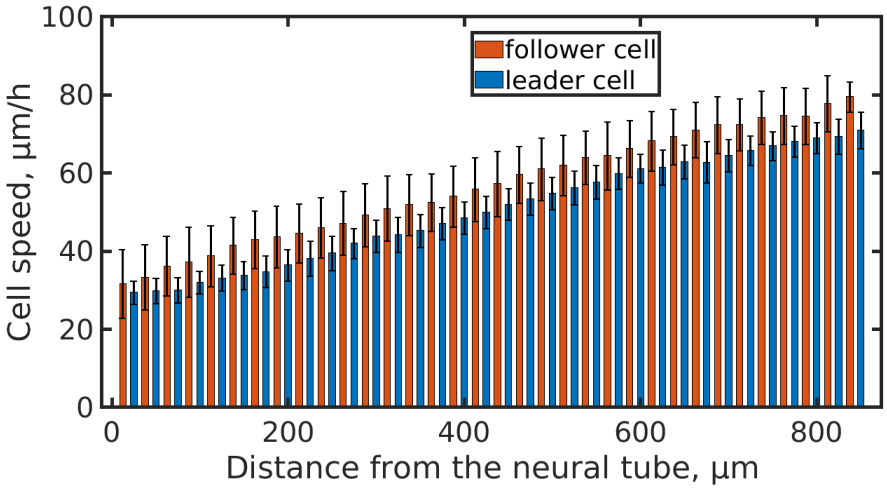


Figure 3.17: Comparison of mean value and standard deviation of leader and follower cell speeds along the domain when the domain growth is uniform. Averages of the five leader cells and five follower cells (chosen based on their entrance time, every twentieth cell starting from the tenth cell) of the stream over twenty simulations. If the cells we track switch phenotypes, we keep track of the speed of the cells with which they switched their phenotypes.

Having looked at the changes in the dynamics of cells when different domain growth profiles are considered, including changes in the furthest distance travelled and observed cell speed, we next apply our modelling framework to investigate the dynamics of NCCs under experimentally observed tissue growth characteristics.

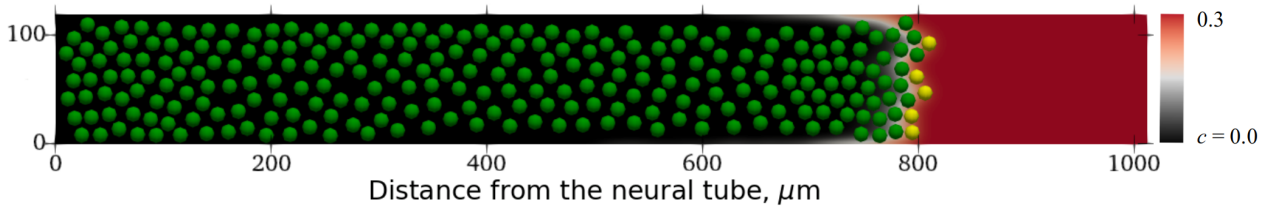
3.5 What does the model predict if we use experimentally observed domain growth profiles?

We use our modelling framework to explore the effects of the spatio-temporal growth profiles of the mesoderm, described in Section 3.1, on the NCC migratory patterns. Note that to be consistent with experimental data, we denote the length of the experiment as 24 hours, even though the cells only enter the domain after six hours and we run the simulations for 18

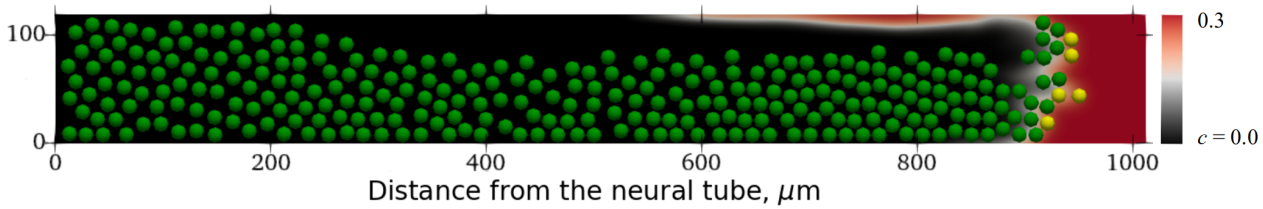
hours. We considered a combination of distal and proximal growth to mimic the empirically measured data presented in Figure 3.3. The experimental data suggest that for the first 18 hours, there is more distal growth, and for the final six hours more proximal growth. Based on these observations, we approximate domain growth as follows:

$$\text{domain grows as } \begin{cases} \text{D3, for } 0 \leq t \leq 18\text{h}, \\ \text{D6, for } 18 < t \leq 24\text{h}, \end{cases} \tag{3.13}$$

where D3 and D6 are described as in Figure 3.8. The model predicts that there must be an increase in input NCC speed for cells to invade the domain in 24 hours (Figure 3.18; compare 42μm/h and 48μm/h). As we observed in Section 3.4, NCC speed is affected by several components: the input speed, advection due to domain growth and volume exclusion. When the input NCC speed is increased, simulations indicate that the stream length monotonically increases (Figure 3.19). This may be verified by visualising the changes in NCC overall speed from the neural tube exit as a function of increasing cell speed from 42μm/h to 51μm/h (Figure 3.20). Note that if the NCC speed is increased too much (51μm/h), then the NCCs reach the end of the domain too quickly and their observed cell speed decreases (Figure 3.20(c)). Together, the model simulations predict that input NCC speed has to be increased from 42 to 48μm/h (approximately 14%) in order to reach the vicinity of the end of the migratory domain if we impose a domain growth profile that approximates the growth seen experimentally.



(a)



(b)

Figure 3.18: Snapshots from the model at 24 hours with enhanced distal domain growth (D3) up to 18 hours and enhanced proximal growth (D6) after 18 hours (Equation (3.13)). (a) NCC input speed 42μm/h, (b) NCC input speed 48μm/h. Yellow circles correspond to leader cells, green circles correspond to follower cells, and c is the concentration of chemoattractant. An increase in input NCC speed in comparison with that for the uniform domain growth case is required to ensure that the cells reach the vicinity of the end of the migratory domain at the correct time.

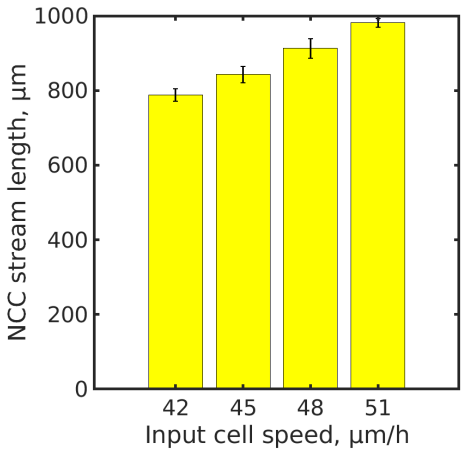


Figure 3.19: NCC stream length averaged over 20 simulations after 24 hours for different input cell speeds. The length of the NCC stream increases monotonically with an increase in input cell speed.

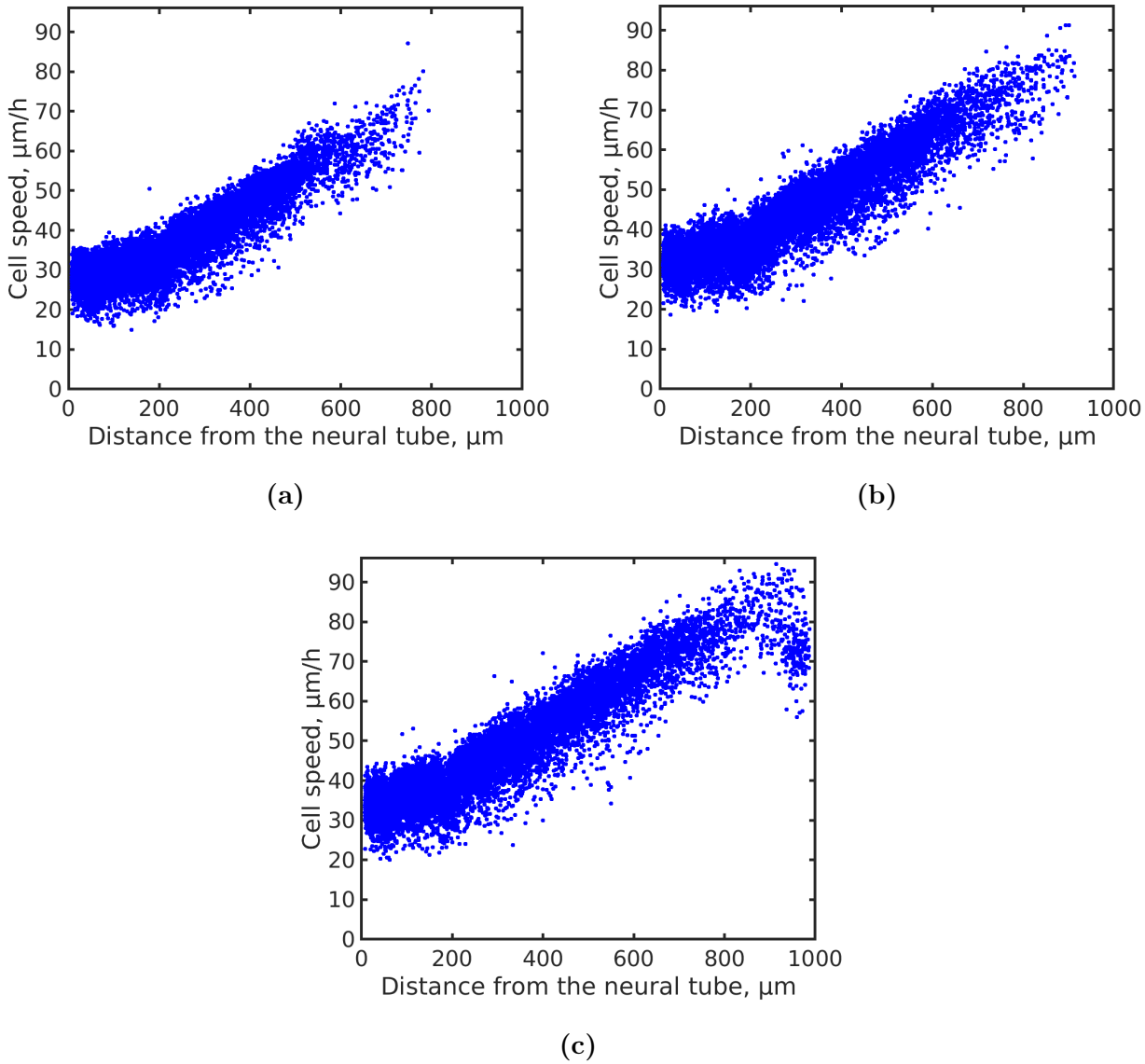


Figure 3.20: Observed leader cell speeds along the domain measured every seven minutes. (a) NCC input speed 42μm/h, (b) NCC input speed 48μm/h, (c) NCC input speed 51μm/h. The speed increases approximately by a factor of three in all three cases. In (c), the cells slow down when they reach the end of the domain due to the zero-flux boundary condition at the right-hand boundary.

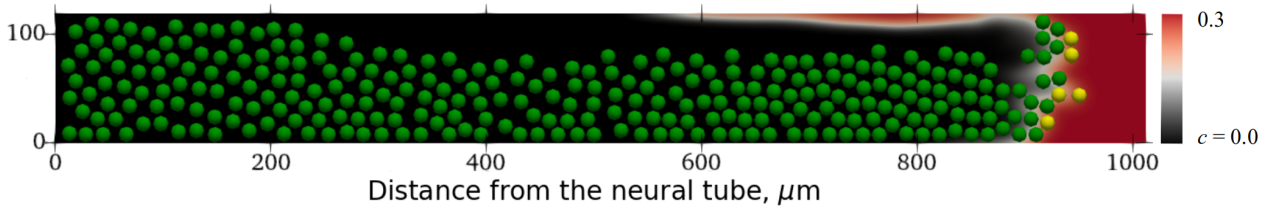
In this section we used computational modelling to investigate the effect of the experimentally observed tissue growth pattern (McKinney et al., 2020) on cell migration, and propose that input NCC speed has to be increased to compensate for the enhanced

initial distal domain growth. We produced NCC speed profiles which demonstrated the changes in observed cell speed along the domain for different input cell speeds. There is (as yet) no experimental data that could be used to verify these speed profiles but these results will be useful when such data sets will become available.

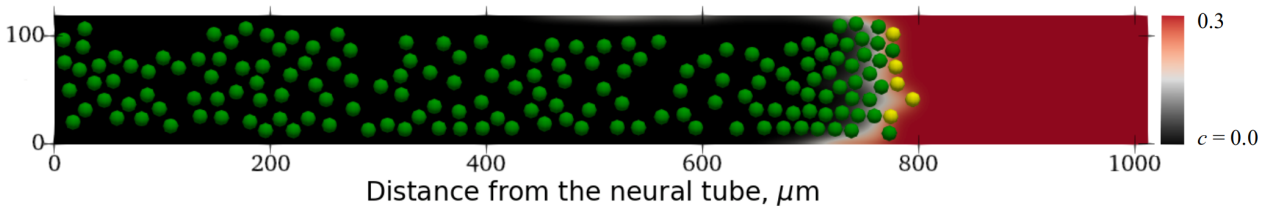
We continue this chapter with a comparison of further experimental results, such as the physical ablation of NCCs and chemical growth inhibition, using our model to provide further insights into the dynamics of NCC invasion.

3.6 Physical ablation of neural crest cells

To further understand the interactions between tissue growth and NCCs, McKinney et al. (2020) performed NCC ablation experiments. They ablated the dorsal one-third of the neural tube from mid-rhombomere 3 to mid-rhombomere 5 in HH9 embryos to significantly reduce the number of premigratory NCCs. *In silico*, we model ablation by delaying the entry of cells into the domain by two hours and reducing the frequency of entry (every 10 time steps instead of every step). We choose to model the ablation in this way based on experimental observations that, after ablation, not only is the entry of the NCCs delayed but also their influx rate is reduced. We use the domain growth profile described in Equation (3.13). Figure 3.21 compares the NCC distribution at 24 hours in the control case and after ablation.



(a) Control case, 292 cells.



(b) Physical ablation, 168 cells.

Figure 3.21: Snapshots from the model at 24 hours with enhanced distal domain growth (D3) up to 18 hours and enhanced proximal growth (D6) after 18 hours for (a) the control case, and (b) after physical ablation of cells. We model ablation by delaying the entry of cells into the domain by two hours and reducing the frequency of entry (every 10th time step). Yellow circles correspond to leader cells, green circles correspond to follower cells, and c is the concentration of the chemoattractant.

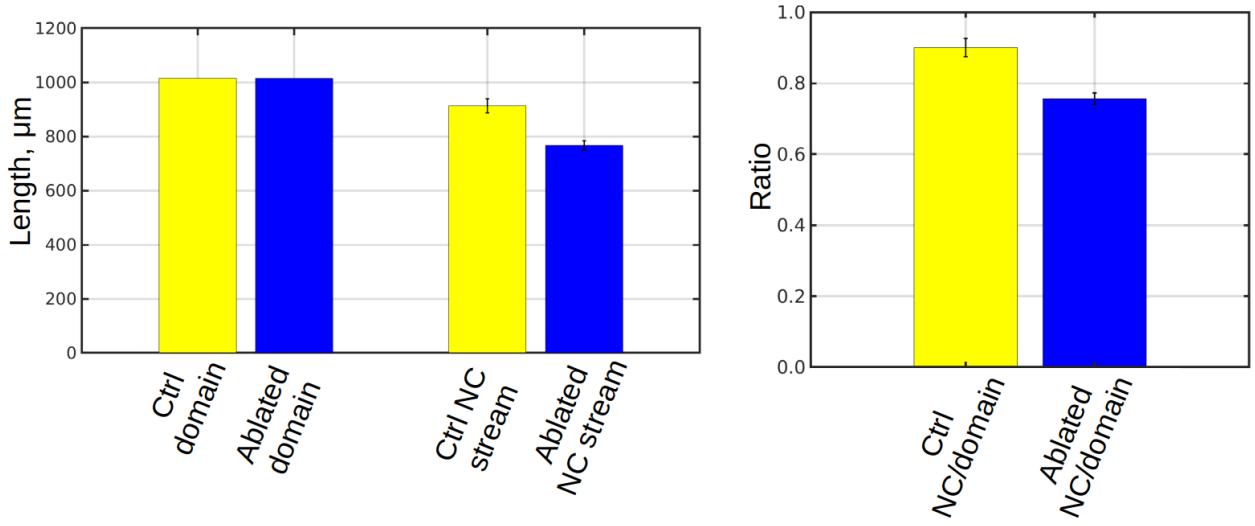
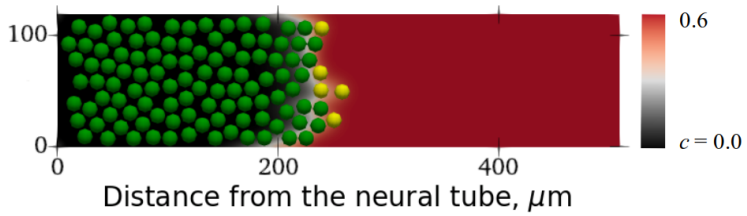


Figure 3.22: Comparison of the length of the domain and average NCC stream length at 24 hours when NCCs are physically ablated, as predicted by the model. Left – length of the domain and NCC stream (NC). Right – ratio of NCC stream length to domain length. NCCs invade the domain to a lesser extent after the ablation but the domain grows to the same length in the control embryos and after the ablation of NCCs. The decrease in ratio is consistent with experimental observations but the results do not fully agree with the experimental findings because the domain length is not altered after the ablation (Figure 3.5).

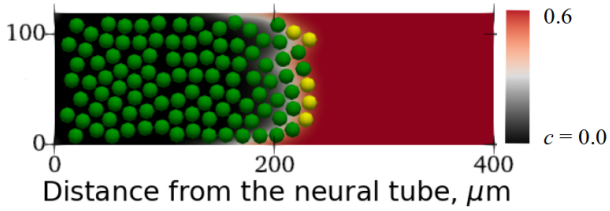
McKinney et al. (2020) measured the length from the neural tube midline to the branchial arches along the NCC migratory pathway. They found that both the length of the domain and the distance travelled by NCCs were significantly reduced in ablated embryos in comparison to controls (Figure 3.5). Simulations showed that the ratio of the migratory domain length to NCC stream length was also reduced after NCC ablation (Figure 3.22). However, since in our modelling framework, domain growth is independent of NCCs, the length of the domain does not decrease when NCCs are ablated. The experimental results clearly show that NCCs influence domain growth and this feedback mechanism has to be incorporated into our modelling framework to correctly replicate the physical ablation experiment. We address this inconsistency in Section 3.8 by suggesting a feedback mechanism.

3.7 Chemical inhibition of mesodermal cell proliferation

In Section 3.1, we highlighted the experimental observation that mesodermal cells proliferate during NCC migration but their density does not change. This suggests that they contribute to tissue growth. To understand whether mesodermal cell proliferation directly affects tissue growth and NCC invasion, McKinney et al. (2020) performed an experiment in which they inhibited mesodermal cell proliferation. In particular, they microinjected a cocktail of Aphidicolin, Hydroxyurea and DiD into the most distal mesoderm that could be reached in HH10 embryos in order to halt proliferation in the mesoderm. *In silico*, we approximate this experiment by reducing the domain growth rate uniformly along the x-axis because the chemical diffuses along the whole domain (Figure 3.23).



(a) Control case.



(b) Chemical growth inhibition.

Figure 3.23: Snapshots from the model at 24 hours with enhanced distal domain growth (D3) up to 18 hours followed by enhanced proximal growth (D6) after 18 hours for (a) the control case, and (b) chemical growth inhibition. We model chemical growth inhibition by a uniform reduction of the domain growth rate parameter. The cells travel almost the same distance in both the control and inhibited cases because, initially, domain growth is distal and the cells are not advected significantly. Yellow circles correspond to leader cells, green circles correspond to follower cells, and c is the concentration of chemoattractant.

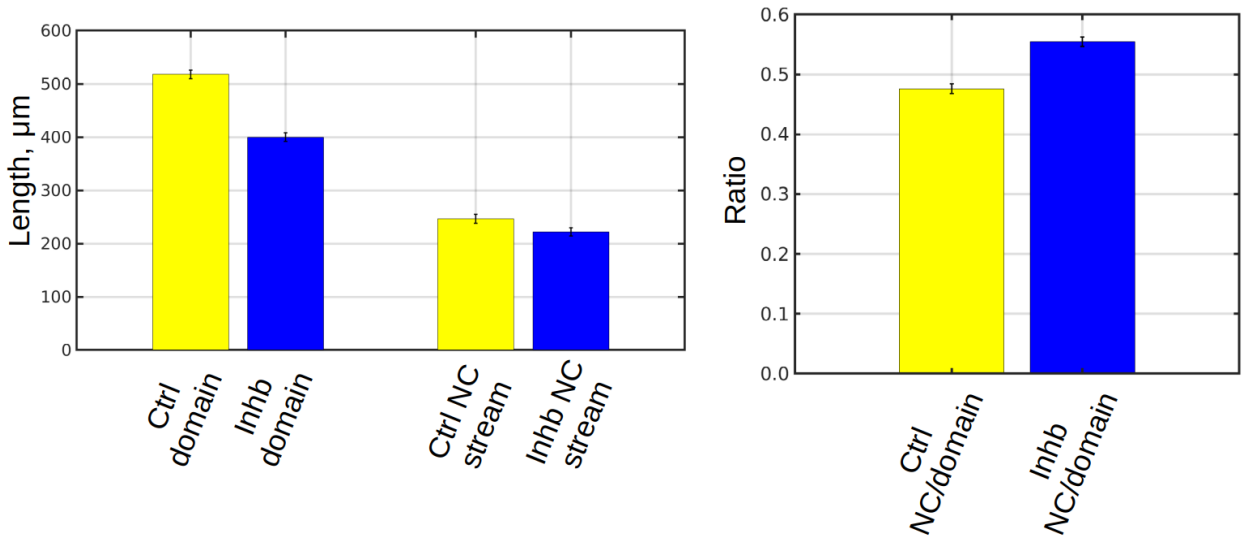


Figure 3.24: Comparison of the length of the domain and average NCC stream length at 12 hours as predicted by the model when domain growth is chemically inhibited by injection. Left – length of the domain and NCC stream. Right – ratio of NCC stream length to domain length. In the treated embryos, the length of the domain is reduced but the NCCs invade the domain to a greater extent in comparison with the control embryos. These results do not agree with experimental findings: in experiments the ratio of NCC stream length to domain length decreases in the treated embryos (Figure 3.6).

McKinney et al. (2020) observed that both the mesoderm within the dorsolateral domain and the NCC migratory stream were shorter in chemically treated embryos (Figure 3.6). In model simulations of inhibited domain growth, the length of the domain and NCC migratory stream were also reduced but, in contrast with experimental results, the ratio of the NCC migratory stream to the domain length increased when the domain growth rate was reduced (Figure 3.24). These results were robust to other biologically realistic parameter changes (results not shown).

Similarly to the NCC ablation experiments, we hypothesise that there must be feedback between the NCCs and tissue growth. We are motivated to do so because experiments suggest that chemical inhibition of cell proliferation in the mesoderm leads to a reduction in tissue growth and, more importantly, alterations in the resulting NCC stream length. In the

following section we will suggest and explore a potential feedback mechanism between NCCs and tissue growth.

3.8 How do neural crest cells affect domain growth?

Experimental results reveal that mesodermal cells are proliferating during NCC migration and yet mesodermal cell density does not increase. Therefore, mesodermal cells are a natural candidate for a contributor to domain growth. Are there any other constituents of the domain that might affect domain growth significantly? NCC ablation experiments suggest that the absence of NCCs reduces the length of the domain. Therefore, NCCs are also likely to induce domain growth. Previously, we have assumed that domain growth is independent of NCCs and, as a result, our modelling framework could not replicate the results of certain ablation experiments (Section 3.6). Here, we consider different ways to incorporate NCC-induced domain growth, namely that there is a stepwise increase in growth rate from the neural tube to the cell front (average position along the x-axis of the leader cells, av_{lead}), ahead of the cell front, or behind the cell front (Figure 3.25). The domain growth rate $\alpha(x)$ for $x \in [0, L_x(t)]$ is defined as follows:

Cell front:

$$\alpha(x) = \begin{cases} 0.02, \text{ if } 0 \leq x < \text{av}_{\text{lead}}, \\ 0.01, \text{ if } \text{av}_{\text{lead}} \leq x < L_x(t). \end{cases} \tag{3.14}$$

Ahead of the cell front:

$$\alpha(x) = \begin{cases} 0.02, \text{ if } 0 \leq x < \text{av}_{\text{lead}} + d, \\ 0.01, \text{ if } \text{av}_{\text{lead}} + d \leq x \leq L_x(t), \end{cases} \tag{3.15}$$

for some distance $d \in (0, 200] \mu$m.

Behind the cell front:

$$\alpha(x) = \begin{cases} 0.02, & \text{if } 0 \leq x < \text{av}_{\text{lead}} - a, \\ 0.01, & \text{if } \text{av}_{\text{lead}} - a \leq x < L_x(t), \end{cases} \tag{3.16}$$

for some distance $a \in (0, 200]\mu$m.

Based on experimental evidence, there is some baseline growth along the whole domain. We did not employ a detailed NCC density-dependent domain growth profile due to several reasons. Firstly, the distribution of NCCs along the domain is almost uniform and, secondly, there is experimental evidence that the reduction of influx of NCCs only affected the density of cells and not invasion and domain length (McLennan et al., 2012).

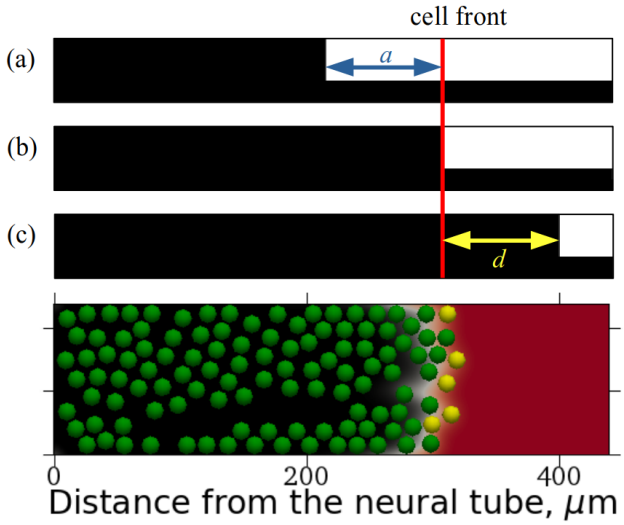


Figure 3.25: Schematics of different NCC-induced domain growth profiles considered. Domain growth is induced from the neural tube (left boundary) to a fixed distance (a) behind the cell front ($a = 100\mu$m); (b) at the average position of leader cells (cell front); (c) a distance d ahead of the cell front ($d = 100\mu$m). Examination of the resulting invasion dynamics show that (c) induces invasive behaviour consistent with observations. Yellow circles represent leader cells, green circles – follower cells. Height of black shading corresponds to the intensity of the domain growth rate.

We run preliminary simulations for the growth profiles shown in Figure 3.25 to

observe which ones can replicate the control case in the most realistic way. We run twenty simulations but only provide snapshots of representative simulations to illustrate the observed behaviour. We observe that if growth is enhanced from the neural tube to the cell front (Figure 3.25(b)) or behind the cell front (Figure 3.25(a)), the cells invade the domain too early (for example, Figure 3.26 shows the case when growth is enhanced right up to the cell front). However, if domain growth is enhanced from the neural tube to the cell front plus a fixed distance ahead of the front (for example, $d = 100\mu$m, where we define d as the distance from the cell front to the position along the x-axis up to which the growth rate is enhanced), then the cells do not invade the domain too early (Figure 3.27). Therefore, we will use this NCC-induced domain growth profile. Biologically, this phenomenon could correspond to NCCs inducing growth ahead of the stream by pushing or displacing mesodermal cells, or secreting a growth regulator chemical. Our simulations show that the results are robust to changes in d ($50\mu\text{m} \leq d \leq 150\mu\text{m}$) (results not shown). For $0\mu\text{m} \leq d < 50\mu\text{m}$, the cells are likely to invade the domain too early, and for $d > 150\mu$m, the cells may not invade the domain sufficiently (results not shown).

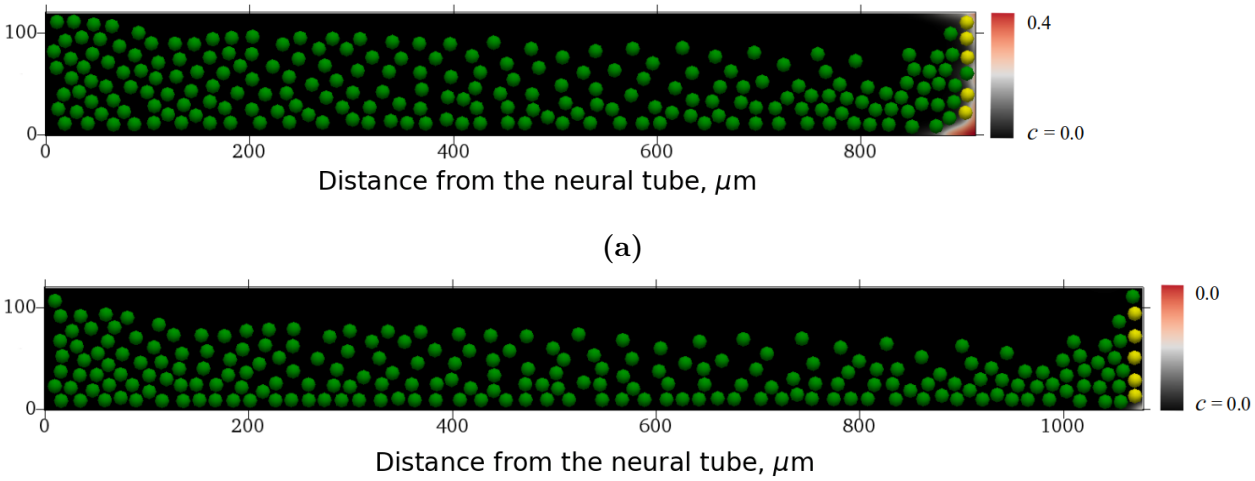


Figure 3.26: Snapshots from the model with the domain growth rate enhanced from the neural tube to the cell front at (a) 21 hours and (b) 24 hours. NCCs have already invaded the domain at 21 hours.

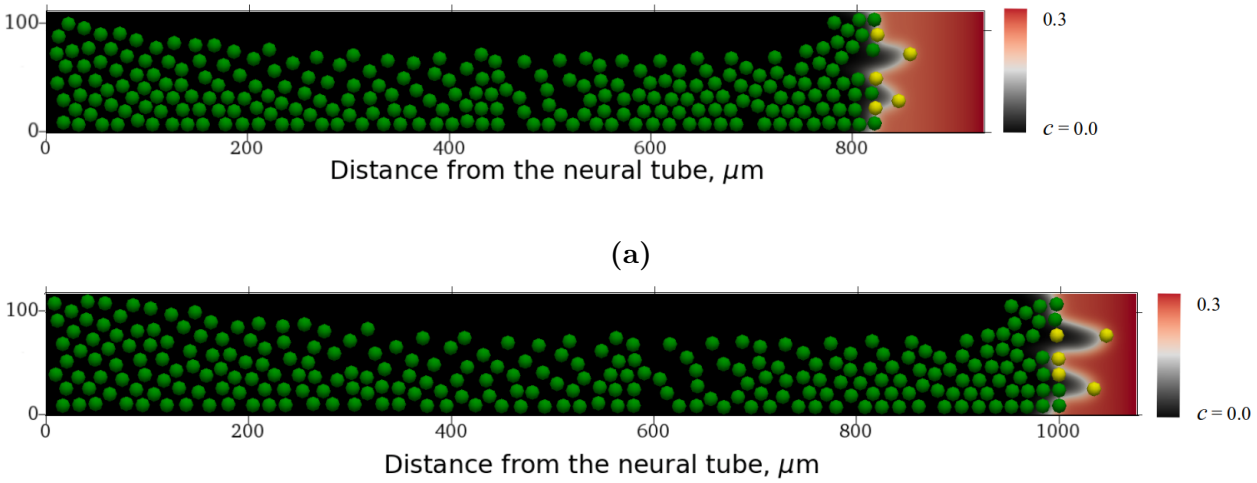


Figure 3.27: Snapshots from the model with the domain growth rate enhanced from the neural tube to the cell front $+100\mu$m at (a) 21 hours and (b) 24 hours.

It is important to observe that the mesodermal BrdU positive cell profile suggests that NCCs actually hinder domain growth during most of their migration (Figure 3.3), and this directly contradicts our hypothesis (namely, that NCCs induce domain growth). However, if NCCs hindered domain growth, then the NCC ablation experiment could not be replicated for any parameter values because ablation of NCCs would lead to an increase in domain length, which is the opposite to what is observed experimentally (Figure 3.22). Hence, it is an open question as to whether mesodermal cell proliferation is the key constituent of domain growth and the evidence from the chemical inhibition experiments is more explicit about the influence of NCCs on tissue growth. Hence, we hypothesise that the profile in Figure 3.3 is not a good representation of the domain growth profile.

Next, we verify whether the NCC-induced domain growth profile enables our model to replicate observations from the physical NCC ablation and chemical growth inhibition experiments.

3.8.1 NCC-induced growth profile: physical neural crest cell ablation

With our new model, in which NCCs induce domain growth, we find that we can now reproduce the experimentally observed patterns. The model predicts that when premigratory NCCs are ablated, the domain grows less (Figure 3.28(a)) and the cells invade the domain to a lesser extent (Figure 3.28(b)), which is in accordance with the experiments (compare Figure 3.28 and Figure 3.5).

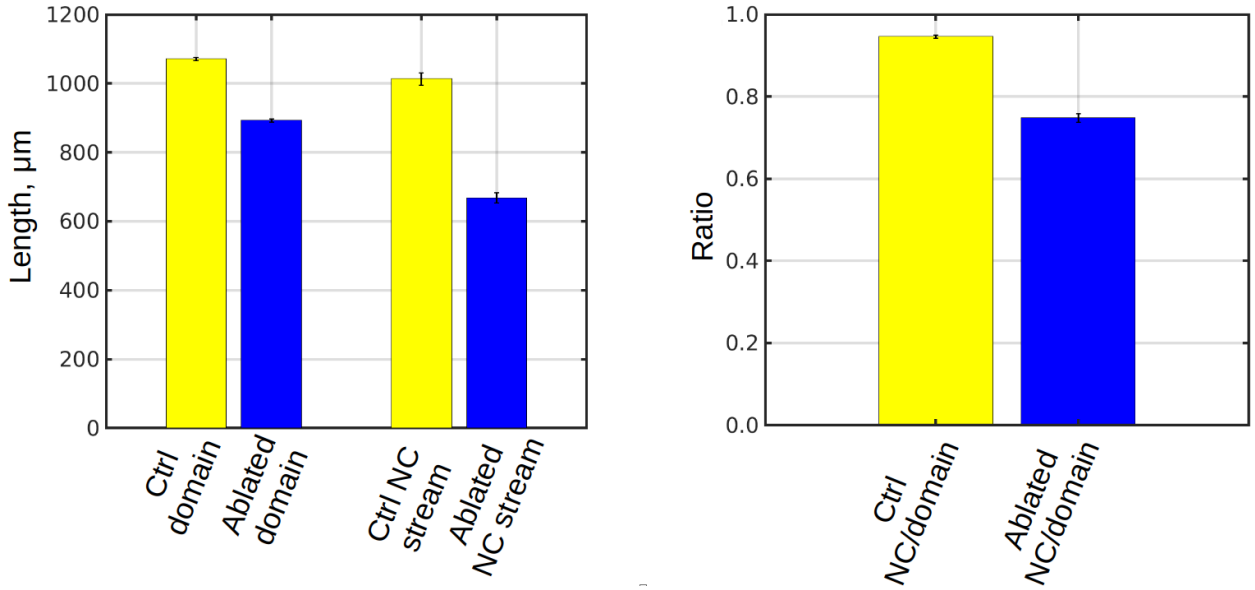


Figure 3.28: Comparison of the length of the domain and average NCC stream length at 24 hours when NCCs are physically ablated, as predicted by the model. Left – length of the domain and NCC stream. Right – ratio of NCC stream length to domain length. After ablation, the domain grows less and NCCs invade it to a lesser extent. These results agree with experimental findings (Figure 3.5).

3.8.2 NCC-induced growth profile: chemical growth inhibition

We start with the chemical growth inhibition experiment, which we model by reducing the growth rate uniformly along the domain (we define this modelling approach as

Hypothesis 1). We observe that for this growth profile the ratio of the NCC stream length to domain length is again opposite to what is observed experimentally, i.e. the model predicts that the ratio is higher in the chemically inhibited case (Figure 3.29). Therefore, we reject Hypothesis 1 and consider alternative ways of how chemical growth inhibition could be modelled.

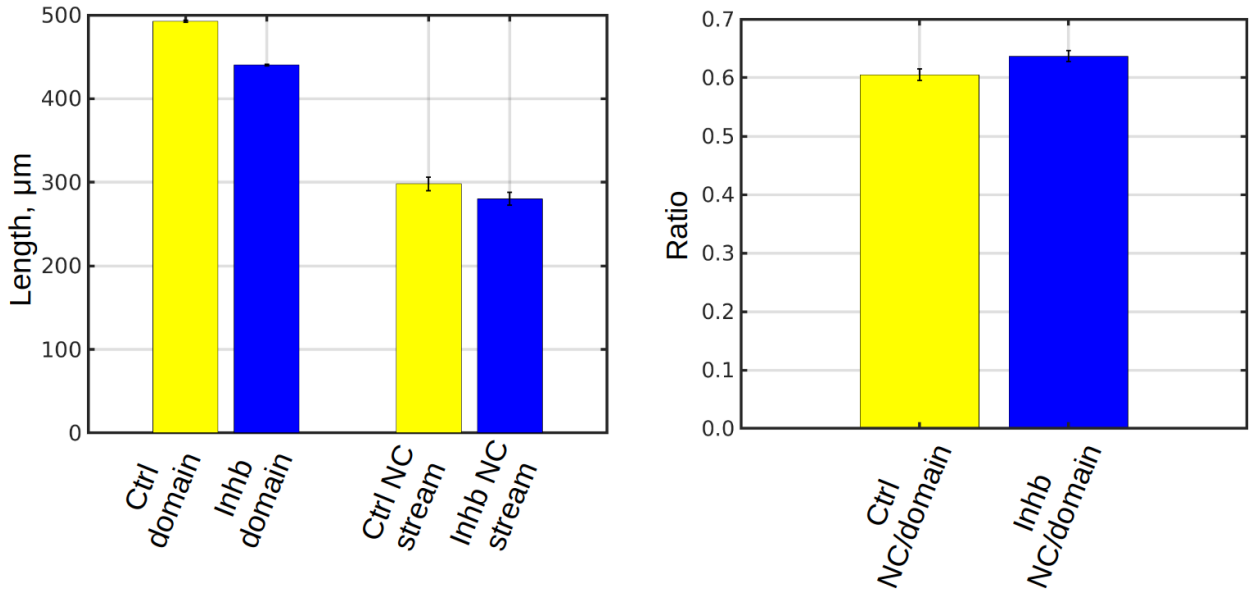


Figure 3.29: Comparison of the length of the domain and average NCC stream length at 12 hours when domain growth is chemically inhibited by injection, as predicted by the model. Chemical growth inhibition is modelled by a uniform decrease in domain growth rate. Left – length of the domain and NCC stream. Right – ratio of NCC stream length to domain length. In the treated embryos, the length of the domain is decreased but NCCs invade the domain to a greater extent in the treated embryos than in the controls. These results do not agree with the experimental findings (Figure 3.6).

Hypothesis 1: chemical growth inhibition is modelled using uniform domain growth rate reduction – REJECT.

We next hypothesise that the growth is inhibited heterogeneously. Biologically, this could correspond to an inhibitory effect of the chemical that depends on the intensity of growth in different regions of the domain. Figure 3.30 demonstrates two different cases that

we consider (Ch1 – the growth is reduced locally, where it is the highest, Ch2 – the growth is reduced uniformly along the domain and even more locally, where it is the highest). However, as in the uniform domain growth rate reduction case, the model predicts that the ratio of NCC stream length to domain length increases after chemical domain growth inhibition (Figure 3.31). Therefore, our modelling results are inconsistent with the biological findings, which suggest the opposite effect.

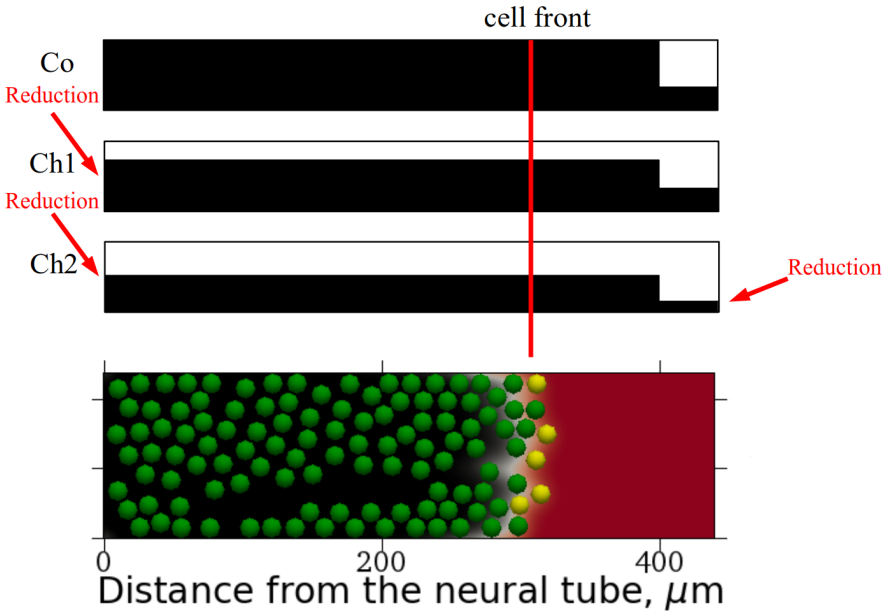


Figure 3.30: Different ways to incorporate chemical domain growth inhibition. Co – control, NCC-induced domain growth profile; Ch1 – the growth is reduced locally, where it is the highest; Ch2 – the growth is reduced uniformly along the domain and even more locally, where it is the highest. Yellow circles represent leader cells, green circles – follower cells. Height of black shading corresponds to the intensity of the domain growth rate.

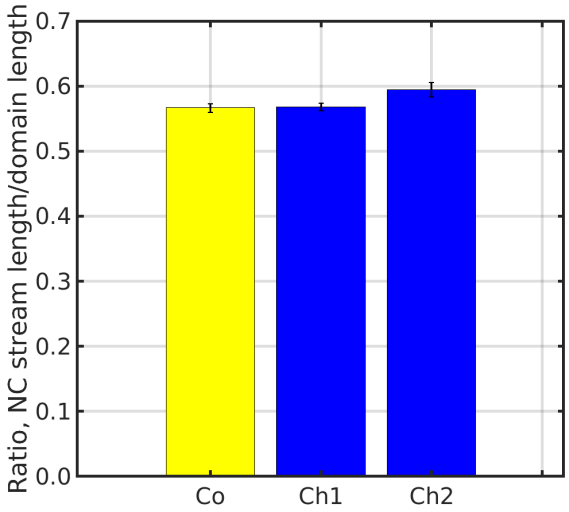


Figure 3.31: Comparison of the ratios of NCC stream length to domain length, as predicted by the model. Co – control, Ch1, Ch2 – chemical growth ablation as described in Figure 3.30. None of the results agree with the experimental findings, which suggest that the ratio of NCC stream to domain length has to decrease (Figure 3.6).

Hypothesis 2: chemical growth inhibition is modelled using heterogeneous domain growth rate reduction – REJECT.

Next, we include an additional feedback mechanism between mesodermal cells and NCCs, namely, if mesodermal cell proliferation is reduced, then NCC directionality is reduced. We include this assumption based on experimental findings which suggest that NCC directionality is enhanced in the presence of mesodermal cells (Figure 3.2(b)). In addition, tissue growth itself may provide a directional signal to NCCs, for example, by elongating ECM fibres, and this could also support the hypothesis that inhibited domain growth rate leads to a decrease in NCC directionality. However, to date, there is no conclusive biological evidence as to what may induce directionality reduction. Therefore, based on simple interpretation that a smaller number of filopodia leads to poorer exploration of the environment, and thus less directional movement, we incorporate directionality reduction in our modelling framework by reducing the number of filopodia sent out at each time step from three to two.

When we model chemical domain growth inhibition as a uniform domain growth rate reduction and NCC directionality reduction, our computational results match the experimental results, i.e. the ratio of domain length to NCC stream length is decreased (Figure 3.32). Therefore, the combination of the uniform reduction in domain growth rate and NCC directionality is sufficient, as model hypotheses, to replicate the experimental observations of the effect of chemical growth inhibition.

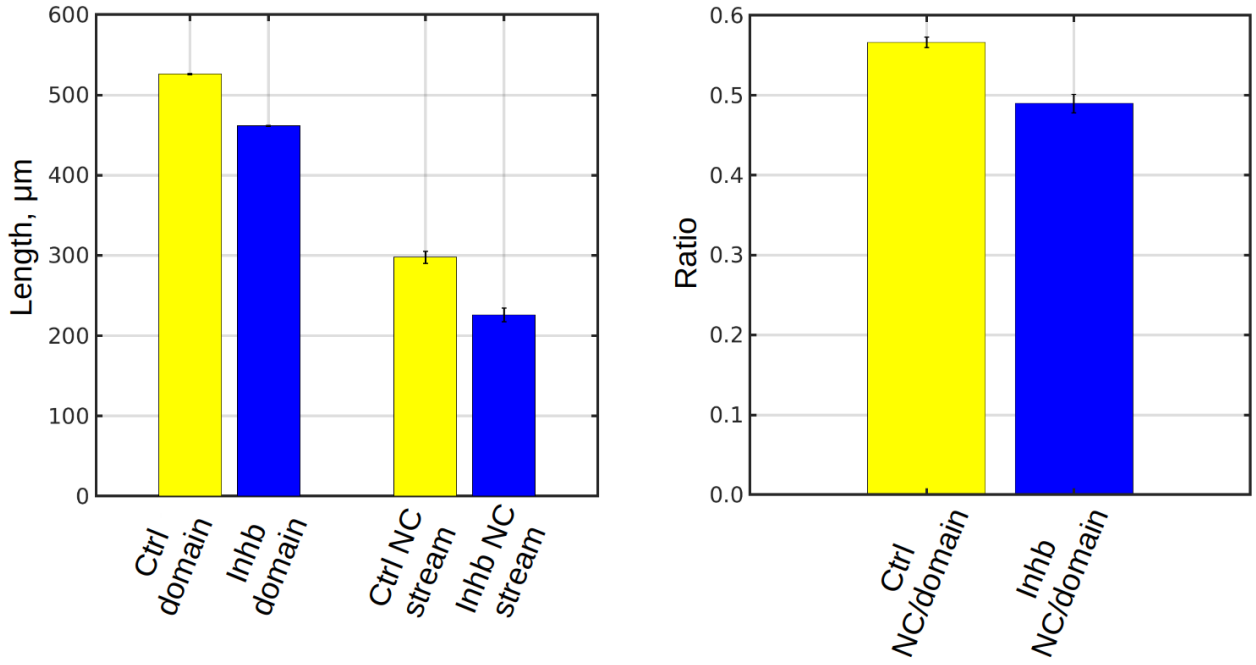


Figure 3.32: Comparison of the length of the domain and average NCC stream length at 12 hours when domain growth is chemically inhibited by injection, as predicted by the model. Chemical growth inhibition is modelled by a reduction in NCC directionality and uniform domain growth rate reduction (Ch2, Figure 3.30). Left – length of the domain and NCC stream. Right – ratio of NCC stream length to domain length. In the treated embryos, the domain grows less and NCCs invade the domain to a lesser extent than in the control case. These results agree with the experimental findings (Figure 3.6).

Hypothesis 3: chemical growth inhibition is modelled using uniform domain growth rate reduction and NCC directionality reduction – ACCEPT.

The incorporation of a NCC-induced growth profile, which allows us to reproduce physical NCC ablation and chemical domain growth inhibition experiments, suggests that there might be a positive feedback mechanism between NCCs and tissue growth. Initially, we assumed that tissue growth is mainly regulated by mesodermal cell proliferation. Now, we hypothesise that tissue growth is influenced by both NCCs and mesodermal cells. McKinney et al. (2020) demonstrated that mesodermal cell proliferation contributes to tissue growth, we term this mesodermal cell-induced tissue growth. We suggest that NCCs also contribute to tissue growth, either simply by displacing mesodermal cells, or by increasing mesodermal cell proliferation and migration, we term this NCC-induced tissue growth. We hypothesise that mesodermal cell-induced tissue growth not only advects NCCs, but also contributes to the regulation of their directionality induced by either enhanced number of mesodermal cells or other factors, such as elongating fibres.

We propose the positive feedback loop between NCCs and tissue growth as an explanation of a robust mechanism for NCC invasion on a growing domain. We leave the biological questions as to what mechanism reduces directionality in NCCs and why mesodermal cell proliferation is likely to be induced by NCCs, open.

3.9 Conclusions and discussion

In this chapter, we investigated the effect of spatially non-uniform domain growth on the collective migration of NCCs. We extended our model to allow for spatially non-uniform domain growth profiles in the x-direction. We identified that simple splitting of the domain into two parts, which grow at different rates, affects the furthest distance travelled by cells. This result motivated us to further explore the impact of heterogeneity of domain growth and question whether it leads to a more robust invasion.

Motivated by the changes in the furthest distance travelled when different domain

growth profiles are implemented, we looked at the observed cell speed throughout migration. In all the cases we considered, there was a clear tendency for the observed cell speed to increase by approximately a factor of three when an exponentially growing, instead of a fixed, domain was considered, and the rate of increase of speed was affected by the growth profiles. We also looked at the differences in the leader and follower cell speed. This study revealed that even though the input follower speed is 1.3 times higher than the input leader cell speed, the actual output ratio is 1.1 for the parameter values that we used. There is also a higher variation in the follower cell speed in comparison with the leader cell speed. These differences can be explained by the significant effect of volume exclusion caused by the crowded environment experienced by follower cells. Detailed experimental data on the cell speed at different stages of cell migration are not yet available but this exploratory study will be important for future comparison with the experimentally observed cell speed. Such a comparison may provide insights into how non-uniformities in domain growth could be inferred from the changes in cell speed.

The next part of the chapter involved investigation of the behaviour of cells in our model in light of experimental results that indicate heterogeneous domain growth. We considered growth at the distal part of the domain for the first 18 hours of NCC migration and growth at the proximal part of the domain for the last of six hours. We identified that using this domain growth profile, input NCC speed has to be increased by 14% in comparison with the uniform domain growth case to ensure successful invasion. We next investigated perturbation experiments and identified that the experiment that involved physical ablation of NCCs suggests that NCCs stimulate domain growth, a feature not yet included in our model. We also found that there was a discrepancy between the experimental and *in silico* results when chemical inhibition of domain growth was introduced. Based on these inconsistencies, we investigated how domain growth may depend on the position of NCCs.

We deduced a NCC-induced domain growth profile to replicate the NCC ablation experiments. We discovered that growth had to be enhanced from the neural tube to a

position along the x-axis ahead of the cell front to avoid unrealistically early invasion. We also demonstrated that NCC directionality has to be reduced, in addition to domain growth reduction, to replicate the impact of chemical domain growth inhibition. This study emphasises the importance of the feedback mechanism between NCCs and tissue growth. NCCs are likely to induce domain growth, either simply by displacing mesodermal cells, or by increasing mesodermal cell proliferation and migration, whereas tissue growth not only advects NCCs, but also contributes to the regulation of their directionality induced by either enhanced number of mesodermal cells or other factors, such as elongating ECM fibres. This feedback mechanism facilitates collective NCC invasion on a growing domain.

To summarise, we hypothesise that non-uniformity of domain growth in space does not hinder collective NCC invasion because there is a feedback loop between the NCCs and their microenvironment. We still require further experiments to validate our hypothesis on the underlying feedback mechanism. More detailed experimental data could help us identify the exact characteristics of NCCs that regulate their directionality. We also need further verification as to how NCCs induce mesodermal cell proliferation. If we had such experimental data, we could further resolve our modelling framework to suggest a more specific feedback mechanism.

Chapter 4

Comparison of different interaction mechanisms in chick and Xenopus

There is an ongoing debate between experimentalists working on Xenopus and chick NCC invasion over the key mechanisms that drive invasion. Different computational modelling frameworks have been used, combined with experimental studies, to identify and evaluate possible underlying mechanisms. In particular, cell-cell repulsion and attraction are thought to be the key driving factors for cranial NCC migration in Xenopus (Szabó et al., 2016; Barriga et al., 2015) but these interactions have not been observed in chick cranial NCCs (Genuth et al., 2018), which are hypothesised to be guided by an NCC-induced chemoattractant gradient (McLennan et al., 2010). There are some physical differences between Xenopus and chick cranial NCCs, for example, Xenopus NCCs are much larger than chick NCCs, and the migratory domain is much longer in chick than in Xenopus (Woods et al., 2014; McLennan et al., 2012). However, it is an open question as to whether these physical differences provide the explanation as to why different biological mechanisms are used to ensure successful invasion (defined in Section 4.4) in these organisms. We do not know whether the specific mechanisms, suggested by previous studies, are the only ones that drive collective invasion in different organisms or whether there are alternative candidate mechanisms that

could equally well explain the same phenomena. The nature of experimental research is such that researchers are often restricted to particular organisms. Moreover, different modelling frameworks and different implementations of underlying mechanisms are often used to support experimental hypotheses. The choice of the modelling framework, as well as the implementation of different hypotheses, may affect the conclusions. Therefore, it is important to investigate whether or not the predictions across different organisms change when a single, consistent modelling framework is used. In this way, we can ask if cell-cell and cell-tissue interaction mechanisms are indeed different at the fundamental level across animal species, or are there some universal rules governing the collective migration of cranial NCCs?

To address these questions, this chapter carries out the first (to our knowledge) comparative study of NCC invasion in Xenopus and chick using a unifying, minimalistic modelling framework. We find that we can capture the mechanisms required for successful invasion in these species using such a framework. Furthermore, we perform a parameter sensitivity analysis to explore under what parameter regimes invasion may occur most efficiently. We compare the results for Xenopus and chick and suggest reasons for the observed differences or similarities.

This chapter is organised as follows: in Section 4.1, we briefly compare the biology behind the migration of chick and Xenopus cranial NCCs. We continue with a review of the key computational frameworks used to model chick and Xenopus cranial NCCs in Section 4.2. We present our new generalised computational model for Xenopus and chick cranial NCCs in Section 4.3. We describe the techniques used in the rest of this chapter in Section 4.4. In Section 4.5, we describe the methods used for comparison of Xenopus and chick NCC invasion. We present our results on successful invasion in Xenopus and chick separately and then compare and contrast them in Sections 4.6-4.8. We finish this chapter with conclusions and a discussion in Section 4.9.

4.1 Biological background

In Chapter 1 (Sections 1.1.1, 1.1.2 and 1.1.3), we described the key mechanisms that are understood to drive collective migration in Xenopus and chick, namely contact inhibition of locomotion (CiL) and co-attraction in Xenopus, and external guidance by a chemoattractant combined with local cell-cell guidance mechanisms in chick. CiL refers to the physical contact of cells leading to the inhibition of movement and, if there is sufficient space nearby, movement away from each other. Therefore, for the sake of simplicity and clarity, in the rest of this work we will refer to CiL as "repulsion".

Figure 4.1 presents the schematics of chick and Xenopus cranial NCC invasion. In this thesis we focus on the rhombomere 4 streams because they are the most extensively studied streams. In chick, NCCs emerge at the neural tube and migrate in a confined stream separated by two NCC-free regions. In Xenopus, NCCs commence their migration from outside the neural tube and, initially, there is no clear distinction between the streams: only at later stages is such a distinction observed. In chick, the neural tube closes before the delamination and migration of NCCs, whereas in Xenopus the neural tube is in the process of closure during delamination and migration (Theveneau and Mayor, 2012).

There are further differences between the chick and Xenopus cranial NCC migratory processes, such as cell size and domain length. We provide specific parameter values and brief discussions of the different biological features included in the computational models that have been proposed for Xenopus and chick in the following section.

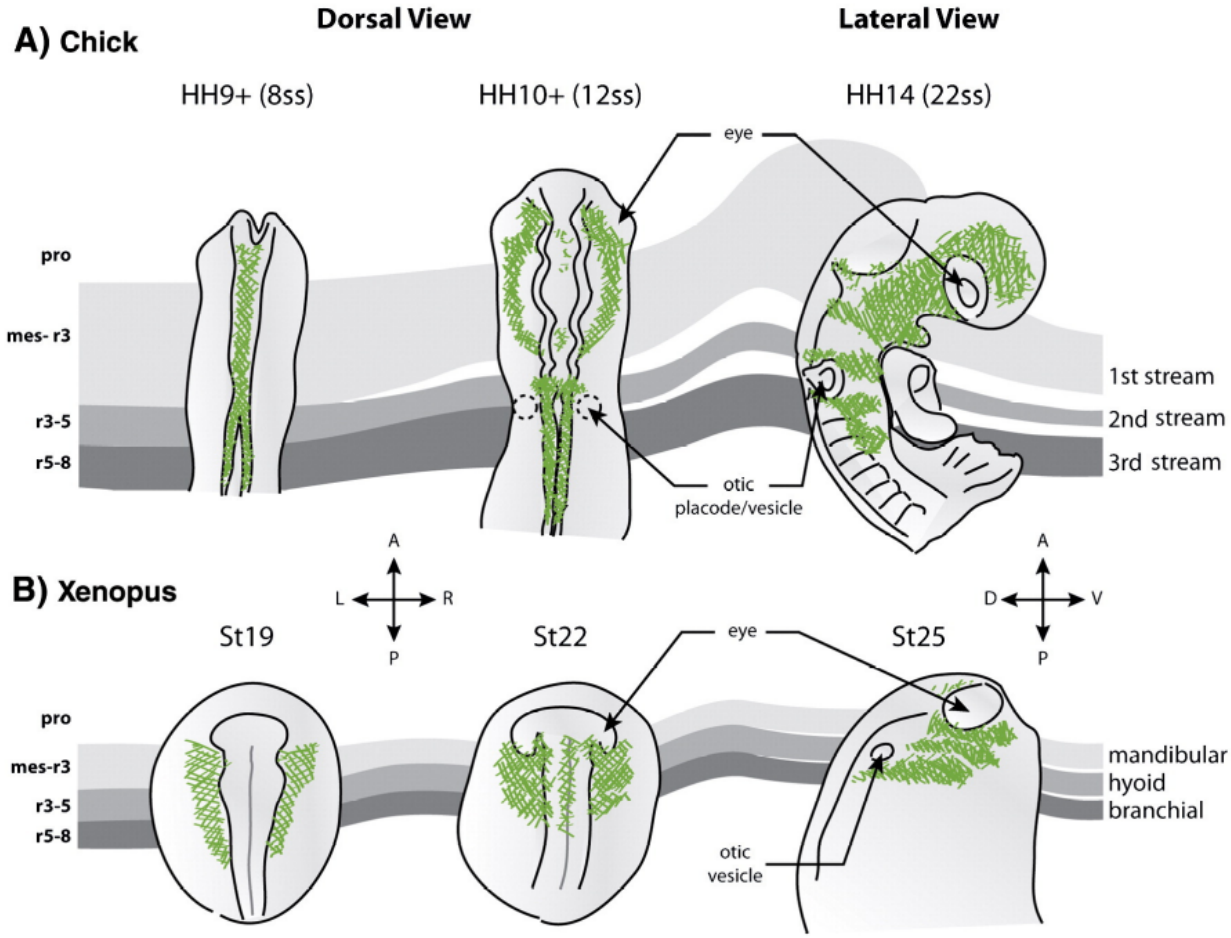


Figure 4.1: Early migration of cranial NCCs (green) with NCCs emerging at different locations and embryonic stages. (A) Migration of chick cranial NCCs. NCCs delaminate from the neural tube and migrate in confined streams. (B) Migration of Xenopus cranial NCCs. NCCs start their migration from outside the neural tube and clear NCC-free regions between the streams only emerge at later stages. Homologous streams in chick and Xenopus are coded in similar shades of grey for comparison. HH stages of chick embryo development; mes, mesencephalon; pro, proencephalon; r, rhombomere; ss, somites; A, anterior; P, posterior; L, left; R, right; D, dorsal; V, ventral. Nieuwkoop and Faber stages of Xenopus embryos. Figure reproduced from Theveneau and Mayor (2012) with permission from Elsevier.

4.2 Detailed review of the key computational models used for cranial neural crest cell invasion in Xenopus and chick

Here we summarise the key differences in the parameters and assumptions of the main models used for the collective migration of chick and Xenopus cranial NCCs (Woods et al., 2014; McLennan et al., 2012). We have already discussed in detail the McLennan et al. (2012) model for chick cranial NCC migration in Section 1.1.4, so here we focus on the model proposed by Woods et al. (2014) for the dynamics of cranial NCC migration in Xenopus. In their model, it is proposed that cellular motion is driven by the sum of a number of applied forces. The equation that governs the migration of a simulated cell is as follows:

$$m\ddot{\boldsymbol{x}}_i = \boldsymbol{F}_i^T, \tag{4.1}$$

where

$$\boldsymbol{F}_i^T = Q\left(a_i(t)\boldsymbol{F}_i^a + \omega_i(t)\boldsymbol{F}_i^\omega + m_i(t)\boldsymbol{F}_i^p\right) + \sum_{k\in C_i}\left(\boldsymbol{F}_{ik}^C + \boldsymbol{F}_{ik}^{Cd} + \boldsymbol{F}_{ik}^{R_{CIL}}\right). \tag{4.2}$$

Here, m is the cell mass, and $\ddot{\boldsymbol{x}}_i$ is the acceleration of the simulated cell with centre at position vector $\boldsymbol{x}_i$. $\boldsymbol{F}_i^T$ is the sum of all the interaction forces that will influence a change in velocity. $\boldsymbol{F}_i^a$, $\boldsymbol{F}_i^\omega$, $\boldsymbol{F}_i^p$, $\boldsymbol{F}_{ik}^C$, $\boldsymbol{F}_{ik}^{Cd}$ and $\boldsymbol{F}_{ik}^{CIL}$ are co-attraction, rotational turning, self-propulsion, contact, contact damping and contact repolarisation forces, respectively. C_i is the set of indices of cells in contact with the cell i (defined such that $C_i = \{k : |\delta_{ik}| \equiv |\boldsymbol{x}_i - \boldsymbol{x}_k| - 2r < 0\}$ where r is cell radius). The coefficient Q sets the co-attraction, self-propelled and rotational turning forces to zero when a simulated cell is in contact with other cells, and the coefficients $a_i(t)$, $v_i(t)$ and $m_i(t)$ are functions of the internal clocks for co-attraction, rotational turning and self-propulsion, respectively. Boundary conditions were incorporated using inward forces at the top and bottom borders of a rectangular domain. There were no boundary conditions specified at the left and right boundaries of the domain. Full details of the model can be found in the Supplementary Information of Woods et al. (2014).

Using their computational model, Woods et al. (2014) suggested that the interplay between the complementary mechanisms of CiL and co-attraction contribute to the motion of the NCCs and no further external guidance cues are needed, as discussed in Section 1.2.1. Woods et al. (2014) assumed that the cells move according to Newton's second law of motion and the inertia of the cells could explain persistent bias in collective cell migration. However, cell migration occurs in a highly viscous environment (low Reynolds number) (Purcell, 1977), so inertial forces are likely to be negligible. Therefore, the assumption of the inertia-based second-order dynamics in the Woods et al. (2014) model may be inaccurate. For this reason, we will incorporate CiL and co-attraction mechanisms into our overdamped modelling framework in a simplified way to explore and compare Xenopus and chick NCC migration.

Next, we discuss the parameters and the assumptions made in the McLennan et al. (2012) model for chick, and the Woods et al. (2014) model for Xenopus (Tables 4.1 and 4.2) that are relevant for this study.

Model	Cell radius, μm	Cell speed, μm/h	Domain length, μm	Domain width, μm	Initial number of cells	Dimension
Xenopus	20.0	≈ 180	850	217	50	2
Chick	7.5	≈ 60	300 to 1100	120	0	2

Table 4.1: Comparison of model parameters: Xenopus – Woods et al. (2014), chick – McLennan et al. (2012).

Model	Number of cells	Mechanism	Final configuration	Time
Xenopus	50 (fixed)	CiL & co-attraction	80% of cells reach arches	until 80% of cells reach arches
Chick	constant influx	chemotaxis, contact or tunnelling	cells cover all the domain	24 hours

Table 4.2: Comparison of model features: Xenopus – Woods et al. (2014), chick – McLennan et al. (2012).

- Cell radius is estimated from nuclear shape measurements in chick (Kulesa et al., 2010). It is not clearly stated how cell radius is measured in Xenopus (Woods et al., 2014). We highlight that during their migration the cells undergo significant morphological changes and thus this parameter is a crude approximation.

- Cell speed is an approximate parameter since there are many cells and they all move at different speeds. Cell speed may also vary during migration (Kulesa and Fraser, 2000; Kulesa et al., 2008).

- McLennan et al. (2012) provides an explicit domain length measurement and demonstrates that the domain grows significantly during NCC migration in chick. In Xenopus, Woods et al. (2014) also provides an explicit domain length measurement but it is assumed that the domain does not grow because growth is insignificant on the time frame of invasion (Gurdon, 1995).

- Domain width is a constant parameter in both cases because the NCC corridor does not expand significantly in the y-direction during the migration (McLennan et al., 2012; Woods et al., 2014).

- Note that in chick models, there are no NCCs initially in the domain. In Xenopus

models, however, there is a cluster of 50 cells initially placed in the domain. This modelling assumption corresponds to most of the cells having delaminated from the neural tube before the start of migration.

- There is a constant influx of cells in chick, which models new cells delaminating from the neural tube. Xenopus NCC modellers consider the dynamics of the cluster of 50 cells with no influx of new cells.

- The final configuration of the cells (model output – criterion for successful invasion) is also based on what the models aim to represent. In chick, it is coverage of the domain by cells after 24 hours, whereas in Xenopus it is 80% of the cells in the cluster leaving the domain through the right-hand boundary, and the efficacy of invasion is measured by comparing the time to invasion. Time to invasion in Xenopus cranial NCC invasion depends on incubation temperature and can vary from 12 to 24 hours (from 22°C to 14°C, respectively) (Alfandari et al., 2010).

- Cell proliferation is not included in either model. This assumption is based on the evidence that NCC mitotic activity is relatively quiescent during migration until the cells reach the branchial arches (Ridenour et al., 2014; Nagatomo and Hashimoto, 2007; Nichane et al., 2008).

We will aim to use the assumptions and parameter values in Tables 4.1 and 4.2 in our minimalistic modelling framework to better understand why different mechanisms are suggested to explain cranial NCC invasion in chick and Xenopus.

4.3 A flexible computational model to incorporate simple cell-cell interactions

We construct a simple computational model to capture the key mechanisms involved in cranial NCC migration. We use a two-dimensional rectangular domain to model NCC invasion in both model organisms but the sizes of the rectangles differ, as described in Table 4.1. In chick, the domain is elongating in the x-direction, whereas in Xenopus, it is fixed. In addition to random movement by the cells, we include the short-range repulsion and longer-range attraction forces which were identified in Xenopus. Based on the finding that the chemoattractant VEGF provides directional bias for the cells, we also include a bias in cell movement. We implement the bias instead of solving directly for the chemoattracant for simplicity.

We use a form of the overdamped Langevin equation (since cell migration is non-inertial and dominated by overdamped dynamics) to describe the dynamics of cells (Van Kampen, 1992):

$$\frac{\mathrm{d}\boldsymbol{x}_i}{\mathrm{d}t} = \sum_{j\neq i} \boldsymbol{F}_{ij} + \beta \boldsymbol{i} + \sqrt{2D}\boldsymbol{R}_i, \qquad i = 1, \dots N, \tag{4.3}$$

where $\boldsymbol{x}_i$ is the position of the ith cell, $\boldsymbol{F}_{ij}$ is the interaction force between cell i and cell j, β is the bias (with $\boldsymbol{i} = (1, 0)$ because bias is only introduced in the x-direction), D is the diffusion constant, and N is the number of cells in the simulation. $\boldsymbol{R}_i(t)$ is a delta-correlated stationary Gaussian process with zero-mean, satisfying

$$\langle \boldsymbol{R}_i(t) \rangle = 0,$$

$$\langle \boldsymbol{R}_i(t), \boldsymbol{R}_i(t') \rangle = \delta(t - t').$$

The interaction force is written as

$$\boldsymbol{F}_{ij} = -\epsilon \frac{\mathrm{d}Z(r)}{\mathrm{d}r} \frac{(\boldsymbol{x}_i - \boldsymbol{x}_j)}{r}, \tag{4.4}$$

where $r = |\boldsymbol{x}_i - \boldsymbol{x}_j|$ and ϵ is the interaction strength parameter. To describe the interactions

we use a Lennard-Jones potential (Jones, 1924):

$$Z(r) = \begin{cases} \left[\left(\frac{\sigma}{r}\right)^m - \left(\frac{\sigma}{r}\right)^n\right], & \text{attraction and repulsion,} \quad (4.5) \\ \left(\frac{\sigma}{r}\right)^m, & \text{repulsion-only,} \quad (4.6) \end{cases}$$

where $m, n > 0$ are natural numbers with $m = 2n$, and σ is the cell diameter. The term with the power m in Equation (4.5) models repulsion, and the term with the power n models attraction, so in the models with repulsion-only, we omit the attraction term (Equation (4.6)). In the standard Lennard-Jones potential $m = 12$ and $n = 6$, but any natural numbers such that $m = 2n$ would model similar behaviour. We will use $n = 4$ and $m = 8$ because of the realistic non-zero potential ranges exhibited in this case (Figure 4.5). In our model, we use the Lennard-Jones potential but there are many other possible functional forms that incorporate short-range repulsion and longer-range attraction, such as the Morse potential, Hertz potential, or a nonlinear spring model (Matsiaka et al., 2018; Byrne and Preziosi, 2003; Murray et al., 2012). We further explain our choice of the Lennard-Jones potential in Section 4.3.1.

We use the Forward Euler method to solve Equation (4.3):

$$\boldsymbol{x}_i(t + \Delta t) = \boldsymbol{x}_i(t) + \Delta t \sum_{j \neq i} \boldsymbol{F}_{ij} + \Delta t \beta \boldsymbol{i} + \sqrt{2D\Delta t}\boldsymbol{\xi}, \quad (4.7)$$

where $\boldsymbol{\xi} \sim \mathcal{N}(\mathbf{0}, I)$ is Gaussian noise (I is the identity matrix). In both model organisms, the constraints on the top and bottom boundaries are incorporated in the algorithm as follows:

1. propose a new position for the cell based on $\boldsymbol{x}_i(t + \Delta t) = \boldsymbol{x}_i(t) + \Delta t \sum_{j \neq i} \boldsymbol{F}_{ij} + \Delta t \beta \boldsymbol{i} + \sqrt{2D\Delta t}\boldsymbol{\xi}$.

2. if a proposed position is inside the domain, accept it. If the proposed cell position is outside the domain, then the cell is moved in the direction $\boldsymbol{x}_i(t + \Delta t) - \boldsymbol{x}_i(t)$ but only to the point at which it is still inside the domain, i.e. the cell centre is at distance of one cell radius away from the boundary.

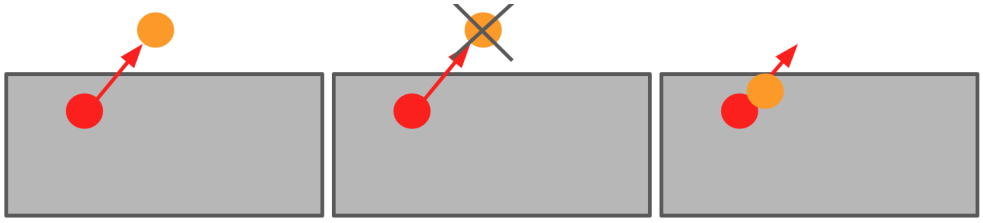
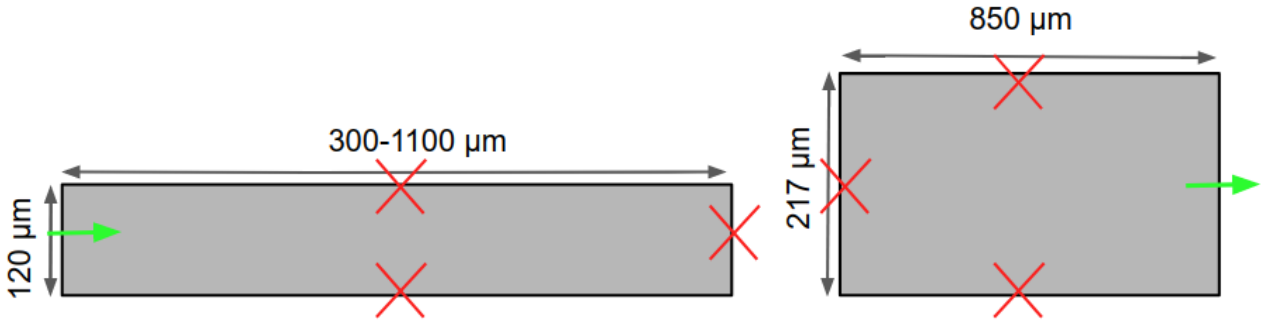


Figure 4.2: An example of the effect of the boundary conditions (on the top and bottom of the domain) on the dynamics of cells. A cell (red circle) is supposed to move to the position marked by the orange circle in the image on the left, but due to the boundary conditions, it moves in the same direction but only until it reaches the boundary, at which point it stops.

Figure 4.2 illustrates the effect of the boundary constraints. In chick, the same boundary constraint holds for the right-hand boundary and there is a constant influx of cells at the left-hand boundary (Figure 4.3(a)). In Xenopus, the above boundary constraint holds for the left-hand boundary but the cells are allowed to leave the right-hand side boundary (Figure 4.3(b)). We impose these boundary conditions based on the features in Table 4.2.



(a) Chick. **(b)** Xenopus.

Figure 4.3: Schematics of domains and boundary conditions for: (a) chick, and (b) Xenopus NCC invasion. Grey rectangle corresponds to domain. Red crosses correspond to the boundary constraint described in Figure 4.2. In (a), the green arrow corresponds to influx of cells. In (b), the green arrow corresponds to outflux of cells. The cells that leave the domain are assumed to enter the branchial arches.

The initial conditions differ in the Xenopus and chick simulations (Table 4.1). In Xenopus, there are 50 equally spaced cells at the left-hand boundary (Figure 4.6(a) in Section 4.6), i.e. for all combinations of $i \in [1, 2, \ldots, 10]$ and $j \in [1, 2, \ldots, 5]$, initial cell coordinates $(x_{0\text{cell}}, y_{0\text{cell}})$ are as follows:

$$x_{0\text{cell}} = kR, \text{ where } k = 2i - 1, \tag{4.8}$$

$$y_{0\text{cell}} = j\frac{L_y}{5} + 0.5\frac{L_y}{5}, \tag{4.9}$$

where R is cell radius and L_y is the width of the domain. In chick, initially, there are no cells in the domain.

Units for the bias, β, are μm/min, for the diffusion constant, D, μm^2/min, and for the interaction strength parameter, ϵ, μm/min. We do not explicitly write them out in the rest of this chapter.

We describe the verification of numerical convergence of Equation (4.7) in Appendix C.

4.3.1 Lennard-Jones potential

We choose the Lennard-Jones potential to describe cell-cell interactions because it easily allows for the force range to be scaled according to cell size (Figure 4.4). Since we do not know the exact forces, we make an assumption that the range spanned by the cell-cell force depends on the cell size, ceteris paribus. Note that we could use different scalings, for example, we could argue that forces exerted by larger cells may be stronger, however, we leave the study of the effects of different scalings for future work.

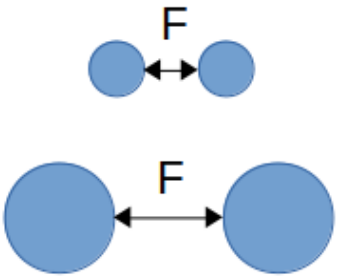


Figure 4.4: We assume that the force exerted on small cells a distance of one diameter apart is the same as the force exerted by larger cells also a diameter distance apart. This is a feature of the Lennard-Jones potential (Equations (4.10)-(4.12)). This scaling corresponds to the biological interpretation that the cell-cell force range depends only on cell size.

The scaling of the interaction strength parameter, ϵ, for cells of diameter σ_1 is as follows:

$$\boldsymbol{F}_{ij} = -\epsilon_1 \frac{\mathrm{d}Z(r)}{\mathrm{d}r} \frac{(\boldsymbol{x}_i - \boldsymbol{x}_j)}{r} = -\epsilon_1 n \left[2 \left(\frac{\sigma_1^m}{r^{m+1}} \right) - \left(\frac{\sigma_1^n}{r^{n+1}} \right) \right] \frac{(\boldsymbol{x}_i - \boldsymbol{x}_j)}{r}, \tag{4.10}$$

where ϵ_1 is the force strength. For any scalar $b > 0$, at $r = b\sigma_1$

$$\boldsymbol{F}_{ij} = -\epsilon_1 n \left[2 \left(\frac{1}{b^{m+1}\sigma_1} \right) - \left(\frac{1}{b^{n+1}\sigma_1} \right) \right] \frac{(\boldsymbol{x}_i - \boldsymbol{x}_j)}{b\sigma_1}. \tag{4.11}$$

For cells with diameter σ_2, we scale $\epsilon_2 = \epsilon_1 \sigma_2 / \sigma_1$, so that at $r = b\sigma_2$

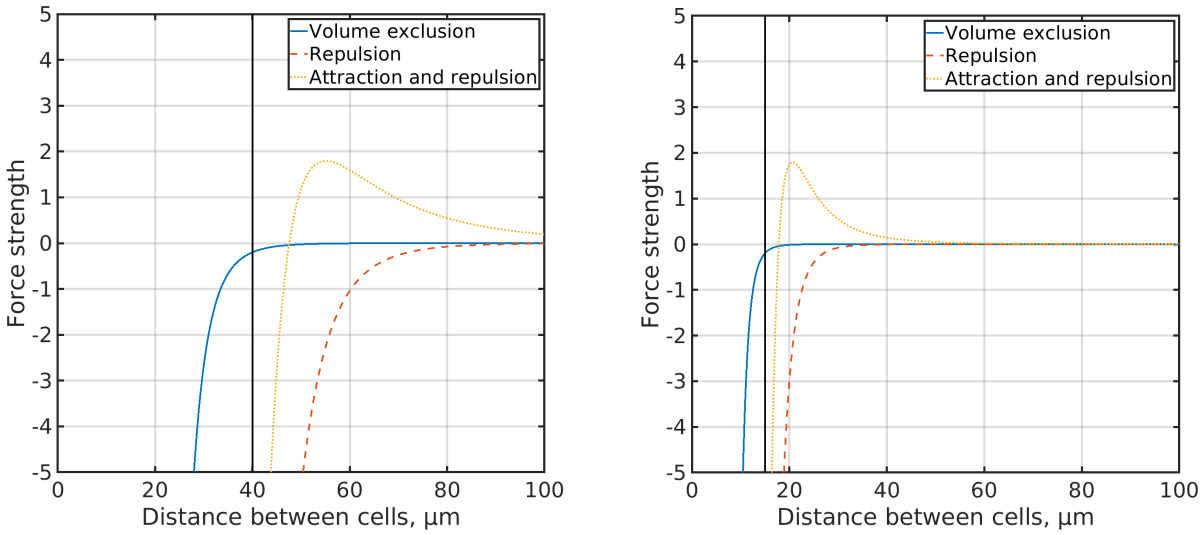
$$\boldsymbol{F}_{ij} = -\epsilon_1 \frac{\sigma_2}{\sigma_1} n \left[2 \left(\frac{1}{b^{m+1}\sigma_2} \right) - \left(\frac{1}{b^{n+1}\sigma_2} \right) \right] \frac{(\boldsymbol{x}_i - \boldsymbol{x}_j)}{b\sigma_2} \tag{4.12}$$

$$= -\epsilon_1 n \left[2 \left(\frac{1}{b^{m+1}\sigma_1} \right) - \left(\frac{1}{b^{n+1}\sigma_1} \right) \right] \frac{(\boldsymbol{x}_i - \boldsymbol{x}_j)}{b\sigma_2}, \tag{4.13}$$

which is equivalent to Equation (4.11) only with the appropriate scaling of the force range σ_2, as illustrated in Figure 4.4.

Figure 4.5 illustrates some properties of our assumed force function. The repulsion-only model, Equation (4.6), can account for volume exclusion for small values of the interaction strength parameter ϵ. For example, if we set $\epsilon = 1$, then the cells would only repel each other when they touch (Figure 4.5(a)). However, if we increase ϵ to 200, then the cells

start repelling each other at larger distances (Figure 4.5(a)). We also provide an example of the attractive and repulsive forces (attraction and repulsion potential in Equation (4.5)) for $\epsilon = 200$ (Figure 4.5(a)). Note that to ensure that we use proportional force ranges when we vary cell diameter, we set $\epsilon_2 = \epsilon_1\sigma_2/\sigma_1$ (compare Figures 4.5(a) and (b)).



(a) Cell diameter = 40μm.

(b) Cell diameter = 15μm.

Figure 4.5: The force arising from the Lennard-Jones potential for different cell parameters. Distance between cells denotes the distance between cell centres. (a) Volume exclusion: repulsion-only potential as in Equation (4.6), $\epsilon = 1$, $m = 8$. Repulsion: repulsion-only potential as in Equation (4.6), $\epsilon = 200$, $m = 8$. Attraction and repulsion: attraction and repulsion potential as in Equation (4.5), $\epsilon = 200$, $n = 4$, $m = 8$. (b) Volume exclusion: repulsion-only potential as in Equation (4.6), $\epsilon = 0.4$. Repulsion: repulsion-only potential as in Equation (4.6), $\epsilon = 75.0$. Attraction and repulsion: attraction and repulsion potential as in Equation (4.5), $\epsilon = 75.0$. In both (a) and (b), the vertical black line indicates the cell diameter in each case.

4.4 Definitions and techniques

In this section we introduce the key definitions and techniques used in this study.

Successful invasion

It is important to note that the definition of successful invasion differs in studies of Xenopus and chick. In Section 4.2, we identified that in Xenopus models, successful invasion requires that 80% of the cells leave the domain (Figure 4.6).

In chick models, successful invasion is the coverage of the domain by a continuous stream (Figure 4.7). It is known that chick cranial NCC migration starts around HH Stage 11 and continues until HH Stage 17 (Kulesa et al., 2010), corresponding to approximately 15-24 hours. So we assume that full coverage has to occur within 24 hours from the start of migration. Therefore, we quantify the coverage of the domain using two criteria. First, the domain has to be fully invaded: we define this as more than five cells in the final 100μm segment in the x-direction of the domain by 24 hours. We choose the threshold value of five cells because if the cells are sparsely distributed, as in the repulsion-only models, then more than five cells can cover the segment of length 100μm (Figure 4.7). However, we acknowledge that there is a trade-off between this threshold parameter and time to invasion (larger threshold value means larger time to invasion). Second, there are no large gaps in the stream, i.e. no stream breakage (an example of stream breakage is presented in Figure 4.8). In the next section we describe how we identify and quantify stream breakage.

In both cases we run the simulations until we observe successful invasion or the final time (24 hours) is reached.

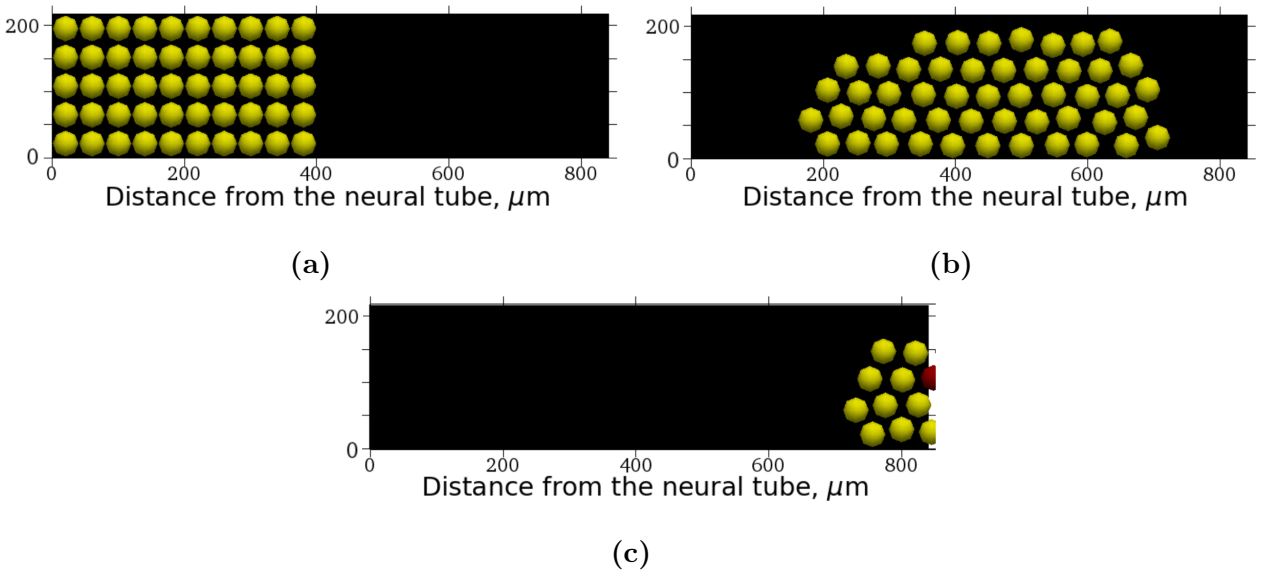


Figure 4.6: NCC migration in Xenopus: (a) initial configuration of cells; (b) intermediate configuration of cells; (c) final configuration of cells which corresponds to an example of successful invasion. Snapshots from the attraction and repulsion model for Xenopus with bias for all cells at (a) zero hours (prior to migration); (b) 10 hours; (c) 24 hours. Parameter values are $\beta = 0.7$, $\epsilon = 200$ and $D = 6$. Yellow circles are NCCs still in the migratory domain and red circles are the cells that have already reached the target. The black background represents the migratory domain.

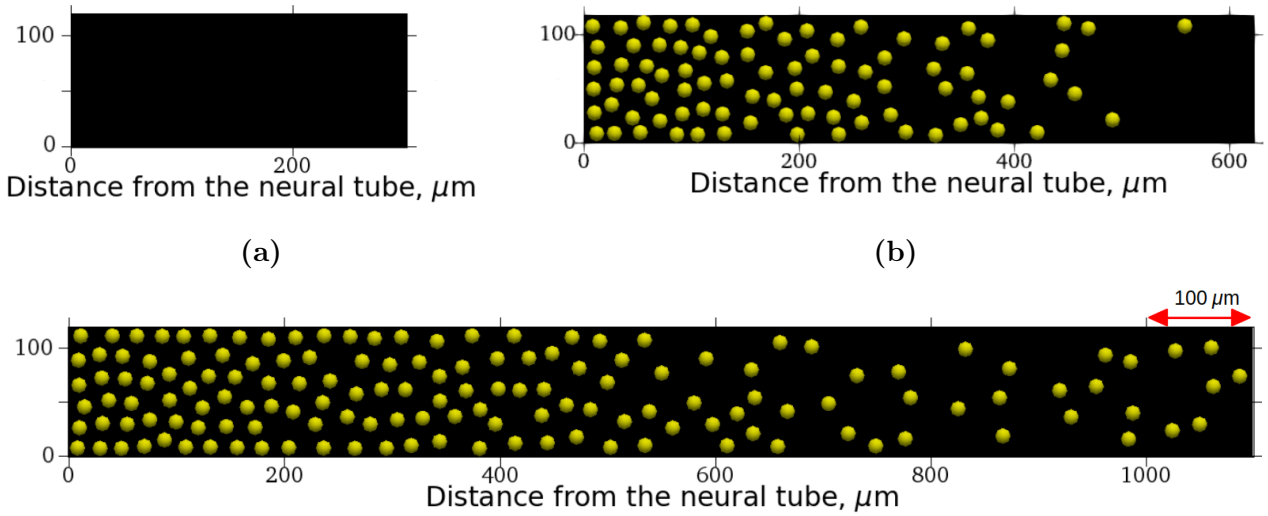


Figure 4.7: NCC migration in chick: (a) initial configuration of cells; (b) intermediate configuration of cells; (c) final configuration of cells which corresponds to an example of successful invasion (there are at least five cells in the final 100μm segment in the x-direction of the domain). Snapshots from the repulsion-only model for chick at (a) zero hours (prior to migration); (b) 10 hours; (c) 24 hours. Parameter values are $\epsilon = 56$ and $D = 6$. Yellow circles represent NCCs. The black background represents the migratory domain.

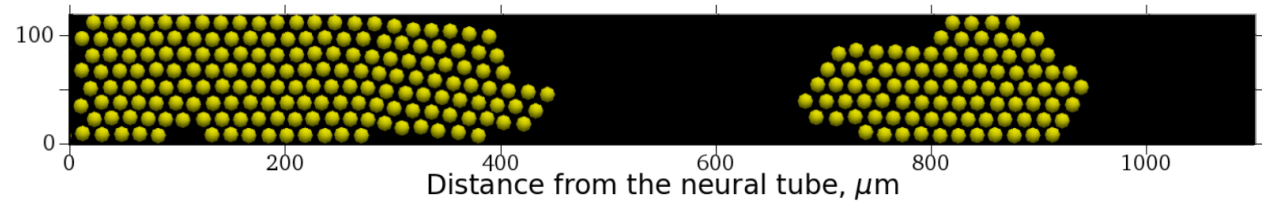


Figure 4.8: Example of stream breakage in chick. Snapshot from the attraction and repulsion model for chick with bias for all cells at 24 hours with $\beta = 0.1$, $\epsilon = 75$ and $D = 4$. Yellow circles represent NCCs. The black background represents the migratory domain.

Stream breakage

To estimate whether a stream is continuous or not, we will use the gap statistic (Tibshirani et al., 2001). The gap statistic is used to estimate the number of clusters formed by the data points of interest. In our case, the data points are cell positions and we define stream breakage to occur if there is more than one cluster of cells in our system (Figure 4.9). The gap statistic method uses the output of any clustering algorithm (Xu and Wunsch, 2005) and a comparison of the change in within-cluster dispersion with that expected under an appropriate null distribution. We will use the K-means clustering algorithm, which partitions data based on the within-cluster sum of squares (Hartigan and Wong, 1979). We choose this method because it is computationally cheap, guarantees convergence and is relatively simple to implement, but there are other clustering methods which could be used, for example, multivariate Gaussian mixture, hierarchical clustering, spectral and nearest neighbour methods (Rodriguez et al., 2019). We use the spatially uniform distribution as the null reference distribution. Below is a detailed description of the method.

Suppose that we have clustered the data (cell positions at the end of a simulation) into k clusters $C_1, C_2, \ldots, C_k$, and we denote by n_r the number of observations in C_m, $m \in [1, \ldots, k]$, i.e. $n_r = |C_m|$. Let D_m be the sum of the pairwise distances for all points in cluster m, i.e.:

$$D_m = \sum_{i,j \in C_m} r_{ij}, \tag{4.14}$$

where r_{ij} is the squared Euclidean distance between cells i and j. We define the within-cluster sum of squares around cluster means, W_k, as follows:

$$W_k = \sum_{j=1}^{k} \frac{1}{2n_j} D_j, \tag{4.15}$$

where the two in the denominator accounts for the double counting of the r_{ij} and r_{ji}. We use $\log(W_k)$, and compare it with its expectation under a null reference distribution, in our

case, the spatially uniform distribution. We define the gap statistic as

$$\text{gap}(k) = \frac{1}{N}\sum_{n=1}^{N}\log(W_{kn}) - \log(W_k), \tag{4.16}$$

where W_{kn} denotes replicates of the reference distribution and N is the sample size from the reference distribution (we set $N = 100$ after checking that larger values of N do not provide more accurate results). Then the optimal number of clusters, $\hat{k}$, is defined as the smallest k such that

$$\text{gap}(k) \geq \text{gap}(k+1) - s_{k+1}, \tag{4.17}$$

where s_k is the simulation error calculated from the standard deviation of the reference distribution replicates, $\text{sd}(k)$, according to the equation

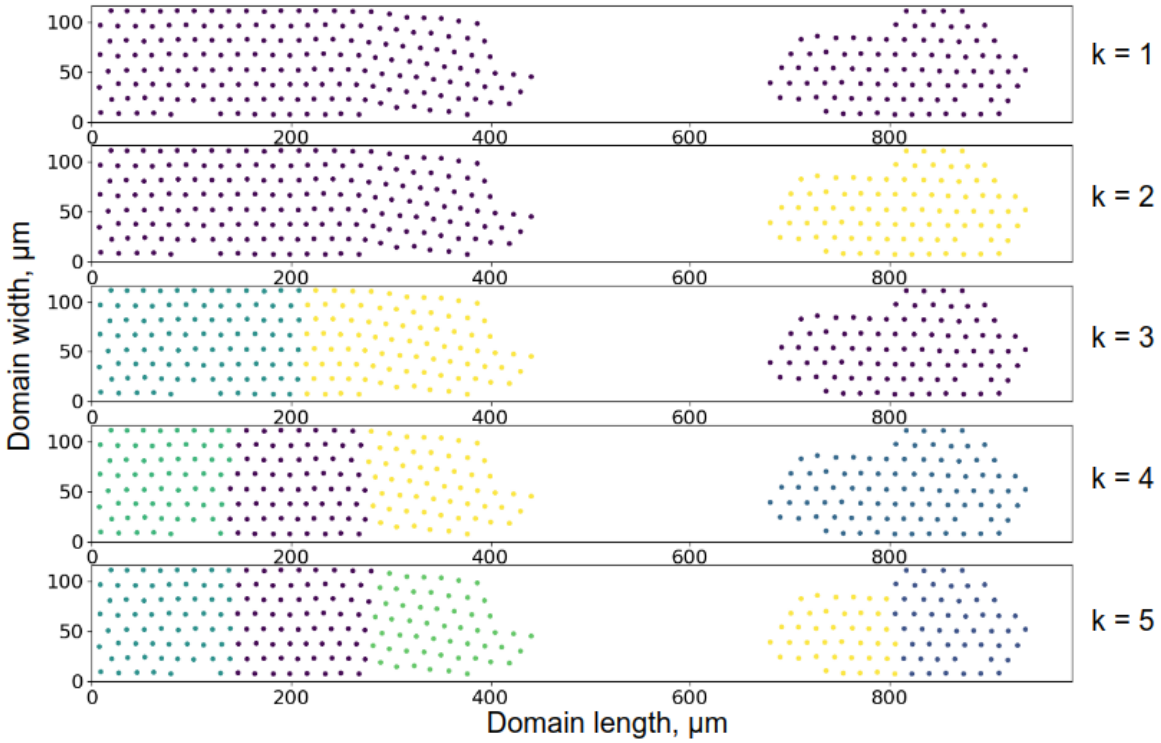
$$s_k = \sqrt{1 + 1/N}\text{sd}(k). \tag{4.18}$$

The standard deviation, $\text{sd}(k)$, can be calculated as follows:

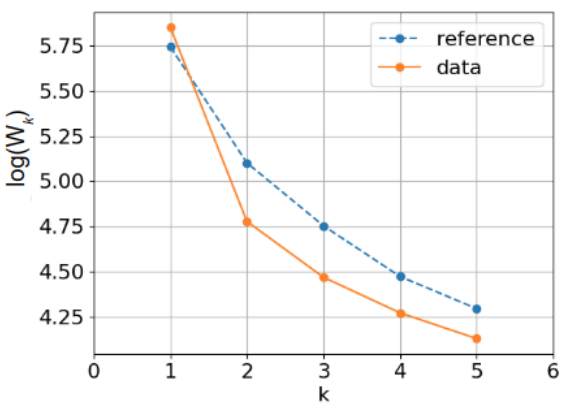
$$\text{sd}(k) = \left[\frac{1}{N}\sum_{n=1}^{N}(\log(W_{kn}) - \bar{w})^2\right]^{\frac{1}{2}}, \tag{4.19}$$

where $\bar{w} = \frac{1}{N}\sum_{n=1}^{N}\log(W_{kn})$.

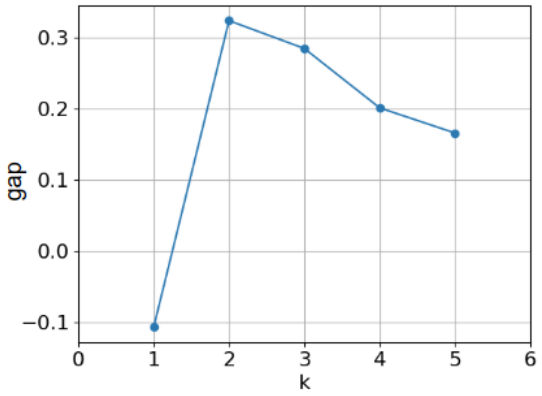
Figure 4.9 demonstrates an example of stream breakage where the optimal number of clusters is two, $\hat{k} = 2$. Figure 4.10 is an example of a continuous stream, where the optimal number of clusters is one, $\hat{k} = 1$.



(a)

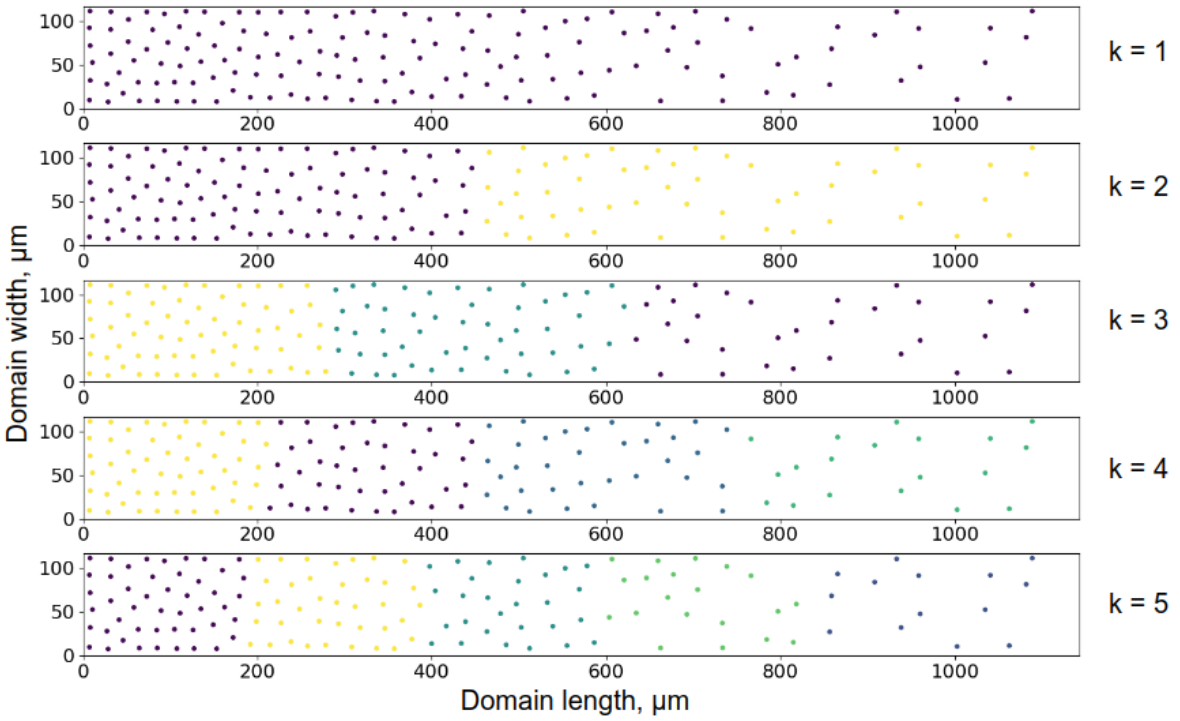


(b)

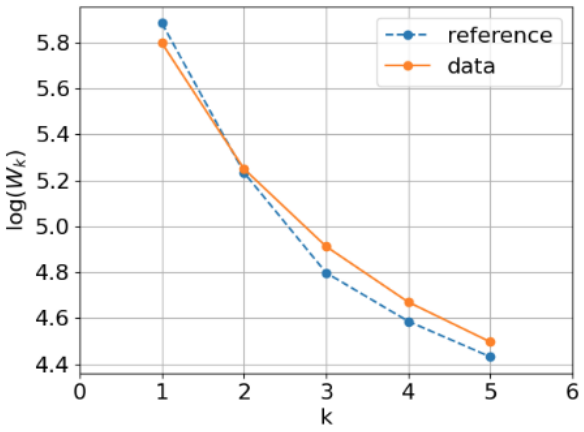


(c)

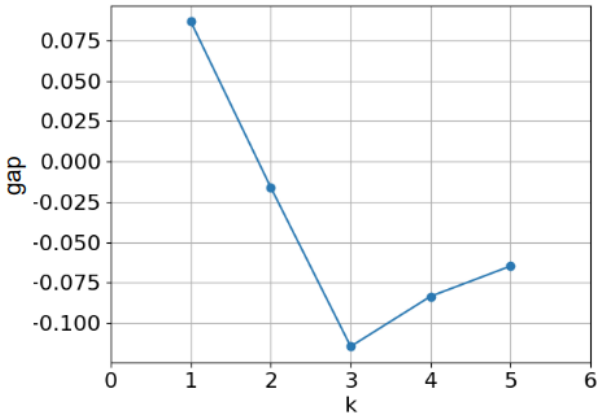
Figure 4.9: Stream breakage estimation using the gap statistic. (a) Cell configuration of an exemplary simulation at $t = 24$ hours for the chick repulsion-only model. The five plots represent the same cell configuration with increasing number of clusters from top to bottom generated by a K-means clustering algorithm. Points represent cell positions. (b) Log of the within-cluster sum of squares around means (Equation (4.15)) for different numbers of clusters and data in (a) and a spatially uniform reference distribution. (c) Gap statistic versus the number of clusters with $\hat{k} = 2$ (Equation (4.17)), $\text{gap}(2) \geq \text{gap}(3) - s_3$ with $s_3 = 0.05$ (Equation (4.18)), so the optimal number of clusters is two. This means that the stream breaks.



(a)



(b)



(c)

Figure 4.10: Stream breakage estimation using the gap statistic. (a) Cell configuration of an exemplary simulation at $t = 24$ hours for the chick attraction and repulsion model. The five plots represent the same cell configuration with increasing number of clusters from top to bottom generated by a K-means clustering algorithm. Points represent cell positions. (b) Log of the within-cluster sum of squares around means (Equation (4.15)) for different numbers of clusters and data in (a) and a spatially uniform reference distribution. (c) Gap statistic versus the number of clusters with $\hat{k} = 1$ (Equation (4.17)), $\text{gap}(1) \geq \text{gap}(2) - s_2$ with $s_2 = 0.07$ (Equation (4.18)), so the optimal number of clusters is one. This means that the stream does not break.

Leaders

McLennan et al. (2012) demonstrated that two NCC phenotypes, namely leaders and followers, are necessary for successful streaming migration. Leaders are guided by an NCC-induced chemoattractant gradient, and followers are guided by the leaders using a contact or tunnelling mechanism. Furthermore, McLennan et al. (2015b) showed that there is a small number of leader cells at the front of the stream. There is no known heterogeneity in Xenopus cranial NCCs. However, to make a consistent comparison, we define leaders in both Xenopus and chick models. In Xenopus, we define the leaders to be the five cells initially at the front of the stream and in chick, the first five cells entering the domain. We only distinguish leaders in the cases when we assume that leaders are biased and followers are not biased. For simplicity and due to the fact that biased leaders move in the right direction more rapidly than the rest of the cells, we do not include phenotype switching, even though it has been observed in chick cranial NCCs.

4.5 Methods

We compare and contrast the dynamics of the model resulting from implementing values of the key parameters that are distinct for Xenopus and chick. We will include the following model parameters and features: cell radius, domain length (fixed vs. growing), domain width, initial number of cells, number of cells and final configuration (Tables 4.1 and 4.2). We include the repulsion and attraction mechanisms that correspond to the CiL and co-attraction mechanisms from the Xenopus models, and bias, which is similar to the chemotaxis parameter from the chick models. Our aim is to use different models (Table 4.3) to identify the key mechanisms that are necessary for successful invasion. For each model, we identify the parameter range within which successful invasion is possible, and the most efficient (based on the criteria: time to invasion for Xenopus; time to invasion and stream breakage for chick). This study will help us to understand whether different mechanisms are

necessary for successful invasion in Xenopus and chick.

Repulsion-only (no bias)
Attraction and repulsion (no bias)
Attraction and repulsion with biased leaders
Repulsion-only with all cells biased
Attraction and repulsion with all cells biased

Table 4.3: We categorise different models by the interaction potentials specified by Equations (4.5) and (4.6), and the extent of bias included in the model. We set the bias, β, to zero in Equation (4.3) for the models with no bias. We set the bias to a non-zero value either for leaders only or for all cells.

For the models in Table 4.3, we run the following simulations. In the models with no bias, we only vary the diffusion constant and the interaction strength parameter. In the models with bias, we perform three different parameter sweeps: 1. fixed bias and varying diffusion constant and interaction strength parameter; 2. fixed diffusion constant and varying bias and interaction strength parameter; 3. fixed interaction strength parameter and varying diffusion constant and bias. For each parameter set we run 100 simulations to account for random variations.

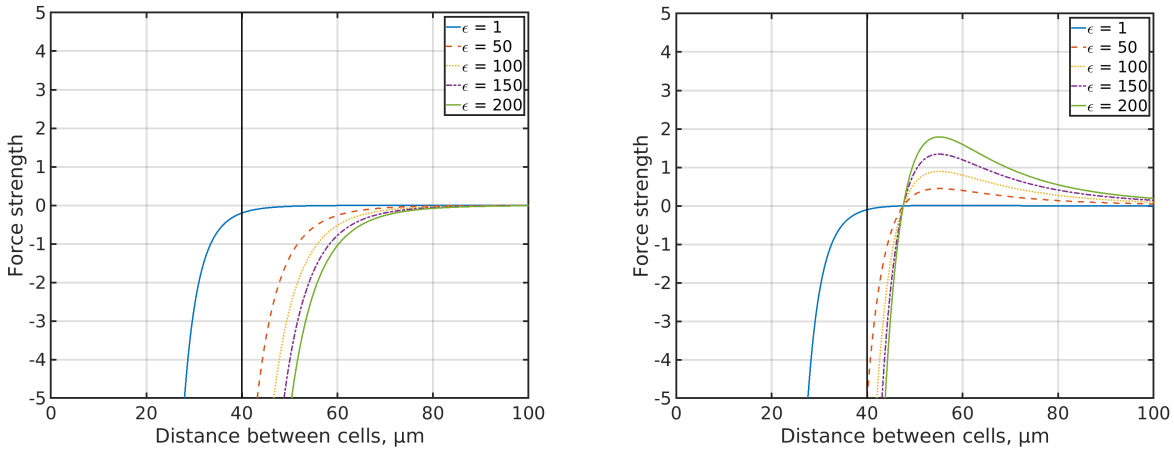
In Xenopus, we provide the data for each model (Table 4.3) with the number of cases in which invasion occurs in 24 hours or less because in real embryos, NCC invasion occurs in 12-24 hours depending on the temperature. For the successful models (time to invasion 24 hours or less), we also compare the time to invasion to suggest which models exhibit invasion in the shortest time period.

In chick, we analyse the number of cases in which invasion occurs in 24 hours or less and compare the likelihood of stream breakage for different models. We also take into account time to invasion for different models that exhibit successful invasion in 24 hours or

less.

4.6 Modelling Xenopus cranial neural crest cell invasion

We start with an investigation of Xenopus cranial NCC invasion. Figure 4.6(a) demonstrates the initial configuration of cells based on the Xenopus model (Woods et al., 2014) and Figure 4.6(c) is an example of successful invasion. It is not the purpose of our model to capture the detailed mechanisms inducing cell movement and cell-cell forces, therefore, we choose the sets of model parameters, namely: bias, β, diffusion constant, D, and interaction strength parameter, ϵ, to replicate a wide range of behaviours rather than the precise biology. For the models with no bias, we vary the diffusion constant ($D = [1, 4, 7, 10, 13]$) and the interaction strength parameter ($\epsilon = [1, 50, 100, 150, 200]$). Figure 4.11 shows how the forces for the repulsion-only, and the attraction and repulsion models vary for different values of the interaction strength parameter, ϵ. For the models with bias, in addition to the diffusion constant and the interaction strength parameter, we vary the bias ($\beta = [0.1, 0.4, 0.7, 1.0, 1.3]$).



(a) Repulsion-only.

(b) Attraction and repulsion.

Figure 4.11: Forces (Equation (4.4)) for (a) the repulsion-only and (b) the attraction and repulsion models. For the repulsion-only model, when the interaction strength parameter ϵ is increased, the repulsion force increases for fixed distance between cells. For the attraction and repulsion model, when the interaction strength parameter ϵ is increased, the attraction force increases for fixed distance between cells.

4.6.1 Xenopus: results

Table 4.4 demonstrates the percentage values of simulations with successful invasion in 24 hours or less for the different models and parameter values. The models with all cells biased are the only ones that exhibit successful invasion in 24 hours. We now explain why that is the case.

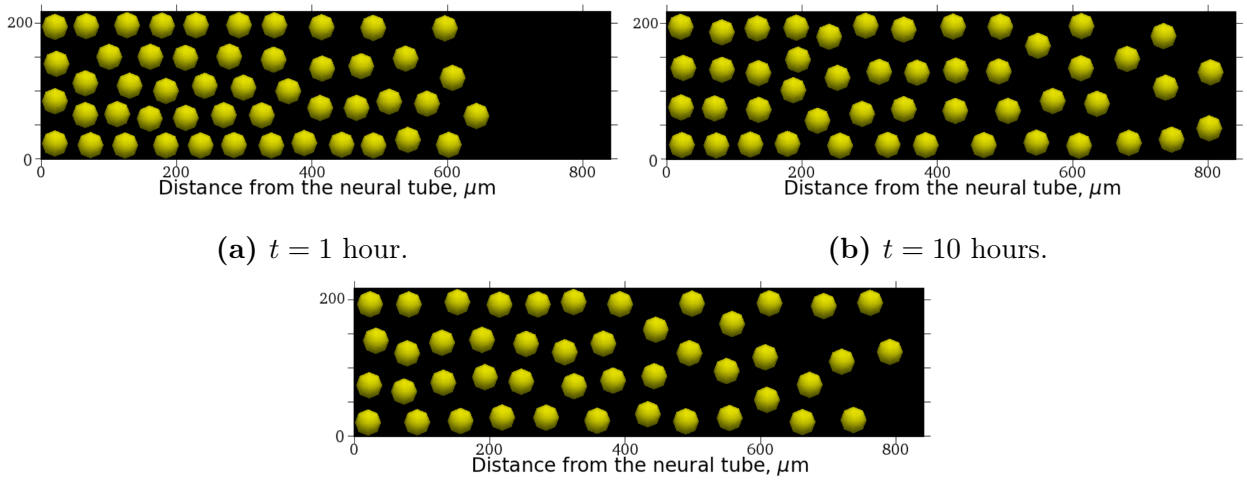
Model \ Fixed	β (= 0.0 if no bias, 0.7 if biased), %	D (= 7), %	ϵ (= 100), %	Average, %
Repulsion-only	0	–	–	0
Attraction and repulsion	0	–	–	0
Attraction and repulsion with biased leaders	0	0	0	0
Repulsion-only with all cells biased	81	56	56	64
Attraction and repulsion with all cells biased	99	60	60	73

Table 4.4: Percentage of simulations with successful invasion in Xenopus in 24 hours or less for different models and parameter values. Successful invasion is only likely when all cells are biased, and most likely when attractive forces are included. Each entry, apart from the average column, correspond to averages of 2500 simulations ($5 \times 5 \times 100$). We run one hundred simulations for each set of parameters (when β is fixed, we vary $D = [1, 4, 7, 10, 13]$ and $\epsilon = [1, 50, 100, 150, 200]$; when D is fixed, we vary $\beta = [0.1, 0.4, 0.7, 1.0, 1.3]$ and $\epsilon = [1, 50, 100, 150, 200]$; when ϵ is fixed, we vary $D = [1, 4, 7, 10, 13]$ and $\beta = [0.1, 0.4, 0.7, 1.0, 1.3]$). For the models with no bias, we only vary the diffusion constant and the interaction strength parameter. The results for each individual parameter set are provided in Appendix D.1. The column labelled "Average" records the average percentage of the simulations with successful invasion in 24 hours or less for all the parameter values.

Xenopus: repulsion-only

If the cells only repel each other and there is no external guidance cue, $\beta = 0$, we find that successful invasion is not possible in Xenopus. Figure 4.12 is a typical example output for this model, showing that the cells disperse and do not travel forward as a group,

and so they do not reach the target as a coherent group. For other parameter values, the dispersion occurs either slower or faster but the cells fail to invade in all the cases.



(a) $t = 1$ hour.

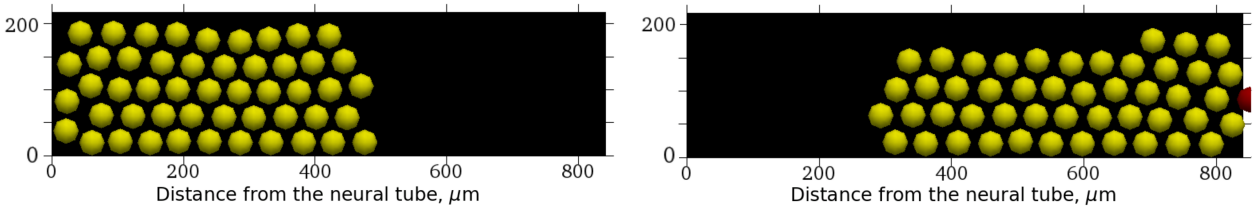
(b) $t = 10$ hours.

(c) $t = 24$ hours.

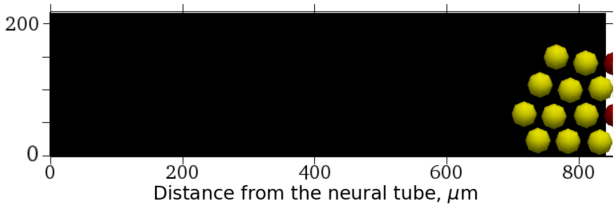
Figure 4.12: Snapshots from the repulsion only model of Xenopus. $D = 4$, $\epsilon = 200$. NCCs spread throughout the domain but fail to invade as a coherent group. Yellow circles are NCCs still in the migratory domain. The black background represents the migratory domain.

Xenopus: attraction and repulsion

When we add attractive forces at longer distances than the repulsive forces (still no bias), it is possible to observe successful invasion, however, it takes longer than 24 hours (for example, see Figure 4.13 with invasion in 40 hours). In most cases, the cells get stuck and do not invade the domain even after 50 hours (Figure 4.14). Therefore, simple attraction and repulsion forces are not sufficient to induce persistent cluster movement in a certain direction.

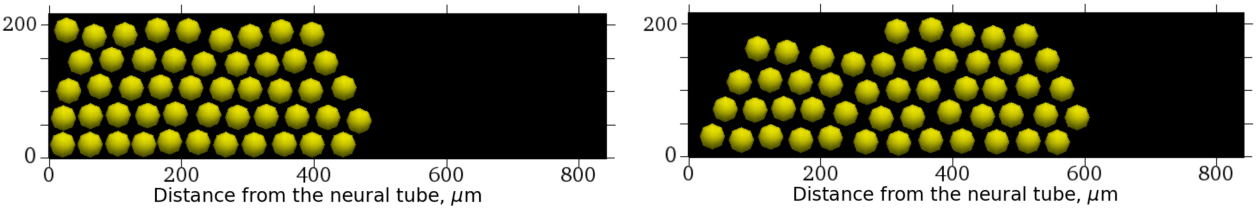


(a) $t = 1$ hour. **(b)** $t = 18$ hours.

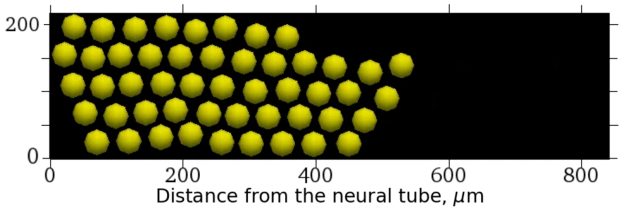


(c) $t = 40$ hours.

Figure 4.13: Snapshots from the attraction and repulsion model of Xenopus. $D = 4$, $\epsilon = 200$. NCCs invade the domain at 40 hours. Yellow circles are NCCs in the migratory domain and red circles are the NCCs that have already reached the target. The black background represents the migratory domain.



(a) $t = 1$ hour. **(b)** $t = 10$ hours.



(c) $t = 50$ hours.

Figure 4.14: Snapshots from the attraction and repulsion model of Xenopus. $D = 4$, $\epsilon = 200$. NCCs are stuck and do not invade the domain even after 50 hours. Yellow circles are NCCs in the migratory domain. The black background represents the migratory domain.

Xenopus: attraction and repulsion with biased leaders

Introduction of biased leaders does not give rise to successful invasion in 24 hours or less (Table 4.4). Similarly to the attraction and repulsion models with no bias, there are some cases with successful invasion after more than 24 hours when bias for the leaders is introduced (results not shown). However, extra guidance by the bias for leaders is not sufficient to induce the whole cluster to move to the branchial arches in a biologically realistic time period.

Xenopus: bias for all cells

Here we summarise the results for the models with all cells biased, with either only repulsive forces or a combination of attractive and repulsive forces. It is intuitive that if we introduce bias for all cells then, if the bias is sufficiently large, the cells will invade the domain. In Table 4.4 we observe that invasion does not always occur in 24 hours when the bias, β, is small ($\beta = 0.1, 0.4$, Appendix Tables D1 and D2). For the same parameter values, there are more cases with successful invasion in 24 hours or less for the attraction and repulsion model than for the repulsion-only model (Table 4.4, compare Appendix Tables D1 and D2). We reason that attractive forces help the cells to stay in a cluster facilitating collective invasion.

To see the difference between the repulsion-only model and the attraction and repulsion model, it is interesting to compare time to invasion for different parameter values (Appendix Figures D.1 and D.2). Figure 4.15 demonstrates that for a small bias, the cells invade more quickly for the attraction and repulsion model, whereas high repulsive forces lead to the longest time to invasion. For large bias, the time to invasion is similar for different models because the bias dominates the dynamics.

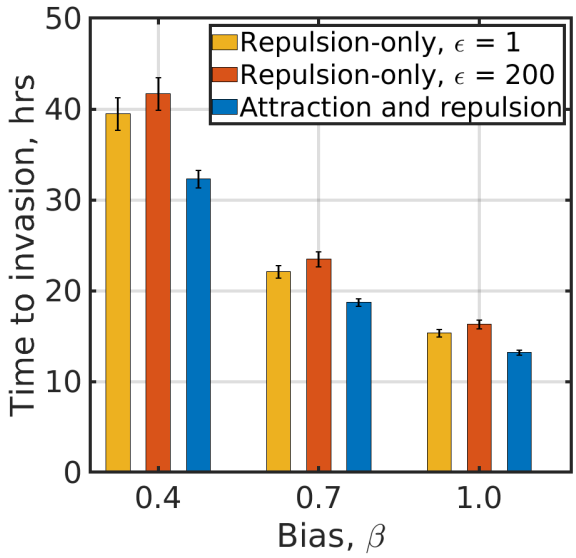


Figure 4.15: Time to invasion for different models, averaged over one hundred simulations. Error bars represent standard deviation. Repulsion-only, $\epsilon = 1$: repulsive forces (repulsion-only potential in Equation (4.6)) with $D = 7$; Repulsion-only, $\epsilon = 200$: repulsive forces (repulsion-only potential in Equation (4.6)) with $D = 7$; Attraction and repulsion model: attractive and repulsive forces (attraction and repulsion potential in Equation (4.5)) with $D = 7$, $\epsilon = 200$. Successful invasion is defined as 80% of cells reaching the target boundary.

4.6.2 Xenopus: conclusions

In the above study, we have used our simple, abstract model to extract the key mechanisms required for successful invasion in Xenopus, and our findings agree with other detailed models in the literature: for example, the Woods et al. (2014) model demonstrated the importance of the interplay between the two complementary mechanisms, CiL and co-attraction, in successful invasion. More specifically, from the investigations above we conclude that we can rule out a few models for Xenopus cranial NCC invasion. For example, the repulsion-only model with no bias cannot drive invasion in Xenopus because the cells simply disperse rather than migrate through the domain in a coherent fashion. In addition, the attraction and repulsion model with no bias, or bias only for leaders (defined in Section 4.4),

does not result in successful invasion on biologically realistic time scales. Therefore, bias for all cells is crucial in our modelling framework to ensure that the cells invade the domain on biologically realistic time scales. At first glance, this result might sound surprising because previous models suggest that attractive and repulsive forces are sufficient to ensure successful invasion (Woods et al., 2014). However, as we mentioned earlier, Woods et al. (2014) assumed that there is a non-negligible inertia for the cells, which could produce persistent directionality (bias).

We have also investigated the efficiency of invasion for different parameter regimes by comparing time to invasion. The repulsion-only model is less efficient than the attraction and repulsion model for all the parameter values we studied. Moreover, an increase in force strength leads to an increase in time to invasion for the repulsion-only model, whereas for the attraction and repulsion model, there is a small decrease in time to invasion for higher forces.

In conclusion, we find that our simple, abstract model still manages to identify the key necessary ingredients for efficient successful invasion in Xenopus cranial NCCs, namely, attraction, repulsion and directional bias.

4.7 Modelling chick cranial neural crest cell invasion

We now explore what mechanisms are crucial for successful invasion in chick. The main changes to the Xenopus model above include a different cell radius, domain length (growing vs fixed), domain width, (initial) number of cells, final configuration and time to invasion (Tables 4.1, 4.2). We implement the simple uniform-in-space domain growth profile inferred from experimental data (Figure 2.4) rather than the NCC-induced profile, identified in Chapter 3, due to the lack of detailed experimental data on non-uniform domain growth profiles. Chick cranial NCCs are smaller (chick cell radius – 7.5μm, Xenopus cell radius –

20.0μm) and in the models for chick, the domain is narrower in the y-direction (120μm in chick and 217μm in Xenopus) and growing in the x-direction. In the models for Xenopus, fifty cells are initially placed on the left-hand side of the domain and there is no influx of cells, whereas in chick, initially, there are no cells, but there is a constant influx of cells from the left-hand side boundary (Figure 4.3). Modellers of Xenopus define invasion as 80% of cells leaving the domain and they study the time to invasion. In chick, the simulations are run for 24 hours and successful invasion is considered if the cells reach the end of the domain in 24 hours or less (more than five cells in the final 100μm of the domain) with no stream breakage.

In the Lennard-Jones potential model, the force strength depends not only on ϵ, but also on cell radius. To rescale for the force strength from Xenopus cells, of radius 20μm, to chick cells, of radius 7.5μm, we therefore must choose different values of ϵ (rescale ϵ by σ_2/σ_1 where $\sigma_1 = 40\mu$m is the Xenopus cell diameter and $\sigma_2 = 15\mu$m is the chick cell diameter). So we consider the interaction strength parameter values $\epsilon = [0.4, 19.0, 38.0, 56.0, 75.0]$. We consider the same diffusion constant and bias values as in Xenopus, namely $D = [1, 4, 7, 10, 13]$ and $\beta = [0.1, 0.4, 0.7, 1.0, 1.3]$.

4.7.1 Chick: results

We recall that successful invasion in chick is verified by two criteria: NCCs invade the domain and there is no stream breakage. We separately consider the data for these two criteria. Table 4.5 shows the percentage values of simulations with invasion for different models and parameter values. In contrast to the Xenopus models (Table 4.4), bias for all cells is not necessary to ensure invasion for chick. For example, in around 30% of simulations for the repulsion-only model invasion occurs in less than 24 hours. Table 4.6 demonstrates that stream breakage occurs in more than 20% of the simulations in the model with biased leaders and more than 5% in the attraction and repulsion model with all cells biased. In the

following sections we explain the results observed in Tables 4.5 and 4.6 in greater detail.

Model \ Fixed	β (= 0.0 if no bias, 0.4 if biased), %	D (= 7), %	ϵ (= 100), %	Average, %
Repulsion-only	33.48	–	–	33.48
Attraction and repulsion	4.12	–	–	4.12
Attraction and repulsion with biased leaders	19.48	4.92	24.96	16.45
Repulsion-only with all cells biased	100	93.56	91.56	95.04
Attraction and repulsion with all cells biased	89.24	80.00	81.40	83.55

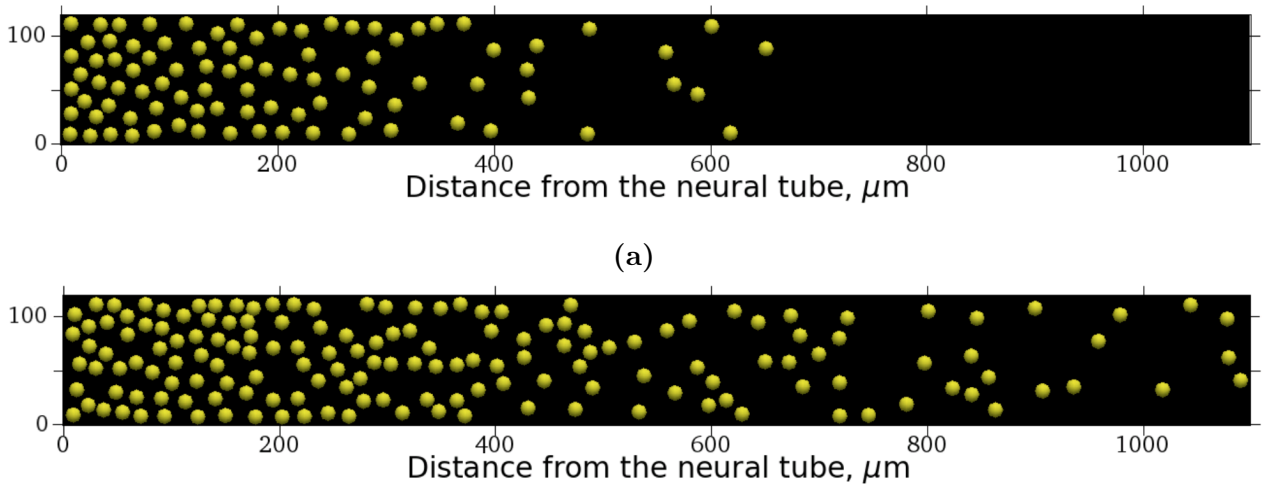
Table 4.5: Percentage of simulations with invasion in chick in 24 hours or less for different models and parameter values. We observe that invasion is most likely when all cells are biased, and when only repulsive forces are included. Each entry, apart from the average column, corresponds to an average of 2500 simulations ($5 \times 5 \times 100$). We run one hundred simulations for each set of parameters (when β is fixed, we vary $D = [1, 4, 7, 10, 13]$ and $\epsilon = [0.4, 19.0, 38.0, 56.0, 75.0]$, note that we fix $\beta = 0.4$ and not $\beta = 0.7$ as in Xenopus because this value allows us to observe more clearly the effect of changes in D and ϵ; if D is fixed, we vary $\beta = [0.1, 0.4, 0.7, 1.0, 1.3]$ and $\epsilon = [0.4, 19.0, 38.0, 56.0, 75.0]$; if ϵ is fixed, we vary $D = [1, 4, 7, 10, 13]$ and $\beta = [0.1, 0.4, 0.7, 1.0, 1.3]$). For the models with no bias, we only vary the diffusion constant and the interaction strength parameter. The results for each individual parameter set are provided in Appendix E.1, Tables E2-E5. The column labelled "Average" records the average percentage of the simulations with invasion in 24 hours or less for all the parameter values.

Model \ Fixed	β (= 0.0 if no bias, 0.4 if biased), %	D (= 7), %	ϵ (= 100), %	Average, %
Repulsion-only	0.08	–	–	0.08
Attraction and repulsion	0.20	–	–	0.20
Attraction and repulsion with biased leaders	12.84	27.64	30.56	23.68
Repulsion-only with all cells biased	1.48	4.16	0.60	2.08
Attraction and repulsion with all cells biased	4.40	8.96	6.44	6.60

Table 4.6: Percentage of simulations at 24 hours or at the time of invasion (if invasion occurs in less than 24 hours) that exhibit stream breakage in chick for different models and parameter values. We observe that stream breakage is most likely when leaders are biased. In the models with all cells biased, stream breakage is more likely for the attraction and repulsion model rather than for the repulsion-only model. Each entry, apart from the average column, corresponds to an average of 2500 simulations ($5 \times 5 \times 100$). We run one hundred simulations for each set of parameters (when β is fixed, we vary $D = [1, 4, 7, 10, 13]$ and $\epsilon = [0.4, 19.0, 38.0, 56.0, 75.0]$; when D is fixed, we vary $\beta = [0.1, 0.4, 0.7, 1.0, 1.3]$ and $\epsilon = [0.4, 19.0, 38.0, 56.0, 75.0]$; when ϵ is fixed, we vary $D = [1, 4, 7, 10, 13]$ and $\beta = [0.1, 0.4, 0.7, 1.0, 1.3]$). For the models with no bias, we only vary the diffusion constant and the interaction strength parameter. The results for each individual parameter set are provided in Appendix E.2, Tables E7-E10. The column labelled "Average" records the average percentage of the simulations with stream breakage for all the parameter values.

Chick: repulsion-only

We begin with a simple repulsion-only model with no bias. Figure 4.16 shows examples of cell configurations in the repulsion-only model for different diffusion values. It can be seen that for a fixed force strength ($\epsilon = 19.0$ in this case), the diffusion constant has to be sufficiently large to ensure invasion (Appendix Table E1). We also find that the time to invasion is decreased for high values of the interaction strength parameter (Appendix Figure E.1). However, it is biologically unrealistic for invasion to occur significantly earlier than at 15 hours. In all the cases for the repulsion-only model, invasion occurred in less than 15 hours but since our study is more qualitative than quantitative we simply claim that small, rather than large, repulsive forces correspond to more realistic invasive profiles. We also recall that the time to invasion is regulated by the threshold value for the number of NCCs in the final 100μm segment of the domain in the x-direction (in our case it is five but for larger values, the time to invasion would obviously increase). We also find that stream breakage is not likely for the repulsion-only model (Appendix Table E6).



(a)

(b)

Figure 4.16: Snapshots of representative simulations of the repulsion-only model on a growing domain in chick after 24 hours. (a) $D = 3$, $\epsilon = 19.0$. (b) $D = 12$, $\epsilon = 19.0$. Yellow circles represent cells.

We conclude that the repulsion-only model can replicate successful NCC invasion in chick, with the limitation that invasion may occur unrealistically quickly, especially for strong repulsive forces.

Chick: attraction and repulsion

We next discuss the effect of the addition of attractive forces at longer distances than the repulsive ones (but still no bias). Figure 4.17 shows some typical examples for different parameter values. Figure 4.17(a) shows the results of a simulation for the case with strong forces ($\epsilon = 75.0$) which do not allow the cells to advance, whereas in Figure 4.17(c) the cells travel up to 1000μm due to strong diffusion ($D = 12$) and weak cell-cell forces ($\epsilon = 19.0$). For this model the only cases with invasion (Appendix Table E2) occur for large values of the diffusion constant and small values of the interaction strength parameter (Appendix Figure E.2). Therefore, we deduce that attractive forces hinder, rather than improve, invasion. Stream breakage is rarely observed because the cells are likely to remain in one cluster due to the attractive forces (Appendix Table E7).

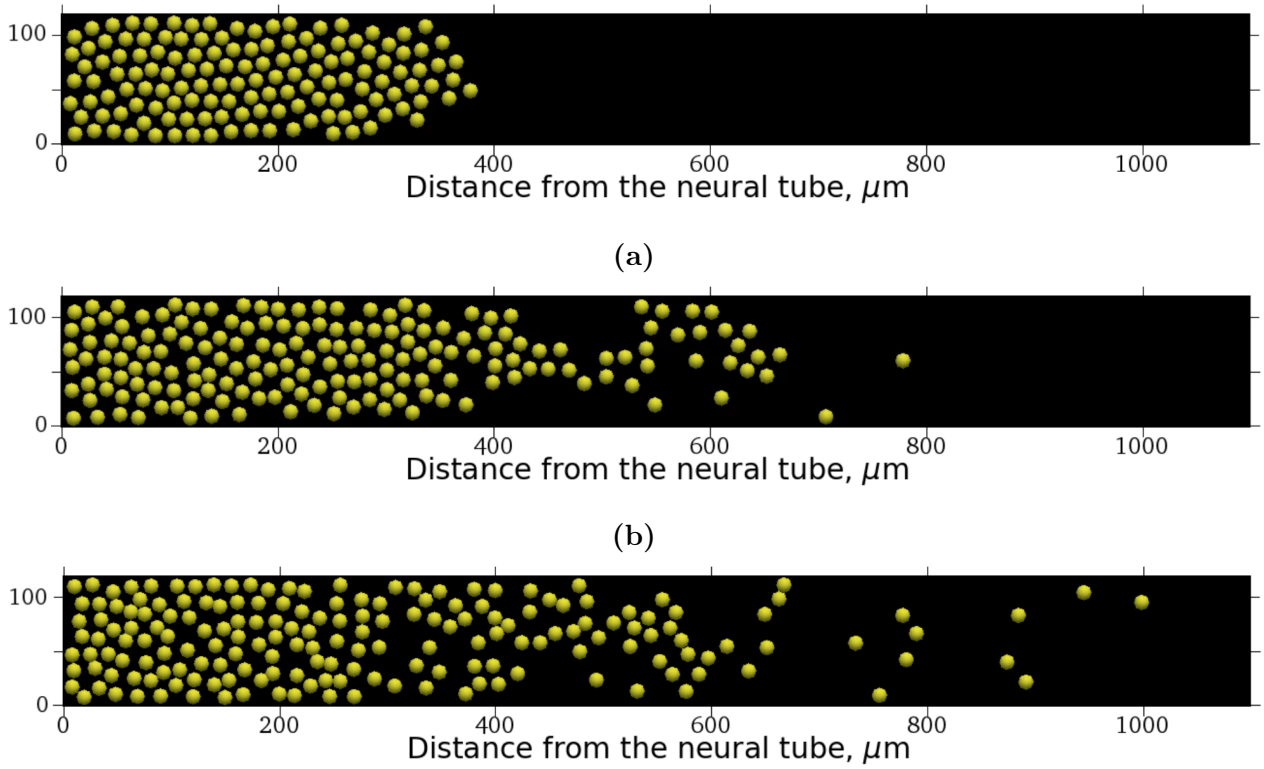


Figure 4.17: Snapshot of representative simulations of the attraction and repulsion model on a growing domain for chick after 24 hours. (a) $D = 6$, $\epsilon = 75.0$. (b) $D = 12$, $\epsilon = 75.0$. (c) $D = 12$, $\epsilon = 19.0$. Yellow circles represent cells.

To conclude, we find that attractive forces impede invasion. Therefore, the repulsion-only model is a better candidate to replicate successful invasion in chick than the attraction and repulsion model.

Chick: attraction and repulsion with biased leaders

Table 4.5 demonstrates that if a bias is introduced for leader cells, then there are more cases with invasion in 24 hours or less. Here, biased leaders can transmit their directional signal to other cells due to cell-cell attractive forces. However, this successful communication does not happen very frequently (Appendix Table E3). In many cases, we observe that

either leaders are too strongly attracted by other cells and they do not manage to advance sufficiently quickly (Figure 4.18(a)), or they move away too quickly and the stream breaks (Figure 4.18(b)). This behaviour leads to, on average, more than a 20% likelihood of stream breakage (Appendix Table E8 lists the parameter values for which stream breakage is most likely). These results suggest that for successful invasion we may need to consider a model in which the interactions between leaders and followers are asymmetric.

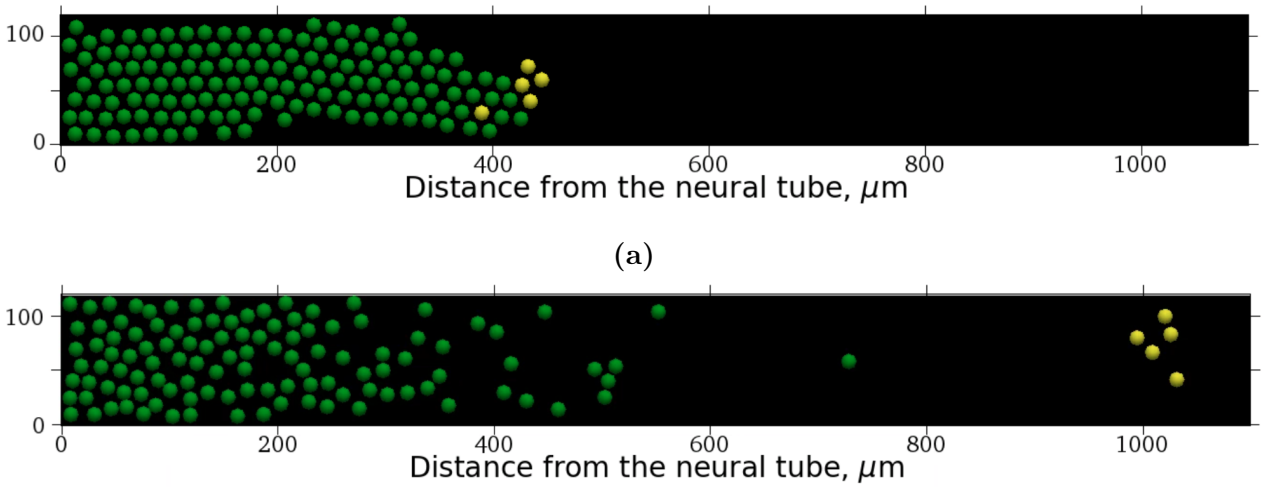


Figure 4.18: Snapshots of the simulations of the attraction and repulsion model for chick with bias for leaders after 24 hours. (a) $D = 4$, $\epsilon = 75.0$, the cells do not advance even though leaders are biased ($\beta = 0.4$ for leaders). (b) $D = 7$, $\epsilon = 19.0$, the stream breaks ($\beta = 0.4$ for leaders). Yellow circles represent leader cells and green circles represent follower cells.

We conclude that the addition of bias for leaders improves cell invasive abilities for the attraction and repulsion model. However, our results suggest that the forces between leaders and other cells are probably not symmetric.

Chick: bias for all cells

Invasion happens in most of the cases when bias is introduced for all cells (Table 4.5). On average, there are more than 10% fewer cases of invasion if the attraction and

repulsion model is used instead of the repulsion-only model. An increase in the interaction strength parameter increases the number of cases with invasion when the repulsion-only model is used (Appendix Table E4), whereas an increase in the interaction strength parameter for the attraction and repulsion model leads to a decrease in the number of cases with invasion (Appendix Table E5). For all parameter values tested, stream breakage occurs only in around 2% of the cases for the repulsion-only model with all cells biased (Appendix Table E9). However, for the attraction and repulsion model with all cells biased, the percentage of cases exhibiting stream breakage is on average around 7% (Appendix Table E10). This increase in stream breakage percentage in comparison with the repulsion-only model is due to the higher probability of cluster formation caused by strong attractive forces.

For the cases with invasion in 24 hours or less, the actual time to invasion is, in most cases, much smaller than 24 hours (Appendix Figures E.4 and E.5). The dynamics occur on a growing domain, so the cells frequently invade the, initially short, domain very early during migration. This is a drawback of this modelling framework. However, as we mentioned earlier, time to invasion is regulated by the threshold value of the number of cells in the final 100μm segment of the domain in the x-direction, so if we chose a higher threshold value, then the time to invasion would increase. In addition, the focus of this study is a qualitative comparison of different migration mechanisms in chick and Xenopus[1]. Nevertheless, larger values of time to invasion are more biologically realistic, therefore, we conclude that small forces in the repulsion-only model and large forces in the attraction and repulsion model lead to the most biologically realistic invasion scenarios (Appendix Figures E.4 and E.5).

To conclude, the models with all cells biased ensure a high percentage of simulations with invasion in 24 hours or less for a range of different parameter values. Invasion occurs quickest for the repulsion-only models with strong forces. However, rapid invasion is not observed in chick – the cells only invade the domain within the timespan of 15-24 hours.

[1] A more detailed parameter space investigation might allow us to find parameter values for which invasion could occur exactly at the right time, but this is not the focus of this study.

We suggest that only a very small bias for all cells would be required for the repulsion-only model (with weak forces) to replicate chick NCC invasion. Large forces in the attraction and repulsion model could also ensure invasion on a realistic timescale but, for these models, the likelihood of stream breakage is higher than for the repulsion-only models.

4.7.2 Chick: conclusions

From the above investigation of the behaviour of different models within the Lennard-Jones modelling framework for chick cranial NCCs, we suggest that the repulsion-only model is the best candidate to replicate experimental findings. Small repulsive forces would have to be carefully tuned to ensure that invasion occurs at the right time. A small bias could be added to help regulate time to invasion. For stronger forces, invasion occurs too quickly.

The attraction and repulsion model, as well as the attraction and repulsion model with bias for leaders only, are both not suitable to replicate successful invasion in chick. The cells only invade the domain if the force strength is so small that the attractive force is almost negligible. In all other cases, the cells simply do not invade the domain sufficiently fast and an increase in the strength of force only impairs invasion. There is also a non-negligible likelihood of stream breakage in the model with biased leaders. Therefore, the addition of attractive forces does not help to mimic invasion in chick. The introduction of bias for leaders does not ensure successful NCC invasion, so we suggest that it is unlikely that the interactive forces are symmetric, and distinctions between different cell types and their interactions have to be carefully investigated in the future.

The introduction of bias for all cells initially seemed to be a safe choice to ensure that NCCs invade the domain in chick. However, in these models, invasion is likely to occur too quickly, in particular for large values of bias. As mentioned earlier, small bias may be tuned with small repulsive forces to ensure a biologically realistic time to invasion. For the attraction and repulsion model, large, rather than small, forces make the model more likely

to replicate collective cell invasion but, due to the attractive forces, there is a higher chance of stream breakage in comparison with the repulsion-only model.

How do these results relate to previous findings?

It is rather surprising that the repulsion-only model was the best candidate to replicate chick cranial NCC invasion because in Chapters 2 and 3 we used a completely different leader-follower model. In that framework, leaders that move up the gradient of chemoattractant guide the followers behind them, either by contact or by tunnelling. The model that we used in this chapter is too simplistic to include all of these subtle features. As such, we are not suggesting the repulsion-only model as a replacement model to explain the collective NCC invasion in chick. However, since the exact cell-cell interaction mechanisms in chick are unknown, we suggest two alternative mechanisms that can replicate chick NCC invasion. We could classify these mechanisms as follows: the leader-follower model in Chapters 2 and 3 could be considered as a "pulling" mechanism, whereas the repulsion-only model corresponds to a "pushing" mechanism.

The possibility of having these two alternative cell-cell interaction mechanisms to explain collective cell invasion reminds us of the ongoing debate as to whether pulling or pushing is the key guidance mechanism in angiogenesis (Tonnesen et al., 2000; Palm et al., 2016). It is difficult to distinguish from experimental data whether the cells are pushed from behind or pulled from ahead, and both mechanisms might be involved. Since the focus of this chapter is to compare chick and Xenopus NCC migration, we continue the discussion on the chick cell-cell interactions and provide a preliminary study in Section 5.2.

4.8 Comparison of the modelling results for Xenopus and chick

In this section we compare and discuss the results for Xenopus and chick NCC invasion under the different modelling frameworks we have explored. Xenopus cranial NCCs travel in a cluster and the optimal migration of that cluster, in the framework of Lennard-Jones potential models, is achieved when attractive and repulsive forces keep the cells in a cluster and there is a bias in cell movement. In chick, there is a constant influx of NCCs and they travel on a growing domain, so repulsive forces help the cells to be pushed forward by cells entering the domain, and domain growth contributes to further advection of the cells. We note that the constant influx of cells, domain growth, and final configuration of cells are the key differences between Xenopus and chick cranial NCCs, and we discuss the importance of these features in the rest of this section.

Cranial NCCs distribute all along the domain (see, for example, the NCC streams in the Xenopus embryo in Figure 4.19) and then contribute to different tissues. For example, NCCs contributing to cranial ganglia stop in a relatively dorsal position, while NCCs forming cartilages and bones of the face will continue further ventrally and invade the branchial arches (Theveneau and Mayor, 2012). Therefore, the modelling of a cluster of cells travelling and leaving the domain in Xenopus is only a modelling assumption and simplification of the biological system (Woods et al., 2014). In chick, the modelling assumption of cells moving as streams is a more accurate representation of the biology. This means that if, in Xenopus, we did not aim to have a travelling cluster but, instead, a spreading out of the cells and formation of streams, then the repulsion-only model, suitable for the chick, would also be suitable for Xenopus (Figure 4.12).

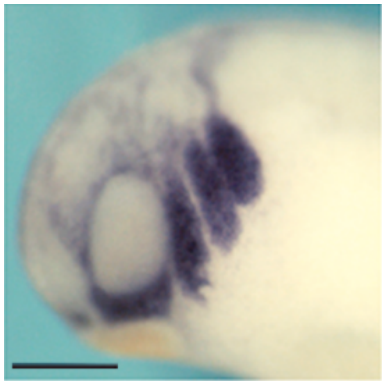


Figure 4.19: Cranial NCCs form streams in Xenopus embryos. Lateral view of a Xenopus embryo with the cranial NCC marker twist at stage 25. Dark streams correspond to NCCs. The scale bar is 200μm. Figure reproduced from Huang et al. (2016) with permission from Elsevier.

Another two key differences between Xenopus and chick entail constant influx of cells and domain growth. To understand the importance of these features, we investigate the dynamics of chick cranial NCCs in their absence. Figure 4.20(b) represents the final configuration of NCCs when we assume that there is constant cell influx, which we define by an attempt to insert a new cell every time step, but the domain length is fixed. Figure 4.20(c) represents the scenario in which the domain is growing but there is limited cell influx, i.e. we assume that the constant influx of cells ceases after 50 cells are in the domain, whereas Figure 4.20(d) depicts the scenario under which the rate of influx is reduced to ensure that around 50 cells are in the domain after 24 hours. We consider these two different ways to model influx reduction to separate the effects of population pressure and cell density. The most evident difference occurs when the domain does not grow (compare Figure 4.20(a) and (b)) with the cells travelling about half the distance in the absence of growth compared to when there is growth. If the rate of cell influx is not reduced, but ceases when 50 cells are in the domain, then invasion is similar to the control case with evidently smaller cell density (compare Figure 4.20(a) and (c)), whereas if the rate is reduced, then the cells invaded the domain to a significantly lesser extent than in the control case (compare Figure 4.20(a) and

(d)). We observe the same tendencies for different parameter values (varying D and ϵ) and the attraction and repulsion model (results not shown). These results imply that domain growth plays an important role in enabling chick cranial NCCs to invade the domain. Cell-cell interactions also play an important role because it is advantageous if the cells constantly enter the domain and, by repelling each other, move forward, in comparison with the case when the entry rate is lower and there is less population pressure. The constant influx of cells into the domain ensures a higher density of cells, which is similar to the presence of a group of cells already in the domain, as in the case of Xenopus. Therefore, we conclude that high cell density close to the neural tube is likely to be a conserved and significant feature across different species.

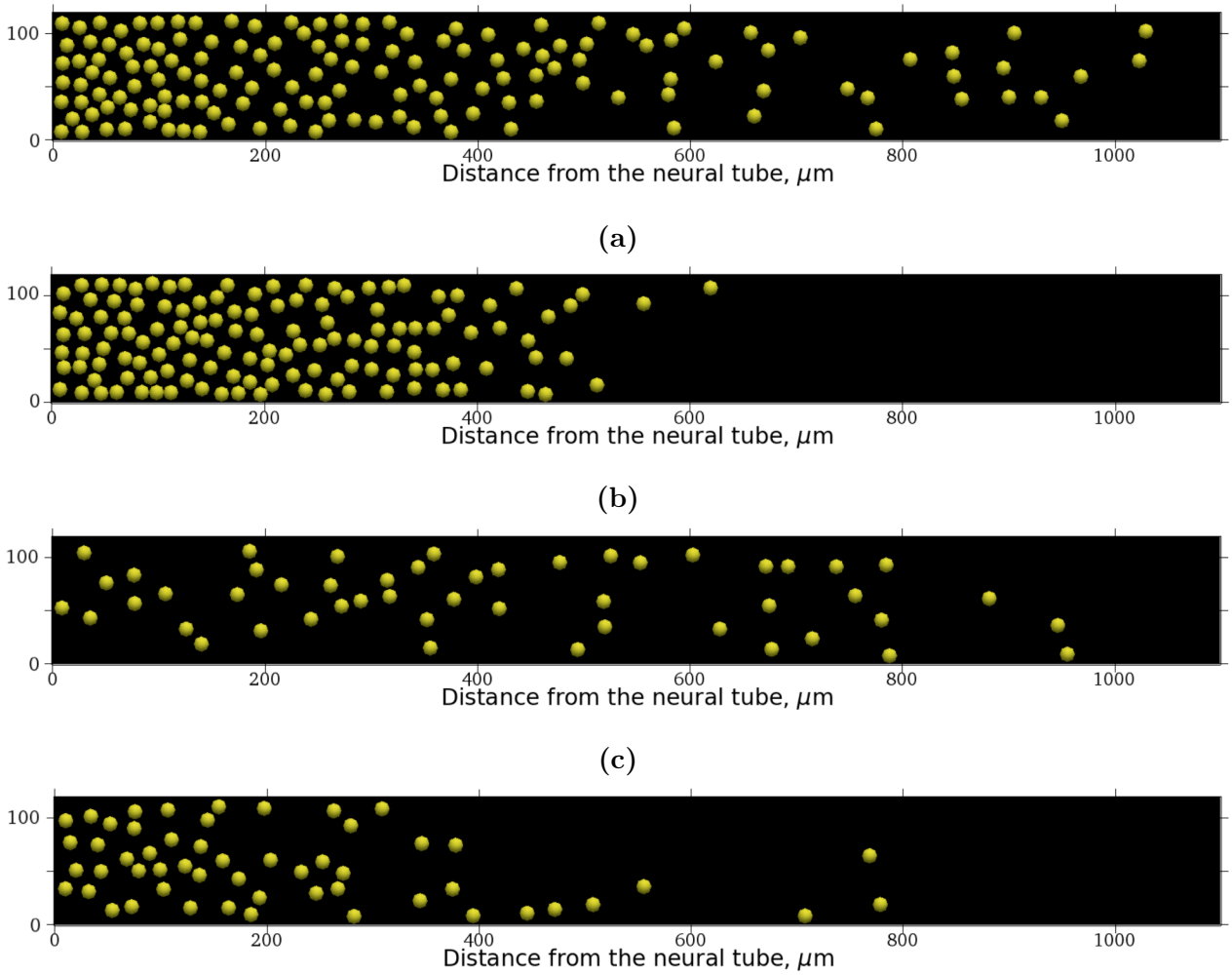


Figure 4.20: Snapshots of representative simulations of the repulsion-only model for chick after 24 hours. $D = 12$, $\epsilon = 19.0$. Yellow circles represent cells. (a) Control case: growing domain and constant cell influx. (b) Fixed domain and constant cell influx. (c) Growing domain with only 50 cells entering the domain. (d) Growing domain, the influx rate is reduced from the control case so that around 50 cells are in the domain after 24 hours (a new cell attempts to enter the domain every 9 min, resulting in 54 cells at 24 hours).

4.9 Conclusions and discussion

In this chapter we developed an IBM with a Lennard-Jones potential to account for cell-cell interactions, to investigate and compare the key mechanisms that drive NCC collective invasion in Xenopus and chick. We included a set of simplified assumptions from the previous computational models for Xenopus and chick.

By exploring the dynamics of NCCs under a range of parameter values, we discovered that in Xenopus, bias for all cells is required to ensure successful invasion (defined by a cluster of cells reaching the branchial arches). The model with attractive and repulsive forces provides more efficient (quicker) invasion than the model with repulsive forces only. In chick, we identified that the repulsion-only model replicates NCC invasion (the cells reach the end of the domain and there is no stream breakage) in the most realistic way.

We identified that differences in the definitions of successful invasion in Xenopus and chick explain why attractive forces facilitate migration in Xenopus but impede it in chick. In all embryos, NCCs are known to form streams before they start differentiating. Therefore, if the assumptions are consistent, namely successful invasion in Xenopus is defined as in chick (the cells reach the end of the domain and there is no stream breakage), then the repulsion-only model would also replicate Xenopus NCC invasion.

Furthermore, we identified that domain growth and constant influx of cells facilitate NCC invasion in chick. The dynamics of chick NCCs occur on a growing domain, whereas in Xenopus the domain is fixed, and the final length of the domain in chick is much longer than in Xenopus. We demonstrated that advection by the growth of the domain in chick is crucial in enabling cells to reach the end of the domain in a realistic time period. The influx of cells also helps invasion by inducing population pressure, especially at the start of invasion, which is similar to the initial cluster of densely packed cells in Xenopus. We conclude that external features of the NCC system, such as advection by domain growth and the influx of cells, help to ensure the robustness of collective cell invasion.

In this chapter, we also obtained the unexpected result that chick cranial NCC invasion can be achieved with the repulsion-only model, which is a pushing, rather than a pulling, mechanism (used in Chapters 2 and 3). We emphasise that the repulsion-only mechanism is a simplification of the interactions involved in the process of NCC migration and we do not attempt to negate the strong evidence of the role of a chemoattractant in the migration of the chick cranial NCCs (McLennan et al., 2010). However, it is important to investigate why we can obtain successful invasion using these two completely different mechanisms. We dedicate a short part of Chapter 5 to investigating this question using previous chick perturbation experiments (McLennan et al., 2012) and the modelling framework developed in this chapter.

To summarise, in this chapter, we conducted the first theoretical study (to our knowledge) which compares chick and Xenopus cranial NCC invasion. We elucidated the reasons why previous computational models may have reached different conclusions for the key mechanisms that drive invasion in different organisms, and we provided some general conclusions as to how simple model features, such as attractive and repulsive cell-cell forces and domain growth, affect collective cell migration.

Chapter 5

Discussion and future work

In this thesis we have provided insights into collective NCC migration using computational modelling techniques coupled with experimental work carried out by our collaborators. We focused on two different modelling frameworks to tackle various biological questions. Using a hybrid IBM incorporating a number of key ingredients of the biology, we investigated the roles of AQP-1, cell confinement and spatially non-uniform domain growth on the dynamics of chick cranial NCC invasion. Then, we used a more high-level abstract model to carry out the first study to identify the differences and similarities of NCC migration across two different species, namely chick and Xenopus. By doing so, we have answered a number of biological questions on the collective migration of NCCs and raised new questions for future research.

This chapter is organised as follows: in Section 5.1 we summarise the key results obtained in this thesis. We provide a preliminary study on the role of repulsive cues in collective chick NCC migration and discuss other areas of future work in the field of collective NCC migration in Section 5.2.

5.1 Summary

In Chapter 2, we extended and modified the cranial NCC invasion model of McLennan et al. (2012, 2015a,b, 2017) to investigate the role of the AQP-1 water channel protein in light of new experimental results. After a review of experimental findings, we considered and, if needed, incorporated into our model the key features shown to be affected by AQP-1, namely NCC speed, filopodium stabilisation, filopodium polarisation, filopodia number and ECM degradation, and used simulations to compare and contrast their effects. We identified that increased NCC speed, stabilised filopodia and enhanced ECM degradation are key features that contribute to the successful invasion of NCCs. In the second part of Chapter 2, inspired by the possible role of the cell inhibitory gene DAN in confining cell movement (McLennan et al., 2017), we investigated how the confinement of the NCC stream was regulated by the extent of the imposed internal confinement boundary. We demonstrated that a partial internal confinement boundary is sufficient to ensure that the NCC stream remains confined in a narrow corridor. We also found that cell tunnelling through the ECM facilitates cell confinement, suggesting that the ECM may also contribute to cell confinement. Thus, in this chapter we have improved our understanding of how directional guidance cues, namely AQP-1 and an imposed confinement boundary, facilitate collective cell migration.

We continued in Chapter 3 with investigation of the impact of spatially non-uniform domain growth on the migration of NCCs. The assumption of spatially uniform domain growth used in the literature, and Chapter 2, was relaxed to take into account new experimental findings which suggest that the growth is spatially non-uniform. We reformulated the equation for the chemoattractant (VEGF) concentration to account for spatially non-uniform growth. Due to the fact that it is not clear precisely how domain growth varies spatially, we investigated a number of simple domain growth profiles, namely splitting the domain into two parts and considering different domain growth rates in those parts. We found that these domain growth profiles affect cell invasive abilities by changing the extent of advection, and thus regulating the observed cell speed. We next tested the impact of domain growth

profiles that attempt to approximate the heterogeneous tissue growth profiles observed experimentally. We identified that cell speed has to be increased to ensure that the domain is fully invaded when experimentally observed non-uniform domain growth profiles are considered. However, we discovered that our current modelling framework does not replicate the results of perturbation experiments, namely those that involve physical ablation of NCCs and chemical inhibition of domain growth. To address these inconsistencies, we considered an NCC-induced domain growth profile. The model was constructed in such a way that we were able to replicate the results of the physical ablation of NCCs experiment. However, to replicate the results of the experiment in which chemical inhibition of domain growth is carried out, we needed not only to uniformly reduce the domain growth rate, but also to reduce NCC directionality. This result suggests a possible feedback mechanism between tissue growth and NCCs: NCCs induce domain growth, and they are directed and advected by domain growth. As such, this chapter has elucidated our understanding of how NCCs and tissue growth may interact and how this interaction may ensure robust NCC invasion. To push this work further, for example, to model mesodermal cells as discrete entities and explicitly include mesodermal-NCC interactions, would require more experimental data. Such data are challenging to acquire given currently available experimental and imaging methodologies.

In Chapter 4, we developed a high-level IBM framework that can account for different cell-cell interactions, namely a model incorporating a Lennard-Jones potential to model cell-cell repulsion and attraction, and a drift term to model directional bias. We used it to explore the differences between the mechanisms necessary for successful invasion in chick and Xenopus. We chose these model organisms because the current hypotheses as to what drives collective NCC invasion in Xenopus and chick are different, and there is an ongoing debate as to why that is the case. Using our single modelling framework, we found that Xenopus NCC invasion was most accurately replicated when we included a directional bias for all cells, and invasion was most efficient when both attractive and repulsive forces were included. In chick, however, bias led to an unrealistically short invasion time. We found, instead, that the repulsion-only model could replicate invasion in chick in the most realistic manner. To

explain these differences, we revisited the definitions of successful invasion and, based on experimental findings, we deduced that the cluster migration considered as the criterion for successful invasion in Xenopus appears to be a modelling assumption rather than an accurate representation of Xenopus NCC migration. Were this criterion changed to the coverage of the domain, as in chick, there would be no contradictions between the mechanisms required for successful invasion in different organisms. We also demonstrated how successful invasion in different organisms may be affected by environmental factors, such as domain growth and constant influx of cells. This comparative study is an example of how computational modelling can contribute to new insights into a biological debate when experimental comparison is not feasible. In this chapter, we have demonstrated how different modelling frameworks and assumptions may lead to different biological predictions, and how a single modelling framework should, ideally, be used to make a consistent comparison.

5.2 Future work

In this thesis we have tackled a number of questions concerning the migration of NCCs. However, many questions still remain to be answered and we discuss some of these in this section. Motivated by the results of Chapter 4, we start this section with a brief study of the role of repulsive forces in collective NCC migration in chick, and then proceed with short discussions on various other areas of future work.

What is the role of repulsive cues in collective neural crest cell migration?

In Chapter 4, we discovered that a repulsion-only mechanism can replicate successful invasion in chick. We postulated that pushing, caused by cell-cell repulsion, rather than pulling, caused by attraction from the cells ahead via chemical or mechanical guidance cues,

may explain collective NCC invasion in chick. This result is rather surprising because in the previous modelling frameworks for chick (McLennan et al., 2012, 2015a,b, 2017), including the one we used in Chapters 2 and 3, pulling was the key underlying mechanism.

Questions on the importance of cell pulling versus pushing are, to a large extent, also unanswered in other cell migration processes. For example, in angiogenesis, there is some evidence that in the formation of new blood vessels, tip (leader) cells pull stalk (follower) cells (Dallinga et al., 2015; Vaeyens et al., 2020) and the opposite, stalk cells push tip cells, also occurs (Palm et al., 2016). Migration of over-crowded groups of cells in developing epithelia and the spread of metastatic cancer cells have also been demonstrated to be driven by pulling and/or pushing (Marinari et al., 2012; Eisenhoffer et al., 2012; Yang et al., 2019; Chen et al., 2013). The fact that these two opposing mechanisms can explain collective cell invasion not only in NCCs, but also in other examples, makes our investigation even more relevant.

We now provide a preliminary study in which we consider a NCC ablation experiment (McLennan et al., 2012) to investigate whether the repulsion-only model can replicate NCC behaviour under this perturbation. This experiment was employed to verify the original model for chick NCC invasion (McLennan et al., 2012) but the model has since been revised due to the observation that there is only a small number of leader cells (McLennan et al., 2015a), so we explore how the predictions might change for the revised model, which we call the revised chemotaxis leader-follower model[1].

Experimental setting: the neural tube is removed from the embryo five hours after the start of NCC migration, thus preventing the entry of the rest of NCC population into the migratory domain.

Experimental observations: after 24 hours, NCCs distribute all along the migratory route (Figure 5.1).

[1]The revised chemotaxis leader-follower model is the same as McLennan et al.'s (2012) model, only with fewer leaders.

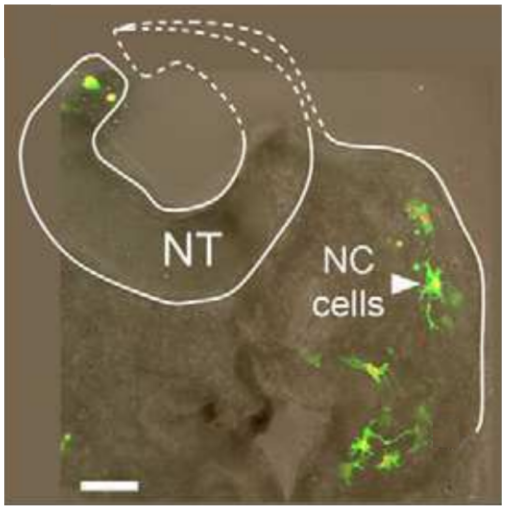


Figure 5.1: Transverse section of an embryo after ablation (dotted line). Representative image 24 hours into migration. NCCs distribute all along the migratory pathway. NT – neural tube, NC – neural crest. Scale bar is 50μm. Figure reproduced from McLennan et al. (2012) with permission from the Company of Biologists Limited.

Simulation method: we model the ablation of NCCs by no longer inserting new cells into the domain after five hours.

Revised leader-follower chemotaxis model prediction: the revised model predicts that NCCs do not spread out as experimentally observed but travel in a cluster (Figure 5.2). The prediction of this experiment for the original McLennan et al. (2012) model was consistent with the experimental observations because they used an assumption that after ablation only leader cells are in the domain. However, later studies have revealed that there is only a small number of leader cells (McLennan et al., 2015a). This new assumption explains why the original model could replicate the observations of the ablation experiment but the revised model, with a smaller number of leaders cells, cannot.

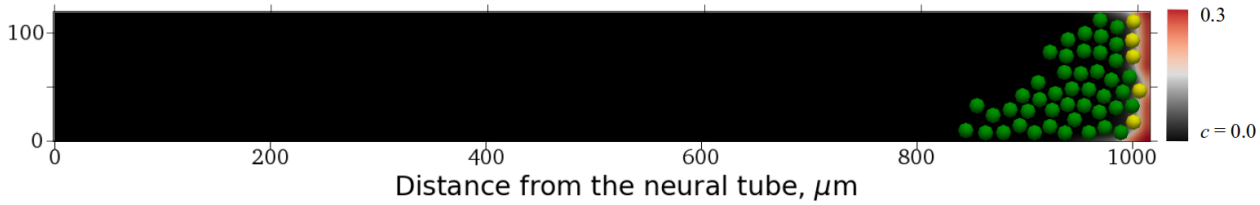


Figure 5.2: Snapshot of a representative simulation of the revised leader-follower chemotaxis model with cell ablation (influx of cells is stopped five hours into the simulation) for chick after 24 hours. NCCs invade the domain but they travel in a small cluster. This behaviour is not in agreement with the biological observations (Figure 5.1). Yellow circles represent leader cells, green circles represent follower cells, and c is the concentration of chemoattractant.

Repulsion-only model prediction: the model predicts that after ablation, the cells spread out after 24 hours (Figure 5.3). This result agrees qualitatively with the experimental observations. We conclude that the repulsion-only model can replicate this result.

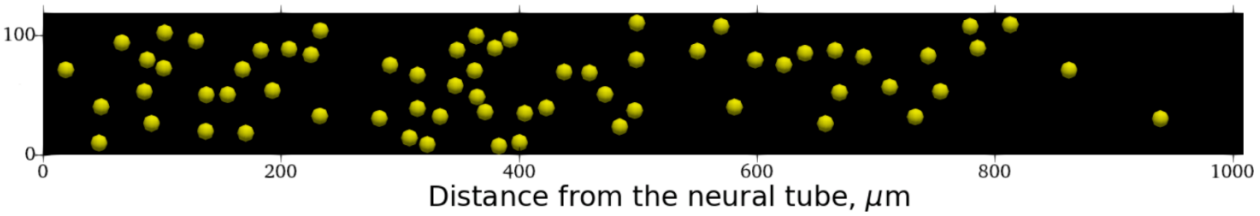


Figure 5.3: Snapshot of a representative simulation of the repulsion-only model with cell ablation (influx of cells is stopped five hours into the simulation) for chick after 24 hours. The density of cells decreases but the cells spread out all along the migratory route. This behaviour is in agreement with biological observations (Figure 5.1) $D = 10$, $\epsilon = 5.0$. Yellow circles represent cells.

These preliminary results indicate that cell-cell interaction mechanisms in chick need further exploration. Repulsive cell-cell interactions may play a role in ensuring full domain coverage under perturbations. It is important to highlight that even though the simple repulsion-only model can replicate the control and ablation experiments, we do not attempt to disprove the role of a chemoattractant in successful invasion. We suggest that a combina-

tion of different mechanisms, such as chemotaxis and cell-cell repulsion, may be present in the system but different factors may be expressed under different environmental conditions. Alternatively, we hypothesise that there may be different sub-phenotypes amongst cells near the front and this feature should be investigated further, so that the revised leader-follower model could replicate the observations of the ablation experiment. To elucidate these hypotheses, our experimental collaborators are currently looking for gene expression factors that could account for repulsive forces. With such experimental knowledge, our study of interaction mechanisms could be pursued further.

Modelling extracellular matrix

We have shown in Chapter 2 that degradation of the ECM may have a significant effect on the migration of, and interactions between, cells. However, the exact mechanism of interaction between the ECM and NCCs is still unknown. Mathematical modelling of cell-cell adhesion, as well as cell-ECM adhesion in cancer, has been successfully used to verify experimental hypotheses and generate new insights into the collective migration of cells (Chaplain et al., 2011; Gerisch and Chaplain, 2008; Sherratt et al., 2009; Kim et al., 2009). Therefore, a more detailed model of the ECM could be employed to investigate the role of ECM-NCC interactions, and the results of such a study could be compared with those on highly invasive cancer cells to shed light on the generalised mechanisms for successful collective invasion.

What confines cells to the stream?

In Chapter 2, we performed a preliminary study on the importance of cell confinement. However, more experimental evidence is needed to verify that confinement is imposed by expression of the inhibitory gene DAN or, perhaps, by other factors. With such experimental results, a further model analysis could be performed to investigate hypotheses on the

length and strength of the inhibitory signal in NCC exclusion zones.

Comparison of Xenopus and chick neural crest cells

Our work on the comparison of chick and Xenopus cranial NCC invasion could be elaborated upon by a more accurate representation of cell-cell forces and directional bias. For example, a memory term could be used to model a persistent random walk and, in such a way, account for the initial directional movement of cells in Xenopus (Van Kampen, 1992; Selmeczi et al., 2005). Careful implementation of attraction and repulsion mechanisms could ensure that bias is induced through these forces (Merchant et al., 2018). Improvements and further analysis of the model could help us make more biologically testable predictions, such as the behaviour of the system under certain perturbations, and provide more detailed insights into the biology.

Continuum limit descriptions

In this thesis we used an individual-based modelling framework to investigate the dynamics of NCCs because of its advantages in preserving the identity and details of individual cells. However, to explore the system mathematically and derive rigorous conclusions on the differences of the dynamics across different species or interaction mechanisms, continuum models may be more powerful. To include the same interactions as in the discrete model, such continuum models should be derived from the IBMs (Dyson et al., 2012; Middleton et al., 2014; Matsiaka et al., 2018; Gavagnin and Yates, 2018), and then employed to efficiently and systematically explore collective NCC invasion.

How does cell response to guidance cues change along the stream?

Further studies are also needed to investigate how the cell response to guidance cues changes along the stream. In this thesis we assumed, based on McLennan et al.'s (2015a,b) work, that there are two cell phenotypes responding differently to signalling cues. However, this binary splitting of cell types is a simplification of the underlying biology, which suggests a range of phenotypes (Morrison et al., 2017). Schumacher (2019) has shown that a model comprising a continuum of phenotypic states is consistent with the experimental results described by Morrison et al. (2017). Further biomarkers for different cell phenotypes along the stream are required to understand the importance of cell heterogeneity in successful invasion.

The role of geometry

Our computational model, as well as all other computational models for NCCs that we discussed, has considered a two-dimensional, flat domain, but in reality, cells are moving through a three-dimensional, curved domain. A natural question to ask is whether the above approximation is justified and if the results would change if domain curvature was included. This question is amenable to computational analysis but has not yet been investigated.

In summary, in this thesis we have made a number of advances in understanding the mechanisms that underly collective NCC migration. In carrying out our investigations, we have raised a number of new questions that provide further avenues for research.

Appendices

A Numerical methods and convergence for Chapter 2

We solve Equation (2.10) using a finite difference method (second-order centred differences in space, and forward Euler in time) with $\Delta x = 1\mu$m, $\Delta y = 1\mu$m and $\Delta t_c = 1$ min. We validate our solution (with no reaction term) by checking that the total concentration of chemoattractant is conserved. We also validate our solution (with fixed reaction term and exponential domain growth) by checking it against the analytical solution for a reaction-diffusion equation on a uniformly growing domain (Simpson, 2015). For simplicity, we use a one-dimensional form of the solution (since the growth only occurs in the x-direction) to the rescaled ($x \in [0, L_0]$) reaction-diffusion equation

$$\frac{\partial c}{\partial t} = D\left(\frac{1}{l(t)^2}\frac{\partial^2 c}{\partial x^2} + \frac{\partial^2 c}{\partial y^2}\right) - kc - \frac{\dot{l}(t)}{l(t)}c. \tag{1}$$

with fixed reaction term, k, on an exponentially growing domain. We use zero-flux boundary conditions and initial conditions[2]:

$$c(x,0) = \begin{cases} c_0, \text{ for } 0 \leq x \leq \beta, \\ 0, \text{ for } \beta < x \leq L_0, \end{cases} \tag{2}$$

is as follows:

$$c(x,t) = \sum_{n=0}^{\infty} a_n \cos(n\pi x)\exp(D(n\pi)^2 t + kt) \tag{3}$$

[2]We choose these initial conditions so that the solution would not be a simple exponential.

where $a_0 = \beta c_0$, $a_n = 2c_0 \sin(n\pi\beta)/n\pi$ and $n \in \mathbb{N}^+$. Results in Figure A.1 compare exact and numerical solutions at $t = 0\text{min}, 10\text{min}, 20\text{min}$, and we see that the exact and numerical solutions are indistinguishable (we also find that the relative average error is less than 10^{-3}). This simplified comparison of our numerical solution with an analytical solution contributes to the validation of our numerical scheme.

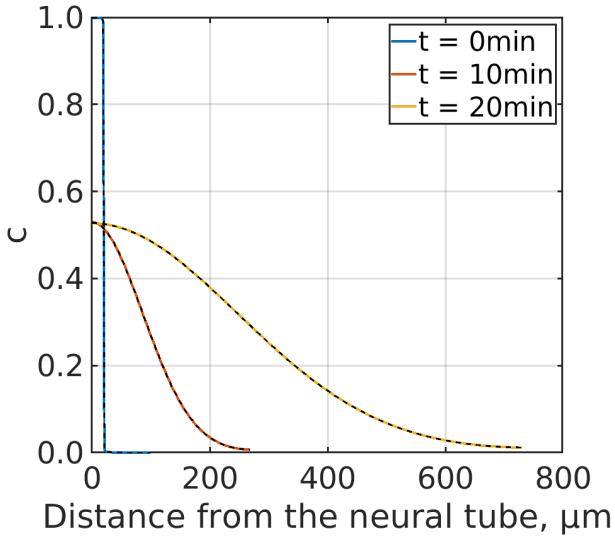


Figure A.1: Comparison of the exact and numerical solutions to Equation (1). The initial conditions are given in Equation (2) with $\beta = 20\mu\text{m}$. Solid lines correspond to exact solution given by Equation (3) and dotted black lines to our numerical solution with $\Delta t = 1\text{min}$ and $\Delta x = 1\mu\text{m}$. $D = 0.01\mu\text{m}^2/\text{min}$, $k = 0.1$ and we assume an exponentially-elongating domain $L_x(t) = L_0 \exp(\alpha t)$ with $\alpha = 0.1\text{min}^{-1}$ and $L_0 = 100\mu\text{m}$.

We choose a time step (for Equation (2.10)) of $\Delta t_c = 1\text{min}$, which is equivalent to the discrete NCC simulation time step (see Table 2.1). These choices are sufficient for the algorithm to converge and resolve accurately the gradient of VEGF. We verify convergence by reducing the space and time steps by a factor of ten and tracking the average relative error with respect to the smallest time and space steps ($\Delta x = 0.1\mu\text{m}$, $\Delta y = 0.1\mu\text{m}$ and $t = 1\text{s}$). We pick the space and time steps with the error less than 10^{-3} and ensure stability using the

von Neumann stability condition (Isaacson and Keller, 2012):

$$\Delta t \leq \frac{1}{2D}\left(\frac{1}{(\Delta x)^2}+\frac{1}{(\Delta y)^2}\right)^{-1}=\frac{h^2}{4D}, \tag{4}$$

where $h=\Delta x=\Delta y$.

In space, the system is of size (340,120), since the space steps are of length 1μm and the initial size of the domain is $340\mu\text{m}\times 120\mu\text{m}$. We use the forward Euler method for its simplicity and since we use a fixed number of space steps on a growing domain, the actual size of space steps in the x-direction increases when domain elongates, so the Neumann stability condition for this method is always satisfied (we verify that it is satisfied for the initial space step).

The simulations were implemented in C++ and the results were imported into ParaView and MATLAB for visualisation.

B Numerical methods and convergence for Chapter 3

We describe how we solve Equation (3.8) from Chapter 3 numerically and verify the convergence of our numerical scheme. In the derivations below, we use a one-dimensional equation because the non-uniform growth is only in the x-direction. We rewrite Equation (3.8) as follows:

$$\frac{\partial C}{\partial t} = D\frac{1}{\Gamma_X}\frac{\partial}{\partial X}\left(\frac{1}{\Gamma_X}\frac{\partial C}{\partial X}\right) - P(C, X, t), \tag{5}$$

where $P(C, X, t)$ is the term that incorporates both the strain rate and the reaction rate, and $X \in [0, X_0]$ with $X_0 = L_x(0)$. We use a midpoint rule in space and forward Euler in time. We provide an example of the derivation of the numerical solution for the value of C at spatial points $i\Delta X$, for $i \in (0, N)$ where N is the final step of the space discretisation. We denote the value $C(i\Delta X, t)$ as $C(i, t)$ for simplicity. The scheme takes the following form:

$$\begin{aligned}
C(i, t+\Delta t) &= \Delta t\left[D\frac{1}{\Gamma_X(i, t+\Delta t)}\frac{\partial}{\partial X}\left[\frac{1}{\Gamma_X(i, t+\Delta t)}\frac{\partial C(i,t)}{\partial X}\right] + P(C, i, t)C(i, t)\right] + C(i, t) \\
&= \Delta t\left[D\frac{1}{\Gamma_X(i, t+\Delta t)}\left[\frac{1}{\Delta X}\left(\frac{1}{\Gamma_X(t+\Delta t)}\frac{\partial C(i,t)}{\partial X}\right)_{i+\frac{1}{2}}\right.\right. \\
&- \left.\left.\frac{1}{\Delta X}\left(\frac{1}{\Gamma_X(t+\Delta t)}\frac{\partial C(i,t)}{\partial X}\right)_{i-\frac{1}{2}}\right] + P(C, i, t)C(i, t)\right] + C(i, t) \\
&= \Delta t\left[D\frac{1}{\Gamma_X(i, t+\Delta t)}\left[\frac{1}{\Delta X}\left(\frac{1}{\Gamma_X(t+\Delta t)}\right)_{i+\frac{1}{2}}\frac{C(i+1,t)-C(i,t)}{\Delta X}\right.\right. \\
&- \left.\left.\frac{1}{\Delta X}\left(\frac{1}{\Gamma_X(t+\Delta t)}\right)_{i-\frac{1}{2}}\frac{C(i,t)-C(i-1,t)}{\Delta X}\right] + P(C, i, t)C(i, t)\right] + C(i, t).
\end{aligned} \tag{6}$$

where

$$\left(\frac{1}{\Gamma_X(t+\Delta t)}\right)_{i+\frac{1}{2}} = \frac{1}{2}\left(\frac{1}{\Gamma_X(i, t+\Delta t)} + \frac{1}{\Gamma_X(i+1, t+\Delta t)}\right). \tag{7}$$

We use zero-flux boundary conditions ($C(0, t) = C(1, t)$ and $C(N, t) = C(N-1, t)$) for $\forall t \in [0, t_{\text{final}}]$, and uniform initial conditions ($C(X, 0) \equiv 1$ for $X \in [0, X_0]$, meaning $C(i, 0) \equiv 1$ for $\forall i \in [0, N]$).

It is challenging to find an analytical solution for the reaction-diffusion equation on

a non-uniformly growing finite domain which we could use to verify our numerical solution. Therefore, we use the manufactured solution method (Roache, 2002) to verify the accuracy of our code. The basic idea of this method is to simply manufacture an exact solution to a modified PDE, and solve that modified equation numerically (results not shown).

To solve the original two-dimensional Equation (3.8) from Chapter 3, we choose $\Delta x = 1\mu$m, $\Delta y = 1\mu$m and $\Delta t_c = 12$s. We verified convergence by reducing the space and time steps by a factor of ten and tracking the average relative error (which is less than 10^{-3}). Note that a time step of 12s is equivalent to the discrete simulation time step for the cell motility model. To ensure stability, we use the von Neumann stability condition (Isaacson and Keller, 2012):

$$\Delta t \leq \frac{1}{2D}\left(\frac{1}{(\Delta x)^2} + \frac{1}{(\Delta y)^2}\right)^{-1} = \frac{h^2}{4D}, \tag{8}$$

where $h = \Delta x = \Delta y$. In space, the system is of size (3400,1200), since the space steps are of length 0.1μm and the initial size of the domain is $340\mu\text{m} \times 120\mu\text{m}$. We use the forward Euler method for its simplicity and since we use a fixed number of space steps on a growing domain, the actual size of space steps in the x-direction increases when domain elongates, so the Neumann stability condition for this method is always satisfied (we verify that it is satisfied for the initial space step).

The simulations were implemented in C++ and the results were imported into ParaView and MATLAB for visualisation.

C Numerical methods and convergence for Chapter 4

We describe how we solve Equation (4.3) in Chapter 4. To solve Equation (4.3) on a fixed or growing domain, we use the Forward Euler method:

$$\boldsymbol{x}_i(t+\Delta t) = \boldsymbol{x}_i(t) + \Delta t \sum_{j \neq i} \boldsymbol{F}_{ij} + \beta \boldsymbol{i} \Delta t + \sqrt{2D\Delta t}\boldsymbol{\xi}_i \tag{9}$$

where $\boldsymbol{\xi} \sim \mathcal{N}(\mathbf{0}, I)$ is Gaussian noise (I is the identity matrix) and $\boldsymbol{i} = (1, 0)$ is the unit vector. If the domain grows, then we update the positions of cells at each time step, i.e. the cells are advected by the growth.

The simulations were implemented in C++ and the results were imported into ParaView and MATLAB for visualisation.

Units for the bias, β, are μm/min, for the diffusion constant, D, μm^2/min, and for the interaction strength parameter, ϵ, μm/min. We do not explicitly write down the units in the rest of this appendix.

To verify the convergence of the simulations, we compare the dynamics of the mass centre of all the cells for different time steps. For simplicity, we only consider the component of the centre of mass, m, in the x-direction:

$$m(t) = \frac{1}{N} \sum_{i \in N} \boldsymbol{x}_i^x(t), \tag{10}$$

where $\boldsymbol{x}_i^x$ is the x-coordinate of the position of cell i and N is the number of cells. Note that all cells are identical, so we do not need to account for different cell masses.

We investigate the convergence of Equation (9). We vary the time step $\Delta t = 0.00125\text{min}, 0.00250\text{min}, 0.00500\text{min}, 0.01000\text{min}, 0.02000\text{min}$ and run simulations for 30 minutes to investigate what happens to the centre of mass. We define the error function as follows:

$$e_{\Delta t}(t) = \left| \frac{m_{\Delta t}(t) - m_{\Delta t_{\min}}(t)}{m_{\Delta t_{\min}}(t)} \right| \tag{11}$$

where $m_{\Delta t_{\min}}$ is the centre of mass for the smallest time step, in our case $\Delta t_{\min} = 0.00125$min. We look at two different initial configurations of cells (Figures C.1(a) and C.2(a)). To ensure that simulations with different values of the time step follow identical dynamics, we generate a fixed series of normally distributed random variables with mean 0 and variance $\Delta t_{\min}$ which we use for random cell movement (Lemons and Langevin, 2002). We first consider the case of ten cells placed away from the boundary. We demonstrate that the algorithm converges for this initial configuration by reducing the time step in Figure C.1. Note that for any smaller values of D, the error is zero during the first 30min (results not shown). We then choose the case of five cells and place them at the left-hand boundary initially, and demonstrate convergence in Figure C.2. We also consider the model with bias $\beta = 0.2$ and demonstrate its convergence in Figure C.3. For our simulations in Chapter 4, we use $\Delta t = 0.01$min, which is sufficient to ensure convergence for the force strength and diffusion values that we use. If one needed to increase the force strength or diffusion constant significantly, the time step would have to be adjusted.

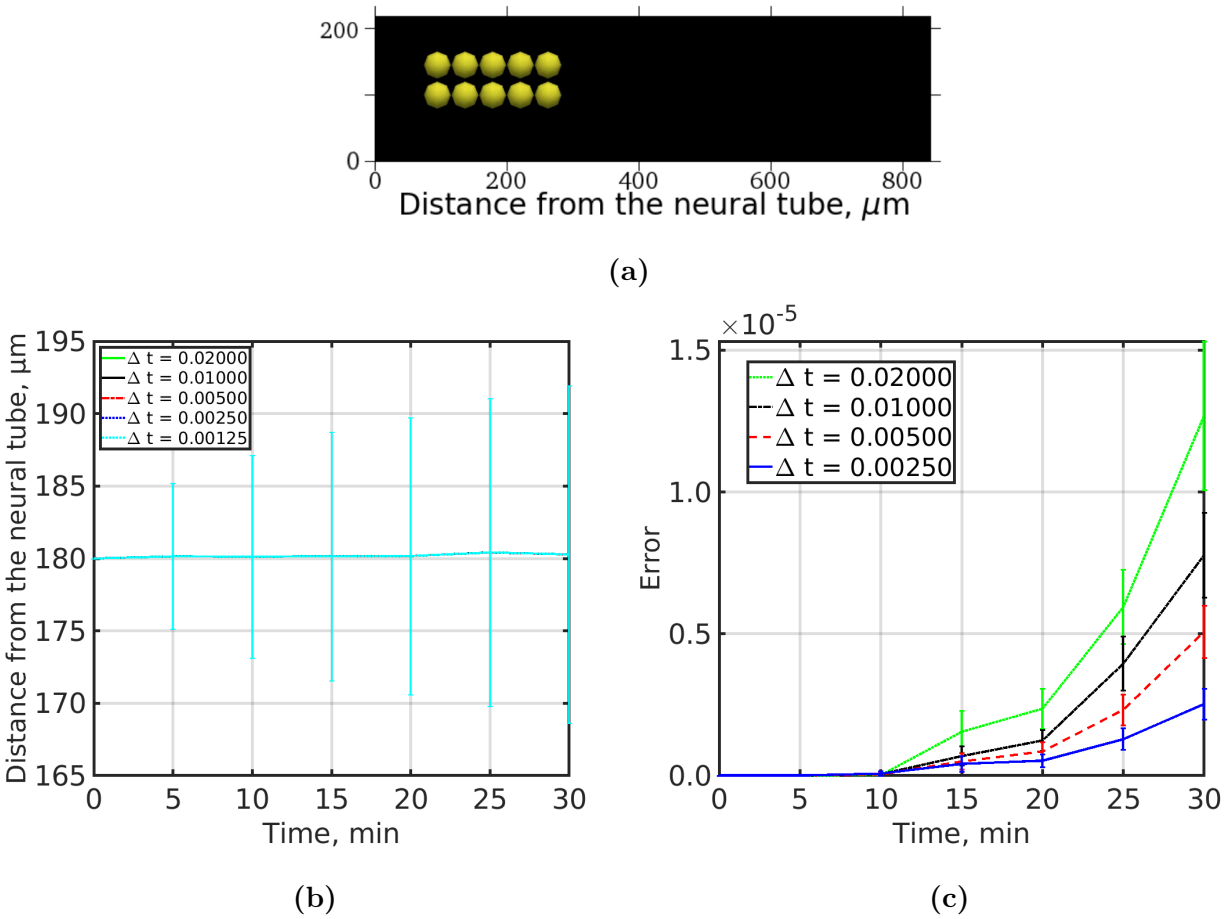
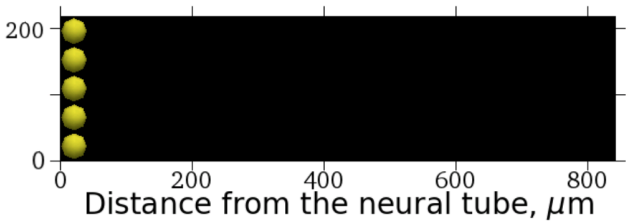
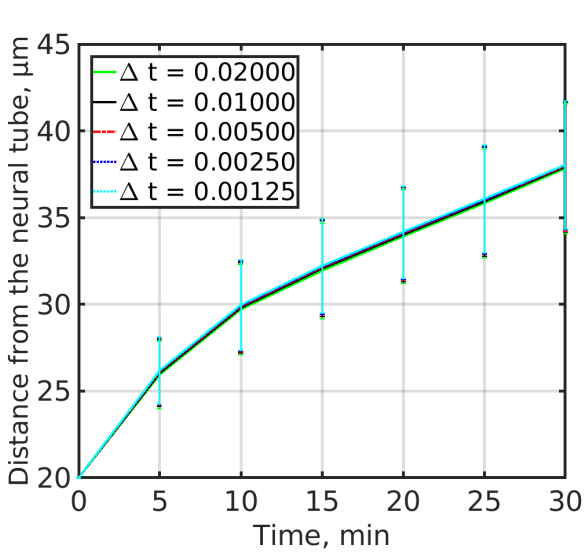


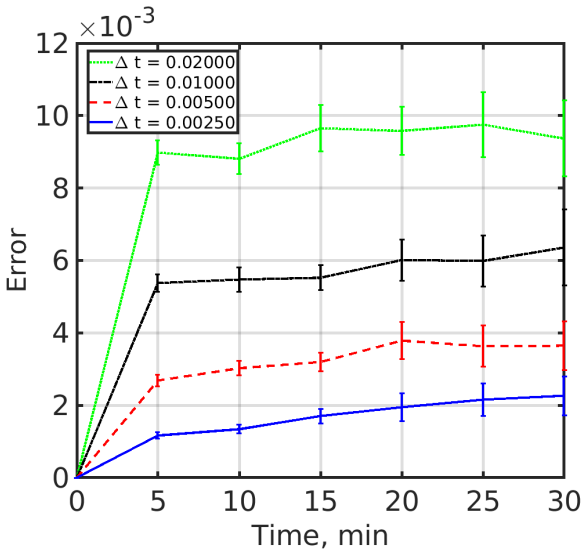
Figure C.1: (a) Initial cell configuration. (b) Average over 1000 simulations of the evolution of the centre of mass defined by Equation (10) for the attraction and repulsion model with $D = 25$, $\epsilon = 200$, $\beta = 0$ for different time steps, error bars represent standard deviation. The time steps are in minutes. The lines are overlapping at this scale. (c) Mean error defined by Equation (11), averaged over all simulations for each time step. Error bars represent standard deviation.



(a)

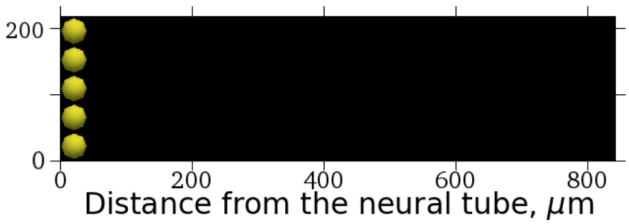


(b)

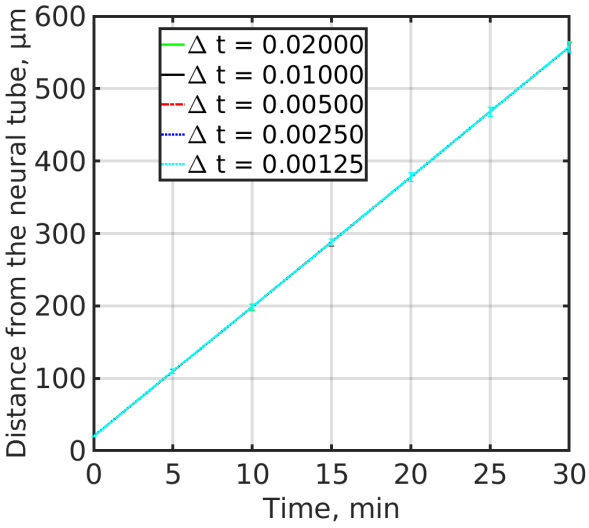


(c)

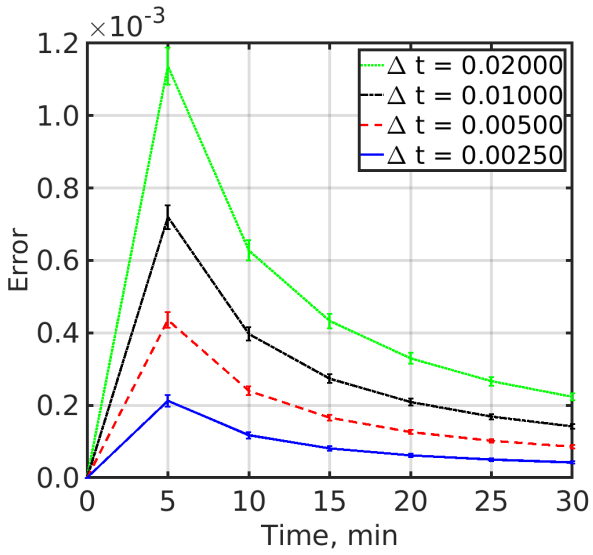
Figure C.2: (a) Initial cell configuration. (b) Average over 100 simulations of the evolution of the centre of mass defined by Equation (10) for the attraction and repulsion model with $D = 5$, $\epsilon = 200$, $\beta = 0$ for different time steps, error bars represent standard deviation. The time steps are in minutes. The lines are overlapping at this scale. (c) Mean error defined by Equation (11), averaged over all simulations for each time step. Error bars represent standard deviation.



(a)



(b)



(c)

Figure C.3: (a) Initial cell configuration. (b) Average over 100 simulations of the evolution of the centre of mass defined by Equation (10) for the attraction and repulsion model with $D = 5$, $\epsilon = 200$ and $\beta = 0.2$ for different time steps, error bars represent standard deviation. The time steps are in minutes. The lines are overlapping at this scale. (c) Mean error defined by Equation (11), averaged over all simulations for each time step. Error bars represent standard deviation.

D Xenopus data

In this appendix we provide extensive data on Xenopus NCC invasion for different models and parameter values.

D.1 Successful invasion

Here we provide the data for successful invasion in 24 hours or less for different Xenopus NCC models. There are no cases with successful invasion in 24 hours or less for the repulsion-only model with no bias, attraction and repulsion model with no bias and attraction and repulsion model with biased leaders.

Repulsion-only model with all cells biased

D \ ϵ	1	50	100	150	200
1	100	100	100	100	100
4	100	94	96	93	93
7	100	76	78	77	73
10	97	70	54	61	63
13	95	49	57	51	56

(a) $\beta = 0.7$.

β \ ϵ	1	50	100	150	200
0.1	0	0	0	0	0
0.4	0	0	0	0	0
0.7	100	76	78	77	73
1.0	100	100	100	100	100
1.3	100	100	100	100	100

(b) $D = 7$

D \ β	0.1	0.4	0.7	1.0	1.3
1	0	0	100	100	100
4	0	0	96	100	100
7	0	0	78	100	100
10	0	0	54	100	100
13	0	0	57	100	100

(c) $\epsilon = 100.0$

Table D1: The number of simulations out of one hundred which exhibit successful invasion in 24 hours or less for the repulsion-only model for Xenopus with all cells biased.

Attraction and repulsion model with all cells biased

D \ ϵ	1	50	100	150	200
1	100	100	100	100	100
4	100	100	100	100	100
7	100	100	100	100	100
10	94	92	100	100	100
13	96	98	100	100	100

(a) $\beta = 0.7$.

β \ ϵ	1	50	100	150	200
0.1	0	0	0	0	0
0.4	0	0	0	0	0
0.7	100	100	100	100	100
1.0	100	100	100	100	100
1.3	100	100	100	100	100

(b) $D = 7$.

D \ β	0.1	0.4	0.7	1.0	1.3
1	0	0	100	100	100
4	0	0	100	100	100
7	0	0	100	100	100
10	0	0	100	100	100
13	0	0	100	100	100

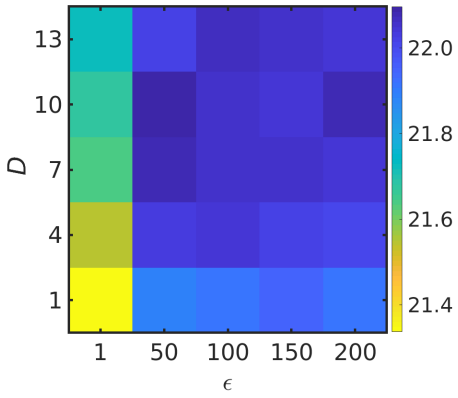
(c) $\epsilon = 100$.

Table D2: The number of simulations out of one hundred which exhibit successful invasion in 24 hours or less for the attraction and repulsion model for Xenopus with all cells biased.

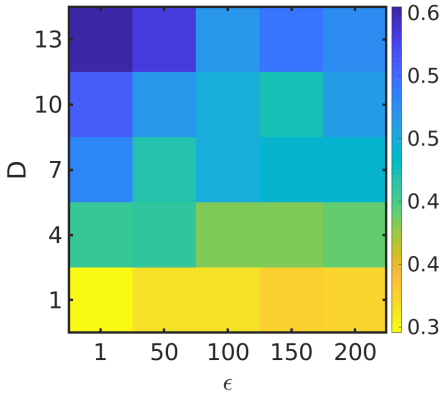
D.2 Time to invasion

In Figures D.1 and D.2, we provide the data of time to invasion for the Xenopus NCC models with all cells biased.

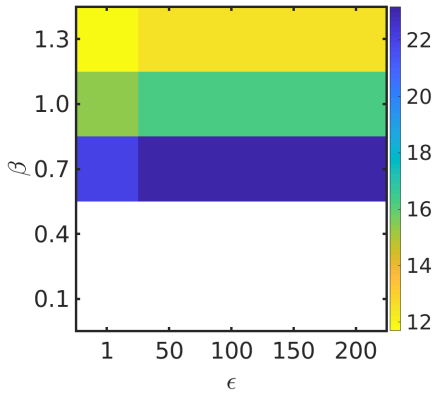
Repulsion-only model with all cells biased



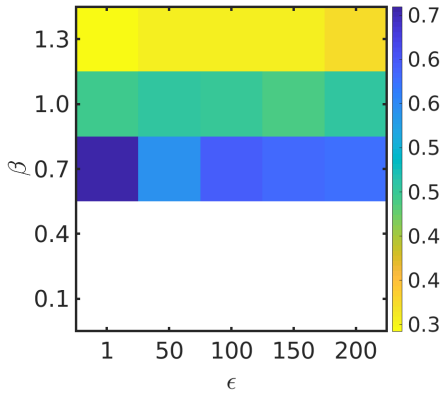
(a) Mean, $\beta = 0.7$.



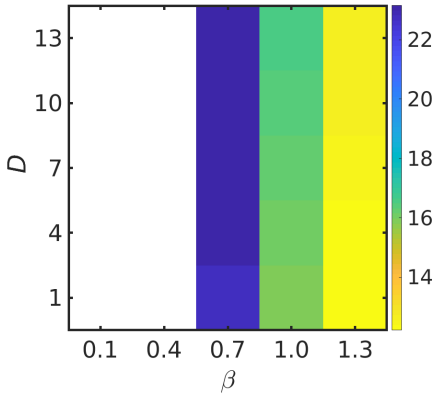
(b) Standard deviation, $\beta = 0.7$.



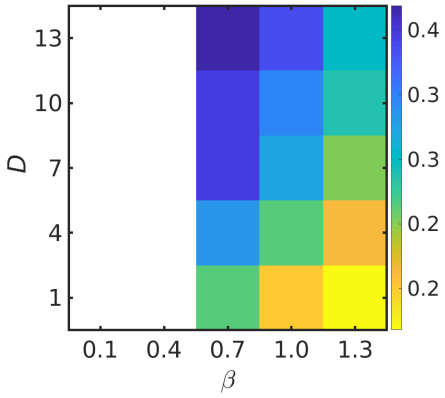
(c) Mean, $D = 7$.



(d) Standard deviation, $D = 7$.



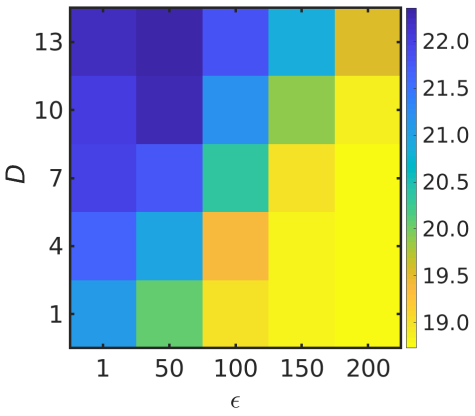
(e) Mean, $\epsilon = 100$.



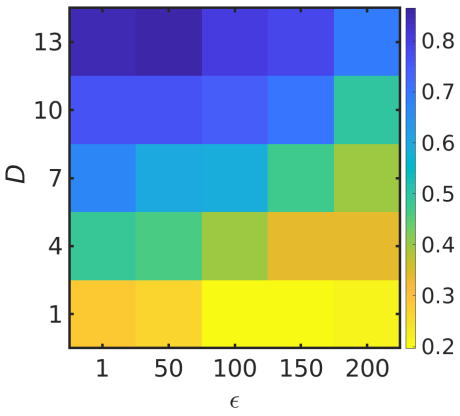
(f) Standard deviation, $\epsilon = 100$.

Figure D.1: Mean and standard deviation of time to invasion for the repulsion-only model with bias for all cells, statistics over the simulations in which successful invasion occurs in 24 hours or less (Table D1). The colour bar represents hours. White colour corresponds to cases in which there are no simulations with invasion in 24 hours or less.

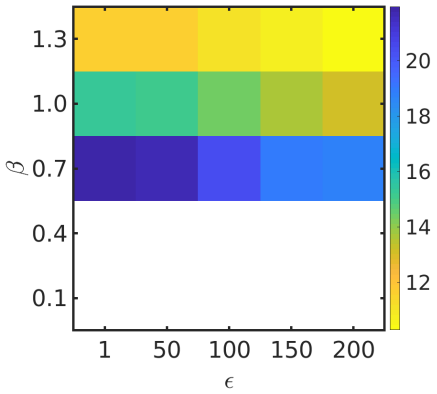
Attraction and repulsion model with all cells biased



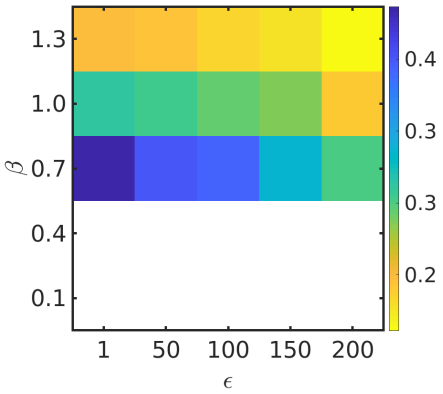
(a) Mean, $\beta = 0.7$.



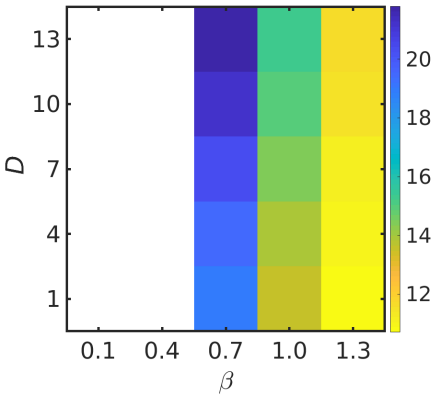
(b) Standard deviation, $\beta = 0.7$.



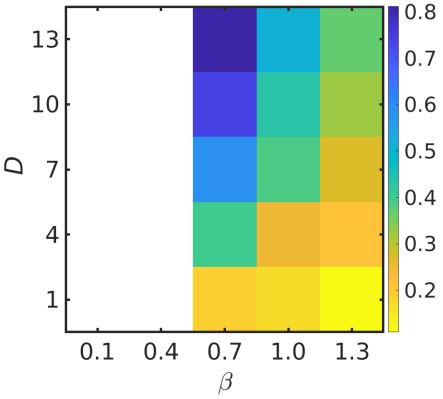
(c) Mean, $D = 7$.



(d) Standard deviation, $D = 7$.



(e) Mean, $\epsilon = 100$.



(f) Standard deviation, $\epsilon = 100$.

Figure D.2: Mean and standard deviation of time to invasion for the attraction and repulsion model with bias for all cells, statistics over the simulations in which successful invasion occurs in 24 hours or less (Table D2). The colour bar represents hours. White colour corresponds to cases in which there are no simulations with invasion in 24 hours or less.

E Chick data

In this appendix we provide extensive data on chick NCC invasion and stream breakage for different models and parameter values.

E.1 Invasion

In Tables E1-E5, we provide data on the number of simulations that exhibit invasion (defined as more than five cells in the final 100μm segment in the x-direction of the domain by 24 hours) for different models and parameter values.

Repulsion-only model

D \ ϵ	0.4	19.0	38.0	56.0	75.0
1	0	0	0	0	0
4	0	0	0	0	0
7	0	0	3	6	16
10	0	63	93	98	100
13	58	100	100	100	100

Table E1: Number of simulations out of one hundred which exhibit invasion in 24 hours or less for the attraction and repulsion model for chick with no bias. We vary the diffusion constant D and the interaction strength parameter ϵ.

Attraction and repulsion model

D \ ϵ	0.4	19.0	38.0	56.0	75.0
1	0	0	0	0	0
4	0	0	0	0	0
7	0	0	0	0	0
10	1	0	0	0	0
13	69	23	5	2	3

Table E2: Number of simulations out of one hundred which exhibit invasion in 24 hours or less for the attraction and repulsion model for chick with no bias. We vary the diffusion constant D and the interaction strength parameter ϵ.

Attraction and repulsion model with biased leaders

D \ ϵ	0.4	19.0	38.0	56.0	75.0
1	0	0	0	0	0
4	0	0	0	0	0
7	4	3	0	0	0
10	49	50	17	1	1
13	100	98	87	49	28

(a) $\beta = 0.4$ for leaders.

β \ ϵ	0.4	19.0	38.0	56.0	75.0
0.1	0	0	0	0	0
0.4	3	3	0	0	0
0.7	9	10	4	1	0
1.0	20	14	5	1	0
1.3	27	23	3	0	0

(b) $D = 7$.

D \ β	0.1	0.4	0.7	1.0	1.3
1	0	0	2	0	0
4	0	0	0	0	0
7	0	0	2	6	4
10	0	27	53	60	59
13	25	87	99	100	100

(c) $\epsilon = 38$.

Table E3: The number of simulations out of one hundred which exhibit invasion in 24 hours or less for the attraction and repulsion model for chick with biased leaders.

Repulsion-only model with all cells biased

D \ ϵ	0.4	19.0	38.0	56.0	75.0
1	100	100	100	100	100
4	100	100	100	100	100
7	100	100	100	100	100
10	100	100	100	100	100
13	100	100	100	100	100

(a) $\beta = 0.4$.

β \ ϵ	0.4	19.0	38.0	56.0	75.0
0.1	0	56	89	96	98
0.4	100	100	100	100	100
0.7	100	100	100	100	100
1.0	100	100	100	100	100
1.3	100	100	100	100	100

(b) $D = 7$.

D \ β	0.1	0.4	0.7	1.0	1.3
1	0	100	100	100	100
4	0	100	100	100	100
7	89	100	100	100	100
10	100	100	100	100	100
13	100	100	100	100	100

(c) $\epsilon = 38.0$.

Table E4: The number of simulations out of one hundred which exhibit invasion in 24 hours or less for the repulsion-only model for chick with all cells biased.

Attraction and repulsion model with all cells biased

D \ ϵ	0.4	19.0	38.0	56.0	75.0
1	100	100	38	0	0
4	100	100	100	100	93
7	100	100	100	100	100
10	100	100	100	100	100
13	100	100	100	100	100

(a) $\beta = 0.4$.

β \ ϵ	0.4	19.0	38.0	56.0	75.0
0.1	0	0	0	0	0
0.4	100	100	100	100	100
0.7	100	100	100	100	100
1.0	100	100	100	100	100
1.3	100	100	100	100	100

(b) $D = 7$.

D \ β	0.1	0.4	0.7	1.0	1.3
1	0	39	100	100	100
4	0	100	100	100	100
7	0	100	100	100	100
10	6	100	100	100	100
13	90	100	100	100	100

(c) $\epsilon = 38.0$.

Table E5: The number of simulations out of one hundred which exhibit invasion in 24 hours or less for the attraction and repulsion model for chick with all cells biased.

E.2 Stream breakage

We provide data on the number of simulations that exhibit stream breakage (defined as more than one cluster of cells) at 24 hours or at the time of invasion (if invasion occurs in less than 24 hours) for different models and parameter values (Tables E6-E10).

Repulsion-only

D \ ϵ	0.4	19.0	38.0	56.0	75.0
1	1	0	0	0	0
4	0	0	0	0	0
7	0	0	0	0	1
10	0	0	0	0	0
13	0	0	0	0	0

Table E6: The number of simulations out of one hundred exhibiting stream breakage for the repulsion-only model at 24 hours or at the time of invasion (if invasion occurs in less than 24 hours). We vary the diffusion constant D and the interaction strength parameter ϵ.

Attraction and repulsion

β \ ϵ	0.4	19.0	38.0	56.0	75.0
1	3	0	0	0	0
4	0	2	0	0	0
7	0	0	0	0	0
10	0	0	0	0	0
13	0	0	0	0	0

Table E7: The number of simulations out of one hundred exhibiting stream breakage for the attraction and repulsion model at 24 hours or at the time of invasion (if invasion occurs in less than 24 hours). We vary the diffusion constant D and the interaction strength parameter ϵ.

Attraction and repulsion with biased leaders

D \ ϵ	0.4	19.0	38.0	56.0	75.0
1	88	90	0	0	0
4	13	25	31	28	1
7	2	3	10	13	9
10	0	1	2	1	1
13	1	0	0	0	2

(a) $\beta = 0.4$ for leaders.

β \ ϵ	0.4	19.0	38.0	56.0	75.0
0.1	0	0	0	2	0
0.4	0	3	12	13	10
0.7	3	6	37	86	48
1.0	4	8	35	87	95
1.3	2	9	39	93	99

(b) $D = 7$.

D \ β	0.1	0.4	0.7	1.0	1.3
1	0	0	90	100	100
4	1	35	97	100	99
7	0	10	32	46	38
10	0	2	3	3	3
13	0	0	1	2	2

(c) $\epsilon = 38.0$.

Table E8: The number of simulations out of one hundred exhibiting stream breakage for the attraction and repulsion model with biased leaders at 24 hours or at the time of invasion (if invasion occurs in less than 24 hours).

Repulsion-only with all cells biased

D \ ϵ	0.4	19.0	38.0	56.0	75.0
1	27	3	0	0	0
4	5	0	0	0	0
7	1	0	0	0	0
10	1	0	0	0	0
13	0	0	0	0	0

(a) $\beta = 0.4$.

β \ ϵ	0.4	19.0	38.0	56.0	75.0
0.1	0	0	0	0	0
0.4	2	0	0	0	0
0.7	8	0	0	0	0
1.0	37	0	0	0	0
1.3	55	1	0	1	0

(b) $D = 7$.

D \ β	0.1	0.4	0.7	1.0	1.3
1	0	1	0	0	0
4	0	0	0	0	0
7	2	0	0	0	0
10	3	1	2	0	0
13	6	0	1	0	0

(c) $\epsilon = 38.0$.

Table E9: The number of simulations out of one hundred exhibiting stream breakage for the repulsion-only model with bias for all cells at 24 hours or at the time of invasion (if invasion occurs in less than 24 hours).

Attraction and repulsion model with all cells biased

D \ ϵ	0.4	19.0	38.0	56.0	75.0
1	28	10	7	1	2
4	18	8	11	5	9
7	0	1	3	0	1
10	3	0	1	2	0
13	0	0	0	0	0

(a) $\beta = 0.4$.

β \ ϵ	0.4	19.0	38.0	56.0	75.0
0.1	0	0	3	5	1
0.4	4	1	0	2	1
0.7	18	7	4	1	1
1.0	42	9	5	8	3
1.3	61	19	15	9	6

(b) $D = 7$.

D \ β	0.1	0.4	0.7	1.0	1.3
1	0	8	1	19	21
4	7	13	6	12	23
7	1	1	7	5	16
10	2	0	2	4	10
13	0	0	0	0	3

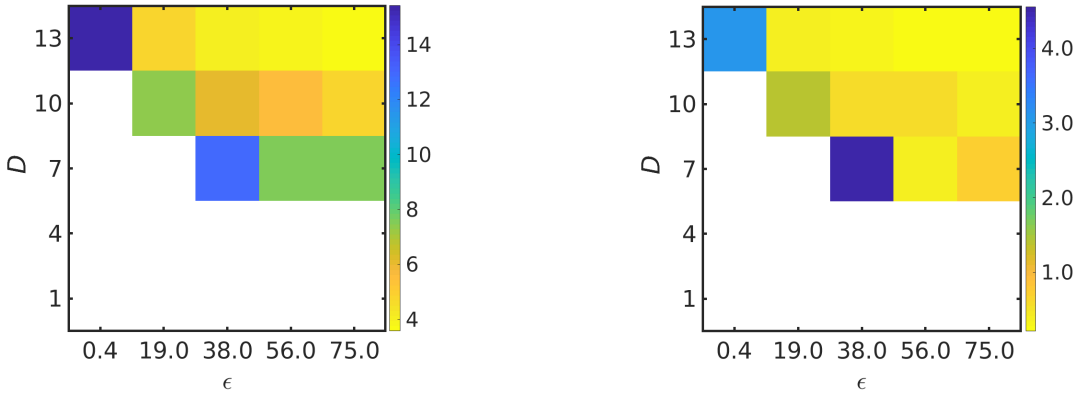
(c) $\epsilon = 38.0$.

Table E10: The number of simulations out of one hundred exhibiting stream breakage for the attraction and repulsion model with bias for all cells at 24 hours or at the time of invasion (if invasion occurs in less than 24 hours).

E.3 Time to invasion

In Figures E.1-E.5, we provide data on the time to invasion within 24 hours or less.

Repulsion-only

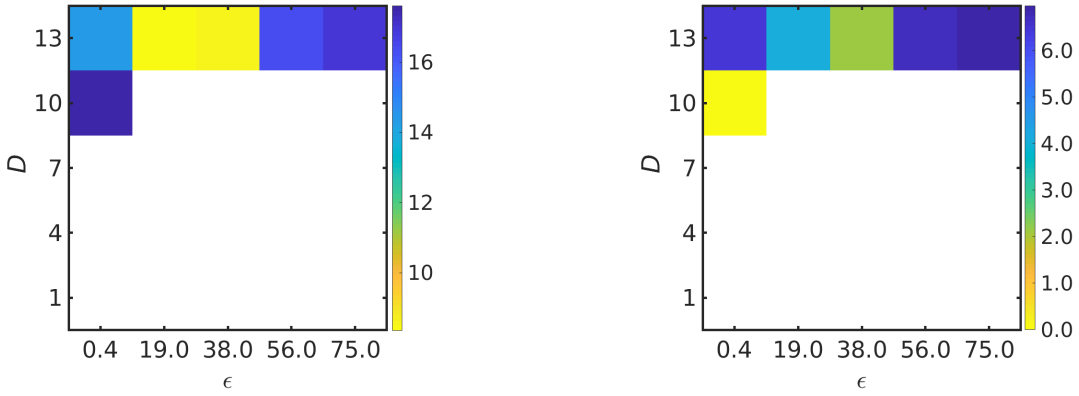


(a) Mean.

(b) Standard deviation.

Figure E.1: Mean and standard deviation of time to invasion for the repulsion-only model, statistics over the simulations in which invasion occurs in 24 hours or less (Table E1). The colour bar represents hours. White colour corresponds to cases in which there are no simulations with invasion in 24 hours or less.

Attraction and repulsion

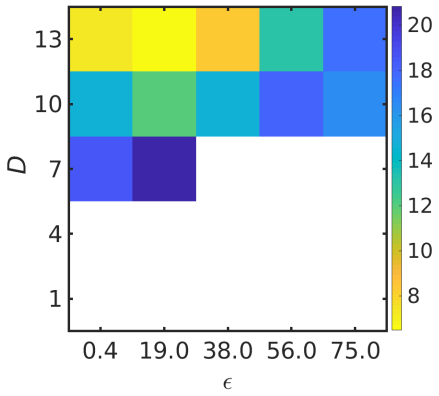


(a) Mean.

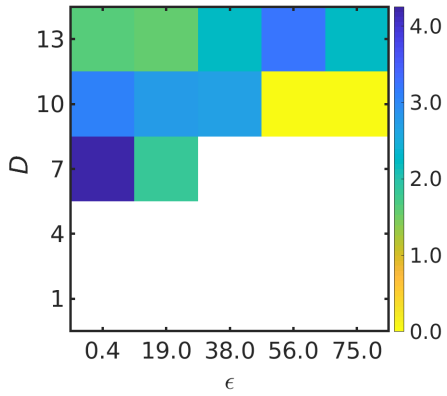
(b) Standard deviation.

Figure E.2: Mean and standard deviation of time to invasion for the attraction and repulsion model, statistics over the simulations in which invasion occurs in 24 hours or less (Table E2). The colour bar represents hours. White colour corresponds to cases in which there are no simulations with invasion in 24 hours or less.

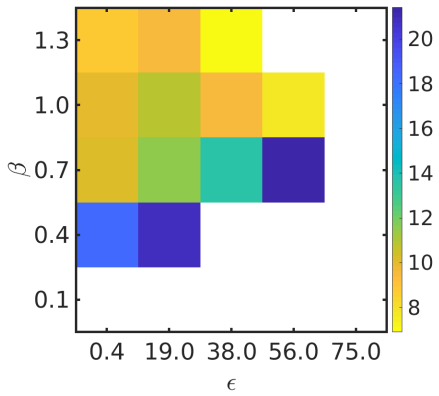
Attraction and repulsion with biased leaders



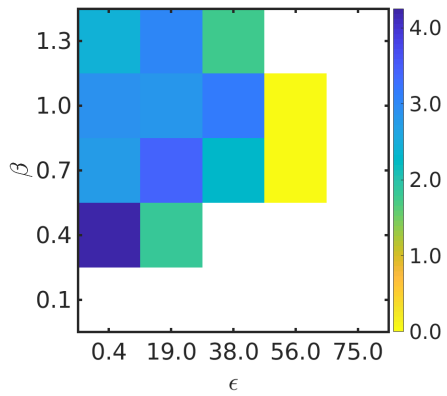
(a) Mean, $\beta = 0.4$ for leaders.



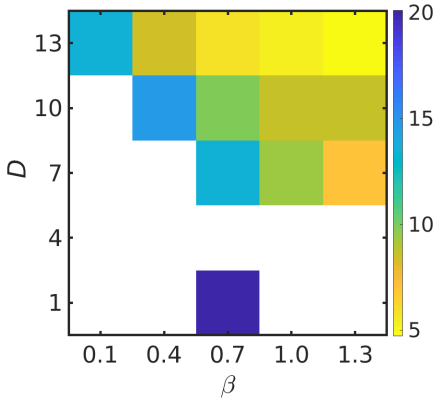
(b) Standard deviation, $\beta = 0.4$ for leaders.



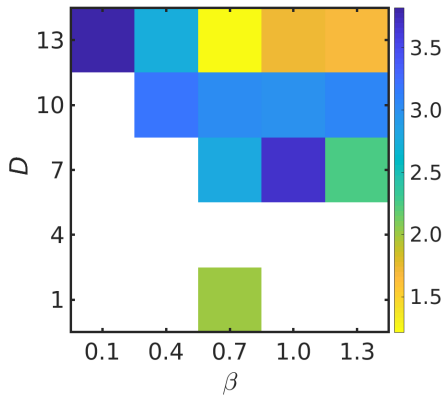
(c) Mean, $D = 7$.



(d) Standard deviation, $D = 7$.



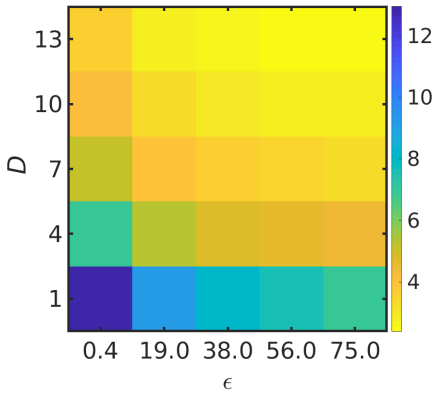
(e) Mean, $\epsilon = 38.0$.



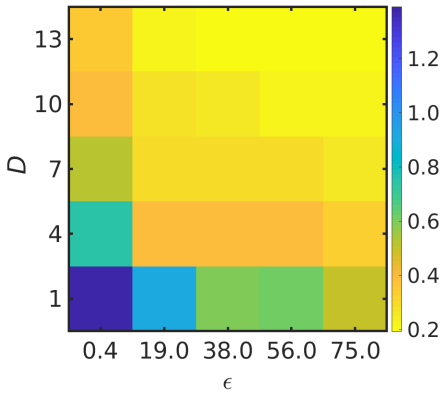
(f) Standard deviation, $\epsilon = 38.0$.

Figure E.3: Mean and standard deviation of time to invasion for the attraction and repulsion model with biased leaders, statistics over the simulations in which invasion occurs in 24 hours or less (Table E3). The colour bar represents hours. White colour corresponds to cases in which there are no simulations with invasion in 24 hours or less.

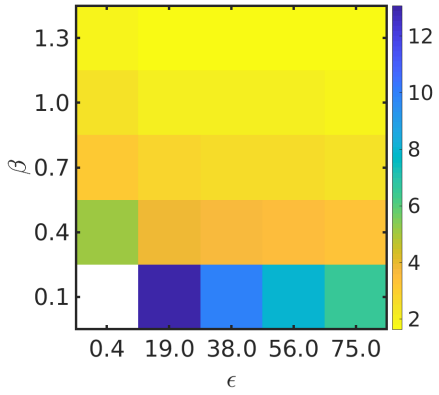
Repulsion-only with all cells biased



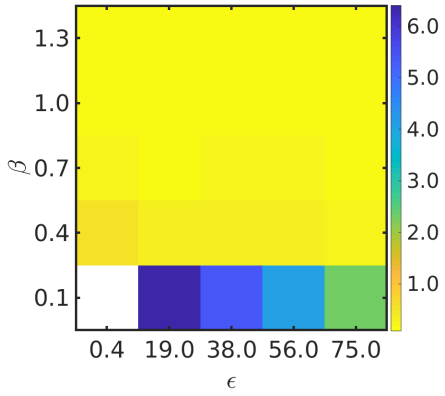
(a) Mean, $\beta = 0.4$.



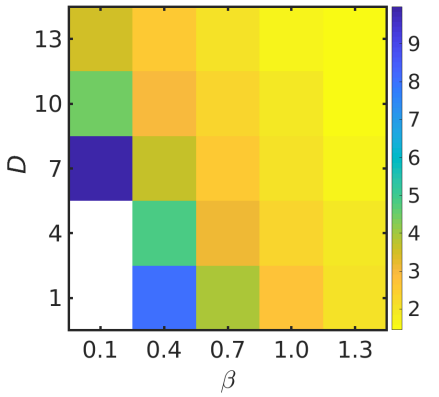
(b) Standard deviation, $\beta = 0.4$.



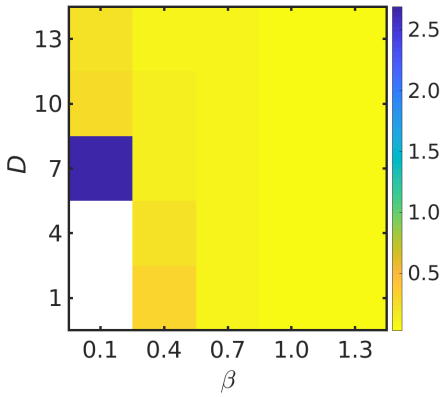
(c) Mean, $D = 7$.



(d) Standard deviation, $D = 7$.



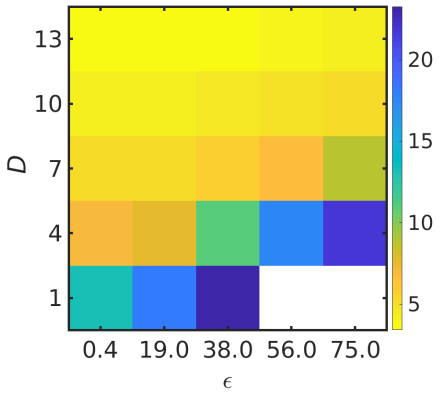
(e) Mean, $\epsilon = 38.0$.



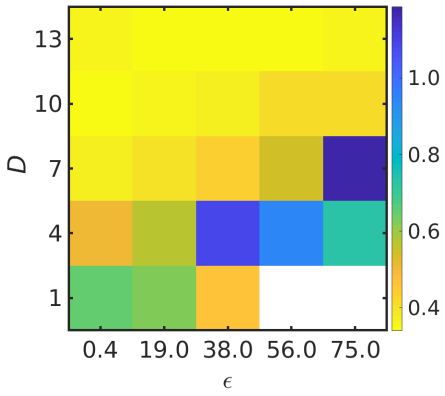
(f) Standard deviation, $\epsilon = 38.0$.

Figure E.4: Mean and standard deviation of time to invasion for the repulsion-only model with all cells biased, statistics over the simulations in which invasion occurs in 24 hours or less (Table E4). The colour bar represents hours. White colour corresponds to cases in which there are no simulations with invasion in 24 hours or less.

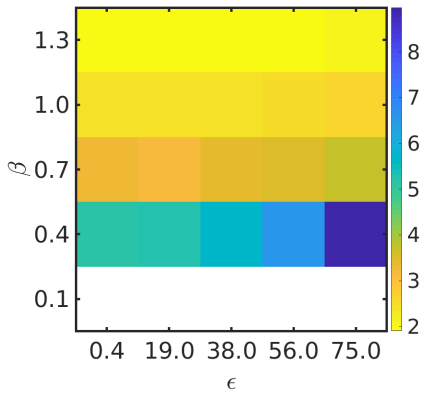
Attraction and repulsion with all cells biased



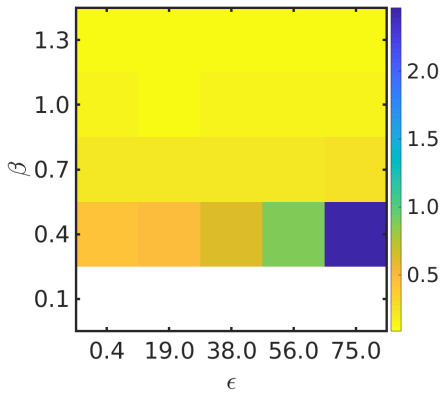
(a) Mean, $\beta = 0.4$.



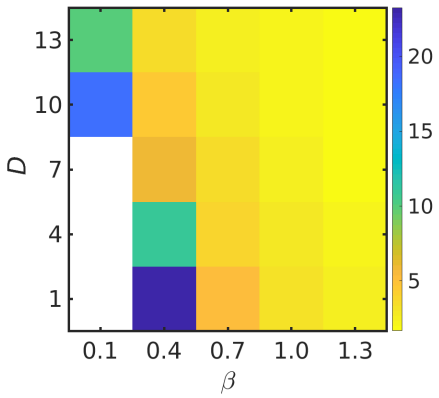
(b) Standard deviation, $\beta = 0.4$.



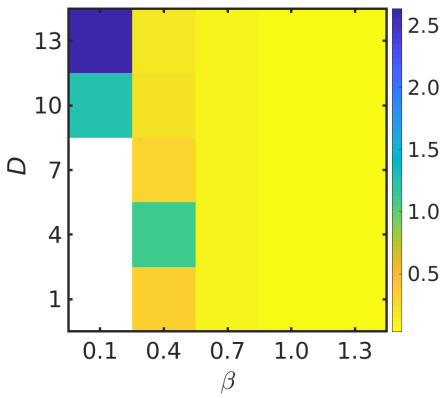
(c) Mean, $D = 7$.



(d) Standard deviation, $D = 7$.



(e) Mean, $\epsilon = 38.0$.



(f) Standard deviation, $\epsilon = 38.0$.

Figure E.5: Mean and standard deviation of time to invasion for the attraction and repulsion model with all cells biased, statistics over the simulations in which invasion occurs in 24 hours or less (Table E5). The colour bar represents hours. White colour corresponds to cases in which there are no simulations with invasion in 24 hours or less.

Bibliography

Abercrombie, M. and Heaysman, J. E. (1953). Observations on the social behaviour of cells in tissue culture: I. speed of movement of chick heart fibroblasts in relation to their mutual contacts. *Experimental Cell Research*, 5(1):111–131.

Alfandari, D., Cousin, H., and Marsden, M. (2010). Mechanism of Xenopus cranial neural crest cell migration. *Cell Adhesion & Migration*, 4(4):553–560.

Banerjee, S., Gordon, L., Donn, T. M., Berti, C., Moens, C. B., Burden, S. J., and Granato, M. (2011). A novel role for MuSK and non-canonical Wnt signaling during segmental neural crest cell migration. *Development*, 138(15):3287–3296.

Barriga, E. H., Trainor, P. A., Bronner, M., and Mayor, R. (2015). Animal models for studying neural crest development: is the mouse different? *Development*, 142(9):1555–1560.

Bellomo, N. and Brezzi, F. (2015). Traffic, crowds, and dynamics of self-organized particles: New trends and challenges. *Mathematical Models and Methods in Applied Sciences*, 25(03):395–400.

Belmadani, A., Jung, H., Ren, D., and Miller, R. J. (2009). The chemokine SDF-1/CXCL12 regulates the migration of melanocyte progenitors in mouse hair follicles. *Differentiation*, 77(4):395–411.

Binder, B. J., Landman, K. A., Newgreen, D. F., Simkin, J. E., Takahashi, Y., and Zhang,

D. (2012). Spatial analysis of multi-species exclusion processes: application to neural crest cell migration in the embryonic gut. *Bulletin of Mathematical Biology*, 74(2):474–490.

Byrne, H. and Preziosi, L. (2003). Modelling solid tumour growth using the theory of mixtures. *Mathematical Medicine and Biology: a Journal of the IMA*, 20(4):341–366.

Carmona-Fontaine, C., Matthews, H. K., Kuriyama, S., Moreno, M., Dunn, G. A., Parsons, M., Stern, C. D., and Mayor, R. (2008). Contact inhibition of locomotion in vivo controls neural crest directional migration. *Nature*, 456(7224):957–961.

Carmona-Fontaine, C., Theveneau, E., Tzekou, A., Tada, M., Woods, M., Page, K., Parsons, M., Lambris, J., and Mayor, R. (2011). Complement fragment C3a controls mutual cell attraction during collective cell migration. *Developmental Cell*, 21(6):1026–1037.

Chaplain, M. A. (2000). Mathematical modelling of angiogenesis. *Journal of Neuro-Oncology*, 50(1-2):37–51.

Chaplain, M. A., Lachowicz, M., Szymańska, Z., and Wrzosek, D. (2011). Mathematical modelling of cancer invasion: The importance of cell–cell adhesion and cell–matrix adhesion. *Mathematical Models and Methods in Applied Sciences*, 21(04):719–743.

Cheeseman, B. L., Zhang, D., Binder, B. J., Newgreen, D. F., and Landman, K. A. (2014). Cell lineage tracing in the developing enteric nervous system: superstars revealed by experiment and simulation. *Journal of The Royal Society Interface*, 11(93):20130815.

Chen, Y., Dodd, S. J., Tangrea, M. A., Emmert-Buck, M. R., and Koretsky, A. P. (2013). Measuring collective cell movement and extracellular matrix interactions using magnetic resonance imaging. *Scientific Reports*, 3:1879.

Clay, M. R. and Halloran, M. C. (2010). Control of neural crest cell behavior and migration: insights from live imaging. *Cell Adhesion & Migration*, 4(4):586–594.

Colombi, A., Scianna, M., Painter, K. J., and Preziosi, L. (2020). Modelling chase-and-run migration in heterogeneous populations. *Journal of Mathematical Biology*, 80(1):423–456.

Conner, M. T., Conner, A. C., Bland, C. E., Taylor, L. H., Brown, J. E., Parri, H. R., and Bill, R. M. (2012). Rapid aquaporin translocation regulates cellular water flow: mechanism of hypotonicity-induced subcellular localization of aquaporin 1 water channel. *Journal of Biological Chemistry*, 287(14):11516–11525.

Crampin, E. J., Gaffney, E. A., and Maini, P. K. (1999). Reaction and diffusion on growing domains: scenarios for robust pattern formation. *Bulletin of Mathematical Biology*, 61(6):1093–1120.

Crampin, E. J., Hackborn, W. W., and Maini, P. K. (2002). Pattern formation in reaction-diffusion models with nonuniform domain growth. *Bulletin of Mathematical Biology*, 64(4):747–769.

Dallinga, M. G., Boas, S. E., Klaassen, I., Merks, R. H., van Noorden, C. J., and Schlingemann, R. O. (2015). Tip cells in angiogenesis. *eLS*, pages 1–10.

Dyson, L., Maini, P. K., and Baker, R. E. (2012). Macroscopic limits of individual-based models for motile cell populations with volume exclusion. *Physical Review E*, 86:031903.

Eisenhoffer, G. T., Loftus, P. D., Yoshigi, M., Otsuna, H., Chien, C.-B., Morcos, P. A., and Rosenblatt, J. (2012). Crowding induces live cell extrusion to maintain homeostatic cell numbers in epithelia. *Nature*, 484(7395):546–549.

Erickson, C. (1985). Control of neural crest cell dispersion in the trunk of the avian embryo. *Developmental Biology*, 111(1):138–157.

Evans, D. J. and Noden, D. M. (2006). Spatial relations between avian craniofacial neural crest and paraxial mesoderm cells. *Developmental Dynamics: an official publication of the American Association of Anatomists*, 235(5):1310–1325.

Friedl, P. and Gilmour, D. (2009). Collective cell migration in morphogenesis, regeneration and cancer. *Nature Reviews Molecular Cell Biology*, 10(7):445.

Gavagnin, E. and Yates, C. A. (2018). Stochastic and deterministic modeling of cell migration. *Integrated Population Biology and Modeling*, 39:37.

Genuth, M. A., Allen, C. D., Mikawa, T., and Weiner, O. D. (2018). Chick cranial neural crest cells use progressive polarity refinement, not contact inhibition of locomotion, to guide their migration. *Developmental Biology*, 444:S252–S261.

Gerisch, A. and Chaplain, M. (2008). Mathematical modelling of cancer cell invasion of tissue: local and non-local models and the effect of adhesion. *Journal of Theoretical Biology*, 250(4):684–704.

Gilbert, S. (2000). *Developmental Biology. 6th edition. The Neural Crest.* Sinauer Associates.

Giniūnaitė, R., Baker, R. E., Kulesa, P. M., and Maini, P. K. (2020a). Modelling collective cell migration: neural crest as a model paradigm. *Journal of Mathematical Biology*, 80(1):481–504.

Giniūnaitė, R., McLennan, R., McKinney, M. C., Baker, R. E., Kulesa, P. M., and Maini, P. K. (2020b). An interdisciplinary approach to investigate collective cell migration in neural crest. *Developmental Dynamics*, 249(3):270–280.

Gurdon, J. (1995). Normal table of xenopus laevis (daudin). *Trends in Genetics*, 11(10):418.

Hacker, A. and Guthrie, S. (1998). A distinct developmental programme for the cranial paraxial mesoderm in the chick embryo. *Development*, 125(17):3461–3472.

Hartigan, J. A. and Wong, M. A. (1979). Algorithm as 136: A k-means clustering algorithm. *Journal of the Royal Statistical Society. Series C (Applied Statistics)*, 28(1):100–108.

Huang, C., Kratzer, M.-C., Wedlich, D., and Kashef, J. (2016). E-cadherin is required for cranial neural crest migration in Xenopus laevis. *Developmental Biology*, 411(2):159–171.

Isaacson, E. and Keller, H. B. (2012). *Analysis of numerical methods.* Courier Corporation.

Jones, J. E. (1924). On the determination of molecular fields. II. From the equation of state of a gas. *Proceedings of the Royal Society of London. Series A, Containing Papers of a Mathematical and Physical Character*, 106(738):463–477.

Kalluri, R. and Weinberg, R. A. (2009). The basics of epithelial-mesenchymal transition. *The Journal of Clinical Investigation*, 119(6):1420–1428.

Kanso, E. and Saintillan, D. (2015). Special issue editorial: Emergent collective behavior: From fish schools to bacterial colonies. *Journal of Nonlinear Science*, 25(5):1051–1052.

Kim, Y., Lawler, S., Nowicki, M. O., Chiocca, E. A., and Friedman, A. (2009). A mathematical model for pattern formation of glioma cells outside the tumor spheroid core. *Journal of Theoretical Biology*, 260(3):359–371.

Kontges, G. and Lumsden, A. (1996). Rhombencephalic neural crest segmentation is preserved throughout craniofacial ontogeny. *Development*, 122(10):3229–3242.

Kulesa, P. M., Bailey, C. M., Kasemeier-Kulesa, J. C., and McLennan, R. (2010). Cranial neural crest migration: new rules for an old road. *Developmental Biology*, 344(2):543–554.

Kulesa, P. M. and Fraser, S. E. (2000). In ovo time-lapse analysis of chick hindbrain neural crest cell migration shows cell interactions during migration to the branchial arches. *Development*, 127(6):1161–1172.

Kulesa, P. M., Morrison, J. A., and Bailey, C. M. (2013). The neural crest and cancer: a developmental spin on melanoma. *Cells Tissues Organs*, 198(1):12–21.

Kulesa, P. M., Teddy, J. M., Stark, D. A., Smith, S. E., and McLennan, R. (2008). Neural crest invasion is a spatially-ordered progression into the head with higher cell proliferation at the migratory front as revealed by the photoactivatable protein, KikGR. *Developmental Biology*, 316(2):275 – 287.

Landman, K. A., Simpson, M. J., and Newgreen, D. F. (2007). Mathematical and experimental insights into the development of the enteric nervous system and Hirschsprung's disease. *Development, Growth & Differentiation*, 49(4):277–286.

Landolt, R., Vaughan, L., Winterhalter, K., and Zimmermann, D. (1995). Versican is selectively expressed in embryonic tissues that act as barriers to neural crest cell migration and axon outgrowth. *Development*, 121(8):2303–2312.

Lemons, D. S. and Langevin, P. (2002). *An introduction to stochastic processes in physics*. Johns Hopkins University Press.

MacGabhann, F., Ji, J. W., and Popel, A. S. (2006). Computational model of vascular endothelial growth factor spatial distribution in muscle and pro-angiogenic cell therapy. *PLoS Computational Biology*, 2(9):e127.

Marinari, E., Mehonic, A., Curran, S., Gale, J., Duke, T., and Baum, B. (2012). Live-cell delamination counterbalances epithelial growth to limit tissue overcrowding. *Nature*, 484(7395):542–545.

Matsiaka, O. M., Penington, C. J., Baker, R. E., and Simpson, M. J. (2018). Discrete and continuum approximations for collective cell migration in a scratch assay with cell size dynamics. *Bulletin of Mathematical Biology*, 80(4):738–757.

Mayor, R. and Carmona-Fontaine, C. (2010). Keeping in touch with contact inhibition of locomotion. *Trends in Cell Biology*, 20(6):319–328.

McKinney, M. C., McLennan, R., Giniunaite, R., Baker, R. E., Maini, P. K., Othmer, H. G., and Kulesa, P. M. (2020). Visualizing mesoderm and neural crest cell dynamics during chick head morphogenesis. *Developmental Biology*, 461(2):184 – 196.

McLennan, R., Bailey, C. M., Schumacher, L. J., Teddy, J. M., Morrison, J. A., Kasemeier-Kulesa, J. C., Wolfe, L. A., Gogol, M. M., Baker, R. E., Maini, P. K., et al. (2017). DAN (NBL1) promotes collective neural crest migration by restraining uncontrolled invasion. *Journal of Cell Biology*, 216(10):3339–3354.

McLennan, R., Dyson, L., Prather, K. W., Morrison, J. A., Baker, R. E., Maini, P. K., and Kulesa, P. M. (2012). Multiscale mechanisms of cell migration during development: theory and experiment. *Development*, 139(16):2935–2944.

McLennan, R., McKinney, M. C., Teddy, J. M., Morrison, J. A., Kasemeier-Kulesa, J. C., Ridenour, D. A., Manthe, C. A., Giniunaite, R., Robinson, M., Baker, R. E., et al. (2020). Neural crest cells bulldoze through the microenvironment using aquaporin 1 to stabilize filopodia. *Development*, 147(1).

McLennan, R., Schumacher, L. J., Morrison, J. A., Teddy, J. M., Ridenour, D. A., Box, A. C., Semerad, C. L., Li, H., McDowell, W., Kay, D., et al. (2015a). Neural crest migration is driven by a few trailblazer cells with a unique molecular signature narrowly confined to the invasive front. *Development*, 142 11:2014–25.

McLennan, R., Schumacher, L. J., Morrison, J. A., Teddy, J. M., Ridenour, D. A., Box, A. C., Semerad, C. L., Li, H., McDowell, W., Kay, D., Maini, P. K., Baker, R. E., and Kulesa, P. M. (2015b). VEGF signals induce trailblazer cell identity that drives neural crest migration. *Developmental Biology*, 407(1):12–25.

McLennan, R., Teddy, J. M., Kasemeier-Kulesa, J. C., Romine, M. H., and Kulesa, P. M. (2010). Vascular endothelial growth factor (VEGF) regulates cranial neural crest migration in vivo. *Developmental Biology*, 339(1):114–125.

Merchant, B., Edelstein-Keshet, L., and Feng, J. J. (2018). A Rho-GTPase based model explains spontaneous collective migration of neural crest cell clusters. *Developmental Biology*, 444:S262–S273.

Middleton, A. M., Fleck, C., and Grima, R. (2014). A continuum approximation to an off-lattice individual-cell based model of cell migration and adhesion. *Journal of Theoretical Biology*, 359:220–232.

Morrison, J. A., McLennan, R., Wolfe, L. A., Gogol, M. M., Meier, S., McKinney, M. C., Teddy, J. M., Holmes, L., Semerad, C. L., Box, A. C., et al. (2017). Single-cell transcrip-

tome analysis of avian neural crest migration reveals signatures of invasion and molecular transitions. *Elife*, 6:1–27.

Mort, R. L., Ross, R. J., Hainey, K. J., Harrison, O. J., Keighren, M. A., Landini, G., Baker, R. E., Painter, K. J., Jackson, I. J., and Yates, C. A. (2016). Reconciling diverse mammalian pigmentation patterns with a fundamental mathematical model. *Nature communications*, 7:10288.

Murray, J. D. (2002). *Mathematical Biology I. An Introduction*, volume 17 of *Interdisciplinary Applied Mathematics*. Springer, New York, 3 edition.

Murray, P. J., Edwards, C. M., Tindall, M. J., and Maini, P. K. (2012). Classifying general nonlinear force laws in cell-based models via the continuum limit. *Physical Review E*, 85(2):021921.

Nagatomo, K.-I. and Hashimoto, C. (2007). Xenopus *hairy2* functions in neural crest formation by maintaining cells in a mitotic and undifferentiated state. *Developmental Dynamics: an official publication of the American Association of Anatomists*, 236(6):1475–1483.

Newgreen, D., Southwell, B., Hartley, L., and Allan, I. (1996). Migration of enteric neural crest cells in relation to growth of the gut in avian embryos. *Cells Tissues Organs*, 157(2):105–115.

Newgreen, D. F., Zhang, D. C., Binder, B., Simpson, M. J., Landman, K. A., Enomoto, H., and Young, H. (2009). Social controls of migration and proliferation of neural crest-derived cells in the gut. *Neurogastroenterology & Motility*, 21(2):9.

Nichane, M., de Crozé, N., Ren, X., Souopgui, J., Monsoro-Burq, A. H., and Bellefroid, E. J. (2008). Hairy2–Id3 interactions play an essential role in Xenopus neural crest progenitor specification. *Developmental Biology*, 322(2):355–367.

Noden, D. M. (1988). Interactions and fates of avian craniofacial mesenchyme. *Development*, 103:121–140.

Painter, K. J., Bloomfield, J., Sherratt, J., and Gerisch, A. (2015). A nonlocal model for contact attraction and repulsion in heterogeneous cell populations. *Bulletin of Mathematical Biology*, 77(6):1132–1165.

Palm, M. M., Dallinga, M. G., van Dijk, E., Klaassen, I., Schlingemann, R. O., and Merks, R. M. H. (2016). Computational screening of tip and stalk cell behavior proposes a role for apelin signaling in sprout progression. *PLOS One*, 11(11):1–31.

Perris, R. and Perissinotto, D. (2000). Role of the extracellular matrix during neural crest cell migration. *Mechanisms of Development*, 95(1):3 – 21.

Plickert, G. and Kroiher, M. (1988). Proliferation kinetics and cell lineages can be studied in whole mounts and macerates by means of brdu/anti-brdu technique. *Development*, 103(4):791–794.

Purcell, E. M. (1977). Life at low Reynolds number. *American Journal of Physics*, 45(1):3–11.

Ridenour, D. A., McLennan, R., Teddy, J. M., Semerad, C. L., Haug, J. S., and Kulesa, P. M. (2014). The neural crest cell cycle is related to phases of migration in the head. *Development*, 141(5):1095–1103.

Rios, A. C., Serralbo, O., Salgado, D., and Marcelle, C. (2011). Neural crest regulates myogenesis through the transient activation of Notch. *Nature*, 473(7348):532.

Roache, P. J. (2002). Code verification by the method of manufactured solutions. *Journal of Fluids Engineering*, 124(1):4–10.

Rodriguez, M. Z., Comin, C. H., Casanova, D., Bruno, O. M., Amancio, D. R., Costa, L. d. F., and Rodrigues, F. A. (2019). Clustering algorithms: A comparative approach. *PLOS One*, 14(1):1–34.

Roycroft, A., Szabó, A., Bahm, I., Daly, L., Charras, G., Parsons, M., and Mayor, R. (2018). Redistribution of adhesive forces through Src/FAK drives contact inhibition of locomotion in neural crest. *Developmental Cell*, 45(5):565–579.

Sanes, D. (2012). *Development of the Nervous System*. 3rd ed. Oxford: Elsevier, Oxford.

Schumacher, L. J. (2015). *A mathematical exploration of principles of collective cell migration and self-organisation*. PhD thesis, University of Oxford.

Schumacher, L. J. (2019). Neural crest migration with continuous cell states. *Journal of Theoretical Biology*, 481:84–90.

Schumacher, L. J., Kulesa, P. M., McLennan, R., Baker, R. E., and Maini, P. K. (2016). Multidisciplinary approaches to understanding collective cell migration in developmental biology. *Open Biology*, 6(6):160056–66.

Selmeczi, D., Mosler, S., Hagedorn, P. H., Larsen, N. B., and Flyvbjerg, H. (2005). Cell motility as persistent random motion: theories from experiments. *Biophysical Journal*, 89(2):912–931.

Shellard, A., Szabó, A., Trepat, X., and Mayor, R. (2018). Supracellular contraction at the rear of neural crest cell groups drives collective chemotaxis. *Science*, 362(6412):339–343.

Sherratt, J. A., Gourley, S. A., Armstrong, N. J., and Painter, K. J. (2009). Boundedness of solutions of a non-local reaction–diffusion model for adhesion in cell aggregation and cancer invasion. *European Journal of Applied Mathematics*, 20(1):123–144.

Simpson, M. J. (2015). Exact solutions of linear reaction-diffusion processes on a uniformly growing domain: Criteria for successful colonization. *PLOS One*, 10(2):e0117949.

Simpson, M. J., Zhang, D. C., Mariani, M., Landman, K. A., and Newgreen, D. F. (2007). Cell proliferation drives neural crest cell invasion of the intestine. *Developmental Biology*, 302(2):553–568.

Streichan, S. J., Valentin, G., Gilmour, D., and Hufnagel, L. (2011). Collective cell migration guided by dynamically maintained gradients. *Physical Biology*, 8(4):045004.

Szabó, A. and Mayor, R. (2016). Modelling collective cell migration of neural crest. *Current Opinion in Cell Biology*, 42:22–28.

Szabó, A. and Mayor, R. (2018). Mechanisms of neural crest migration. *Annual Review of Genetics*, 52:43–63.

Szabó, A., Melchionda, M., Nastasi, G., Woods, M. L., Campo, S., Perris, R., and Mayor, R. (2016). In vivo confinement promotes collective migration of neural crest cells. *Journal of Cell Biology*, 213(5):543–555.

Szabo, B., Szöllösi, G., Gönci, B., Jurányi, Z., Selmeczi, D., and Vicsek, T. (2006). Phase transition in the collective migration of tissue cells: experiment and model. *Physical Review E*, 74(6):061908.

Teddy, J. M. and Kulesa, P. M. (2004). In vivo evidence for short-and long-range cell communication in cranial neural crest cells. *Development*, 131(24):6141–6151.

Theveneau, E., Marchant, L., Kuriyama, S., Gull, M., Moepps, B., Parsons, M., and Mayor, R. (2010). Collective chemotaxis requires contact-dependent cell polarity. *Developmental Cell*, 19(1):39–53.

Theveneau, E. and Mayor, R. (2011). Collective cell migration of the cephalic neural crest: The art of integrating information. *Genesis*, 49(4):164–176.

Theveneau, E. and Mayor, R. (2012). Neural crest delamination and migration: from epithelium-to-mesenchyme transition to collective cell migration. *Developmental Biology*, 366(1):34–54.

Theveneau, E., Steventon, B., Scarpa, E., Garcia, S., Trepat, X., Streit, A., and Mayor, R. (2013). Chase-and-run between adjacent cell populations promotes directional collective migration. *Nature Cell Biology*, 15(7):763–72.

Tibshirani, R., Walther, G., and Hastie, T. (2001). Estimating the number of clusters in a data set via the gap statistic. *Journal of the Royal Statistical Society: Series B (Statistical Methodology)*, 63(2):411–423.

Tonnesen, M. G., Feng, X., and Clark, R. A. (2000). Angiogenesis in wound healing. *Journal of Investigative Dermatology Symposium Proceedings*, 5(1):40 – 46.

Tosney, K. W. (1982). The segregation and early migration of cranial neural crest cells in the avian embryo. *Developmental Biology*, 89(1):13–24.

Tucker, R. P. and Erickson, C. (1986). The control of pigment cell pattern formation in the California newt, Taricha torosa. *Development*, 97(1):141–168.

Vaeyens, M.-M., Jorge-Peñas, A., Barrasa-Fano, J., Steuwe, C., Heck, T., Carmeliet, P., Roeffaers, M., and Van Oosterwyck, H. (2020). Matrix deformations around angiogenic sprouts correlate to sprout dynamics and suggest pulling activity. *Angiogenesis*, 23(3):315—324.

Van Kampen, N. G. (1992). *Stochastic processes in physics and chemistry*, volume 1. Elsevier.

Woods, M. L., Carmona-Fontaine, C., Barnes, C. P., Couzin, I. D., Mayor, R., and Page, K. M. (2014). Directional collective cell migration emerges as a property of cell interactions. *PLOS One*, 9(9):1–10.

Wynn, M. L., Rupp, P., Trainor, P. A., Schnell, S., and Kulesa, P. M. (2013). Follow-the-leader cell migration requires biased cell–cell contact and local microenvironmental signals. *Physical Biology*, 10(3):035003.

Xu, R. and Wunsch, D. (2005). Survey of clustering algorithms. *IEEE Transactions on Neural Networks*, 16(3):645–678.

Yang, Y., Zheng, H., Zhan, Y., and Fan, S. (2019). An emerging tumor invasion mechanism about the collective cell migration. *American Journal of Translational Research*, 11(9):5301.

Zhang, D., Brinas, I. M., Binder, B. J., Landman, K. A., and Newgreen, D. F. (2010). Neural crest regionalisation for enteric nervous system formation: implications for Hirschsprung's disease and stem cell therapy. *Developmental Biology*, 339(2):280–294.